The Role of Spin in Triplet-Triplet Annihilation Upconversion

Andrew Danos

A thesis submitted in fulfilment of the requirements for the degree of Doctor of Philosophy

The University of New South Wales

School of Chemistry

Faculty of Science

December 2017

THE UNIVERSITY OF NEW SOUTH WALES
Thesis/Dissertation Sheet

Surname or Family name: Danos

First name: Andrew Other name/s:

Abbreviation for degree as given in the University calendar: Phd

School: School of Chemistry Faculty: Faculty of Science

Title: The role of spin in triplet-triplet annihilation upconversion

Abstract

Chemical systems that exhibit photochemical upconversion *via* triplet-triplet annihilation have been studied using a range of fluorescence, absorption, and magnetic spectroscopy techniques. Each part of this investigation furthers understanding of how the emitter properties govern both the efficiency of the overall upconversion process, and the spin dependent annihilation step. Developing this fundamental understanding is vital to enable rational design of high performance emitters, and in turn unlock the potential of upconversion in applications across photovoltaics and light emitting diodes.

Time-resolved and steady-state fluorescence emission spectroscopy was used to compare the performance of a standard upconversion system to one with a deuterated emitter. For perylene, deuteration was found to decrease the rate constant for first order non-radiative losses by 16%, while leaving other electronic and kinetic parameters unchanged. This selective control over one of the emitter properties allowed for straightforward and direct comparison between the systems, and resulted in a 45% increase in upconverter performance under low intensity excitation.

Transient absorption spectroscopy was used to characterise a range of commonly used emitter species. The family of emitters investigated were found to be largely similar in their decay kinetics, indicating that any comparative advantage comes about primarily through different intrinsic efficiencies of the annihilation step. A system with two emitter species was also studied, and its superior performance attributed to an improved rate of exciton transport, rather than annihilation events between heterogeneous emitter pairs.

Finally, magnetic field effects and resonance spectroscopy were pursued as ways to probe the nature of spin mixing in the annihilation event. Fibre based experimental platforms were developed to enable these techniques for air sensitive solutions, although resonance signal remained elusive. Nonetheless, modelling the effects of static magnetic fields on upconversion emission reveals the critical importance of emitter pair orientation as the spins interact. In the absence of external magnetic fields, this orientation factor is identified as the key determinant of the annihilation outcome, rather than the individual spin states of the interacting triplets as was previously thought.

FOR OFFICE USE ONLY Date of completion of requirements for Award:

ORIGINALITY STATEMENT

'I hereby declare that this submission is my own work and to the best of my knowledge it contains no materials previously published or written by another person, or substantial proportions of material which have been accepted for the award of any other degree or diploma at UNSW or any other educational institution, except where due acknowledgement is made in the thesis. Any contribution made to the research by others, with whom I have worked at UNSW or elsewhere, is explicitly acknowledged in the thesis. I also declare that the intellectual content of this thesis is the product of my own work, except to the extent that assistance from others in the project's design and conception or in style, presentation and linguistic expression is acknowledged.'

Signed ……..

Date ……..

Declaration of Authorship

I hereby declare that this submission is my own work and to the best of my knowledge it contains no materials previously published or written by another person, or substantial proportions of material which have been accepted for the award of any other degree or diploma at UNSW or any other educational institution, except where due acknowledgement is made in the thesis. Any contribution made to the research by others, with whom I have worked at UNSW or elsewhere, is explicitly acknowledged in the thesis. I also declare that the intellectual content of this thesis is the product of my own work, except to the extent that assistance from others in the project's design and conception or in style, presentation and linguistic expression is acknowledged.

Andrew Danos

. . . . . .

Date

. . . . . .

Abstract

Chemical systems that exhibit photochemical upconversion *via* triplet–triplet annihilation have been studied using a range of fluorescence, absorption, and magnetic spectroscopy techniques. Each part of this investigation furthers understanding of how the emitter properties govern both the efficiency of the overall upconversion process, and the spin dependent annihilation step. Developing this fundamental understanding is vital to enable rational design of high performance emitters, and in turn unlock the potential of upconversion in applications across photovoltaics and light emitting diodes.

Time-resolved and steady-state fluorescence emission spectroscopy was used to compare the performance of a standard upconversion system to one with a deuterated emitter. For perylene, deuteration was found to decrease the rate constant for first order non-radiative losses by 16 %, while leaving other electronic and kinetic parameters unchanged. This selective control over one of the emitter properties allowed for straightforward and direct comparison between the systems, and resulted in a 45 % increase in upconverter performance under low intensity excitation.

Transient absorption spectroscopy was used to characterise a range of commonly used emitter species. The family of emitters investigated were found to be largely similar in their decay kinetics, indicating that any comparative advantage comes about primarily through different intrinsic efficiencies of the annihilation step. A system with two emitter species was also studied, and its superior performance attributed to an improved rate of exciton transport, rather than annihilation events between heterogeneous emitter pairs.

Finally, magnetic field effects and resonance spectroscopy were pursued as ways to probe the nature of spin mixing in the annihilation event. Fibre based experimental platforms were developed to enable these techniques for air sensitive solutions, although resonance signal remained elusive. Nonetheless, modelling the effects of static magnetic fields on upconversion emission reveals the critical importance of emitter pair orientation as the spins interact. In the absence of external magnetic fields, this orientation factor is identified as the key determinant of the annihilation outcome, rather than the individual spin states of the interacting triplets as was previously thought.

Acknowledgements

A great many people deserve my recognition and thanks for the roles they have played over the course of this research project.

To the laserlab postdocs, whether ultrafast, gas phase, or ultraslow. Thank you for your patient instruction, encouragement, and technical support over the years. Particular mentions go Tim Schulze, Miroslav Dvořák, and Klaas Nauta in these regards. Thanks also to Rowan MacQueen and Murad Tayebjee for sharing in interesting work on parallel projects. Most of all, thank you Dennis Cheng, for absolutely everything from start to finish.

To my informal team of moral supporters, who gave generously of their time when the times were toughest. Thank you Meredith Jordan, Alex Argyros, Ellen Braybon, and Olha Krechkivska for your advice, perspective, and waterproof shoulders. Each of you provides proof by example that the faustian aspects of success in this profession can be resisted, and even overcome. Thanks as well to Mum and Dad for patient advice and support during later administrative challenges.

To the office and lab buddies, all of whom have since gone on to bigger and better things. Congratulations and thanks to Drs Tom Keevers, Derrick Roberts, Mitch Quinn, and even former demonstratees Nate Davis and Kelvin Lee. Our day-to-day shenanigans were a large part of what made the science so enjoyable. Know that you left laserlab impoverished by your departures, but that the best parts of it endure with us.

To the other good friends I leave behind; Vineeth Yasasrapudi, Callan Wilcox, Yu Liu, Jo Guse, Alireza Kharazmi, and Keiran Rowell. I wish you all the luck in the world, in the sincere hope that you need none of it.

Finally to my deerest dears, Miranda and Henry. Thank you for all of your love and support. For that alone, the hardships have been bearable — and worthwhile.

Contents

List of Figures

Abbreviations

a-Si	Amorphous silicon
BPEA	9,10-bis(phenylethynyl)anthracene
CBPEA	2-chloro-9,10-bis(phenylethynyl)anthracene
c-Si	Crystalline silicon
CW-	Continuous-wave
DPA	9,10-diphenylanthracene
EL	Electroluminescence
ESR	Electron Spin Resonance
FCF	Frank-Condon factor
ISC	Intersystem crossing
ML	Magnetoluminescence
ODMR	Optically detected magnetic resonance
OEPPd	Palladium (II) octaethylporphyrin
(O)LED	(Organic) light emitting diode
PAH	Polycyclic aromatic hydrocarbon
PL	Photoluminescence
PQ_4Pd	Palladium (II) tetrakisquinoxalinoporphyrin
PV	Photovoltaics
SQ	Shockley-Queisser
TA	Transient absorption
TET	Triplet energy transfer
TPTBPt	Pt(II) meso-tetraphenyl tetrabenzoporphine
TR-	Time-resolved
TTA	Triplet-triplet annihilation
UC	Upconversion

Chapter 1

Introduction

> *"Do you think enlightenment should be easy? It is not.*
> *Everyone alive has already spent all the time that ever was upon the way,*
> *some with more energy than others."*
>
> —Narrator, *Saiyūki (Monkey)*, NTV 1978–1980

This chapter introduces the concept of photochemical upconversion *via* triplet-triplet annihilation — a promising technology in the field of third generation photovoltaics. The background and general motivations for research in this area are discussed, and the molecular processes involved in upconversion leading from initial absorption to final emission are detailed.

Particular attention is then given to the spin of the emitter triplets. Annihilation occurs when two excitons fuse to form a higher energy emissive singlet, and understanding how this process depends on the spin states of the participating excitons forms the central motivation for this body of work. The potential for static and resonant magnetic fields to exert control over annihilation is explored in terms of the spin states of individual excitons and of interacting pairs.

Finally, general methods to detect and influence populations of triplet excitons are presented briefly. Development of experiments that apply these methods form the content of subsequent chapters, each aimed towards gaining a more complete understanding of the annihilation step and the overall upconversion process.

1.1 Energy Consumption and the Role of Photovoltaics

1.1.1 Energy and Civilisation

Humans are unique amongst life on Earth in our advanced ability to adapt our environment to suit our needs, rather than adapting ourselves to it. Energy is required to make these adaptations, as they often involve a decrease in local entropy; for example assembling a house from disorganised bricks, or creating a temperature gradient with a refrigerator. Unfortunately the human body is endowed with only a modest ability to store or expend energy, which limits the scope of environmental transformations that can be achieved by an individual.

From this starting point, the historical progress of humanity and civilisation can be understood as a cyclical, lurching effort to overcome this innate limitation. New technologies are developed that give access to new sources and forms of energy. These energy sources are then used to expand our control over our environment. Using this control to increase quality of life, leisure time, and population size then provides the necessary conditions for the development of yet more advanced technology.

The successive revolutions of this cycle mark out critical milestones in the development of human civilisation. Early stone tools allowed human muscle to reshape stone and wood into shelter and weapons for hunting. Later, mastery of fire unlocked the chemical energy of the wood to provide light and heat for nocturnal activity and cooking. Much later, steam engines allowed conversion of heat into motion, which together with energy-rich fuels such as coal began the industrial revolution. Today oil is the preferred fuel, and the energy released from its combustion can also be converted into electricity for long distance transmission, and storage in batteries. [1]

The self-reinforcing nature of this virtuous cycle has resulted in exponential growth of global energy demand, gross world product, and population over the last two centuries. [2–6] These growth trends are shown in Figure 1.1, and stimulate reasonable concerns about how long such growth can be sustained on a planet of finite resources.

1.1.2 Satisfying Current and Future Energy Demand

Despite considerable advances in the scale of energy production, the primary underlying process has not changed significantly since ancient times. Now, as then, combustion of fuels in atmospheric oxygen is used to convert chemical energy to heat — either for immediate and direct use, or conversion and storage in some other form of energy.

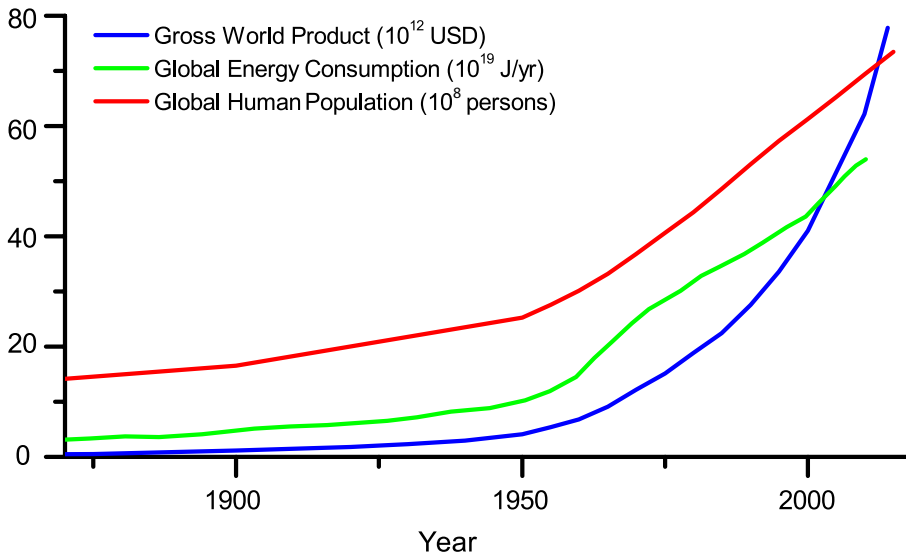

FIGURE 1.1: Exponential growth of global population,[4,5] energy consumption,[6] and gross world product.[2,3]

The combustion process usually releases carbon dioxide as a waste product though, and invariably consumes the fuel.

In order to satisfy growing domestic energy demand, nations must therefore secure exclusive access to ever larger fuel reserves, leading to geopolitical tensions in cases where these reserves exist outside national borders.[7,8] More recently, energy related tensions have been compounded by the additional need to mitigate the effects of carbon dioxide emissions on atmospheric thermal properties and climate.[9,10] Technically, the simplest way to do this is to limit the scale of global fuel combustion, but without viable and scalable alternative energy sources this outcome seems unlikely to occur.

In contrast to fuel combustion, renewable energy sources are those which are not significantly depleted by human use. Additionally, the ongoing use of most forms of renewable energy (but not all) do not negatively impact the local or global environment. Primitive methods of harnessing renewable energy have existed alongside simple combustion for most of human history — in the form of windmills, waterwheels, or sun drying of garments or food. It is only in recent decades that using renewables for large scale electricity generation has been seriously considered and pursued. The allure of these renewable sources lies in their potential to provide energy security without the ongoing need for fuels, while simultaneously supporting reductions in carbon dioxide emissions alongside growing energy consumption.

Of the different forms of renewable energy, solar is uniquely advantaged as a potential alternative to fuel combustion due to its geographical ubiquity and potential scale. In 2015 global energy consumption was equivalent to 5×10^{20} J, while in the same period approximately 4×10^{24} J of solar radiation was received across the surface of the Earth.[1,11]

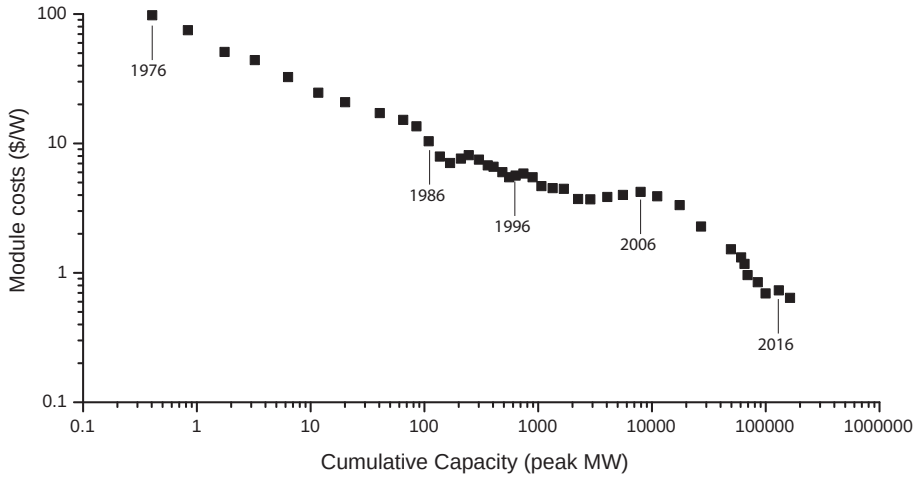

FIGURE 1.2: Trends in PV costs and installed capacity.[12]

Using photovoltaic (PV) cells allows this energy to be converted directly into electricity, without the need for moving parts or working fluids. Even taking into account the considerable challenges presented by conversion efficiency, intermittency, and storage, the vast quantities of available energy make pursuing solar PV as a core replacement technology an attractive proposition.

The main disadvantage of PV, and the enduring barrier to widespread deployment, is cost. Although PV installations operate with low maintenance and zero ongoing fuel costs, the high temperature manufacturing steps associated with silicon refining and doping lead to a large (although rapidly falling) upfront cost in establishing capacity.[12–14] While the equivalent setup costs for building new coal or nuclear plants are similarly high, in many cases this infrastructure already exists and need not be commissioned a second time. To become an economically favourable replacement technology, the large upfront cost of PV must fall to become competitive with the (smaller) ongoing costs of other established technologies.

Nonetheless, as PV manufacturing costs continue to decline and energy conversion efficiencies grow, this balance has begun to shift in recent years.[15,16] Figure 1.2 shows the historic trends in PV costs, and how research and market forces are leading to accelerating growth in installed PV capacity.[12] While total installed peak PV capacity is still far below average global consumption ($\sim 1.6 \times 10^7$ MW), extrapolating the trends in this figure indicate that a crossover point is likely to occur in the middle of this century. This outcome cannot be taken for granted though, as maintaining the trend of decreasing costs will require a sustained (if not growing) effort to deliver ever greater advances in PV manufacture and technology.

1.1.3 Operation and Limitations of Semiconductor Photovoltaics

Apart from reducing fundamental manufacturing costs and exploiting economies of scale, the other key approach to improving PV competitiveness is to develop devices with higher energy conversion efficiencies. Such devices would require fewer manufactured cells to provide the same energy output, with a potentially lower upfront cost. A brief consideration of the mechanism of electricity generation by PV devices reveals key areas in which there is large headroom to improve PV efficiencies.

On a microscopic level, typical semiconductor PV devices work by first absorbing photons of solar radiation. The energy of the photon promotes an electron from the valence band to the conduction band of the material, which is physically separated from the resulting valence band hole by electric fields across the device. Before separation, the excited yet bound electron-hole pair is referred to as an exciton. The separation of charges in the active layer of the device results in the setup of a usable voltage across its edges, and for photons with energies equal to the bandgap of the material (E_g) this simple treatment is sufficient. In contrast, photons with energies larger than the bandgap are absorbed, but any energy in excess of E_g is lost through rapid thermalisation of charge carriers back to the edges of their bands. Photons with energies lower than the bandgap cannot excite valence band electrons, and are not absorbed at all. These three processes are illustrated in Figure 1.3.[17–19]

Since the spectrum of solar radiation contains photons across a broad range of frequencies, it is not possible for a single bandgap material to efficiently absorb them all. Instead, an optimal compromise exists between high bandgap materials absorbing more efficiently from a restricted part of the solar spectrum, and low bandgap materials absorbing more broadly but less efficiently. Figure 1.4 shows how this choice controls the

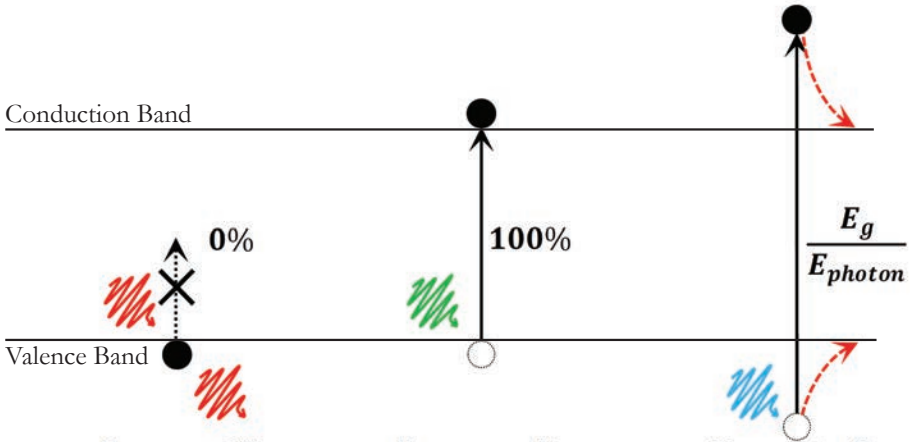

FIGURE 1.3: Semiconductor absorption efficiencies for low (red), matching (green), and high energy (blue) photons.

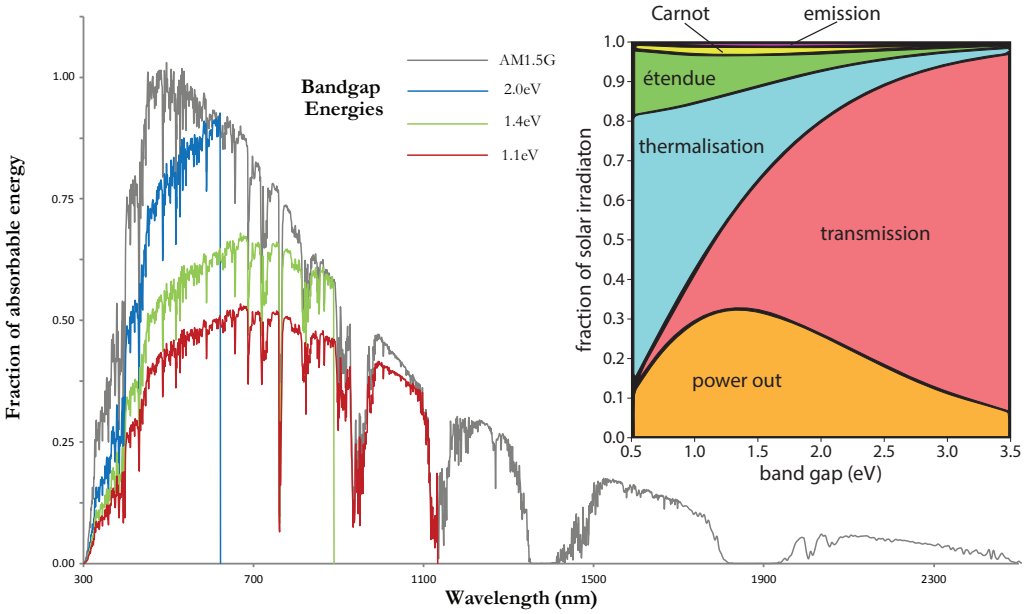

FIGURE 1.4: Absorbable fractions of the solar spectrum (AM1.5G *via* NREL RRDC) for materials with different bandgaps. Inset with device loss mechanisms reproduced with permission from Tayebjee *et al.*, copyright 2015 American Chemical Society.[23]

amount of absorbable energy for different bandgap materials at different wavelengths, with the ideal bandgap maximising the integral. By considering this balance as well as other unavoidable sources of thermodynamic energy losses for real devices (such as the black body emission of the PV device itself), it can be shown that a material with a bandgap of 1.34 eV is best matched to the output of the Sun, and has a limiting conversion efficiency of 33.7 %.[20,21] Further analysis can even attribute the energy losses to different mechanisms, with the Figure 1.4 inset visualising the potential efficiency gains associated with addressing each mechanism for different bandgap energies.[22,23] In sequence, Figures 1.3, 1.4, and 1.4 inset indicate (visually) how this limiting conversion efficiency and optimum material bandgap are calculated from first principles.

Along with its abundance and extensive use in computing, the implications of this Shockley-Queisser (SQ) limit helps explains the historical dominance of silicon — with a bandgap of 1.1 eV — as a ubiquitous PV material. Despite this advantage, purifying and processing raw silicon remains the biggest manufacturing cost factor for modern PV devices.[24–26] Replacing crystalline silicon (c-Si) with cheaper thin film materials such as amorphous silicon (a-Si) or CdTe was until recently envisaged to be the next breakthrough in PV research, and efforts to develop these films have been designated "second generation" PV. Unfortunately for researchers in this area, sustained investment in c-Si manufacturing technology and capacity over the last five years (primarily in China) has resulted in the costs of first generation PV modules dropping below the less mature thin

film technologies, obviating their main competitive advantage and curtailing further research funding.[27] Dye-sensitised cells similarly promised a short route to high efficiency and low cost modules, but the initially steep trajectory of cell efficiencies seemed to stall soon after their discovery.[28–36] It remains to be seen whether similar recent excitement about perovskite cells — another thin layer technology — will translate into competitive and market ready devices.[37]

1.2 Spectral Management and Upconversion

1.2.1 Overcoming Semiconductor Limitations

In contrast to second generation approaches, third generation PV encompasses efforts to directly overcome the SQ limit, which crucially only applies for *single bandgap* materials exposed to radiation *from the Sun*. As a result, third generation approaches can be roughly partitioned into those that introduce additional band structure to the absorbing material, and those that modify the solar spectrum.[38] Both of these approaches have the potential to be applied to or directly incorporate first generation c-Si cells, and so are safely complimentary rather than precariously competitive with the mature c-Si PV industry.[39–41]

Examples of third generation technologies include hot carrier cells, in which high energy charge carriers are extracted before they can thermalise.[42] Tandem cells use multiple semiconductor layers stacked upon each other, with the highest bandgap materials on top to efficiently absorb high energy photons while passing low energy photons to lower bandgap materials deeper in the device.[43–45] Similarly, gratings or other dispersive optical elements can be used to separate the solar spectrum spatially and direct different wavelength ranges to separate PV devices with carefully matched bandgaps.[46] These approaches result in extremely high efficiency devices (over 45 % in some cases), but ones that are also significantly more expensive than single bandgap devices due to their complex and multi-stage manufacturing process[28,43]

Spectral management is perhaps the most "human" of third generation approaches, as it attempts to adapt the distribution of solar radiation to match the PV device, rather than adapting the cell to its surroundings. The ideal illumination for a single bandgap device would be monochromatic with photon energy equal to the bandgap, as this would allow complete and efficient absorption. To adapt the solar spectrum more closely to this ideal, upconversion (UC) and downconversion processes can be used to combine low energy photons into higher energy ones, and to split higher energy photons into multiple lower energy ones respectively.

As spectral management aims to change the illumination rather than the cell, it is broadly compatible with existing PV technologies and manufacturing processes. Rather than reinventing the c-Si "wheel", this approach can work in tandem to further improve it and other PV technologies.[47–50] Spectral management also broadens the scope of PV research to include materials with bandgaps that would otherwise be considered too high or too low for any kind of efficient device. The inherent challenge of spectral management is that photons rarely interact with each other, and must be coaxed into doing so through their interactions with matter.

1.2.2 Spectral Management by Coherent Processes

Practical methods of achieving UC (and downconversion) have existed for over half a century, and exploit nonlinearity in the optical response of certain crystals. The classical electric polarisation response of a material exposed to an electric field, such as that of an electromagnetic wave, is given by a Taylor series in the applied electric field:

$$\mathbf{P} = \epsilon_0(\chi^1\mathbf{E} + \chi^2\mathbf{E}^2 + \chi^3\mathbf{E}^3 + \ldots) \tag{1.1}$$

where $\mathbf{P}$ is the polarisation of the material, $\mathbf{E}$ is the electric field, ϵ_0 is the vacuum permittivity, and χ^n are the different order terms of the material susceptibility. Most materials have vanishingly small values of χ^2 and higher order terms, and so these are ignored in normal circumstances and low intensity illumination. The resulting linear relation between $\mathbf{P}$ and $\mathbf{E}$ means that wave modes can usually only propagate in a material if they have the same frequency as the driving mode.[51,52]

For materials in which χ^2 is non-zero, exposure to high intensity electromagnetic waves causes the $\chi^2\mathbf{E}^2$ term to become non-negligible. The effect of this extra term is to allow new wave modes to propagate in the material with different frequencies, and to allow energy to be transferred between these modes. The new mode frequencies are $2\omega_1, (\omega_1 + \omega_2), (\omega_1 - \omega_2), 2\omega_2$, and zero, with the specific values of ω_1 and ω_2 determined by the birefringent properties and physical orientation of the nonlinear material relative to the polarisation of the driving mode. The new modes are also constrained by the frequency of the driving mode (ω_d), with $\omega_d = \omega_1 + \omega_2$. In practice, ω_1 and ω_2 are set by carefully matching the wavevectors of the driving mode, desired output mode, and optical axes of the nonlinear material.

For UC, second harmonic generation is achieved when $\omega_1 = \omega_d$, resulting in a doubling of the driving mode's frequency in the $2\omega_1$ output mode. The other resulting allowed modes with $\omega = 0$ correspond to optical DC rectification; an interesting effect, but one

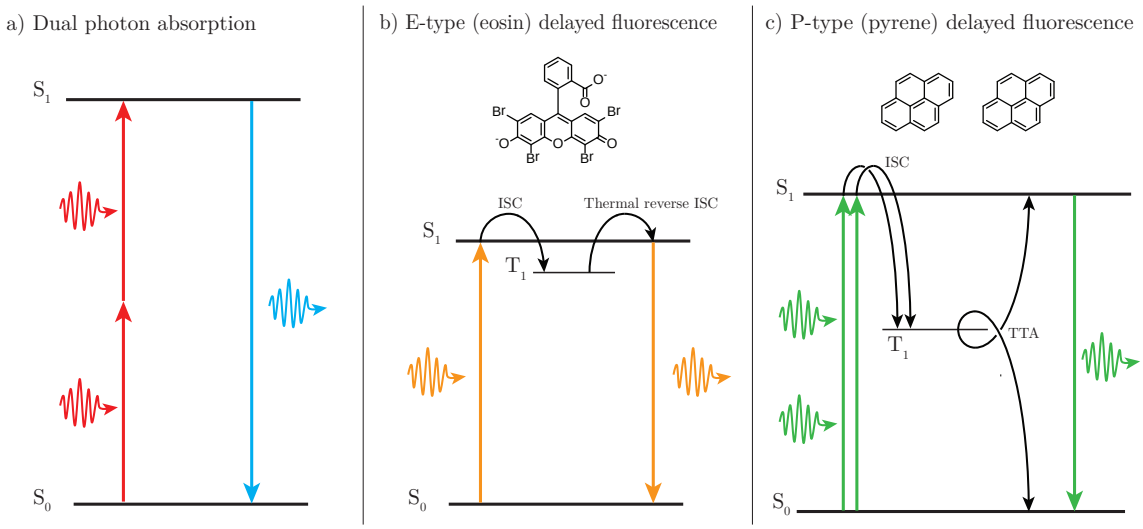

FIGURE 1.5: Molecular absorption and emission processes relevant to upconversion: a) dual photon absorption, b) e-type delayed fluorescence, c) p-type delayed fluorescence.

that finds fewer applications than the driving of higher frequency outputs such as the second harmonic. For downconversion, a choice of $\omega_d > \omega_1 > \omega_2$ allows for generation of frequencies lower than ω_d in the $(\omega_1 - \omega_2)$ and $2\omega_2$ modes. More generally, multiple sequential second or higher harmonic UC steps can be used to generate a high frequency output beam. This beam can then be used as ω_d in a final wavelength tuning stage, and downconverted to generate an arbitrary output — provided that a sufficiently powerful primary excitation source exists. These kinds of photon alchemy are the operating principles behind the tunable femtosecond laser and self-pumped optical parametric oscillator used for experiments in Chapters 2 and 3.

Similar to exploiting the nonlinear response of $\mathbf{P}$, another approach to achieving UC involves higher order absorptivities of some molecules. Although the absolute amount of light absorption grows linearly with low illumination intensities, simpler versions of the Beer-Lambert law can be extended with a second order term corresponding to absorption of two photons simultaneously under strong illumination.[53] Dual photon absorption can lead to the excitation of molecular states energetically inaccessible by individual photons, and subsequent emission from higher frequencies than the excitation source. The energy levels and transitions associated with this process are shown in Figure 1.5a.

Despite the different paradigms for electromagnetic radiation used to explain these phenomena, their common reliance on nonlinear response is no coincidence. Nonlinear responses also feature in other forms of UC, and are a reflection of the necessity for matter to mediate the interaction between two photons. Both of the above forms of spectral management therefore require large intensities in order to access higher order material response terms. For dual photon absorption, this high intensity determines the probability that a molecule will encounter two photons simultaneously — a positional

coherence of sorts. For nonlinear crystals the existence of a driving "mode" also implies that this mode is itself phase coherent. The phase matching conditions that determine ω_1 and ω_2 subsequently make phase coherence of ω_d a strict requirement.

These coherence and intensity requirements ultimately preclude nonlinear optics and dual photon absorption from applications in third generation PV, as solar radiation is neither phase coherent nor sufficiently intense (without concentration) to allow these approaches to significantly alter the shape of the solar excitation spectrum.

1.2.3 Incoherent Photochemical Upconversion

In order to achieve UC without an intense and coherent source, some mechanism must be used to store the energy of one photon in preparation for the arrival of a second. Although discovered at around the same time as the first demonstrations of UC by nonlinear optics, it is only in recent years that delayed fluorescence has been used to develop incoherent versions of UC.[54–58]

Two distinct kinds of delayed fluorescence were first observed in eosin and pyrene, from which they derived their labels e-type and p-type.[59,60] Both versions begin with the molecule absorbing a photon to access a singlet excited state. For most kinds of emissive molecules (and even the majority of the individual molecules in a sample capable of delayed fluorescence) this absorption is followed by prompt fluorescence with lifetimes in the range of picoseconds to nanoseconds.[61] For some molecules, intersystem crossing (ISC) allows excitation to transfer to the triplet state, where it can remain stable for some microseconds due to the spin forbidden nature of phosphorescence and other non-radiative decay processes back to the singlet ground state. As a result, the triplet state itself can act as temporary storage for the energy of an absorbed photon, in the form of triplet excitons.[62]

For e-type delayed fluorescence, a small energy gap between the singlet and triplet state can allow for thermal repopulation of the singlet state *via* reverse ISC. Upon reattaining singlet multiplicity the excited molecule then fluoresces as normal, but with a significantly extended (temperature dependant) lifetime measured relative to the excitation pulse — hence the term delayed fluorescence. The energy levels and transitions associated with this process are shown in Figure 1.5b.[59]

For p-type delayed fluorescence, interactions between pairs of excited triplets can lead to triplet-triplet annihilation (TTA). One of the possible outcomes of TTA is that the excitation energies of both participants are transferred to a single molecule in a singlet state, while the other triplet exciton is quenched. While such transitions would be

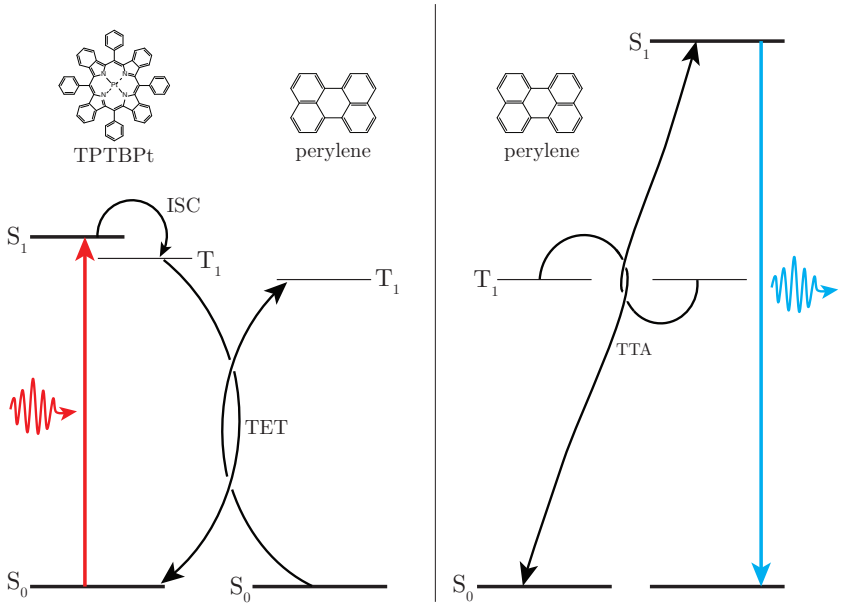

FIGURE 1.6: Absorption and emission in sensitised photochemical TTA upconversion.

spin forbidden individually, TTA proceeds while conserving the total spin of the pair. The singlet excited molecule can then fluoresce as normal, once again with an extended lifetime relative to the excitation. This process is shown in Figure 1.5c. [58,60]

Observant readers will note that neither of the above processes result in actual UC if high energy photons were used to initially excite the molecules. To generate photons that are unconverted relative to excitation, a separate triplet sensitiser can be used instead of relying on ISC in the fluorescent emitter molecule. [63–65] The process of UC then expands to begin with absorption and ISC in the sensitiser, triplet energy transfer (TET) from the sensitiser to the emitter, followed by TTA and fluorescence by the emitter. [66] UC is then achieved in systems where the sensitiser absorption is lower in energy than the emitter fluorescence, and this has been demonstrated for a variety of systems. [67] The use of a triplet sensitiser also allows for the use of emitter fluorophores with strongly forbidden ISC and extended triplet lifetimes, while also solving the associated problem of how to then effectively populate these triplet states in the first place. The overall TTA-UC process is shown as an energy level diagram in Figure 1.6.

Use of a triplet sensitiser may also allow for e-type systems to perform UC in a unimolecular process analogous to laser cooling. This form of UC has received far less attention than p-type TTA though, as it has a significantly restricted potential for changing photon energies. Whereas TTA combines the energy of two photons, e-type upconversion can only add phonon energies on the order of k_bT to the original excitation. [68,69]

The use of molecular triplet states to store photon energy means that UC *via* TTA does not require phase coherent excitation. An examination of the rate equations governing

this kind of UC in Chapter 2 will show that high intensity excitation, though advantageous, is not strictly necessary either. As a result, developing UC with photochemical systems capable of TTA has become a leading research theme in third generation PV over the last decade. The majority of these UC systems have been solution based, but more recently have also been demonstrated in gel and colloidal systems.[70–77] In addition to UC applications, further understanding of the mechanism for TTA has broader significance to downconversion. Singlet fission, the reverse process of TTA, involves a singlet exciton splitting into two triplet excitons, which may be utilised more efficiently by a low bandgap device than the original photon.[78–82]

While other forms of UC and even incoherent UC do exist (for example using erbium ions in optical fibres),[83–86] for the remainder of this document "UC" will be used to refer specifically to the sensitised photochemical incoherent UC *via* TTA described above — except where explicitly stated otherwise.

1.2.3.1 Applications in Electroluminescent Devices

Alongside PV applications, TTA and UC are also being actively investigated as ways to expand and improve the operation of light emitting diodes (LEDs), and in particular ones based on organic semiconductors (OLEDs).[87–96] This is not entirely surprising, as the mode of operation for OLEDs is similar to molecular fluorescence, and almost exactly the reverse of that for PV devices. In OLEDs, electrical contacts inject electrons and holes into opposite ends of the device, and light is emitted when they recombine.

In order to be able to combine, the electron and hole must be spin paired to first form a singlet exciton — similar to the excitons generated by light absorption in a PV device. Normal electrical contacts inject uncorrelated charge carriers into the device, and so the multiplicity of a randomly formed exciton can be determined by considering the coupling of two spin-$\frac{1}{2}$ particles, as given by the Clebsch-Gordon coefficients:[97]

$$\begin{aligned} |1\,1\rangle &= |\uparrow\rangle\,|\uparrow\rangle \\ |1\,0\rangle &= \tfrac{1}{\sqrt{2}}\left(|\uparrow\rangle\,|\downarrow\rangle + |\downarrow\rangle\,|\uparrow\rangle\right) \\ |1\,{-1}\rangle &= |\downarrow\rangle\,|\downarrow\rangle \end{aligned} \qquad (1.2)$$

$$|0\,0\rangle = \tfrac{1}{\sqrt{2}}\left(|\uparrow\rangle\,|\downarrow\rangle - |\downarrow\rangle\,|\uparrow\rangle\right)$$

where the combined spin exciton wavefunctions on the left are represented by $|S\,m_s\rangle$ for total spin S and spin sublevel m_s. The spin wavefunctions of the constituent electrons

and holes are represented on the right by $|\uparrow\rangle$ and $|\downarrow\rangle$, both with total spin $\frac{1}{2}$ and spin sublevels of either $\pm\frac{1}{2}$.[98,99]

Once again assuming that spin up and spin down electrons and holes are equally numerous, this results in excitons forming with triplet multiplicity ($S = 1$) in 75 % of cases, and singlet multiplicity ($S = 0$) only 25 % of the time. The triplet excitons cannot emit directly, and although their formation need not be a direct loss mechanism, the time taken for the exciton to dissociate and reform as a singlet (or undergo ISC) gives a window of opportunity for other loss mechanisms to act before emission.[100–106] An analogous problem will arise when the multiplicity of a triplet pair undergoing TTA is considered in Chapter 4.

One way to address the problem of triplet exciton formation in LEDs is to incorporate phosphorescent dyes as dopants. These serve a dual role, providing a mechanism for triplet excitons to emit through phosphorescence, as well as for conversion of triplet to singlet excitons. This reverse ISC is often assisted by the same spin-orbit coupling that makes phosphorescence weakly allowed in these compounds, and is commonly introduced by the presence of heavy metallic nuclei.[107–110]

In OLEDs that contain dopants capable of TTA, this process provides another channel by which triplet excitons can contribute to the device luminescence. Active TTA channels have therefore been proposed as an explanation for the particularly high efficiencies of some blue emitting OLEDs.[87,111–113] The high energies accessible through TTA (enough to cause irreversible damage to the emitter) have also been identified as a potential cause of the rapid ageing of the same blue OLEDs.[114–117] Going further, TTA enabled rubrene OLEDs have even been shown to perform solid state "upconversion", producing photons with higher energies (in eV) than the applied voltage.[96,118]

1.3 Probing the Properties of the Emitter Triplet

1.3.1 Describing Spin in Excitons and Exciton Pairs

The spin interaction that occur during TTA remains the least well understood step in the overall UC process, making it difficult to predict or design high efficiency UC systems. As this step occurs exclusively between emitter species, the broad aim of this research project has been to understand how spin and other properties of the emitter determine overall UC performance. As a solid foundation for this understanding, it is vital to establish a coherent description of the spin states relevant to the TTA process.

Triplet excited emitter molecules can be described in the same way as the solid state triplet excitons in Equation 1.2. Both contain an excited electron and hole pair (or equivalently, two spin unpaired electrons), and the main difference between them is the confinement of the exciton to a single emitter molecule in solution based UC systems.[119,120] It should be noted that while the three resulting wavefunctions ($|1\,\pm 1\rangle$ and $|1\,0\rangle$) always form a spanning basis set, they will only be eigenstates when strong magnetic fields are applied in the laboratory z axis.

In contrast, in the absence of external magnetic fields the exciton spin tends to align with one of the three axes of the emitter molecule it resides upon.[121] In the molecular frame of reference the wavefunctions of the spin eigenstates are given by a Cartesian basis set ($|x\rangle, |y\rangle$, and $|z\rangle$) which can also be constructed by coupling the spin of pairs of spin–$\frac{1}{2}$ particles.[122,123] This basis set is also spanning, and is related to the previous basis set by the following equations:[98,124,125]

$$\begin{aligned} |1\,1\rangle &= \tfrac{1}{\sqrt{2}}(|x\rangle + i\,|y\rangle) \\ |1\,{-1}\rangle &= \tfrac{1}{\sqrt{2}}(|x\rangle - i\,|y\rangle) \\ |1\,0\rangle &= |z\rangle \end{aligned} \tag{1.3}$$

Having established a description of the individual triplet states, a similar treatment can then be used to describe pairs of excitons as they undergo TTA. The Clebsch-Gordon coefficients link together the wavefunctions of the coupled spin 1 particles and the total spin of the pairs:[126]

$$\begin{aligned} |2\,2\rangle &= |1\,1\rangle\,|1\,1\rangle \\ |2\,1\rangle &= \tfrac{1}{\sqrt{2}}(|1\,1\rangle\,|1\,0\rangle + |1\,0\rangle\,|1\,1\rangle) \\ |2\,0\rangle &= \tfrac{1}{\sqrt{6}}(|1\,1\rangle\,|1\,{-1}\rangle + 2\,|1\,0\rangle\,|1\,0\rangle + |1\,{-1}\rangle\,|1\,1\rangle) \\ |2\,{-1}\rangle &= \tfrac{1}{\sqrt{2}}(|1\,{-1}\rangle\,|1\,0\rangle + |1\,0\rangle\,|1\,{-1}\rangle) \\ |2\,{-2}\rangle &= |1\,{-1}\rangle\,|1\,{-1}\rangle \\ \\ |1\,1\rangle &= \tfrac{1}{\sqrt{2}}(|1\,1\rangle\,|1\,0\rangle - |1\,0\rangle\,|1\,1\rangle) \\ |1\,0\rangle &= \tfrac{1}{\sqrt{2}}(|1\,1\rangle\,|1\,{-1}\rangle - |1\,{-1}\rangle\,|1\,1\rangle) \\ |1\,{-1}\rangle &= \tfrac{1}{\sqrt{2}}(|1\,{-1}\rangle\,|1\,0\rangle - |1\,0\rangle\,|1\,{-1}\rangle) \\ \\ |0\,0\rangle &= \tfrac{1}{\sqrt{3}}(|1\,1\rangle\,|1\,{-1}\rangle + |1\,{-1}\,\rangle\,|1\,1\rangle + |1\,0\rangle\,|1\,0\rangle) \end{aligned} \tag{1.4}$$

where both the individual (right) and exciton pair wavefunctions (left) are again represented by $|S\,m_s\rangle$. Linear algebra can then be used to express a specific spin wavefunction

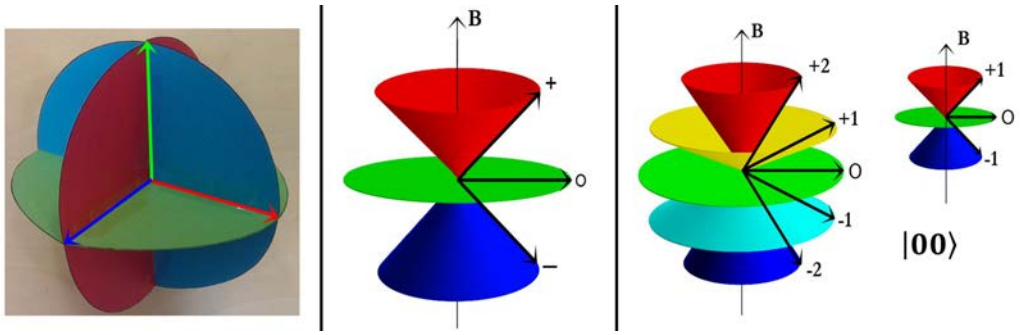

FIGURE 1.7: Visualisations of the Cartesian ($|x\rangle, |y\rangle$, and $|z\rangle$, left), high field ($|1 \pm 1\rangle$ and $|1\,0\rangle$, middle), and total spin triplet pairs (right). For all states except $|0\,0\rangle$, the total spin vectors precess across the coloured surfaces.

from one basis set in terms of wavefunctions from any of the other two bases. For example, $|0\,0\rangle = \frac{1}{\sqrt{3}}(|x\rangle\,|x\rangle + |y\rangle\,|y\rangle + |z\rangle\,|z\rangle)$. Calculating the overlap between two arbitrary wavefunctions allows their similarity to be quantified, and is simplified by the fact that all of the above basis sets elements are mutually orthogonal. The high field, Cartesian, and coupled spin basis sets are visualised in Figure 1.7.

Of all the combined spin wavefunctions in Equation 1.4, $|0\,0\rangle$ is perhaps the most important for TTA. This singlet pair state is the one that two triplet excitons must access in order for TTA to successfully lead to fluorescence. By inspecting its composition or by calculating projections, it can be shown that not all triplet pairs are able to form the singlet pair state (for example $|1\,1\rangle\,|1\,1\rangle$). The prevalence and ultimate fate of this and other non-emissive pair states remains an open question, and is examined further in Chapter 4.

1.3.2 Indirect Measurement of Triplet Excitons

Small polycyclic aromatic hydrocarbons (PAHs) are often selected as emitter species in UC systems for their high fluorescence quantum yields and long triplet lifetimes. [58,127] This choice makes the emitter triplet difficult to measure directly, as these properties are a result of strongly forbidden transitions both into and out of the triplet state. As a result, this state often cannot be directly prepared optically, which precludes its isolated study in single component systems. Original studies of p-type delayed fluorescence avoided this problem by using PAHs with more accessible triplet states (self-sensitised by ISC), but that would therefore be less effective in UC systems. [60,125,128]

Instead, the presence and properties of UC emitter triplets are most commonly revealed indirectly through measurement of UC fluorescence following sensitiser excitation and TTA. The UC fluorescence intensity depends primarily on the concentration of triplet excitons as well as the efficiency of the overall UC process, with the efficiency of TTA

incorporated as a factor in the overall efficiency. By comparing the relative fluorescence intensities as experimental conditions are varied, the effect of different UC parameters can be determined.

Examples of this approach include: excitation power series to investigate the effect of different triplet concentrations on the UC emission intensity, [129] applying static magnetic fields to influence triplet pair interactions and the efficiency of TTA, [128,130] and using resonant fields to potentially bias the population distribution of individual triplet spin states and the pair states they can form. In all of these methods the effect on individual triplets and their interactions must be inferred from the resulting changes in fluorescence, often with models used to explain and rationalise the observed changes.

Somewhat more advanced, time-resolved fluorescence experiments can also be used to determine the rates of processes and lifetimes of excited species relevant to UC. Such processes include TET, triplet quenching and non-radiative decay, bimolecular decays, along with the overall lifetimes of the sensitiser and emitter triplets. Both continuous-wave (CW) and time-resolved (TR) spectroscopies have been used extensively in this project to investigate the properties of emitter triplet in UC. The specific experiments are described in detail in the following chapters, and feature heavily in Chapter 2.

1.3.3 Direct Measurement of Triplet Excitons

Techniques to detect and measure triplet excitons directly do exist, but usually involve even more advanced spectroscopic methods. One conceptually straightforward way of doing this is to examine the spin allowed optical absorptions from the triplet excited state into higher excited triplet states, as shown in Figure 1.8a. This technique is analogous to conventional absorption spectroscopy (where molecules are excited from their ground state), but requires an additional initial excitation of the sensitiser to prepare emitter triplets — followed by a second illumination to determine their absorbance. The triplet state is short lived compared to the timescales of CW absorption spectroscopy, and its absorption features diminish as its population decays. As a result this technique is commonly performed in a time-resolved manner, tracking the changes in absorbance following excitation. This practice is reflected in the different names for this technique, including transient absorption (TA), photo-induced absorption, and absorption difference spectroscopy. TA methods have been used successfully to study a variety of UC systems, and are examined further in Chapter 3. [131,132]

A second class of allowed transitions that can be used to detect and study triplet states includes those between the different molecular spin sublevels themselves. The absorption and emission of microwaves associated with these transitions form the basis of electron

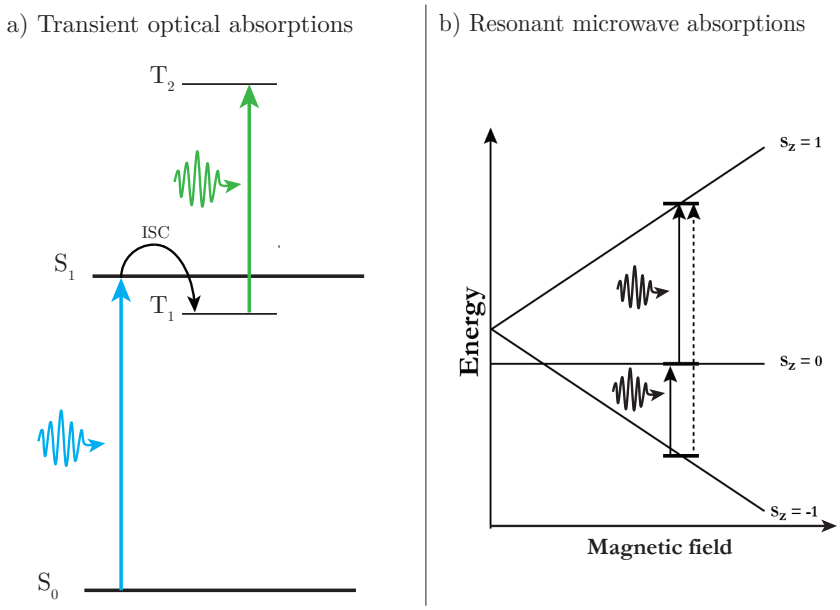

FIGURE 1.8: Transitions of triplet states that allow direct their observation in a) transient absorption, and b) ESR experiments.

spin resonance spectroscopy (ESR).[133–135] This is entirely analogous to the the radio frequency nuclear spin transitions targeted by nuclear magnetic resonance (NMR), and the same suite of pulsed techniques can also be used to interrogate the electronic spin systems.[136–141]

For simpler CW-ESR, the Zeeman splitting between the $|1\ \pm 1\rangle$, and $|1\,0\rangle$ triplet states is typically varied by sweeping an external magnetic field, while the microwave reflectivity of a resonant sample cavity (at a constant frequency) is tracked throughout. When the magnetic field causes a splitting that matches the energy of the microwave frequency, the reflectivity of the cavity changes as the sample absorbs or emits more radiation. Heterodyne mixing of the source and reflected microwaves is often employed to improve sensitivity, and so data is generated as a derivative trace of the absorptions.[98,142,143] Figure 1.8b shows the transitions responsible for simple ESR signals from a triplet excited state.

Combined with indirect fluorimetry, microwave detection ESR and optically detected magnetic resonance (ODMR) have the potential to greatly advance understanding of the role of spin in the TTA event. For example, higher multiplicity triplet pair states have a larger number of allowed transitions, allowing their associated multiplet signals to be identified in singlet fission solutions.[144] Similar measurements of TTA systems would allow the potential existence of quintet pair states to be confirmed or conclusively ruled out. More advanced pulsed ESR techniques can also be used to track the evolution of the individual spin states.[145,146] Developing ESR techniques to investigate the spin mixing during TTA in UC systems is the main experimental theme of Chapter 4.

Chapter 2

The Effect of Deuteration on Perylene Upconversion

"Daily, the clever man learns something.
Daily, the wise man gives up some certainty. Perhaps."

—Narrator, *Saiyūki (Monkey)*, NTV 1978–1980

The core work presented in this chapter has been published as an article in *The Journal of Physical Chemistry Letters*:

> Andrew Danos, Rowan W. MacQueen, Yuen Yap Cheng, Miroslav Dvořák, Tamim A. Darwish, Dane R. McCamey, and Timothy W. Schmidt, "Deuteration of Perylene Enhances Photochemical Upconversion Efficiency", *J. Phys. Chem. Lett.* 2015, **6**, 3061-3066

A.D. and T.W.S. initially developed the idea of deuteration as method to improve upconversion emitter performance. T.A.D. provided advice on chemical deuteration feasibility, as well as samples of partially deuterated perylenes. A.D. performed the experiments with technical assistance from R.W.M. (upconversion action spectra), Y.Y.C., and M.D. (time-resolved fluorescence). A.D. analysed the data, and prepared the manuscript with T.W.S. and input from D.R.M.

This publication was a direct result of research undertaken towards this PhD, and several figures are reproduced here with permission, copyright 2015 American Chemical Society.

Expanding beyond the scope of the original article, this chapter also provides more detailed discussions of the motivations for this work, the mechanism of the deuteration effect, as well as progress made towards applying the effect to light emitting diodes.

2.1 Challenges in Optimising Upconversion Efficiency

A primary goal in applied UC research is to design systems which are as efficient as possible. In an ideal system, each and every pair of absorbed photons would result in the emission of a single upconverted photon. Such a system would provide the maximum possible photocurrent enhancement to a coupled solar cell, regardless of the operating mechanism of that cell. Throughout this document "100 %" will be used to label the maximum photon conversion efficiency of UC, considering the input to be a singular pair of absorbed photons. It is also possible to define UC efficiency on a per-photon basis, leading to a maximum achievable value of 50 %. At present there is no widespread consensus on which definition to use, and special care must be taken when considering reported UC efficiencies from different sources. [67]

Although the description of the UC mechanism in the previous chapter makes the process seem qualitatively straightforward, the quantitative reality is somewhat more complex. A variety of exciton loss mechanisms exist between initial sensitiser absorption and final UC emission, invariably resulting in reported efficiencies far below 100 %. [67] To list just a few of these mechanisms: excited sensitisers may undergo TTA between themselves, an excited sensitiser or emitter may decay *via* radiative or non-radiative unimolecular processes, pairs of excited emitters might undergo TTA to a non-emissive pair state, or at any time molecular oxygen might quench triplet excitons directly. [147–149] The relative importance of different loss mechanism also changes in different regimes of excitation power and exciton concentrations. [129,148,150,151] This non-linear physical behaviour makes the process of understanding UC efficiencies similarly non-linear, in a metaphorical sense.

Overall photon conversion efficiencies of novel UC systems are nonetheless routinely measured and published. [67,152–161] This can be done, for example, by comparing the emitter fluorescence following direct excitation and after excitation of the sensitiser, using monochromatic beams of known intensity. [151,162] Efficiencies are also commonly calculated by relative actinometry, where UC fluorescence intensity is compared to fluorescence of a well characterised fluorophore standard such as methylene blue. [163]

Sadly, reported efficiencies are usually presented simply as benchmark figures and advances are rarely discussed in terms of the spectroscopic and kinetic parameters that control the various loss mechanisms. Thankfully this trend seems to be reversing in recent years, demonstrating a welcome rise in the analytical sophistication and rigour of the broader UC research community. [67] These parameters — discussed in the following sections — are largely intrinsic to the chosen sensitiser (S) and emitter (E). Substituting either molecule therefore causes several of these parameters to change, often in unpredictable ways and with competing effects on the overall efficiency. Comparing the

efficiencies of significantly different UC systems therefore provides little insight towards optimising efficiencies further, as a unique cause for the differences usually cannot be unambiguously identified.

The philosophically ideal experiment to understand UC efficiencies would involve comparing efficiencies in systems that differ in only one parameter at a time, and thus teasing out the importance of each factor individually and empirically. The main challenge frustrating efforts in this regard is that typical synthetic chemistry techniques used to create homologous classes of compounds are non-selective when it comes to the spectroscopic and kinetics properties of interest. Even "slight" modifications such as halogenation or methylation can have large impacts on the electronic properties of S or E, making them unsuitable for direct comparison — as discussed in the next section. [162,164,165]

Quantitative models do exist, and can predict the effect of multiple simultaneous parameter changes, but even with significant simplifications these models are chronically underutilised in explaining relative differences in system efficiencies. [166,167] This is likely because the rate constants and spectroscopic parameters used by these models are sometimes difficult to measure, and only known approximately even for commonly used emitters. Without robust experimental verification, it is sometimes unclear how applicable these models are beyond the specific experiments they are developed for. These circumstances set up a vicious cycle; the lack of tabulated parameters prevents widespread comparison of models to experiments, which prevents robust experimental verification of the models, which in turn discourages any concerted effort to tabulate these parameters in the first place.

This disconnect between fundamental and applied studies ultimately hampers deliberate, rational design of optimised UC systems, and in particular optimisation of the UC emitters for which spin is known to play a role. These unfortunate circumstances are exacerbated by the fact that novel low efficiency systems — which would give valuable complementary insight on what *not* to do — go largely unreported by scientific journals. Nonetheless, recent history shows that progress is possible once theory and experiments progress in tandem, and models gain a critical mass of usage. A good example of this is the now widespread use of the mixed kinetics model developed by Castellano *et al.* and popularised by Cheng *et al.* to describe time-resolved UC photoluminescence decay following pulsed laser excitation. [162,168]

Two clear paths to progress are therefore identified. The first of these is to show leadership in tabulating relevant molecular parameters across a range of UC systems, for use by others in comparing efficiency measurements to models. Work towards this outcome is summarised in Chapter 3, Table 3.1. The other path is to devise UC systems in which efficiencies *can* be compared directly, and verify quantitative models one parameter at

a time. The main achievement of the work presented in this chapter was to show that deuteration of the emitter can be used to accomplish this second outcome. That deuteration was also found to increase the efficiency of a specific perylene UC system is a happy but welcome coincidence.

2.1.1 Comparing Similar Emitters

A good example of how chemically similar compounds may be unsuitable for direct comparison can be found in two commonly used emitters: 9,10-bis(phenylethynyl)anthracene (BPEA), and its halogenated analogue 2-chloro-9,10-bis(phenylethynyl)anthracene (CBPEA). Figure 2.1 shows that the electron withdrawing chlorine atom is able to red-shift both the absorption and emission spectra of CBPEA by about 10 nm (0.06 eV). As the energies of the singlet and triplet states differ only by the exchange integral (to first order), it seems reasonable to suggest that the triplet state energies would also differ by a similar amount. Molar extinction coefficients are not shown in the figure, but remain roughly the same for both at about $3.5\times10^4\,\mathrm{M^{-1}cm^{-1}}$ at the peak absorbance.[169]

This change in singlet state energies alone could greatly impact the overall efficiency of a UC system, for example by changing the amount of UC fluorescence that is reabsorbed by a specific sensitiser compound. This "recycling" of excitons invariably leads to lower overall efficiency, by consuming pairs of triplet excitons to (re)generate individual ones.

In addition to changing the degree of exciton recycling, substituting CBPEA and BPEA has significant impact on the rate of TET between S and E. The rate constant for this process (k_{TET}) has been reported as $1.8\times10^9\,\mathrm{M^{-1}s^{-1}}$ for CBPEA, while for BPEA it is determined in a later section of this document to be only $6.7\times10^8\,\mathrm{M^{-1}s^{-1}}$ with an identical sensitiser.[168] This difference in rates may be due to the increased enthalpic driving force as excitation is transferred from the (higher energy) S triplet state to

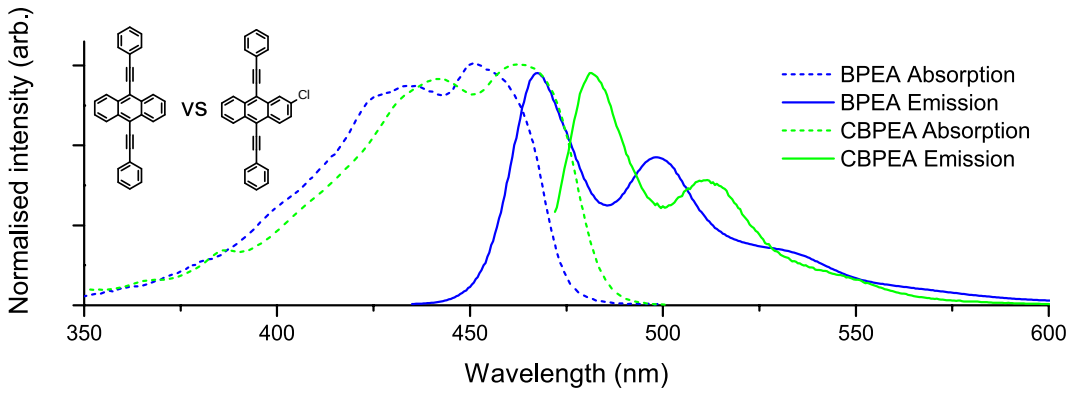

FIGURE 2.1: Absorption and emission spectra of BPEA (left structure, blue traces) and CBPEA (right structure, green traces).

populate the (lower energy) E triplet state. Based on its longer wavelength fluorescence, the triplet state energy is likely to be lower in CBPEA than BPEA, making this process yet more exothermic. Indeed, very low rates of TET are reported when this process is made slightly endothermic by deliberate choice of S and E.[170] In Chapter 4, for a system in which this process would be even more exothermic, no UC is observed at all. Even in otherwise identical conditions, the difference in TET rates would result in a faster population growth of CBPEA triplets, a larger peak CBPEA triplet concentration, and therefore different relative activity of otherwise identical exciton loss mechanisms.

The rate constants for second order decay (k_2, defined below) are also different between CBPEA ($5.6\times10^9\,\mathrm{M^{-1}s^{-1}}$) and BPEA ($6.5\times10^9\,\mathrm{M^{-1}s^{-1}}$).[168] Although not as large, this relative difference cannot be dismissed as less important, as k_2 ultimately describes the class of second order decays of which TTA is a key member. At risk of exhausting the reader, it seems likely that other important parameters should be different as well, such as the rate constant for first order decay (k_1), efficiency of the TTA process (η), and the quantum yield of emitter fluorescence for singlet excitons (Φ).

It should be noted that the rate constants reported for CBPEA were in systems with dimethylformamide (DMF) as solvent, whereas toluene was used for BPEA experiments presented and analysed in the next chapter. As with the definition of UC efficiency itself, the lack of a widespread standard amongst researchers in this field frustrates direct comparisons of reported measurements. With only one notable exception in section 4.4.1, toluene was used as the solvent in all experiments presented in document.

Without a direct comparison in otherwise identical conditions, the possibility remains that CBPEA and BPEA may be more intrinsically similar than the above comparisons indicate. The difference in k_2 can alternatively be explained largely (but not entirely) by a linear dependance on the limits of the diffusional rate constant in these solvents, determined primarily from their viscosities. These values are $8.3\times10^9\,\mathrm{M^{-1}s^{-1}}$ for DMF and $1.1\times10^{10}\,\mathrm{M^{-1}s^{-1}}$ for toluene at room temperature.[168,171] Although TET also relies on diffusion to some extent, diffusion as a sole determining factor would lead to opposite ordering of the rate constant sizes for CBPEA and BPEA. DMF is significantly more polar than toluene though, and this might contribute to a larger rate of TET. This could potentially occur by DMF energetically stabilising the molecular electric dipoles (or intermolecular charge transfer states) associated with energy transfer. In turn, this stabilisation would support the formation of larger dipole moments (or lower activation energy barriers to a charge transfer state), and subsequently enable energy transfer with a larger rate constant. Indeed, opposite effects of solvent polarity on energy transfer rates have been recently reported for protic and aprotic solvents, though the precise mechanism is yet to be determined.[172]

Nonetheless, the above comparison demonstrates how — even in an ideal comparison — molecules as similar as CBPEA and BPEA may be too intrinsically dissimilar to give unambiguous evidence about how individual UC component parameters impact overall UC system efficiencies. Without this bottom-up, quantitative understanding to guide synthesis efforts, more cynical observers may claim the majority of high efficiency UC systems reported in the last decade are merely a result of lucky choices of synergistic sensitiser and emitter compositions.

2.1.2 Spectroscopic Matching Conditions

All hope is not lost though. Even without the assistance of models, certain truths seem self-evident for the design of highly efficient UC systems. Following the UC process chronologically, a by-no-means comprehensive list of essential criteria includes the following properties.[166,173]

The sensitiser must be highly absorbing at some "long" wavelength, either due to a high extinction coefficient or high concentration, or both. It must then be able to rapidly undergo ISC to convert the singlet excitation to triplet multiplicity, ideally with a moderate exothermicity so as to restrict reverse ISC and access back to the singlet state. This requirement means that "good" sensitisers are often found amongst classes of molecules that are highly phosphorescent, with heavy metal atoms incorporated to assist spin-orbit coupling.[58,174]

The emitter then must have its own triplet energy level for excitation to transfer to, again ideally somewhat lower than the sensitiser's to energetically prevent reverse TET. The emitter triplet energy level should also be greater than half the energy of its own first singlet excited state, so that the energies of two excitons can populate this level exothermically through TTA. The emitter fluorescence must then occur at a shorter wavelength than the sensitiser absorption, lest the system instead generate unimpressive TTA downconversion. Finally, the emitter must be highly fluorescent so that the singlet exciton generated by TTA has a reasonable chance to decay emissively.

As mentioned above, the emission from E must not substantially overlap with any of the absorption bands of the system, or lossy recycling will occur. The absorption bands of E itself are usually trivially avoided due to Kasha's rule and the associated Stokes shift of molecular emission relative to absorption. Avoiding S absorptions requires selection of compounds with carefully matched spectra, so that a window of transparency exists between the long wavelength absorption used to excite and any other higher energy absorption features in the UC system.

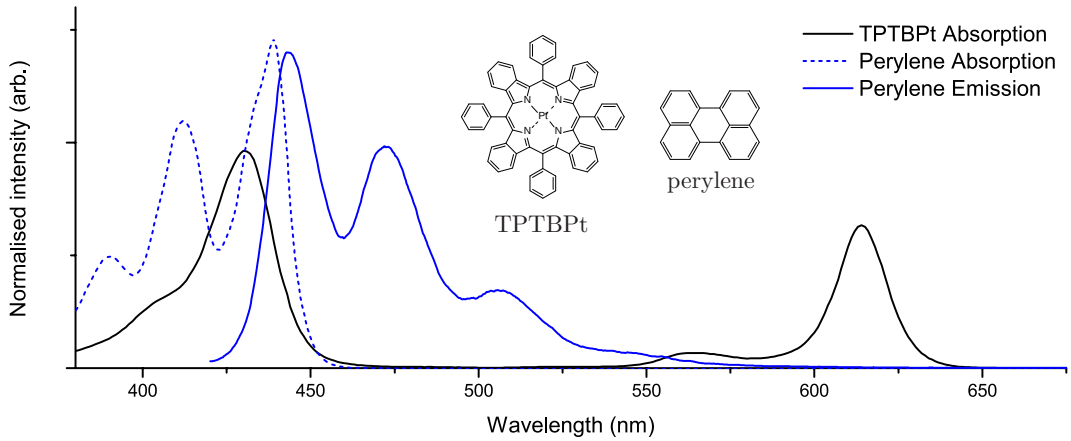

FIGURE 2.2: Absorption and emission spectra of TPTBPt and perylene. Note that the emission band of perylene resides mostly outside of the TPTBPt absorption features.

Luckily the bulk of these conditions are regularly met by systems comprised of metallated porphyrins as sensitisers and small PAHs as emitters.[67,166] Figure 2.2 shows how the spectra of Pt(II) meso-tetraphenyl tetrabenzoporphine (TPTBPt) and perylene are well matched in these regards. Although not shown in the figure, the phosphorescence emission of TPTBPt (red edge at ∼800 nm or 1.54 eV, shown in Figure 3.9) indicates that the energies of two TPTBPt triplets should be sufficient to populate the perylene singlet state (which emits photons with no more than 3 eV). These materials are also commercially available in large quantities, to the great relief of many synthetically challenged physical "chemists" — including the author.

2.1.3 Rate Equation Modelling

Beyond spectroscopic properties, analysis of mathematical models is also able to give some insight on how the various kinetic parameters of S and E should impact the overall efficiency. These kinds of models continue to be a reliable qualitative starting point in identifying research directions for improved UC efficiency.[166] Following on from the description of the processes leading to UC in section 1.2.3, the rate equations governing these steps are set out below in chronological order.

A sensitiser molecule is excited and undergoes rapid ISC:

$$\frac{d[^1S^*]}{dt} = k_\phi[^1S] - k_{ISC}[^1S^*] \tag{2.1}$$

where $[^1S]$ is the concentration of singlet ground state sensitiser molecules, and $[^1S^*]$ is the concentrations of singlet excited sensitiser molecules. The term $k_\phi[^1S]$ describes the rate of absorption and excitation of the sensitiser, while k_{ISC} is the rate constant

for ISC connecting its singlet and triplet states. Although $[^1S]$ and $[^1S^*]$ should strictly be conserved, the assumption is routinely made that $[^1S^*] \ll [^1S]$, leaving $[^1S]$ approximately unchanged by this excitation. Furthermore, ISC is assumed to be the most rapid decay process for $[^1S^*]$, with direct fluorescence from $[^1S^*]$ negligible.

The triplet sensitiser is then quenched by an emitter molecule, or *via* other first or second order decay processes:

$$\frac{d[^3S^*]}{dt} = k_{ISC}[^1S^*] - k_{TET}[^3S^*][^1E] - k_1[^3S^*] - k_2[^3S^*]^2 \tag{2.2}$$

where $[^3S^*]$ is the concentration of triplet excited sensitiser molecules, and similar notation is used for multiplicity and excitation of the emitter. TET from S to E is governed by the rate constant k_{TET}, while k_1 and k_2 correspond to first order and second order decay processes. At this stage the sensitiser has played its role of sensitising excitation of emitter triplets.

Despite being treated separately, TET is itself also an example of a first order process (technically quasi-first order with approximately constant $[^1E]$), but is held apart from other k_1 processes here as it is not a loss mechanism in the overall UC process. Other examples of first or quasi-first order processes include phosphorescence or quenching by oxygen, while second order decay is usually attributed to TTA between sensitiser molecules. Reminiscent of Equation 1.1, higher order loss terms may exist, but these would correspond to reactions involving exceedingly rare collisions of three or more excitons, and are not considered further. In real UC systems, large concentrations of emitter are regularly used so that the $k_{TET}[^3S^*][^1E]$ is the dominant negative term in Equation 2.2, and other loss mechanisms can be neglected.

Finally in this sequence of events, emitter triplet excitons (populated by TET) decay through a variety of processes which are also categorised as either first or second order in triplet exciton concentration:

$$\frac{d[^3E^*]}{dt} = k_{TET}[^3S^*][^1E] - k_1[^3E^*] - k_2[^3E^*]^2 \tag{2.3}$$

As discussed for the sensitiser, higher order loss terms may exist but are not observed in experiments, and the assumption is made that $[^3E^*] \ll [^1E]$ — leaving $[^1E]$ approximately unchanged by this transfer of excitation. Another possible decay term is one in $[^3S^*][^3E^*]$, representing heterogeneous TTA between S and E triplets. Heterogeneous TTA is considered in Chapter 3 in a system comprised of two distinct emitter species,

although TTA between sensitiser and emitter S and E is routinely neglected in this document and in other studies of UC. This simplification is also based on the assumption that $[^3E^*] \ll [^1E]$, with TET therefore assumed to dominate the decay of $[^3S^*]$. Having made these assumptions, any effect of heterogeneous decay on $[^3E^*]$ would manifest as a small contribution to its k_2.

It should be noted that the constants k_1 and k_2 in Equations 2.2 and 2.3 are not the same, but describe first and second order decay of either S or E depending on context. The focus of this work, however, is the properties of the emitter triplet. Therefore throughout this document k_1 and k_2 will be used in reference to E triplet decay processes, except where explicitly stated otherwise. In a similar way, superscripts labelling the multiplicity of ground and excited states will be omitted, as the only electronic states of significant interest are the ground state (E) and the triplet excited state (E^*). This is a choice made to enhance clarity, and somewhat necessitated by a proliferation of subscripts and superscripts in more complicated rate equations that feature in later chapters (for example, Equation 3.13).

The resulting UC fluorescence then comes about *via* bimolecular TTA, which is included in Equation 2.3 with all other second order processes in the term $k_2[E^*]^2$. The per-volume rate of generation of photons (in $\mathrm{M\,s^{-1}}$, and proportional to the fluorescence intensity) is then determined by this same term, weighted for the probability of second order decay events leading to emitter singlet emission:

$$I = \Phi \frac{\eta}{2} k_2 [E^*]^2 \tag{2.4}$$

where η is the fraction of second order decays in which TTA populates the E^* singlet state, with a factor of two introduced to account for the 2:1 ratio of emitter triplets consumed and emitter singlets generated by TTA. The symbol Φ then represented the quantum yield of fluorescence for the E^* singlet, although this symbol will also appear in later equations to denote quantum yields of other processes. For clarity, Φ_F will be used for fluorescence (and other subscripts for other processes) in circumstances where equations would be otherwise ambiguous. Experimentally, the relative magnitudes and kinetics of UC fluorescence can be easily measured, and used to indirectly investigate the behaviour of E^*.

From the model presented above, several additional routes towards improving UC systems become apparent. The key realisation to be made from this modelling is that for efficient UC the term $k_2[E^*]^2$ must be made to dominate Equation 2.3, as all processes described by k_1 correspond to loss mechanisms.

2.1.3.1 Improving the Sensitiser

As S is uninvolved in the TTA event leading to UC, it is unlikely to have any influence on the emitter k_2. Instead, in order to maximise $[E^*]$, the sensitiser can only generate and then transfer excitation as rapidly as possible — with minimal losses to other processes along the way.

The rate of sensitiser excitation, described by $k_\phi[S]$, can be maximised by using highly absorbing molecules at large concentrations. In practice, sensitiser concentrations are often limited by low solubilities and by concentration induced aggregation quenching. Nonetheless, many sensitisers with large molar extinction coefficients exist, and reflective or luminescent solar concentrators can be used to further increase k_ϕ.[175–178]

Once excited, rapid ISC can be achieved using the heavy atom effect. The presence of large nuclei such as platinum or palladium allows spin-orbit coupling to exchange angular momentum between electron orbital angular momentum and electron spin. Metallated porphyrins and other chelating macrocycles are particularly effective in this regard, as their heavy atom is in constant close proximity to the electronic system that they perturb.[179–181]

Once S^* excitation is on the triplet manifold it just needs to survive long enough for a successful collision with another E molecule so that TET to proceed. As a result it is important that the sensitiser k_1 and k_2 are small, giving S^* a long intrinsic triplet lifetime. Unfortunately in this regard the heavy atom effect cuts both ways, and both phosphorescence and non-radiative decay can be large contributing mechanisms to k_1 in sensitisers containing heavy metal atoms. E-type delayed fluorescence can also occur in the sensitiser if ISC from the excited singlet to triplet states is not sufficiently exothermic to prevent thermal activation of the reverse. In contrast, processes that contribute to the sensitiser k_2 involve collisions between two S^* molecules. As a result, sensitiser k_2 can be minimised by using sterically bulky molecules that slow their diffusion and frustrate close collisions, although this approach can also have detrimental consequences on the solubility of S and on k_{TET}.[182,183]

It seems highly unlikely that a single molecule could satisfy all of the above requirements simultaneously. Thankfully, both the sensitiser k_1 and k_2 become irrelevant if $k_{TET}[E]$ is sufficiently large, and collisions with E are frequent. For small, mobile, and highly soluble emitters, this can almost always be achieved with a large $[E]$ — even when k_{TET} is small. As a result, comparative efficiency studies (such as this one) almost always focus on the emitter rather than the sensitiser, as it seems there is little remaining headroom to meaningfully improve the intrinsic properties of currently used sensitisers, apart from perhaps their cost.[67,132,184,185]

2.1.3.2 Improving the Emitter

For any chance of UC proceeding, the newly formed E^* must itself survive long enough to collide with a second E^* molecule. This will inevitably occur when $[E^*]$ is sufficiently large and collisions are frequent. In this context "sufficiently large" can be defined as $k_1 \ll k_2[E^*]$, and occurs for the typically low values of $[E^*]$ if k_2 is big and k_1 is small.

As a result it is important for the emitter to also have a small k_1, and a long triplet lifetime. Any process that couples the singlet and triplet manifolds of the isolated emitter would contribute to k_1, and so heavy metals or expansive PAHs are usually avoided.[186] Although this is undoubtedly the correct approach for applied UC systems, it also presents challenges for fundamental studies. The isolation of the triplet E^* state means that it can only be practically populated by sensitisation, and is unlikely to be detectable by phosphorescence either. This means that k_1 cannot be easily measured in isolation, nor by elementary spectroscopic techniques. A similar situation for k_2 is likely the reason why these constants are not widely reported, even for common UC emitters.

As the second order processes described by k_2 require collisions between E^* triplets, smaller molecules that diffuse faster are generally more effective as UC emitters. Fused rings are a common structural motif for UC emitters, as the associated electron delocalisation is a spatially compact way for these molecules to have emission in the visible or near IR wavelength regions of interest for UC applications. At these small sizes ($\lesssim$6 fused rings), the strong spin-orbit coupling present in larger PAHs (such as C_{60} fullerenes) does not significantly diminish their fluorescence either.

Having collided, it is then important that η is large so that these collisions result in UC fluorescence. This parameter is associated with the ability for the exciton pair to access the emissive singlet pair state $|0\,0\rangle$, and remains one of the least well understood aspect of UC systems. It has been argued that η should not be able to exceed 11 % (1/9), based on the average multiplicity of a random pair of E^* triplets. Values of η in excess of 0.6 have since been reported for rubrene, conclusively demonstrating that this approach is too simplistic.[162] More recently, values of η for perylene have been reported to even approach 1, suggesting that there may indeed be no fundamental limit the efficiency to TTA.[187] Magnetic fields are thought to alter η through the interaction of E^* spin states, and this idea is further explored in Chapter 4. The similar need for advanced spectroscopic methods in its measurement means that the values of η for commonly used emitters are even less well known than k_1 and k_2.

Finally, the emitter must be highly fluorescent from the singlet excited state, quantified by a large value of Φ. Like η though, this parameter appears intrinsic to the chosen emitter, and it is similarly unclear how this might be deliberately altered by external

factors or chemical modification. Instead, highly efficient UC emitters are often simply selected from the subset of compounds already known to have a large Φ. Large values of Φ are also extremely advantageous for OLEDs, and so there is a strong overlap between the compounds commonly used as UC emitters and as OLED emissive layers. This selection bias, along with preferential reporting of high efficiency UC systems, has resulted in nearly exclusive use of PAHs in reported UC systems.[58,154,172,188] It is simultaneously disappointing and exciting to think that entire classes of UC emitters may exist undiscovered, outside the scope of current research trends.

2.1.4 Steady-State Efficiency Regimes

For eventual applications of UC and for experiments performed under constant excitation, the rate models in the previous section can be extended by enforcing steady-state conditions. All derivatives are set to zero, and by assuming TET is indeed the dominant decay mechanism in Equation 2.2, Equation 2.3 can be rewritten as:

$$\frac{d[E^*]}{dt} = 0 = k_g[S] - k_1[E^*] - k_2[E^*]^2 \tag{2.5}$$

where the expected leading term has been amalgamated to k_g, representing the combined rate of E^* generation by sequential absorption by, ISC in, and TET from S.

Intuitively it then seems reasonable (although perhaps pessimistic) to assume that first order decay processes will dominate the overall decay of emitter triplets, with $k_1[E^*] \gg k_2[E^*]^2$. As the first order decay processes all represent loss mechanisms, this assumption defines a "low efficiency" regime of operation. Although this assumption will later be shown to fail in certain circumstances, using it reduces Equation 2.5 to:

$$[E^*] = \frac{k_g[S]}{k_1} \tag{2.6}$$

Combining this with Equation 2.4 yields an expression that connects the kinetic parameters of E^* to the rate of generation of UC photons (again proportional to intensity):

$$I = \frac{k_2 k_g^2 [S]^2 \eta \Phi}{2k_1^2} \tag{2.7}$$

The absolute intensity by itself is usually not directly measurable, as it corresponds to the total fluorescence intensity generated by a volume of uniform upconverter solution, emitted isotropically. Nonetheless, the signal measured by real instruments is often

taken to be proportional to this expression, or to some volume integral describing non-uniform upconverter geometries. The main usefulness of this expression is that it links the excitation power (incorporated in k_g) to the fluorescence intensity.

Complementary to the above approach, a "high efficiency" regime can also be defined. In this regime, $k_1[E^*] \ll k_2[E^*]^2$, and the majority of E^* triplets decay via second order processes. In this regime Equation 2.5 instead reduces to:

$$[E^*]^2 = \frac{k_g[S]}{k_2} \tag{2.8}$$

and Equation 2.7 instead becomes:

$$I = \frac{\eta\Phi}{2} k_g[S] \tag{2.9}$$

which is the maximum rate of UC fluorescence expected from Equation 2.4 for a specific value of $[E^*]$, generated by excitation of S and quantitative energy transfer from S^*.

Comparing Equations 2.7 and 2.9 reveals interesting practical differences between the high and low efficiency regimes. As expected, in the low intensity regime the amount of UC fluorescence grows with k_2 and diminishes with k_1. The emission intensity also grows quadratically with k_g, reflecting the non-linear dependance on changes in $[E^*]$. At higher powers the dependance on k_g is only linear, as each additionally generated E^* already has a reasonable chance to collide with another E^*, once a sufficiently large background concentration has been reached.

Indeed, k_g is one of the few parameters for which Equation 2.7 can be easily verified. Since the rate of generation depends on the intensity of the excitation beam, k_g can be varied externally by changing the optical power incident on a UC system. This power series comparison can be performed on the exact same UC sample, leading to an ideal experiment where all other system parameters remain the same. The widely observed behaviour of UC systems in these experiments is that a log-log plot of emission and excitation intensities changes from an initial gradient close to 2 to a gradient closer to 1.[129,150] These gradients represent the indices of the power laws relating the plotted quantities, and the change signals the expected rollover from the low efficiency to the high efficiency regime. The rate of excitation necessary to access the high efficiency regime can even be quantified by setting Equations 2.7 and 2.9 equal to each other:[150]

$$k_g[S] = \frac{k_1^2}{k_2} \tag{2.10}$$

Finally, it should be noted that Equation 2.5 can be solved analytically without the need for further simplifying assumptions. Applying the quadratic formula and excluding the solution with $[E^*] < 0$ yields an expression for $[E^*]$:

$$[E^*] = \frac{\sqrt{k_1^2 + 4k_2k_g[S]} - k_1}{2k_2} \tag{2.11}$$

This solution can be used to fit experimental data, but unlike Equations 2.6 and 2.8 it does not easily yield clear insight on how changes in each parameter impact the overall fluorescence intensity. As a result, this analytic solution is often overlooked in favour of simpler analysis in terms of high and low efficiency regimes.

2.1.5 Deuteration and Triplet Lifetime

As discussed previously, results like Equation 2.7 are useful but remain difficult to verify experimentally. The emitter parameters Φ, η, k_1, and k_2 each seem intrinsic to the emitter, and cannot be easily varied in isolation. Even an experiment as simple as comparing different values of $[S]$ is challenging, as this will also impact the amount of UC fluorescence that is reabsorbed by S.

Nonetheless some experiments can still be proposed. Excitation power series are already an established way to see the effect of changing k_g, while leaving the system otherwise identical. In later chapters magnetic fields are investigated as a way to alter η in individual UC systems, while the diffusional component of k_2 could be varied by lowering the temperature and viscosity of the solvent (although this would simultaneously alter k_{TET} and any thermally activated processes). Quenching of $[E^*]$ by oxygen can be treated as a quasi-first order process and would add to the value of k_1 to aid in its study, but additional quenching of S^* would then also compete with TET.

Chemical deuteration of the emitter is one of the few other methods identified to selectively change k_1. Unlike other chemical substitutions, there is little expected effect on the electronic system (spectra and Φ), nor molecular size, mobility, or packing (η, diffusion, and k_2). Indeed, some deuterated PAHs are already known to exhibit extended triplet lifetimes (smaller values of k_1) in crystal and gas phase studies.[189–191] This is explained by an inhibition of non-radiative decay pathways involving ISC from E^* to high vibrational states on the E ground state. For these reasons, deuterated emitters were investigated as ideal candidates to compare the relative effects of varying k_1 on UC performance, and potentially verify the models that generate results like Equation 2.7.

2.2 Methods

2.2.1 Sample Preparation and Characterisation

The hydrogen isotopologue of perylene (h-perylene) was purchased from L. Light & Co. Ltd., while perylene-d_{12} with 98% isotopic purity (d-perylene) was purchased from Sigma-Aldrich. The sensitiser, TPTBPt, was purchased from Frontier Scientific and chosen because its absorption features neatly avoid the fluorescence band of perylene (as shown in Figure 2.2). Spectral grade toluene was used as a solvent, and all compounds were used without further purification.

Upconverting solutions with 1 mM of either perylene isotopologue and 0.1 mM of TPTBPt were prepared in toluene for the collection of action spectra. For time-resolved fluorescence experiments, concentrations of 2.5 mM of perylene and 0.25 mM of TPTBPt were used. These 10:1 ratios of emitter to sensitiser were chosen to facilitate rapid TET from S^* to E. In order to ensure close to identical concentrations of sensitiser in comparative samples, the solutions were prepared by dispensing equal volumes of a common sensitiser stock solution. To minimise the possibility of deuterium exchange with solvent during storage, emitter stock solutions were prepared from the dry powders as soon as was practicable before measurement. Any deuterium exchange that may have occurred before measurement would have only reduced the emitter enrichment, and led to the final calculated size of deuteration effect being a conservative underestimate.

The concentrations of the emitter stock solutions were checked prior to combination with the sensitiser by comparing their absorption spectra, and similar checks were performed for the concentrations of the final solutions. Absorption spectra were collected using a Cary 4E UV-Visible spectrophotometer, or Cary 50 Bio UV-Visible spectrophotometer depending on availability. To compare the isolated photophysical properties of the perylene isotopologues, fluorescence emission and excitation spectra of dilute solutions were collected using a Cary Eclipse fluorimeter.

To remove oxygen, upconverting solutions were transferred into a custom glass cuvette, with an attached glass-blown bulb and gas-tight teflon tap. With the liquid sample in the bulb and the tap attached to a diffusion-pumped vacuum line, three freeze-pump-thaw cycles were applied at 3×10^{-3} mbar of vacuum and a temperature of 77 K (applied directly with liquid nitrogen). The tap was then sealed, the cuvette removed from the vacuum line, and the sample transferred from the bulb to the cuvette by tilting — ready to measure.

All upconverting samples were measured using the same cuvette, which had a $1\,\mathrm{cm}^2$ square cross section. Between measurement samples the cuvette was washed extensively

with toluene, acetone, ethanol, and water until no hint of blue perylene fluorescence could be observed visually in additional supernatant toluene.

2.2.2 Upconversion Action Spectroscopy

At low excitation powers the fluorescence from UC can be exceedingly weak. As a result, it becomes difficult to measure the fluorescence with sufficient precision that small differences between samples can be detected and compared. Additionally, UC in real measurements occurs not just where the excitation beam first hits the sample, but at greater optical depths as well. To address these issues an "action spectroscopy" method had been recently developed by Dr. Rowan MacQueen, and was used to investigate deuterated UC samples.[70,192]

This method involves exciting the UC sample with a constant intensity pump beam, to give a large background [E^*]. A low power probe is then repeatedly pulsed on the sample, and lock-in amplification used to extract the linear component of detector response that is induced by the probe only. The larger background [E^*] makes the probe beam more effective at generating UC fluorescence, resulting in an enhanced signal compared to the probe in isolation. Fluorescence generated by the pump beam does not modulate at the lock-in frequency, and so does not add to to the measured signal. The probe beam is swept through different wavelengths, causing fluorescence sometimes by excitation of the sensitiser and subsequent UC, and at other times by direct excitation of the emitter.

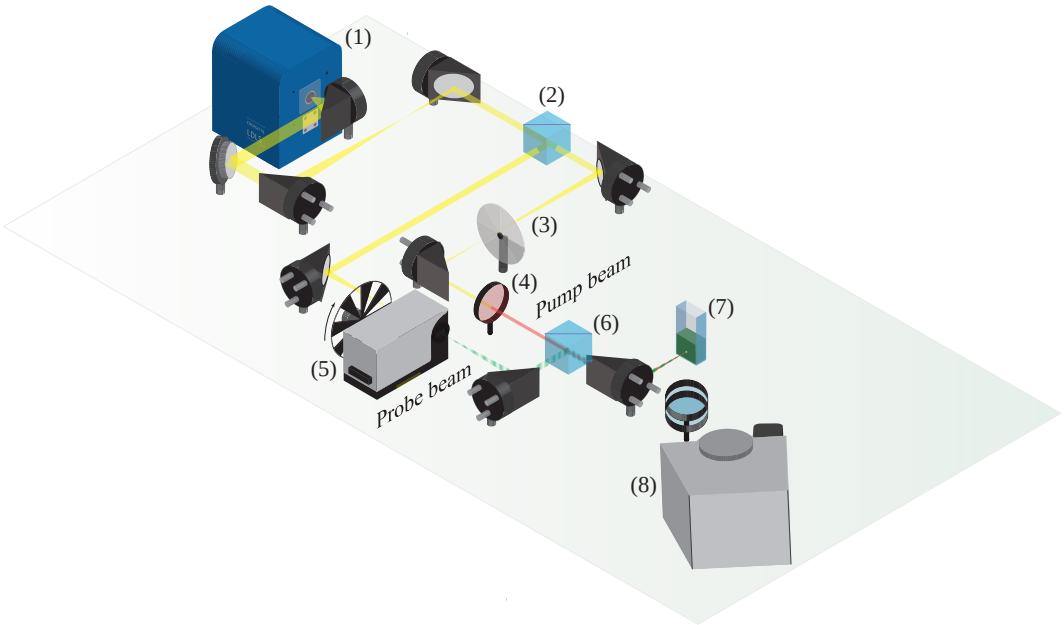

FIGURE 2.3: Experimental setup for collection of action spectra, reproduced with permission from Danos *et al.*, SI copyright 2015 American Chemical Society.[193] Numerical equipment labels are described in the text.

Figure 2.3 shows how this was achieved in practice. Light from a single broadband optical source (1) was split into two beams (2). One of these beams passed through a long-pass filter (4) so that it could only excite the sensitiser (570 nm cutoff for TPTBPt). The other beam passed through a chopper wheel and monochromator (5). The two beams were then recombined (5) and focussed collinearly on a UC sample (7). A portion of the isotropic UC fluorescence was then imaged on the slits of a spectrograph (8). The spectrograph passed wavelengths corresponding to the emitter fluorescence (470 nm for perylene) to a photomultiplier tube (PMT), which gave a voltage signal proportional to the fluorescence intensity. Lock-in amplification at the chopper wheel frequency was then achieved in software. A neutral density filter wheel (3) allowed action spectra to be collected at a range of pump beam intensities, with pump power quantified by temporarily placing a diode optical power meter at the sample position. Without any further analysis this method can be thought of as a more sensitive version of lock-in quasi-CW fluorescence excitation spectroscopy, assisted by the use of the pump beam.

Since the lock-in amplification of the voltage signal extracts the linear component of fluorescence response to the probe beam, the measured signal is proportional to the first derivative of this fluorescence with respect to the probe beam power. A multiplicative constant representing instrument response factors is included to yield the fitting function:

$$f(\lambda) = A\frac{dI}{dI_{pr}} = A\left(\frac{dI_{UC}}{dI_{pr}} + \frac{dI_F}{dI_{pr}}\right) \tag{2.12}$$

where $f(\lambda)$ is the action spectrum itself, I_{UC} is the fluorescence from UC, I_F is the fluorescence from direct emitter excitation, and I_{pr} is the intensity of the probe beam.

A detailed consideration of the probe beam propagating through the sample allows the calculation of $[E^*]$ and thus also I for volume elements at different depths, using low efficiency regime Equations 2.6 and 2.7. The total detected fluorescence intensity and its derivatives can then be calculated by summing across these volume elements and attenuating each by the sample's own absorbance from that depth. This allows Equation 2.12 to be rewritten as:

$$f(\lambda) = A\left[\Phi_F\frac{\alpha^e_{pr}(\lambda)}{\alpha_{pr}(\lambda)+\alpha_F} + \Phi_{TTA}\frac{\alpha^s_{pr}(\lambda)}{\alpha_{\mathcal{P}u}+\alpha_{pr}(\lambda)+\alpha_F}\right] \tag{2.13}$$

where different instances of α are the absorptivities of the sensitiser (superscript s), emitter (superscript e), or whole sample (no superscript) to the pump (subscript $\mathcal{P}u$), probe (subscript pr), or emitter fluorescence (subscript F). These values are related to the decadal molar absorptivities (ϵ) by $I(z) = I_0 10^{-\epsilon c z} = I_0 e^{-\alpha z}$. The constants Φ_F

and Φ_{TTA} are the quantum yields for fluorescence following direct emitter excitation, and for fluorescence from TTA of sensitiser excited emitters respectively. [192]

The allure of this analysis is that it was designed to extract the absolute overall UC efficiency ($\Phi_{UC} = \Phi_F \Phi_{TTA}$) for vastly different UC systems, without the need for kinetics measurements nor resorting to relegating the actual UC mechanism and excitation profile to a black box. For the comparison of deuterated emitter UC (with Φ_F assumed to be identical — although this assumption is reexamined in section 2.4.5), determining Φ_{TTA} this way would have empirically revealed the size of any deuteration enhancement to UC efficiency at different pump powers.

2.2.3 Time-Resolved Upconversion Fluorescence

Used here in tandem with action spectroscopy, time-resolved photoluminescence (TRPL) is a well established method for characterising UC systems. In this method a UC sample is hit with pulsed excitation to generate some initial $[S^*]$ and subsequent $[E^*]$, which then decays through first and second order processes. [162] The specific aim of using TRPL in this study was to determine k_1 for the normal and deuterated emitters, and then see whether the model equations in section 2.1.4 predict the same changes in Φ_{TTA} as measured through action spectroscopy.

Figure 2.4 shows how TRPL measurements were achieved in practice. An Acton/Princeton iCCD spectrograph/camera was used to collect UC fluorescence following excitation by the 615 nm output of a TOPAS OPA pumped with a Clark MXR CPA 2210 femtosecond laser running at 1 kHz repetition rate. The electronic gating of the CCD was set at an appropriate width, delay, and number of repetitions for the specific experiment, and triggered by the laser's own timebase circuitry. In this case 1 μs intervals were used from 100 ns to 900.1 μs after the laser pulse, with 1000 shots averaged at each time-point. Measurements were then repeated at several excitation pulse energies using neutral density filters to attenuate the excitation, with a power meter used to quantify the pulse energies at the sample position. In these experiments six pulse energies were used, in the range of 150 nJ to 12 μJ.

Equation 2.4 was used to relate the TRPL signal back to $[E^*]$, which then evolves according to a modified version of Equation 2.3:

$$\frac{d[E^*]}{dt} = \delta(t - t_0)[E^*]_0 - k_1[E^*] - k_2[E^*]^2 \tag{2.14}$$

where $\delta(t)$ is the Dirac delta function, and $[E^*]_0$ is the initial population of emitter triplets excited by the laser pulse at time t_0. The use of $\delta(t)$ here implies that the

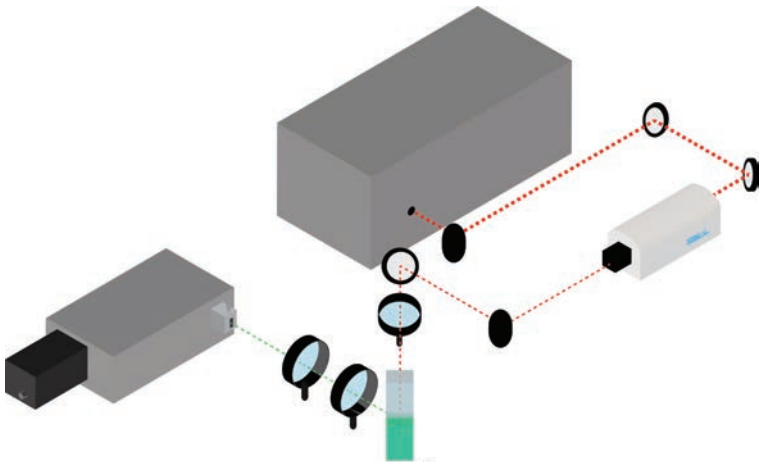

FIGURE 2.4: Experimental setup for collection of TRPL spectra, reproduced with permission from Danos *et al.*, SI copyright 2015 American Chemical Society.[193] The output of the Clark MXR (depicted in red) is used to drive the TOPAS OPA, which provides tunable excitation for the UC sample (green cuvette). The resulting UC fluorescence (depicted in green) is then recorded using the camera.

sensitiser processes leading to TET all happen rapidly, and that any $[S^*]$ is fully quenched in the time between excitation and the first acquisition frame of UC fluorescence. At times before t_0, $[E^*]$ takes a value of zero.

Equation 2.14 is then an ordinary differential equation initial value problem. The solution to this equation is:

$$\frac{[E^*]}{[E^*]_0} = A\frac{1-\beta}{e^{k_1 t} - \beta} \tag{2.15}$$

with A as a scaling factor, and fitting parameters k_1 and β. In this equation and henceforth, t is measured from the arrival of the excitation laser pulse, equivalent to specifying that $t_0 = 0$. Normalising by $[E^*]_0$ means that the same mathematical expression can also be used to fit normalised traces of $\sqrt{I}$, with I itself proportional to the actual signal. Although the parameter A is not theoretically necessary (it should always be identically 1), here it was found to assist the fitting and is thought to help account for noise present in the initial data point used for normalisation.

The parameter β corresponds to the initial fraction of triplet decay which occurs through second order processes, although this fraction decreases as time progresses and $[E^*]$ diminishes. Although not utilised here, β can also be related to the overall fractions of triplet decay that occur through first (f_1) and second order processes (f_2):

$$\begin{aligned} f_1 &= \tfrac{\beta-1}{\beta}\ln(1-\beta) \\ f_2 &= 1-\tfrac{\beta-1}{\beta}\ln(1-\beta) \end{aligned} \tag{2.16}$$

where f_1 and f_2 summing to unity reflects the assumption no significant fraction of triplet decays occur through third or higher order processes (and this assumption is used to derive the expression for f_2 from f_1).

From β and $[E^*]_0$, k_2 can also in theory be determined by:

$$k_2 = \frac{1}{[E^*]_0}\frac{\beta k_1}{1-\beta} \tag{2.17}$$

The challenge in using Equation 2.17 is that $[E^*]_0$ is not straightforward to measure for real systems, and that use of a single value implies that fluorescence is only being collected from the very front of the sample. This challenge can be overcome by estimating the excitation pulse power density or by using TA methods, but for this study meant that the absolute value of k_2 was not extracted. By assuming that $[E^*]_0$ grows linearly with increasing pulse power ($[E^*]_0 = BE_L$ for laser power E_L, and some scale factor B), a relative comparison of Bk_2 between the normal and deuterated emitters could still be performed.

2.3 Results and Discussion

2.3.1 Sample Preparation and Characterisation

Pleasingly, dilute solutions of both normal and deuterated perylenes were found to have identical absorbance, fluorescence emission (with 410 nm excitation), and excitation spectra (observing emission at 470 nm). This strongly indicates that the electronic systems of the deuterated isotopologue are not greatly perturbed by deuteration, and that η and Φ should also remain the same — although this was not confirmed directly. The absorption and emission spectra are shown in Figure 2.5, while the fluorescence excitation was identical in shape to the absorption spectra.

The relatively high noise levels in these spectra were a result of the low concentrations used, which were necessary to avoid inner filter effects impacting the shape of the spectra — collected by the Cary Eclipse fluorimeter at right angles to excitation. Later action spectra and TRPL measurements were performed in a front facing geometry, and so higher concentrations could be used in those cases leading to lower noise.

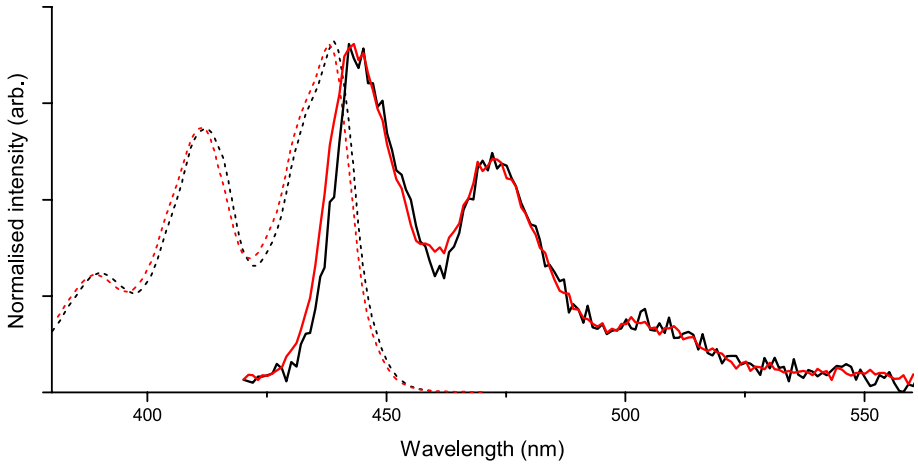

FIGURE 2.5: Absorption (dashed, same scale for 0.1 mM solutions) and emission (solid, 410 nm excitation, normalised) spectra of h-perylene (black) and d-perylene (red).

The thorough removal of oxygen after three cycles of degassing was supported by observing immediate blue fluorescence of the UC solutions when illuminated by a 630 nm diode laser pointer. In contrast, trace oxygen remaining in UC solutions can be identified by a slow (∼1 s) build up of UC fluorescence as local concentrations of molecular oxygen are depleted through light activated reactions with PAH rings, while UC fluorescence is completely absent in oxygen rich solutions.[148,149]

2.3.2 Upconversion Action Spectroscopy

Even more pleasingly, the action spectra generated for the normal and deuterated UC samples showed almost identical fluorescence response to probe beam excitation of the emitter (although d-perylene signal was consistently greater than h-perylene). Identical artefact peaks were observed at 470 nm, corresponding to scattering of the probe excitation beam through the detector monochromator. The rest of the response at shorter wavelengths broadly matched the absorption spectrum of perylene itself — as expected for what are essentially fluorescence excitation spectra — with modulation due to additional short wavelength absorptions of the sensitiser. In contrast, there was a significantly larger relative response from the d-perylene sample when the probe beam excited only the sensitiser at long wavelengths. This raw qualitative result immediately showed that the deuterated emitter was performing TTA better than the hydrogen isotopologue, and was found to be true for all pump powers used.

Small variation in the peak emission intensities (corresponding to 445 nm excitation) were thought to be due to variability in detector sensitivity or pump beam power drift, although this was not investigated further to confirm. Instead, the h-perylene spectra were scaled up to normalise the peak response. The fact that each h-perylene spectrum

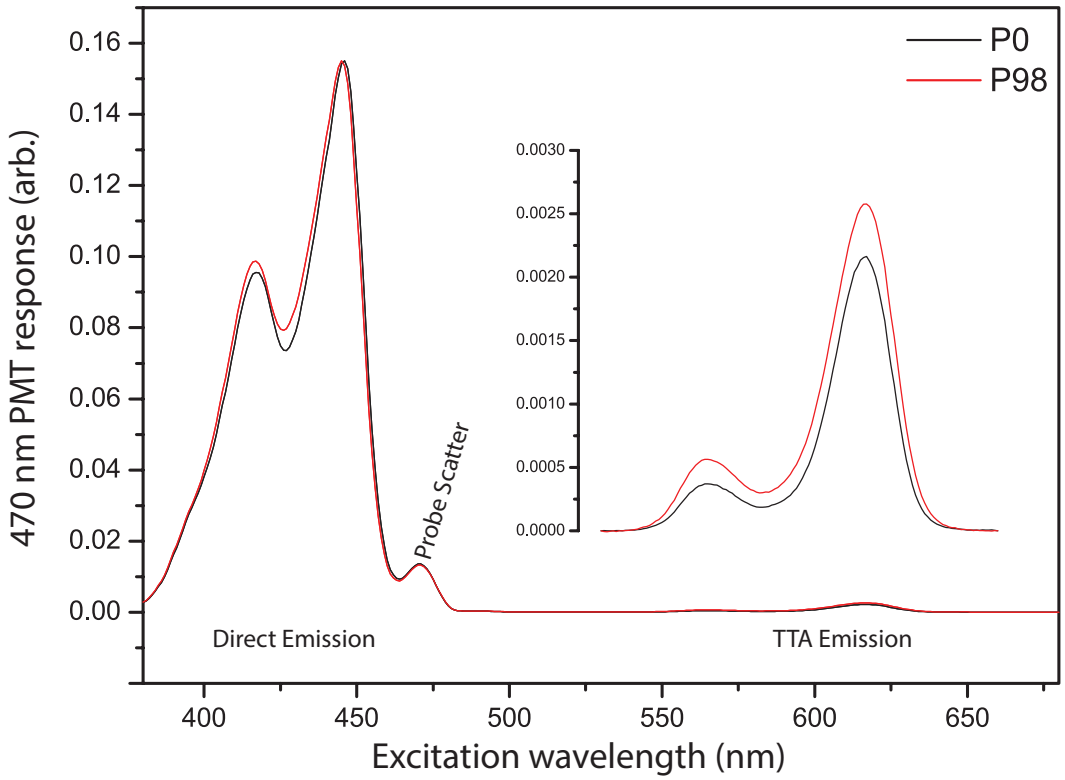

FIGURE 2.6: Representative action spectra of normal (P0) and deuterated (P98) UC systems. Inset with vertically offset and rescaled signal in the UC response region.

was scaled *up* to match its d-perylene counterpart means that the relative d-perylene enhancements in the UC wavelength regions were slightly diminished before further analysis, and that later estimates of the size of the deuteration effect are conservative underestimates. Table 2.1 lists the scaling factors used for the h-perylene spectra with different pump powers, and example action spectra for both isotopologues are shown in Figure 2.6. In this and subsequent figures, the normal and deuterated UC samples are referred to as P0 and P98 respectively, reflecting their emitter deuterium content. A consistent colouring scheme is also used for data figures, with black traces belonging to P0 and red traces to P98.

Significantly less pleasing than the raw results, all attempts to fit the action spectra using Equation 2.13 were met with failure. An example of the best attainable fitting is shown in Figure 2.7. By using the sample absorption spectra and amalgamating Φ_F into A in Equation 2.13, the model for the action spectra can be reduced to only two free parameters for fitting; one that controls the overall height (A), and one for the

TABLE 2.1: Scaling factors for P0 action spectra at 445 nm direct response peak.

Pump Power (mW)	0	2.4	3.3	4.5	4.5	6.4	9.8	16.2	16.2	30	160
Scaling factor (%)	1.6	1.3	1.6	2.5	3.9	2.4	3.2	3.4	4.0	3.5	1.3

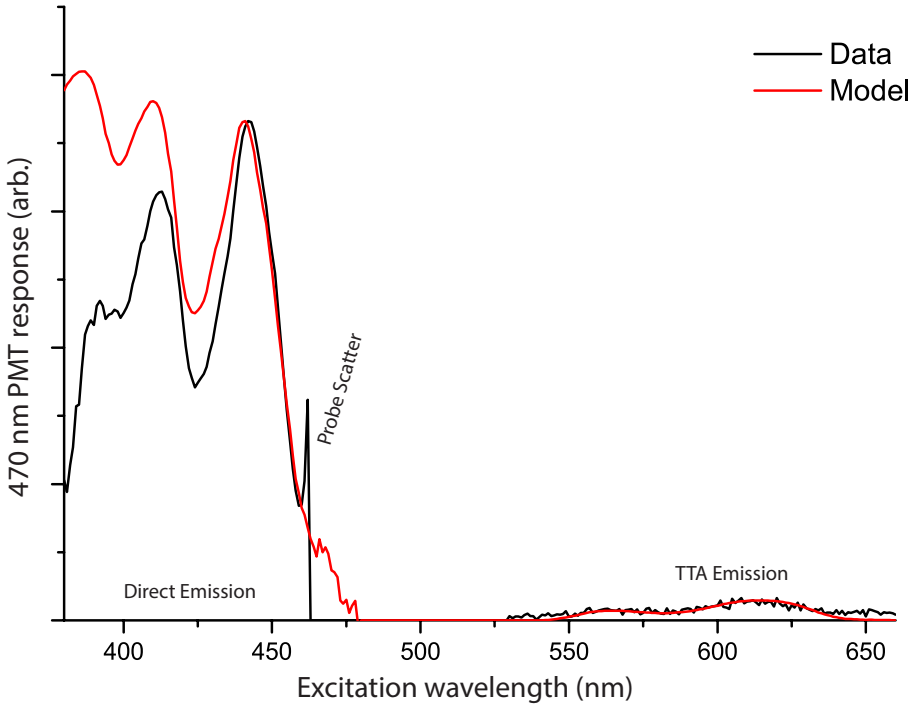

FIGURE 2.7: Representative fit quality achievable using original action spectrum model (Equation 2.13). In this dataset, prioritisation of the UC response region causes poor fitting at shorter wavelengths, although no set of fitting could be found which adequately described wavelengths below 425 nm. The 470 nm emission wavelength scattering peak was (mostly) removed from the data in this instance, causing the artefact spike and precipice in this region.

ratio between the direct and UC fluorescence response (Φ_{TTA}). Unfortunately no set of A and Φ_{TTA} could be found that adequately fit both regions simultaneously. The model action spectra were also found to be particularly ill-fitting for wavelengths shorter than 425 nm, and no set of fitting parameters could be found that modelled this region adequately (even when ignoring the fit quality at longer wavelengths). These model fits were not found to improve by incorporating additional attenuation terms for the low wavelength sensitiser absorption of the UC solution, nor the glass cuvette it was held in. This poor fitting was observed for action spectra at all pump powers, for later high resolution probe wavelength scans (1 nm steps), and across multiple replications of the entire experiment. After extensive troubleshooting, it eventually became clear that a different approach to data analysis was required in this case.

In hindsight, the author proposes that the critical flaw in the action spectrum model is likely its assumption of UC operating in the low efficiency regime. Results like Equation 2.7 feature heavily in the derivation of Equation 2.13 from Equation 2.12, and an alternate analysis of the perylene UC action spectra presented below indicates that even the spectra taken with the lowest pump power were already in the rollover regime between

low and high efficiency operation. The successful application of the action spectra modelling in the original publication is likely a result of using lower pump powers in that study, deliberately chosen to emulate the k_g accessible from solar radiation. By restricting operation to the low power regime, practical limitations of the fitting model may have escaped earlier identification. This difference is compounded by the unmeasured (but probably unequal) intrinsic efficiencies of the perylene and rubrene UC systems investigated, leading to the onset of high efficiency at different pump powers for the different emitters.

Indeed, the action spectrum model may in future be updated using the more general Equation 2.11 as its basis of derivation. Unfortunately this approach would require foreknowledge of the emitter k_1 and k_2 in order to extract Φ_{TTA}. Determining these parameters would then necessitate TRPL measurements, an additional characterisation step that the action spectrum method was initially designed to avoid. Clearly further work remains to be done in developing this method for widespread use.

At the time of this work, a simpler modelling scheme was proposed to analyse the CW fluorescence data. By reframing the action spectrum instrument as simply a more sensitive version of a CW excitation fluorimeter, and treating the P0 sample as a reference standard, the increase in *relative* UC performance for P98 could still be determined. The disadvantage of this approach was that the absolute values of Φ_{TTA} for the different emitter systems were no longer accessible.

Following normalisation at the 445 nm direct excitation response peak, a linear baseline correction was applied across the UC response region (530 to 660 nm), and the response curve integrated across this region to yield a single number for comparison. The values of these action integrals are plotted against pump beam power in Figure 2.8, and immediately demonstrate the superior performance of P98. For reasons mentioned above and described below, the linear to sub-linear rollover seen in Figure 2.8 is interpreted as evidence that operation in the low efficiency regime was an inappropriate assumption to make for these data sets, explaining earlier difficulties in applying the action spectrum model. The axes in Figure 2.8 were chosen to best display this rollover from 0–30 mW.

The dashed lines in Figure 2.8 were then generated by fitting Equation 2.11 at different pump powers and applying Equation 2.4 to determine the magnitude of fluorescence response. Additional scaling factors were necessary to match this modelling to the horizontal and vertical axes of Figure 2.8, making the absolute values of the parameters used to solve Equation 2.11 somewhat meaningless. Nonetheless, the behaviour of the model curves are useful in describing the differences in UC response at high and low pump powers. The non-zero intercepts in this figure correspond to measurements taken with only the probe beam, and the biasing pump beam blocked.

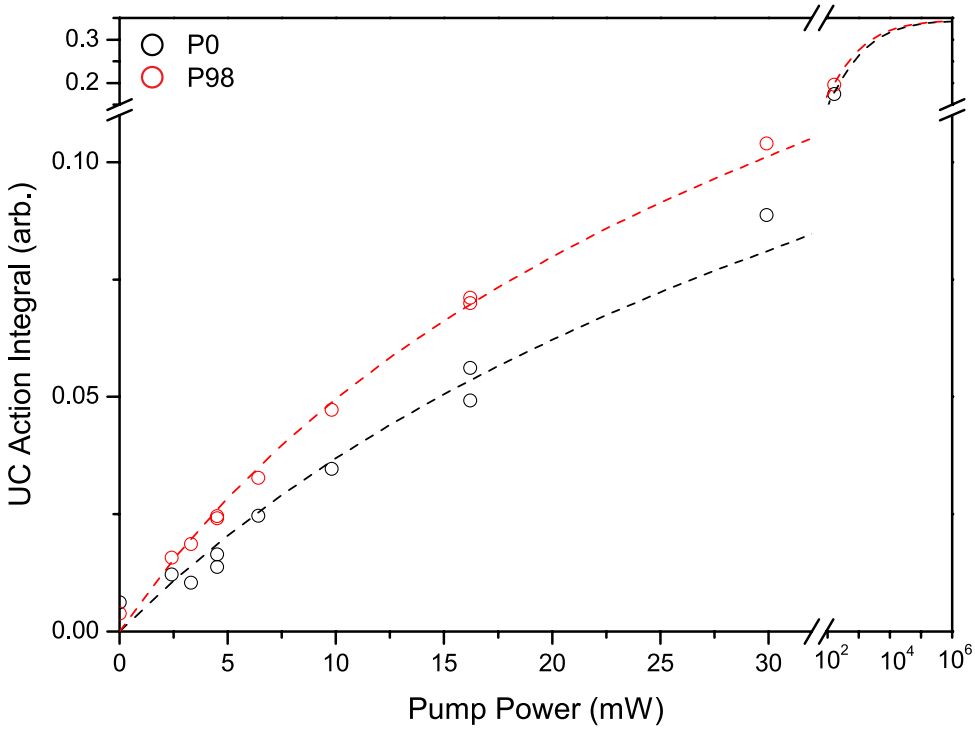

FIGURE 2.8: Changes in UC action spectrum integral with different pump powers. Dashed model curves generated from scaled solutions of Equation 2.11.

To extract the relative increase in UC performance of the P98 system, the nature of the lock-in amplification (Equation 2.12) was first taken into consideration as the basis of a new model. The action spectrum response across the UC region was taken to be proportional to the derivative of UC fluorescence intensity with respect to the probe beam intensity:

$$M \propto \frac{dI_{UC}}{dI_{pr}} = \frac{d}{dI_{pr}} \left(\frac{k_2 k_g^2 [S]^2 \eta \Phi}{2k_1^2} \right) \tag{2.18}$$

where M is the value of the action spectrum signal, and I_{UC} is given by Equation 2.7 in the low efficiency regime. Since the different UC samples had the same spectral shape in the UC region, the integrals of signal in this region are also taken to be proportional to the derivative in Equation 2.18. Additionally, since there were no absorbance features for perylene in the UC response region, all of the fluorescence intensity was assumed to be the result of UC, justifying the use of Equation 2.7 to expand I and exclusion of terms in I_F from Equation 2.12.

To evaluate the expression in Equation 2.18 and relate it to the data in Figure 2.8, the derivative of M with respect to the pump power was determined by splitting k_g into components describing excitation by the separate probe and pump beams:

$$\begin{aligned}\frac{dM}{dI_{\mathcal{P}u}} \propto \frac{d}{dI_{\mathcal{P}u}}\left(\frac{dI_{UC}}{dI_{pr}}\right) &= \frac{d^2}{dI_{\mathcal{P}u}dI_{pr}}\left(\frac{k_2(k_{g_{\mathcal{P}u}}+k_{g_{pr}})^2[S]^2\eta\Phi}{2k_1^2}\right) \\ &= \frac{k_2[S]^2\eta\Phi}{2k_1^2}\frac{d^2(I_{\mathcal{P}u}\sigma_{\mathcal{P}u}+I_{pr}\sigma_{pr})^2}{dI_{\mathcal{P}u}dI_{pr}} \\ &= \frac{k_2[S]^2\eta\Phi}{k_1^2}\sigma_{\mathcal{P}u}\sigma_{pr}\end{aligned} \tag{2.19}$$

where the two versions of σ represent the absorptivities of the sample to the pump and probe beams, and are both independent of I_{pr} and $I_{\mathcal{P}u}$. Due to its reliance on Equation 2.7, this result is only appropriate for low values of $(I_{\mathcal{P}u}+I_{pu})$, and the pump and probe intensities are taken to be independent of each other.

Examining the final result of Equation 2.19, the identical absorption and emission spectra of h-perylene and d-perylene indicate that Φ and σ should be identical in the P0 and P98 samples. Special care was taken to ensure $[S]$ was uniform during sample preparation, while the similar molecular sizes and electronic systems were used to justify taking k_2 and η to also have identical values. The latter assumption would subsequently be confirmed for k_2 by TRPL, and together these allow Equation 2.19 to be rewritten in terms of the only remaining molecular parameter expected to be impacted by deuteration (k_1):

$$\frac{dM}{dI_{\mathcal{P}u}} = \frac{\kappa}{k_1^2} \tag{2.20}$$

where κ is a combination of constants that were expected to be the same for P0 and P98. Equation 2.20 implies that the action integral signal should initially grow linearly with pump power (when in the low efficiency regime), with a gradient proportional to the inverse square of k_1.

Pleasingly, the action spectra integrals indeed grew approximately linearly with pump power at first, corresponding to operation in the low efficiency regime. Gradients were calculated using the data in Figure 2.8 over the range of pump powers from 0 to 10 mW. These gradients corresponded to the "response efficiencies" of the P0 and P98 UC solutions. A crude ratio of power in to signal out, the values of these gradients should be related to the UC efficiency by an unknown scaling factor that relates the emission intensity and action integral. Although absolute UC efficiencies could not be calculated without this scaling factor, a relative comparison could still be made. Since the only difference between these samples was the emitter species, the changes in the efficiency were attributed entirely to enhancement by deuteration. The P0 sample had a gradient of $(30\pm7)\times10^{-4}$ while the P98 sample had a gradient of $(44\pm1)\times10^{-4}$ (95 % confidence

intervals, arbitrary units), a 46±21 % relative efficiency enhancement due to deuteration. Using Equation 2.20, the 46 % increase in UC efficiency could be equated to a 17 % decrease in the value of k_1 of d-perylene. This difference was found to be in close agreement with direct measurement of k_1 by TRPL, discussed in the next subsection.

Further inspection of Figure 2.8 quickly reveals that this linear trend does not really hold for pump powers as small as ∼5 mW, and the gradients of tangents to the model curve at this power are already significantly smaller than the average gradients of the data points. Choosing 10 mW as the cutoff for the low efficiency regime allowed for a more significant statistical analysis, as well as again ensuring a conservative underestimate of the deuteration effect size. This nonlinear behavior nonetheless explains earlier difficulties applying the action spectrum model in Equation 2.13, as these UC samples were already in the rollover region between low and high efficiency operation even for the lowest pump powers used. The additional sensitivity of the initial action spectrum modelling method to these non-linearities is likely due to recursive applications of Equation 2.7 in calculating the absorption and emission intensity depth profiles, with small inaccuracies at the front face compounding exponentially with depth. As the analysis leading to Equation 2.20 does not take excitation or emission propagation into account, it has the advantage of being more robust to the onset of the high efficiency regime.

At higher pump powers the P98 still consistently outperformed the P0 sample, but by a diminishing relative margin. This trend is continued in the model curve, showing the deuteration enhancement vanish at very high powers. This is to be expected though, as in the high efficiency regime the amount of UC fluorescence no longer depends on k_1 or k_2, as given by Equation 2.9. This convergence provides further circumstantial evidence for the argument that h-perylene and d-perylene should not be significantly different in terms of η, as they would otherwise approach values that differ by the same ratio as their values of η. The larger initial gradient of the P98 sample and the common final values also imply that the P98 must enter into the high efficiency regime at lower pump powers, giving the P0 response a chance to "catch up". This as well is expected, as the threshold pump intensity is known to grow with k_1.[150]

2.3.3 Time-Resolved Upconversion Fluorescence

For TRPL measurements, the CCD output data files were imported into MATLAB as a two dimensional array. The array indices corresponded to wavelength and time, while the array values corresponded to the response of pixels to the fluorescence. By sampling values of this array well separated from the UC fluorescence (in both time and wavelength), a background value corresponding to the CCD dark response could be

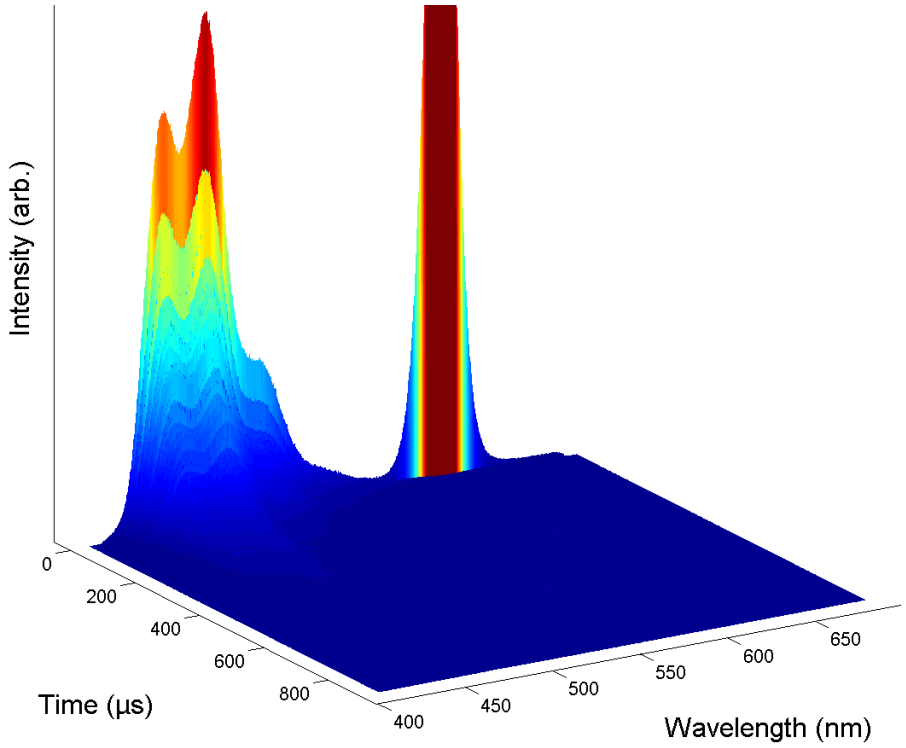

FIGURE 2.9: Representative TRPL spectrum of a P0 UC sample, showing 615 nm excitation in first frame only and shorter wavelength perylene emission decaying over hundreds of microseconds.

calculated and subtracted from all array values. Figure 2.9 shows one of these arrays after background subtraction, with the initial 615 nm excitation pulse visible in the first time slice only. The resulting UC fluorescence then decays over several hundreds of microseconds, retaining the same spectral shape throughout. The slight difference in the shape of the TRPL spectra compared to the CW fluorescence emission spectra was attributed to the inner filter effect, arising from reabsorption of escaping shorter wavelength fluorescence by the sample itself.

To prepare the TRPL spectra for fitting with Equation 2.15, the pixel response was first integrated over the UC emission region, chosen as 461 to 491 nm to avoid regions of high reabsorption. The resulting traces were then normalised to the initial time point, and a square root applied to convert the kinetics of I_{UC} into those of $[E^*]$. A representative set of TRPL decays are shown in Figure 2.10 for scans of the P0 and P98 samples with similar excitation pulse energies (7 and 5.5 μJ respectively). Although the UC fluorescence intensity for the P98 sample starts higher in the figure, the widening divide between the traces immediately indicates a more rapid fluorescence decay in the P0.

Figure 2.11 shows additional log plots of the TRPL decays for excitation with different pulse energies. All of these plots are approximately linear, indicating that the $k_1[E^*]$ term in Equation 2.14 dominates at these long times measured. At early times and high

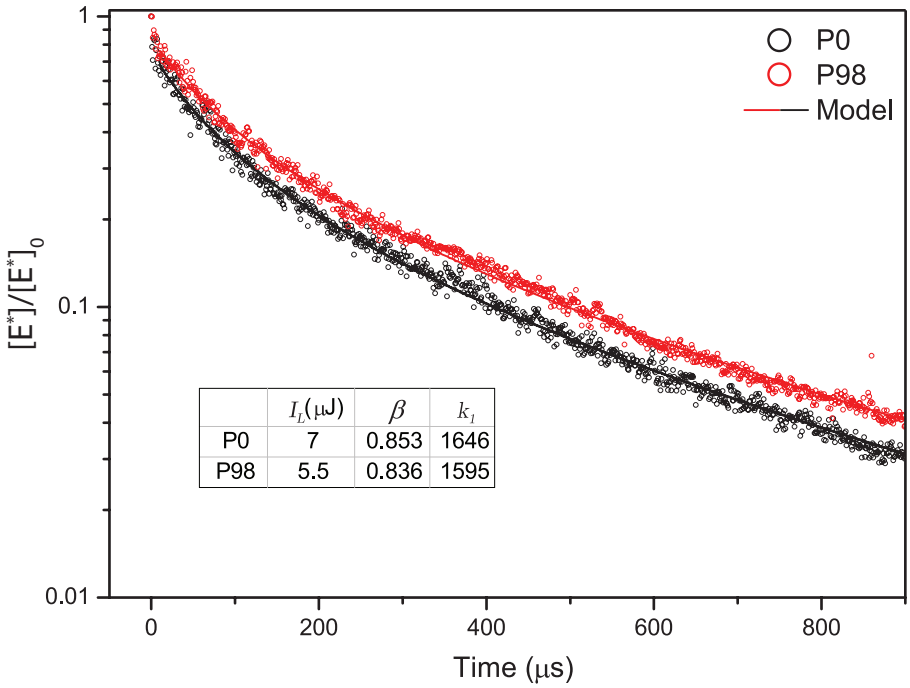

FIGURE 2.10: Representative kinetics of the UC emission from TRPL. The solid lines correspond to the best fits using Equation 2.15 with parameters in the inset.

excitation energies (vertically offset traces), small deviations from exponential decay arising from the $k_2[E^*]^2$ term can also be seen.

Fitting Equation 2.15 to the different TRPL traces yielded several sets of values for A, k_1 and β for both the P0 and P98 samples. Although k_2 could not be calculated directly from Equation 2.17 without $[E^*]_0$, the product Bk_2 could still be calculated from the measured pulse energies of each TRPL measurement and by assuming the same value of B for both UC samples. Sets of the parameter values from different pulse energy scans were combined by averaging, with 95 % confidence intervals calculated using the expression $\frac{2\sigma}{\sqrt{n}}$, where σ is the standard deviation of the elements the set and n is the number of elements. Figure 2.12 shows the comparison of the averaged k_1 and Bk_2 values, with error bars corresponding to the stated confidence intervals.

From this analysis the absolute values of k_1 were found to be 1780±76 s^{-1} for h-perylene, and 1484±110 s^{-1} for d-perylene. This represents a relative decrease of 17 ± 9 % upon deuteration, in close agreement to the action spectrum modelling. Despite large confidence intervals, the similar values of Bk_2 ($(2.6\pm1.3)\times10^7$ and $(2.2\pm1.8)\times10^7$)) support the assertion that k_2 does not change for d-perylene, which was assumed in earlier analysis of action spectra.

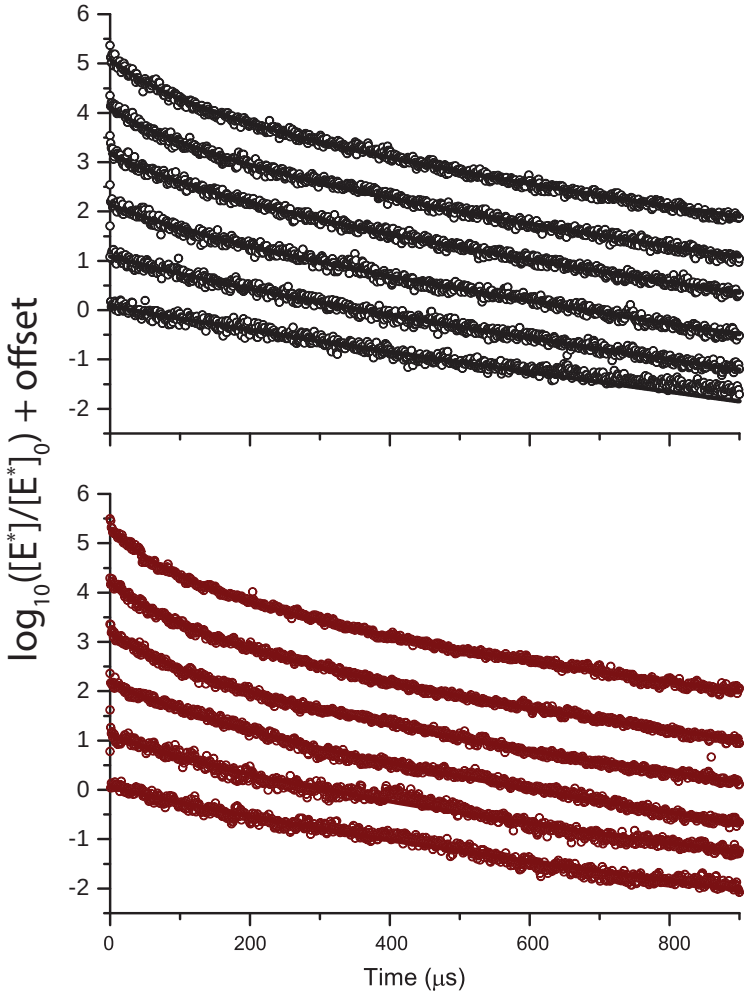

FIGURE 2.11: TRPL kinetics traces at different excitation pulse energies, with fitted model curves given by Equation 2.15. Traces with higher energies are offset upwards, with black traces corresponding to spectra from the P0 sample and red ones to P98.

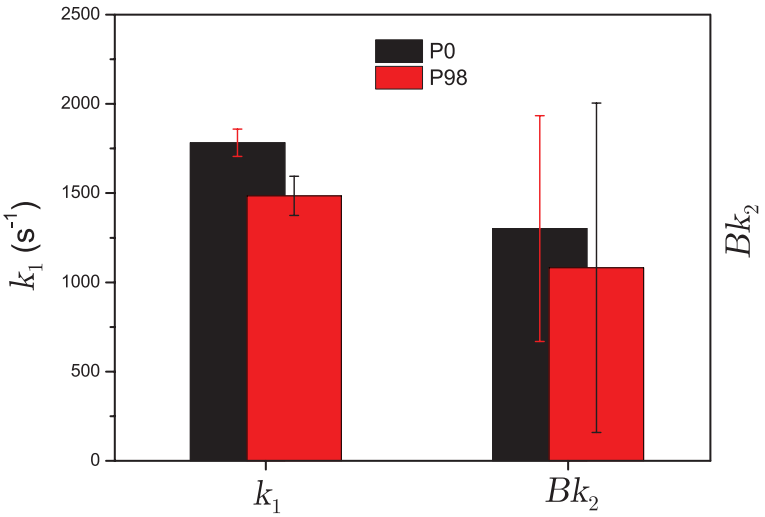

FIGURE 2.12: Combined rate constants for P0 and P98 derived from TRPL kinetics.

2.4 Outlook and Further work

2.4.1 General Comments

The primary aim of this work was to confirm that the effect of emitter k_1 on UC efficiency was well described by the quantitative models presented in section 2.1.3. Deuteration of the emitter was expected to selectively reduce k_1 (and increase efficiency), giving a comparison as scientifically "ideal" as one could reasonably hope for. The fact that the difference in k_1 measured directly from TRPL so closely matched the necessary difference required to explain the difference in action spectra provides strong experimental support for the models used for each independent method. It also strongly supports the pervading assumption that the other molecular parameters were indeed unaltered by deuteration.

In regards to this stated aim, and overcoming early challenges in modelling and data analysis, the project was deemed a complete success. This would still have been the case had a decrease in UC efficiency (increase in k_1) been observed for d-perylene, as long as such a decrease was in agreement with predictive models. The fact that efficiency did in fact increase then came as an added bonus, and no doubt made subsequent publication of the result significantly smoother.

The rest of this chapter details progress towards additional experiments and analysis arising from the original publication, including preliminary work on TTA OLEDs.

2.4.2 Size of the Deuteration Effect

Compared to other studies of perylene though, the absolute values of k_1 reported here were surprisingly large. In similar TRPL studies, perylene k_1 was reported to be just $200\,\mathrm{s}^{-1}$, while in crystal studies of similar PAHs these rates were most commonly in the range of $0.1\,\mathrm{s}^{-1}$.[191,194] Furthermore, in the same crystal studies other deuterated PAHs often yielded much larger reductions in k_1 — as large as 85 % for pyrene and over 50 % for many others. As the crystal studies were performed in low temperature conditions (77 K), the smaller difference at room temperature may be explained by the existence of a thermally activated curve crossing between vibrationally excited triplet states and very highly excited vibrational levels on the electronic ground state. This would increase the rate of non-radiative decay for both h-perylene and d-perylene at higher temperatures, most likely by similar absolute amounts, and therefore decrease the observed relative difference in k_1. Investigation of low temperature rate constants is difficult in UC systems though, as collisional TET and TTA processes effectively cease when the solvent freezes.

Thermally activated curve crossings cannot be used to explain the reported TRPL results though, as these were also performed at room temperature. Similarly, TA experiments in the next chapter also yielded significantly smaller values of k_1 for perylene. Experimental uncertainties in that study were not small enough to claim a significant difference between h-perylene and d-perylene, but both were in the range of $\sim 450\,\mathrm{s}^{-1}$.

It is possible that the removal of oxygen during sample preparation was not rigorous enough, leading to larger values of k_1 through its particularly effective quenching of triplet excitons.[148,149] Since both the P0 and P98 samples were prepared identically, it seems reasonable to claim that oxygen's contribution to the measured k_1 values should have been the same for both, and that its potential presence in this study does not invalidate the conclusion that d-perylene has a lower "intrinsic" k_1 than h-perylene. While an estimate of the oxygen concentration cannot be made without perylene's actual k_1 (and the rate constant of its quenching by oxygen), the absolute difference in both intrinsic and measured k_1 values for P0 and P98 would still be preserved given equal contributions from oxygen quenching, and here lies in the range of of 110–$482\,\mathrm{s}^{-1}$. The lower end of this range is consistent with the values of k_1 for P0 and P98 measured in the next chapter (Table 3.1, $\sim 450\,\mathrm{s}^{-1}$), and indicates that the true size of the deuteration effect on k_1 may be as large as 25 % — enhancing relative UC efficiency by over 70 %.

2.4.3 Mechanism of the Deuteration Effect

To investigate what size of deuteration effect might be expected for perylene, quantum chemical calculations were performed to model the non-radiative decay process described by the intrinsic component of k_1. This decay was taken to arise from ISC coupling of the triplet ground state to isoenergetic singlet vibronic states, followed by rapid thermalisation back to the ground state.[195] The rates of these transitions were estimated using the Fermi golden rule, as well as the Frank-Condon approximation to separate electronic (ψ) and vibrational (ϕ) components of the overall wavefunctions (Ψ):[196]

$$\begin{aligned} k_1 = \frac{2\pi}{\hbar} \left|\langle \Psi_2 \left|\mu\right| \Psi_1 \rangle\right|^2 \rho = \frac{2\pi}{\hbar} \left|\langle \psi_2 \left|\mu\right| \psi_1 \rangle\right|^2 \left|\langle \phi_2 | \phi_1 \rangle\right|^2 \rho \\ \propto \left|\langle \phi_2 | \phi_1 \rangle\right|^2 \rho \end{aligned} \tag{2.21}$$

where μ is the element of the Hamiltonian that promotes ISC, and ρ is the density of states in the region of the singlet manifold (subscript 2) that is coupled to the triplet (subscript 1) by ISC. As the electronic systems of the perylenes were taken to be identical, and only the relative difference in k_1 was sought, this leaves only $\left|\langle \phi_2 | \phi_1 \rangle\right|^2$ as the

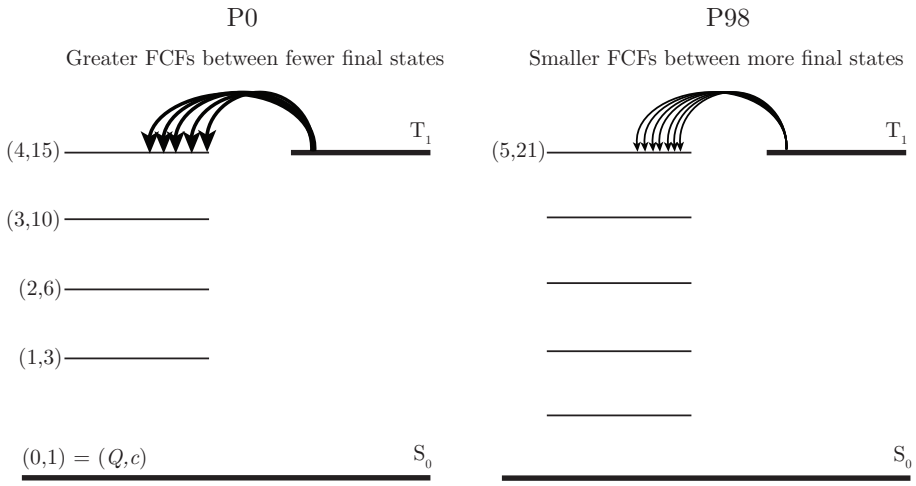

FIGURE 2.13: Balance of FCFs and density of states that determine k_1 in perylene.

relevant factor of the wavefunction for comparison. This overlap integral of vibrational wavefunctions is commonly referred to as the Frank-Condon factor (FCF) for a particular transition, and features heavily in the theory of vibrational transitions and infrared spectroscopy.[197]

For small PAHs like perylene, the allowed final states (for which ISC is energy conserving) are well separated, and so the density of states is not well defined. Furthermore, the FCFs for transitions to each vibrational final state need not be identical, as is implied by the simple multiplication by the density of states. Therefore, instead of evaluating Equation 2.21 as a product between some average FCF and a nebulous density of states, a discrete sum was instead constructed over the set of allowed final states:

$$\begin{aligned} k_1 &\propto \sum_c \left(\left(\prod_m \langle \phi_m(q_m) | \right) | \phi_1 \rangle \right)^2 \\ c &= \begin{pmatrix} Q+M-1 \\ M-1 \end{pmatrix} \end{aligned} \tag{2.22}$$

where the final states (of total number c) are represented by products of vibrational modes ϕ_m each populated by q_m vibrational quanta. In this way the vibrational density of states is replaced by the summation across the different final states, the number of which is determined combinatorially as the ways to distribute Q indistinguishable vibrational quanta amongst M distinguishable vibrational modes.

The energies of C-H vibrational modes are larger than those of equivalent C-D modes, and so ISC will proceed towards vibrational states with additional quanta (larger Q)

in deuterated molecules.[198] While the increase in the number of vibrational quanta will reduce the FCFs for these transitions, the number of possible final states available (c) will increase with increasing Q. The overall effect on k_1 depends on the balance of these competing effects, which are shown pictorially in Figure 2.13.

To evaluate Equation 2.22 for perylene, calculations were first performed by Dr Murad Tayebjee to allow estimation of Q, M, and $\langle\phi_2|\phi_1\rangle$. Geometries, energies, and vibrational modes of the electronic triplet excited and singlet ground states of both h-perylene and d-perylene were calculated using the B3LYP functional and 6311++G basis set under D_{2h} symmetry with the GAMESS-US package. A displacement vector associated with the ISC transition was calculated from the atomic displacements between the singlet and triplet molecular geometries. Large projections with this transition displacement vector were used to identify 16 vibrational modes (from the total of 90) that were active in mediating ISC.

To calculate FCFs, harmonic potentials were constructed for each of the 16 active singlet vibrational modes. The ground state vibrational wavefunction of each mode was then duplicated and shifted along its vibrational coordinate by an amount proportional to the projection of that mode's atomic motions with the transition displacement vector. The effect of this was to express the triplet state state geometry in terms of the singlet state plus a vibrational correction term (the transition displacement vector) constructed in the basis set of singlet vibrational modes. The product of these shifted modes was therefore taken to represent the vibrational ground state of the triplet excited state, and FCFs were then calculated between it and pure singlet states up to the 90^{th} vibrational overtone in each mode (no vibrational states comprised of combinations of different modes were considered at this stage). Although no vibrational overtone would perfectly match the energy of the triplet state, the FCF for the imagined (non-existent) isoenergetic transition was then determined by linear interpolation of the FCFs for the two overtones closest in energy to the triplet state.

From the size of the FCFs interpolated to the triplet state energy, only three modes were identified as having a significant contribution to ISC. As a result, M in Equation 2.22 was taken to have a value of 3. The energies of these modes were similar, and averaged to give $3179\,\mathrm{cm}^{-1}$ and $2349\,\mathrm{cm}^{-1}$ for h-perylene and d-perylene respectively. All three of these modes corresponded to C-H vibrations, which was expected since C-C modes were unlikely to be significantly affected by deuteration, and therefore unlikely to contribute to the change in k_1. Compared to other displacement vector active modes, these three also had the largest energies — requiring the fewest quanta to match the triplet energy and thus yielding better FCFs with the vibrational base of the triplet state. This in part justifies the omission of other low energy modes in comparing k_1.

The number of vibrational quanta needed in these averaged modes to reach the triplet energy determined Q, which after dividing the triplet energy by the mode energy was rounded to the nearest integer to give 4 for h-perylene and 5 for d-perylene.

With FCFs calculated and M and Q determined, Equation 2.22 could be used to estimate the ratio of k_1 for h-perylene and d-perylene. Doing so yielded a prediction of a 5000-fold decrease for d-perylene — qualitative matching but quantitatively much larger than the mere 16 % observed change. This difference is likely a reflection of the crude nature of these calculations, which do not begin to take into account solvent or temperature effects. Alternatively, it may be further indication that experimental factors such as oxygen ingress and model assumptions mask a much larger relative difference in the intrinsic values of k_1 for P0 and P98 samples.

To better emulate the conditions of this calculation it may be possible to perform gas phase studies of the perylene triplet, with no oxygen or solvent. As previously mentioned though, the isolation of the perylene triplet state often requires a sensitiser to populate, and it is unclear how this could be achieved for bare perylene gasses. Covalent self-sensitised dyads may be possible to produce and study in this way, but would require careful consideration of how to eliminate influences from the sensitiser (and dyad interactions) on the properties of the perylene. [199,200]

2.4.4 Widespread Applicability

2.4.4.1 Partially and Selectively Deuterated Perylene

The perylenes compared in this study were either fully deuterated, or fully hydrogenated. The analysis of the vibrational modes in the previous section highlighted three main contributors to non-radiative decay, which also happens to match the number of symmetry unique hydrogen sites on perylene. This is probably coincidental as none of these modes had large vibration amplitudes localised on specific kinds of hydrogen site, but it remains an open question whether deuteration of specific sites on perylene may contribute more or less to the overall suppressing effect on k_1. In phosphorescence studies of other small PAHs the effect of deuteration has been found to be simply additive for some, but may be site selective for others. [190,191]

To investigate these possibilities, three additional perylenes were produced by Dr Tamim Darwish at the Australian Nuclear Science and Technology Organisation's National Deuteration Facility (ANSTO NDF). The structures of these partially deuterated perylenes are shown in Figure 2.14, with isotopic substitution characterised by mass spectrometry

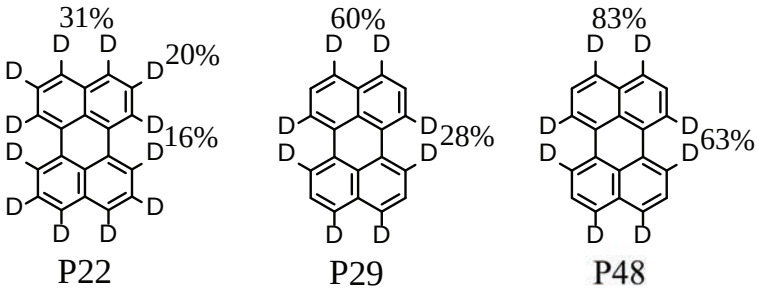

FIGURE 2.14: Structures of partially and selectively deuterated perylenes.

as well as ^{1}H and ^{13}C NMR. Inspection of these structures indicates that different reaction conditions were able to give some selectivity over the deuterium exchange sites. As a result, these compounds could be used along with P0 and P98 to construct a solvable set of linear equations to reveal the weighting of different site deuteration towards the total value of k_1. Equal weightings would correspond to the deuteration effect being purely additive, while unequal ones would unmask some sites as being more important in controlling k_1.

Following the pattern established for P0 and P98, UC samples made using these perylenes were labelled P48, P29 and P22 based on the average deuterium content. Although they were found to display UC with TPTBPt the emission colour was white rather than blue, and when these compounds were studied using TRPL their kinetics were found to be very different than the P0 and P98 samples. An extremely rapid decay component dominated at early times, and traces could not be fit using the same Equation 2.15 as earlier. An example of this is shown in Figure 2.15 for P22. It is possible that perhaps

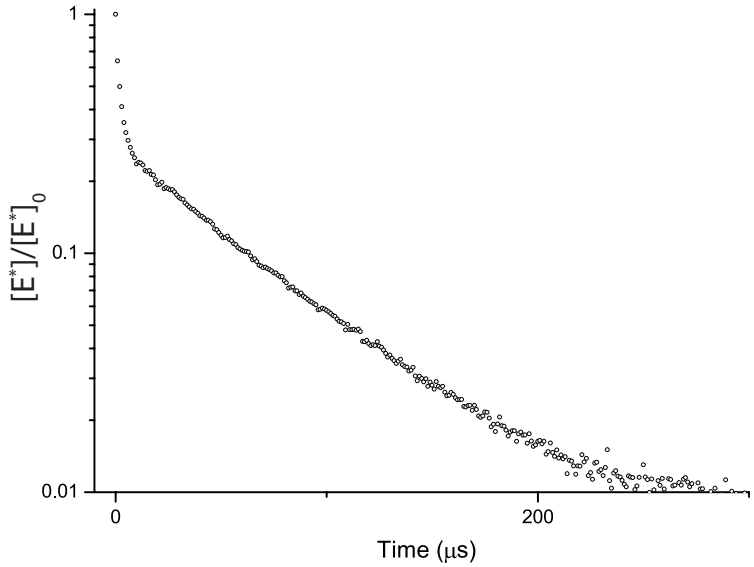

FIGURE 2.15: Representative kinetics of a P22 UC sample. Note the rapid early decay despite a significantly truncated horizontal axis compared to other figures.

the longer time kinetics could have been fit with a first order process, but the presence of the new and unknown rapid decay process meant that any conclusions drawn from blind application of the mixed kinetics model would be highly suspect.

As these perylenes were synthesised rather than purchased, a speculative explanation for their difference in kinetics may be that impurities generated during synthesis remained in the received compounds. As the pKa of PAH hydrogens is approximately 43 (that is, they are highly non-labile), the high pressures and acidic conditions necessary to promote deuterium exchange may have led to decomposition of some reactant perylene molecules, forming efficient quenching fragments.[201,202] Unfortunately, significant portions of the received perylenes were consumed in preparing the first round of measurement solutions, and additional studies were not prioritised due to their scarcity. In what is perhaps a case of sour grapes on the part of the author, it was later noted that the largest expected difference in k_1 (that between P0 and P98) was only barely resolvable with the methods employed above. As a result, measurements of the intermediate perylene systems were unlikely to yield statistically significant results anyway.

2.4.4.2 Other UC Emitters

While this study focussed solely on perylene, it immediately raised the prospect that other commonly used UC emitters might also be enhanced by deuteration. To investigate this, deuterated versions of rubrene, DPA (9,10-diphenylanthracene), and BPEA were also synthesised at the NDF. Figure 2.16 shows the substitution locations for these compounds, with purities in excess of 97 % for all substituted sites. Once again, characterisation of these compounds was achieved through MS and both ^{1}H and ^{13}C NMR.

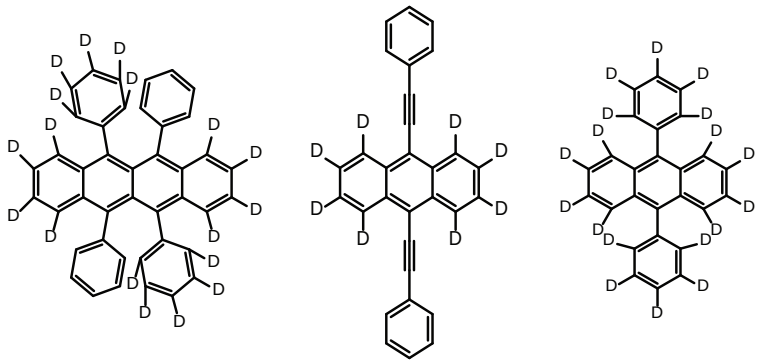

FIGURE 2.16: Structures of deuterated rubrene, BPEA, and DPA.

For these other PAHs, isotopic substitution on the core was pursued ahead of side groups, as these core hydrogens were expected to be more active in determining overall photophysical properties. In this categorisation, perylene only has core hydrogens. Deuteration of side groups has been shown to have some effect in electroluminescent polymers, although this was explained in terms of device morphology and spin coherence. [203]

While the original concept of the action spectroscopy method would have been ideal for rapid screening of these compounds for differences in Φ_{TTA}, the difficulties previously encountered applying this method for perylene UC meant that this was not attempted a second time. Instead, TA methods were used to determine absolute values of both k_1 and k_2 for these compounds, as well as k_{TET} between S^* and E. Work on this topic is the central focus of the next chapter, and is summarised in Table 3.1.

2.4.5 Deuteration and Singlet Lifetime

In the preceding analysis (and in the following chapters), it has been assumed throughout that deuteration should have no effect on the emitter electronic properties relevant to TTA (primarily η and Φ). For η this is retrospectively justified for perylene by the convergence of P0 and P98 TTA emission at high pump powers, as seen in Figure 2.8.

During examination of this document it has been raised that the arguments for an decreased triplet k_1 in deuterated perylene (section 2.4.3) might also apply to the singlet excited state. That is, reduced FCFs between the base of the emissive singlet state and vibronic levels on the singlet ground state could suppress internal conversion — similarly to how it has been proposed to suppress ISC from the triplet state. This would increase the emitter singlet lifetime (τ_s) and thereby potentially increase Φ, also casting some doubt on the conclusions drawn here by attributing all changes to differences in k_1. Indeed, deuteration effects on Φ and τ_s in excess of 20 % have been shown for some other molecules. [204]

The easiest way to address these concerns would have been to explicitly measure Φ and τ_s for the two perylene isotopologues (as well as for other deuterated emitters DPA, BPEA, and rubrene). The value of Φ is determined by comparing the ratio of sample absorbance and emission (often with the aid of a reference standard for instrument calibration), while τ_s can be determined using ultrafast TRPL measurements. Changes in the singlet lifetime are related to Φ by:

$$\Phi = \frac{\text{photons emitted}}{\text{photons absorbed}} = \frac{k_r}{k_r + k_{nr}} = k_r \tau_s \tag{2.23}$$

where k_r is the rate constant for radiate decay from the singlet excited state, and k_{nr} is the combined rate constant for all forms of non-radiative decay. Although these experiments were not performed during this project, circumstantial evidence indicates that any possible change in Φ upon deuteration would have only minimal effects on the conclusions drawn about k_1.

In the first instance, action spectra measurements of P0 and P98 gave very similar 470 nm emission intensities when the perylene was directly excited. While this does not allow the absolute value of Φ to be determined for either, comparing their emission signal from identical excitation (in identically absorbing samples) allows the relative difference to be determined. Indeed, the small differences in emission intensities were previously attributed to variation in detector sensitivity or pump beam power, and the fact that the P98 emission was consistently stronger than the P0 dismissed as a coincidence. The raw action spectra were normalised at 445 nm using the scaling factors given in Table 2.1, although these might instead have represented an increase in Φ on deuteration of 2.6±0.6 %.

The follow-on effect of this potential change in Φ remain similarly small. The ratio of gradients used to determine relative changes in k_1 (46±21 %, using Equations 2.19 and 2.20) would be modulated by an additional prefactor of 0.98, representing the ratio of emitter Φ. This results a variation well within the confidence intervals of the measurements and the calculated final value of the deuteration effect on k_1, even when the entire difference between P0 and P98 emission is attributed to changes in Φ.

More generally, the large values of Φ for the hydrogen isotopologues of all TTA emitters used in this project restricts the scale of their potential increase upon deuteration. For h-perylene, its Φ of 0.9 means that $k_r = 9 \times k_{nr}$, using Equation 2.23.[205] Although k_{nr} represents a range of deactivation processes (many of which would be unlikely to change upon deuteration), applying an overestimate blanket 16 % reduction in k_{nr} for d-perylene would only result in an increase of Φ by ∼1 %. The change in Φ is only about ∼2 % even if the maximum speculated 25 % change in k_1 is applied fully to k_{nr}, although it should be noted that a change in k_1 of this size was not observed in TRPL measurements. On this basis it appears that the earlier assumptions of detector variability are the most likely explanation for the numbers in Table 2.1.

For DPA, BPEA, and rubrene — with Φ of 0.9, 0.87, and 0.98 respectively[206–208] — similar arguments show that their values of Φ do not have headroom to rise significantly; k_r already dominates k_{nr} in each of these compounds, and reducing k_{nr} further has limited effects. This is in contrast to the triplet state, where the absence of a dominant k_r gives changes in k_{nr} more pronounced effects.

2.5 Applications to Light Emitting Diodes

2.5.1 Effect of Deuteration in OLEDs

As discussed in section 1.2.3.1, OLED performance naturally suffers from the excess formation of non-emissive triplet excitons. In order to emit, these excitons must survive long enough to dissociate and reform with other partners as singlets, or to undergo typically slow processes like phosphorescence or TTA. In both normal, phosphorescent, and TTA enhanced OLEDs, it stands to reason that a longer triplet lifetime (smaller k_1) would result in improved performance — with fewer triplet excitons lost to non-radiative decay before emissive processes can occur. For OLEDs that use small PAHs or organic polymers as their emissive layer, this deuteration enhancement has been previously demonstrated.[209–212]

Due to their high Φ_F and visible emission, there is strong overlap between the classes of compounds used for small molecule OLEDs and as UC emitters, including perylene. Having established a lower k_1 and better UC performance for d-perylene, a natural extension of this work was to then see if it also performed better than normal perylene when incorporated into OLEDs. Although access to facilities and training for OLED fabrication was not readily available, collaboration with scientists at the Commonwealth Science and Industrial Research Organisation (CSIRO) and at the University of Queensland (UQ) proved initially fruitful in pursuing this research direction. Progress in this further work is presented in this section in the form of a self-contained "mini-chapter".

2.5.2 Device Fabrication and Characterisation

Two sets of OLEDs were initially secured for study. The first device was provided by Dr Ajay Pandey and was made of ITO / 32 nm rubrene / 25 nm C_{60} fullerene / Ag, a device structure which has received recent interest due to its peculiar emission properties.[96,213] The second set of devices had perylene included as an emissive layer, and were prepared by Drs Scott Watkins and Karl Weber at the CSIRO Future Manufacturing Flagship. The devices were all based on a published small molecule device structure, comprised of 165 nm ITO / 35 nm NPB / 35 or 60 nm CBP / 25 nm Alq_3 / 1 nm KF / 200 nm Al (+50 nm TcTa passivation).[214] A control device (35 nm CBP) was provided with the same above layer structure, along with ones where the CBP layer was co–deposited along with either h-perylene or d-perylene at a nominal 2 % concentration. Although higher perylene concentrations may have led to more easily observed TTA emission, here a lower concentration was chosen to prevent large changes in electron and hole transport properties frustrating comparison of device emission. Other studies of OLEDs

have shown that TTA can play a critical role in emission output at concentrations as low as 10 %.[215] No control device was provided for the thicker CBP layer devices, nor one in which CBP was replaced by ADN.

For the perylene OLEDs, a broad range of standard characterisations were performed by CSIRO staff immediately following fabrication. These included IV curves, LV curves (equivalent to CW electroluminescence or EL), colour calibration, and efficiency measurements. Once received, additional characterisation was performed or planned for the different OLEDs as part of a collaborative effort at the University of Sydney. For the rubrene OLED, IV curves were measured by Thomas Keevers, while CW and TREL scans were performed using a function generator outputting a controllable square wave as a driving voltage for the OLEDs, while simultaneously also providing a triggering source for the same camera used previously in TRPL. Delay increments in the camera software were used to collect emission spectra at different times across the drop of the driving voltage, analogous to the end of the excitation pulse in TRPL. Preliminary analysis of the rubrene TREL data was performed by Dr Miroslav Dvořák.

2.5.3 Results and Discussion

2.5.3.1 Rubrene OLED

For the rubrene/C_{60} OLED, its ability to generate yellow emission characteristic of rubrene (∼2 eV photons) from driving voltages as low as 1.3 V already strongly suggested that some kind of UC process was active. This seemed reasonable, as the low voltage electronic excitation would still provide plenty of triplet excitons able to undergo TTA. The IV curves of this device also indicated the rapid onset of large currents and luminescence at this threshold voltage. CW EL spectra were collected for a range of voltages both above and below this threshold, and matched the shapes of early frames in the time-resolved spectra presented in Figure 2.17. Two main bands of emission were identified, a strong one in the visible and a weak one in the NIR range. Emission from these features was integrated to give the single numbers plotted against voltage in Figure 2.18, and were thought to come from TTA (strong emission) along with some kind of low energy trap or charge transfer state recombination (weak emission).

On the log plot, the LV curve for this OLED appears to undergo a regime change similar to that described by Equations 2.7 and 2.9 for solution based UC, with the gradient (corresponding to the index of the power law relating these quantities) changing between two separate values below and above the critical voltage. Instead of changing k_g with stronger optical excitation for the UC system, here a larger voltage was assumed

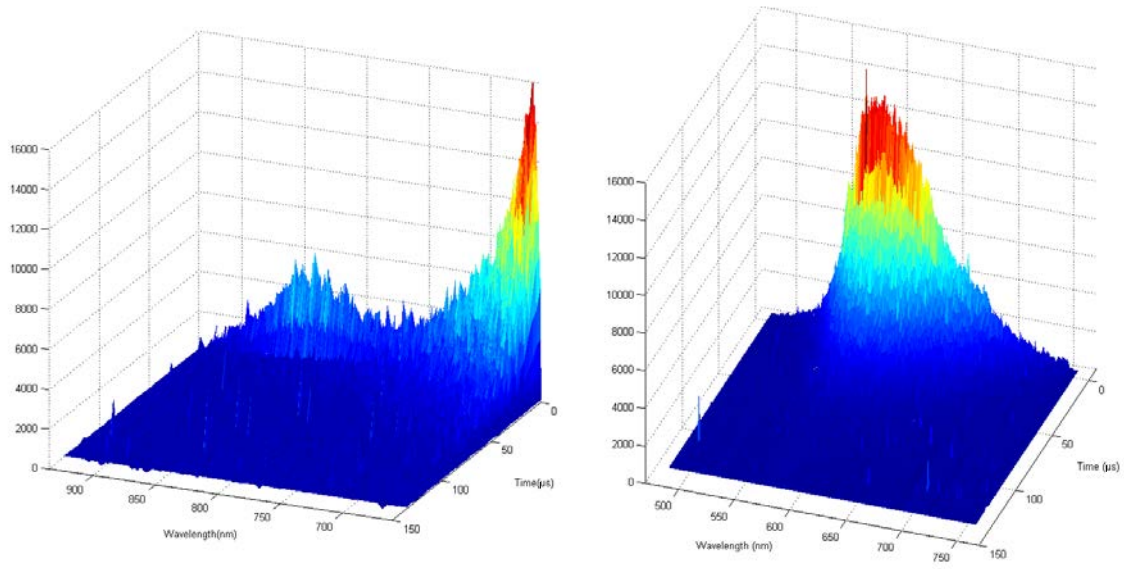

FIGURE 2.17: Representative TREL spectra of the rubrene/C_{60} OLED driven at 4 V. The smaller NIR emission feature was detected using higher camera gain settings for the spectrum on the left, and is partially occluded by noise spikes at times beyond 50 microseconds. The larger peak in the right of that spectrum is due to overlap with the edge of the visible emission, which is appropriately scaled in the spectrum on the right.

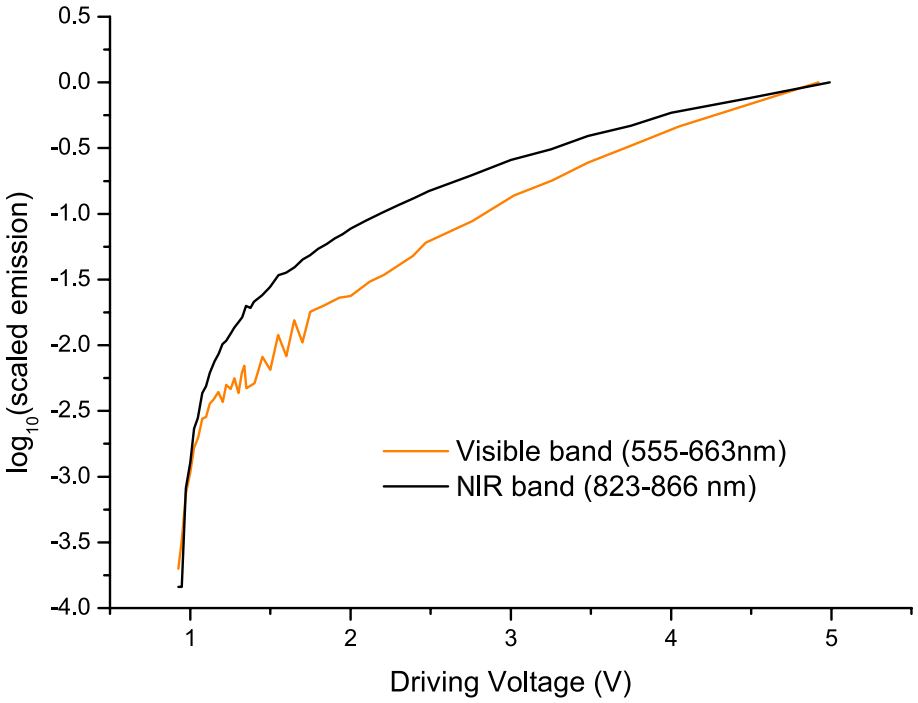

FIGURE 2.18: CWEL of the rubrene/C_{60} OLED visible and NIR emission bands.

to lead to a higher concentration of triplet excitons in the device, pushing it into the high efficiency region for TTA.

Time-resolved versions of the "turn off" TREL spectra were also collected at a handful of different voltages, with examples shown in Figure 2.17. These are analogous to the TRPL spectra collected after a short laser excitation pulse generates a population of triplets that then begin to decay. When the driving voltage was between 1.3 and 2 V, traces generated from these spectra were found (by Dr Dvořák) to be reasonably fit with double exponential functions, in a way reminiscent of some early and less sophisticated UC TRPL studies. In these cases the fitting works because there is a slow and a fast process draining the population of triplet excitons, leading to two characteristic lifetimes. The double exponential fitting has since been superseded by Equation 2.15, as the two "lifetimes" suggested by the exponential model are not completely independent processes, but rather first and second order decay of the same pool of triplet excitons. Nonetheless the reasonable fitting found here was further confirmation that TTA was occurring in the device. Emission in the NIR region was fit with a single exponential, with a short lifetime thought to correspond to the rapid recombination rate for some lower energy (hence longer wavelength) trap or charge transfer state. [216]

At higher voltages an additional exponential function was required in the fitting of the visible emission, with a much larger amplitude and faster decay rate than before. This component was thought to be due to direct electric excitation of rubrene singlet emission once the applied voltage was large enough to achieve this. Even in this case, a small amplitude exponential with roughly the same decay constant as the faster of the two at lower voltages was still found in the fitting, implying that TTA was still occurring. The difference in the exponential amplitudes indicated that the TTA component was not the dominant emission mechanism at these larger voltages though, which is not surprising considering the much larger expected rate constant direct for singlet emission.

Additional data collection along with more advanced spectroscopic methods had been planned for this device, including magnetic field effects on its emission and use of magnetic resonance to probe its spin coherence lifetimes. [217–223] Unfortunately at this stage the device's performance had significantly decayed, to the point where the emission was no longer visible to the unaided eye. Additional sets of devices were sought but could not be secured, limiting the scope of this and further investigation. In light of the results obtained for rubrene in Table 3.1, a quantity of deuterated rubrene was also sent to UQ to see if it produced a higher efficiency OLED, although this did not result in the receipt of additional devices for measurement. Completely reliant on collaborators for fabrication, research on this kind of device could not be pursued further from this point. Instead, studies of this kind have been published by others in the years since. [96]

2.5.3.2 Perylene OLED

For the control and h/d-perylene CSIRO devices, all three were found to have "normal" shapes of IV and LV curves. The onset of green emission (2 eV photons) at ~4 V for devices with perylene and 5 V for the control device indicated that perylene TTA was not a significant contributing factor to this emission, although perylene was having some effect to lower the threshold voltage. Furthermore, the similar colour profiles of the perylene and control devices indicated that emission was coming from the CBP or Alq_3 or NPB layers in all devices, and not directly from the blue emitting perylene.

Of critical interest, the absolute efficiencies of the different devices are shown in Figure 2.19. Compared to the control device, the h-perylene doped OLED saw an almost 100 % increase in output efficiency, and 150 % for d-perylene. Similar changes were also seen for a set of devices with thicker NPB layers, with uniform enhancements across the pixels in the devices (narrow box plots). Since perylene itself was not emitting directly, this efficiency increase was suspected to arise from the perylene triplet excitons being able to survive long enough to undergo other emissive processes, instead of decaying more rapidly through non-radiative pathways in CBP (or other layers) alone. The possibility also existed that heterogeneous TTA between perylene and CBP triplets was populating the CBP singlet excited state to enhance the green emission. A similar heterogeneous TTA UC system would be studied in greater depth later, with key results presented in the next chapter.

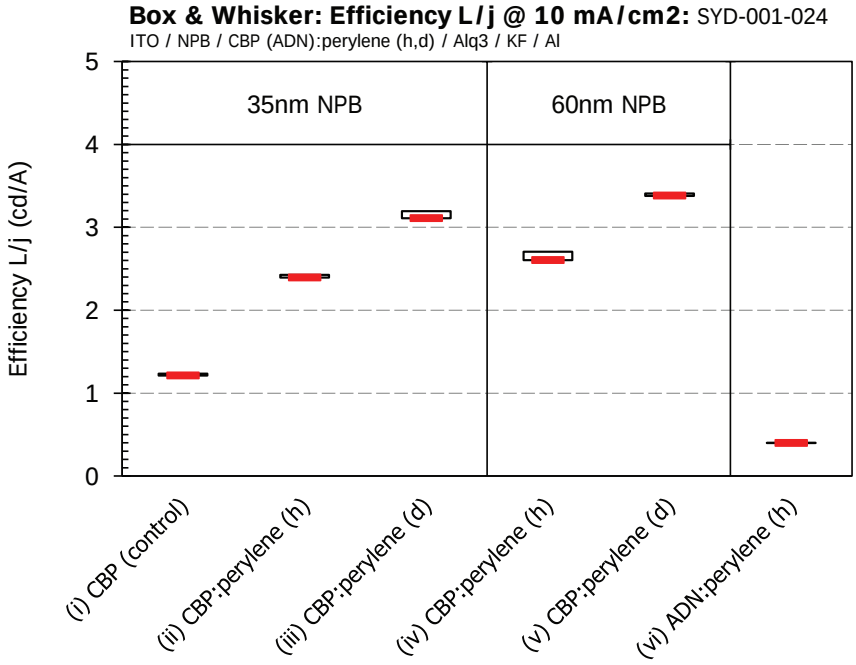

FIGURE 2.19: Absolute efficiencies of perylene OLEDs.

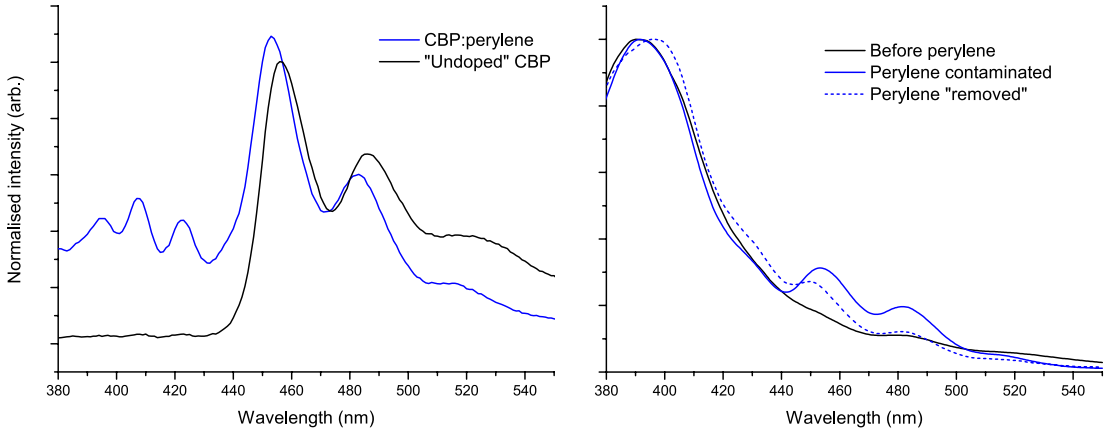

FIGURE 2.20: Emission spectra of perylene contaminated devices and films. Left are EL spectra of TcTa/CBP/TPBi devices with and "without" perylene doping the CBP layer. Right are PL spectra of CBP films deposited before perylene was introduced to evaporation chamber, when it was deliberately codoped, and when it had been "removed" from the glovebox evaporator.

As with the rubrene OLED, a battery of tests were planned for these devices — including advanced magnetic resonance techniques to better understand the identity and dynamics of charge carriers. Like the rubrene device though, the operational lifetime of these devices was shorter than the time needed to prepare for these measurements, with the device encapsulation rated for only two weeks. Thankfully, a second set of devices was later secured thanks to the generosity of Dr Jenny O'Connell, also at the CSIRO, intended as replicas of the first batch.

Inconsistencies with the second batch of OLEDs began to emerge when they too were characterised at the CSIRO. All were found to emit in the blue rather than green. At first this was thought to be the result of omitting Alq_3 from the new device layer structure, but latter emission spectra of these devices and of co-deposited films showed that they all contained a contribution matching the fluorescence emission spectrum of perylene. This even included the emissive layers of control devices, which were supposed to be free of perylene. Emission spectra of these devices (EL) and films (PL) are shown in Figure 2.20, and should be compared with the solution perylene emission in Figure 2.5.

Closer inspection of all devices produced in that layer deposition glovebox (including those from unrelated projects) showed that they all now displayed this perylene emission in varying degrees, indicating that the compound had extensively contaminated the deposition chamber. This was attributed to the surprisingly high volatility of perylene, which would have allowed far more of the material to evaporate onto devices (and the rest of the chamber) than was expected from tooling factor calibrations. Material remaining on the chamber surfaces would then be deposited onto subsequent devices as well. Thorough cleaning of the glovebox (including all vertical surfaces, and necessitating a full strip down) resulted in these features vanishing in devices produced afterwards

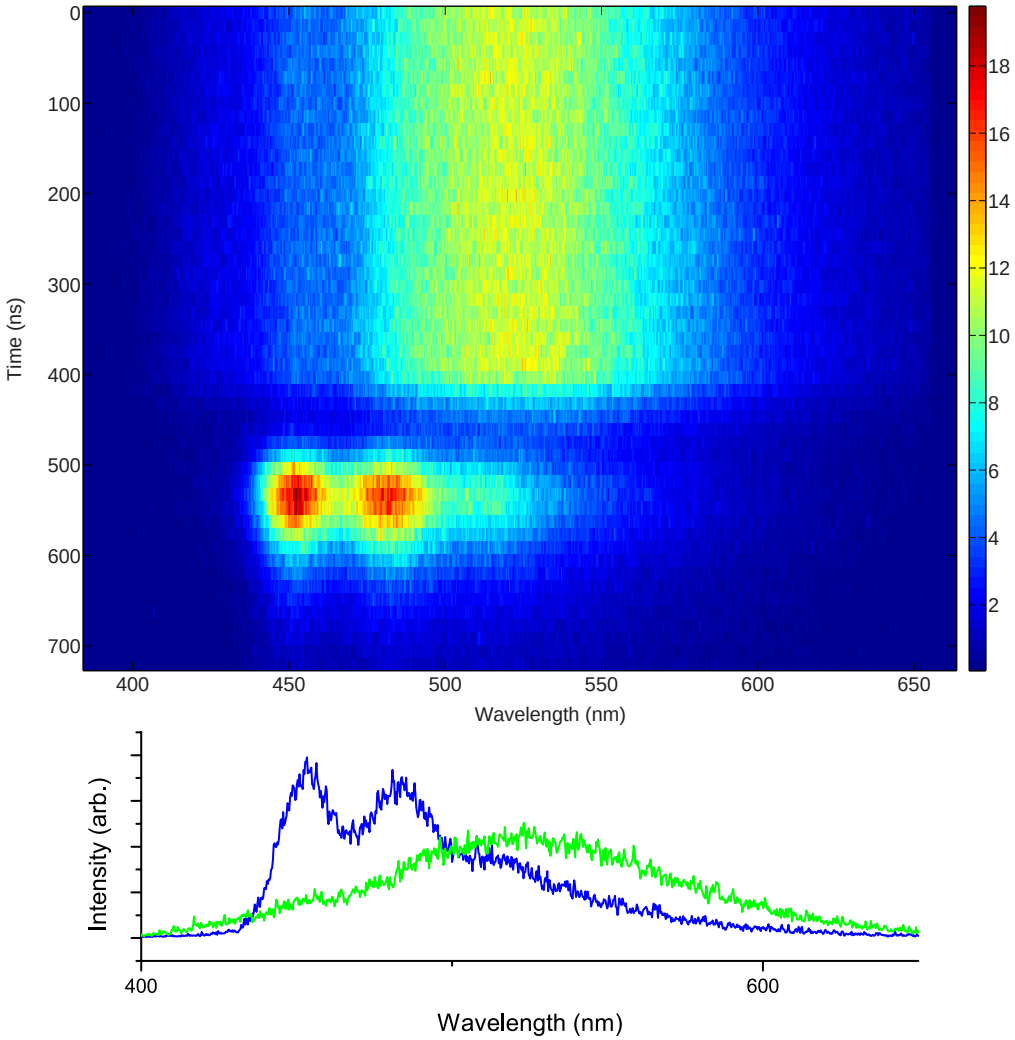

FIGURE 2.21: Time-resolved electroluminescence spectrum of perylene control OLED from original batch with 10 V rectangular wave driving. Intensity colour scale in arbitrary units. Wavelength slices of the spectrum through "on" (green) and peak 450 nm emission (blue) are reproduced for comparison to other emission spectra of perylene.

but also in several weeks of downtime for the Manufacturing flagship group. Sadly but understandably, no more devices were produced after this point.

The ability for perylene vapour to completely contaminate the fabrication glovebox immediately cast doubt upon the composition of the first set of devices as well. Despite their considerable ageing by this point, one of the control devices from the initial batch was set up for TREL measurement to see whether perylene emission could be seen in it as well. Sure enough, shortly after the CW emission spectrum had decayed a large emission feature could be seen that matched the emission of perylene. This feature is shown in Figure 2.21 along with the kinetics and time evolution of the spectrum, revealing that it occurs only after the complete decay of the initial emission.

The presence of perylene in the initial control devices then cast doubt on the composition of and results from all the others from CSIRO. Most probably, perylene vapour would have also contaminated the glovebox in the initial fabrication run as well, causing variable amounts to be deposited into different devices and for the different isotopologues to cross contaminate each other. As a result, this meant that the efficiency increases shown in Figure 2.19 may have just been due to different amounts of perylene dopant, and any claim of deuteration enhancement of the OLEDs cannot be fully justified.

Nonetheless, the fact that the higher energy perylene emission occurred at all in the second batch lends further support to the hypothesis that perylene normally assists this emission through heterogeneous TTA. It is possible that once singlet excitons are rapidly depleted amongst the green emitting component, blue emitting homogeneous TTA from the remaining perylene triplets then becomes the dominant mode of emission. The tail of this blue emission might even be fit with Equation 2.15 to even more strongly suggest that TTA is active, although this was not attempted here. Perylene TTA would rarely occur under a constant driving voltage as the perylene is a dilute dopant and awash amongst CBP triplets, which could be why blue emission was not noticed in earlier CW measurements and why it becomes visible only after CBP emission decay.

Thus, while the enhancement of the perylene devices by deuteration cannot be conclusively confirmed (or quantified) due to contamination, the results from the "control" device qualitatively suggest that TTA nonetheless contributes. If this is the case, then enhancement of the TTA channel by deuteration would lead to further increases in the overall OLED performance. It is not clear though why the perylene emission occurs more brightly than the "on" CBP emission (after the device has been switched off), nor why it only appears after the rest of the emission has already decayed to almost nothing. This kinetic effect in particular warrants further investigation, although this was beyond the scope of this initial work with OLEDs.

2.5.4 Outlook and Further Work

In general, the kinetics of EL can reveal the activity of TTA emission in an OLED by extracting amplitudes of the prompt (normal) and delayed (TTA) components of the total emission. As a result, this method should also be able to determine what proportion of the deuteration enhancement of OLEDs comes about by enhancing TTA, compared to simple extension of triplet lifetimes to allow singlet exciton formation.[87] As for UC, better understanding of the parameters that give rise to high efficiency devices (like smaller k_1) will no doubt pave the way to rational design of optimised OLED emissive layer compounds, and the development of devices that exploit TTA. Similarly, a broader understanding of TTA would allow it to be disabled in devices where it contributes to accelerated emissivity decay.

The inescapable conclusion to be drawn from the challenges documented in this study is that the rapid ageing of experimental OLED layer structures necessitates unbroken, intimate collaboration between device fabricators and spectroscopists. Indeed, collaboration by itself may not be enough, and further progress in this area is likely to come from research groups that amass the infrastructure and expertise to both fabricate and characterise OLEDs internally.

Chapter 3

Characterising Upconversion with Transient Absorption

"In all the universe there are only two constants, and these are one. There will be change, and something that changes."

—Narrator, *Saiyūki (Monkey)*, NTV 1978–1980

In this chapter, methods and challenges associated with experimental determination of absolute upconversion rate constants are first outlined. Transient-absorption spectroscopy is identified as a promising technique for fundamental studies in this area.

The operation of a custom built transient absorption spectrometer is then presented in detail. A range of upconversion systems were measured using this setup, and rate constants for key steps in the upconversion process are extracted and discussed.

The same methods are then applied to an upconversion system simultaneously comprised of two species of emitter. This hybrid system had been previously shown to perform better than the sum of its parts in steady-state experiments. Here, kinetics offers further insight into the mechanism for this "hybrid vigour".

Several advantages, limitations, and future improvements to the spectrometer are identified. It is expected that this type of experiment will become increasingly popular in fundamental studies of UC and other photophysical systems.

Finally, observations are collected from this and other experiments regarding the photostability of UC systems under powerful illumination. Concerns regarding the durability of UC devices under solar radiance are evaluated, and the key molecular parameters determining longevity examined.

3.1 Challenges in Measuring Kinetic Rate Constants

As discussed in Chapter 2, selecting high efficiency emitters for UC systems requires knowledge of their two triplet decay rate constants, k_1 and k_2. In an ideal system k_1 should be as small as possible, and k_2 as large as possible. Furthermore, any experiment that attempts to modulate UC fluorescence with external magnetic fields or resonance is likely to do so through the parameters η or k_2. For these reasons it is important to have access to experimental methods that can reliably determine k_1 and k_2 — both for developing novel emitters for applications, and as base values for comparative fundamental studies. The initial aim of this work was to tabulate k_1 and k_2 for a range of commonly used UC emitters under identical conditions, and was later expanded to include characterisation of a novel hybrid system.

As demonstrated in Chapter 2, acquiring experimental values for one of these parameters is not overly complex. Fitting the normalised square root of TRPL data with the mixed kinetics rate model (Equation 2.15) is an effective way to extract k_1, although care must be taken to measure out to very long times (very low $[E^*]$) so that this fitting can be made with certainty. For molecules that have radiative first order decay processes (like phosphorescence from S^*) determining k_1 is even easier, as the emission intensity can be fit directly with a single exponential that has k_1 in the exponent.

Unfortunately it is not as straightforward to extract k_2 from these kinds of measurements. The mixed kinetics model can yield values for k_2 using Equation 2.17, but only when $[E^*]_0$ is also known — essentially reversing earlier normalisation of fluorescence intensity. Attempts to estimate $[E^*]_0$ in TRPL experiments can be made from the excitation power as well as assumptions about beam size, uniformity, and attenuated propagation into the sample.[162] While this approach is theoretically valid, the analysis of action spectra in Chapter 2 demonstrates how model assumptions do not always apply to real systems. As a result, a more direct method of measuring k_2 was sought.

3.1.1 Other Methods to Determine Kinetic Rate Constants

Apart from TRPL, two other general techniques are considered for the task of investigating k_2. The first of these is comparison of steady-state (CW) fluorescence intensities. By measuring changes in the fluorescence following some perturbation and using Equation 2.4, relative changes in η or k_2 can be detected. This forms the basis for magnetic field experiments in Chapter 4, but is inadequate for determining absolute values of k_2 without a well characterised reference standard. Furthermore, without detailed modelling

there is a requirement that only one parameter can vary in the comparison, and while this may be the case for deuteration and magnetic fields, it is not true in general.

Alternatively, TA methods can be used. The common theme to all implementations of this method is that a pulsed pump beam temporarily excites a population of E^*, while the transmission of a probe beam is used to generate time-resolved absorption spectra following the excitation. When applied to UC, the presence of E^* can be determined from new absorption features that grow as this state is populated, rather than indirectly though its UC fluorescence. These new absorption features may arise from spin allowed excitation of E^* to higher electronic states, which for UC studies lie both on the triplet manifold. Applying the Beer-Lambert law as $[E^*]$ decays (and these new absorption features vanish) gives a direct window to the kinetics of $[E^*]$. Similarly, the bleach and gradual restoration of absorption features associated with ground state S and E can also be used to track the excited state kinetics. [131]

The main challenge in using TA is that the typically small values and changes in $[E^*]$ result in only small changes in the absorption. Using larger excitation powers can increase $[E^*]_0$ and make these features easier to detect at early times, but as $[E^*]$ decays this advantage will be lost at long times. Instead, high power probe beams and sensitive detectors are required to give reasonable sensitivity to changes in absorption throughout the timescale of the measurement. The significant investment required for two moderately powerful tunable light sources means that TA measurements are not as widely used as their utility would otherwise suggest, with TRPL still the predominant characterisation technique for UC systems.

One way TA measurements can be performed is to take advantage of the very large peak powers associated with femtosecond lasers. In ultrafast TA a single light source is able to provide both the pump and probe beams at independent wavelengths, as the available peak optical power is sufficient for these pulses to drive two or more separate nonlinear crystals (as described in section 1.2.2), or supercontinuum generating materials which operate on a similar premise. The high pulse repetition rates of these lasers also allows large data sets to be collected relatively quickly, although this advantage is somewhat offset by the modest pulse energies that limit signal to noise ratios for single shot measurements. The main limitation of this approach is that, due to their common origin, the delay between these two beams is intrinsically small. This delay can be varied using reflection stages to increase the path length of one beam relative to the other, but the large speed of light makes this impractical for delays larger than about ten nanoseconds. As a result, ultrafast TA is (appropriate to its name) most suitable for studying ultrafast phenomena, such as singlet or charge transfer state lifetimes. [82,224–227]

The decay kinetics of UC are typically in the range of hundreds of microseconds, and the need to measure out to long times therefore makes ultrafast TA unsuitable.[168] A complementary implementation of TA that can access these larger timescales involves using a broadband CW lamp and a separate pulsed laser, synchronised by much slower electronic triggering. In this approach, light from the laser may be used as the pump beam while transmission of the lamp as probe is used to determine the sample absorption. As with TRPL, a time-resolved detector then allows absorption spectra (calculated from transmission intensity) to be collected at different times after the pump pulse. As this variation of TA does not require such large laser pulse powers (to drive multiple wavelength tuning stages), it can often be achieved using more commonly available Q-switched Nd:YAG nanosecond lasers. Due to both the timescales it can investigate and the hardware it uses, this implementation is often referred to as ns-TA, to contrast it to the ultrafast version.

3.1.2 Rate Equation and Transient Absorption Modelling

The rate equations governing UC in the context of a TA experiment are almost identical to the ones used for TRPL. Restating Equation 2.3 gives an appropriate rate equation for the emitter:

$$\frac{d[E^*]}{dt} = k_{TET}[E][S^*] - k_1[E^*] - k_2[E^*]^2 \tag{3.1}$$

For the sensitiser, ISC is assumed to rapidly build an initial population of S^* ($[S^*]_0$) following excitation, which then decays through TET and other first or quasi-first order processes:

$$\frac{d[S^*]}{dt} = -k_{TET}[E][S^*] - k_s[S^*] \tag{3.2}$$

where k_s is the value of k_1 for the sensitiser, but given a different symbol here to distinguish it from the emitter k_1. In this treatment second order processes for S^* decay are not considered, and this is justified by the typically large values of $[E]$ used in experiments (leading to rapid TET). Factorising the terms in Equation 3.2 and taking $[E]$ to be approximately constant allows it to be solved analytically with a single exponential decay. Combining this solution with Equation 3.1 yields a single differential equation, in which $[S^*]$ and $[E^*]$ are decoupled:

$$\frac{d[E^*]}{dt} = k_{TET}[E][S^*]_0 e^{-(k_{TET}[E]+k_s)t} - k_1[E^*] - k_2[E^*]^2 \tag{3.3}$$

In the limit where $[S^*]$ decays very rapidly, Equation 3.3 approaches the same expression given in Equation 2.14. Unfortunately the mixed kinetics solution used the the previous chapter to fit TRPL data only works in this special case, and not in the general case described by Equation 3.3 where TET from $[S^*]$ may persist throughout the duration of the experiment. This also means that using laser fluence and sensitiser extinction is not always sufficient to determine $[S^*]$ from $[S^*]_0$, as k_s and k_{TET} are also required.

As with TRPL, UC fluorescence sampled by a TA spectrometer will scale linearly with $[E^*]^2$. The signal detected from this fluorescence also depends on the fraction and efficiency of sampling, as determined by the specific experimental setup. Combining all of these pre-factors with Equation 2.4 gives:

$$M = \Lambda[E^*]^2 \tag{3.4}$$

where M is the size of the signal generated by the fluorescence, and Λ is a single scaling factor that takes into account both molecular and experimental hardware behaviour.

Additionally, in a TA experiment the probe beam transmission of the sample is measured at different wavelengths and probe delays. From the transmission, the absorption and concentration of absorbing species can be determined using the Beer-Lambert law:

$$A(\lambda, t) = \log_{10}\left(\frac{I_0(\lambda)}{I(\lambda, t)}\right) = \epsilon(\lambda)c(t)l \tag{3.5}$$

where A is the absorbance, λ is the wavelength, and t is time after the pump pulse. The symbols I_0 and I represent the intensity of the probe beam before and after passing through the sample. Specific to the sample itself, ϵ is the molar extinction coefficient, c is the concentration of the absorbing species, and l is the optical pathlength. The dependencies of each of these terms has been made explicit in Equation 3.5, reflecting the assumptions that the incident probe beam is stable in time, and that ϵ and c are independent of each other. For the experiments presented in this chapter, l took a value of 1 mm throughout.

In contrast to TRPL data with its normalised square root, Equation 3.5 (and also Equation 3.6 below) shows that the TA signal changes linearly with concentration. Furthermore, the lack of any hardware related scaling factors in A (eliminated in the division of I and I_0) allows the absolute concentrations of absorbing species to be calculated from the absorbance when ϵ is known. Conservation of the total number of S molecules and E molecules also means that the growth of $[S^*]$ can be monitored by the complementary bleach of S absorption, and similarly for $[E^*]$ and $[E]$.

3.1.2.1 Sample Composition Considerations

When considering TA as a method to investigate UC, an additional practical question regarding sample composition soon becomes apparent. In TRPL and action spectroscopy the concentrations of the UC components are not a primary concern, as fluorescence is imaged predominately from the front face of the sample where excitation is strongest. Using large $[S]$ is a sensible approach, as it maximises the fluorescence intensity (Equations 2.7 and 2.9), as well as restricting beam propagation deep into the sample. As long as $[E]$ is large compared to $[S]$ (and therefore also $[S^*]$), the rate of TET will be rapid enough that the mixed kinetics solution will still be usable for fitting fluorescence kinetics traces.

In contrast, for TA the sample must be transmissive enough that the light emerging from the sample is still detectable, which limits the use of large $[S]$ and long path length cells. Furthermore, Equation 3.5 implicitly assumes that the concentration of the absorbing species is spatially uniform, and can be described by a single number. This will be the case for standard absorption spectroscopy of ground state species, but for photo-excited species like S^* or E^* the same equation can be exponentiated to show that $I = I_0 \times 10^{-\epsilon c l}$, which applies just as much to the pump beam as the probe. As a result, the local concentration of excited species will fall exponentially across the depth of the sample when pump and probe beams are focussed collinearly on the sample, and using a single value to represent this concentration will not always be appropriate.

A compromise must therefore be reached when selecting UC solution concentrations for TA. On one hand, the sample must have absorbance low enough that the transmitted probe light can be easily measured, and that the pump beam intensity is roughly uniform across the sample. On the other hand, for rapid TET and an appreciable amount of UC to occur, both $[S]$ and $[E]$ must be high. Using small path length sample cells (low l) can allow more concentrated samples to still have a low absorbance, but the choice of a specific sample concentration must still balance these competing effects — constrained by the limitations of available sample cells and detection hardware.

3.2 Methods

3.2.1 Sample Preparation and Characterisation

A range of of commonly used UC emitters were selected for characterisation by TA. Perylene was purchased from L. Light & Co. Ltd., while DPA, BPEA, and rubrene were purchased from Sigma-Aldrich.

To excite the different emitters, different sensitisers with appropriate triplet energy levels were necessary. With the shortest wavelength fluorescence, DPA was paired with palladium (II) octaethylporphyrin (OEPPd). As in the previous chapter perylene was paired with TPTBPt. Both rubrene and BPEA were sensitised using palladium (II) tetrakisquinoxalinoporphyrin (PQ_4Pd). TPTBPt and OEPPd were purchased from Frontier Scientific, while PQ_4Pd came from stocks accumulated within the group from elsewhere. In addition to these default pairings, systems of perylene and PQ_4Pd, rubrene with TPTBPt, and rubrene and BPEA together with PQ_4Pd were also investigated. These additional S and E pairings were chosen as model systems to further investigate endothermic TET, moderate UC reabsorption and recycling, and hybrid emitter effects respectively.

Deuterated versions of the emitters were also investigated for several of the aforementioned S and E pairings, and received from Sigma-Aldrich (perylene) or the ANSTO NDF (all others). Perylene was deuterated to 98 % isotopic purity, while the sites of deuteration for DPA, BPEA, and rubrene are shown in Figure 2.16.

Concentrations of sensitisers were chosen to give final solutions with a maximum absorbance of 0.1 OD (optical density, although formally unitless) for the porphyrin Q band absorption features in the 1 mm thick absorption cells. This choice was somewhat arbitrary, resulting in pump beam transmission of 80 % at the excitation wavelengths. As a result, the single values of $[S^*]$ calculated from TA spectra in later sections actually represent averages of an exponential distribution across the sample cell. Due to the small path length of the cell and relatively low absorbance the pump intensity fell approximately linearly across it, and so the actual values of $[S^*]$ at any location could vary by up to 10 % from the average value. Emitter concentrations were then chosen so that emitter molecules outnumbered sensitiser molecules by at least a factor of ten, allowing reasonably prompt TET. In practice, these choices gave sensitiser concentrations in the range of 1–10 μM, emitter concentrations measured in the hundreds of μM, and allowed both absorption features and UC fluorescence to be readily detected.

Stock solutions were prepared using anhydrous toluene in an inert glovebox, with ambient $[O_2]$ maintained below 1 ppm. The S and E solutions were allowed to exchange gasses with their surroundings overnight to remove any residual oxygen, mixed in equal volumes to make UC systems, and then sealed in a 1 mm thickness absorption cell with a teflon tap. This process replaced the freeze-pump-thaw procedure used in Chapter 2.

The actual concentrations of UC and S solutions were also checked by CW absorption spectroscopy using a Cary 50 Bio UV-Visible spectrometer. These absorbance measurements were independently confirmed by comparison to transient absorption spectra collected before the arrival of the pump pulse.

3.2.2 A Broadband Transient Absorption Spectrometer

A variation of ns-TA was used for this study, taking advantage of the specific capabilities of available equipment. Figure 3.1 shows how this was achieved in practice. The same spectrograph and CCD used previously for TRPL allowed time-resolved detection of a range of wavelengths simultaneously, and an internal diffraction grating could be rotated to pass different wavelength ranges to the detector. The same broadband optical source used to collect action spectra provided ample and continuous illumination across the visible and near infrared. By using the entire wavelength range of the lamp as a polychromatic probe beam, its transmission (and therefore sample absorbance) could be determined for a range of wavelengths from single acquisition frames on the CCD, avoiding the need to scan through probe wavelengths. A trolley mounted tunable pulsed laser was then used as the pump beam, and also to triggered the CCD acquisition with a delay that could be varied in software.

Reflective fibre couplers were used extensively in this setup to more easily direct the pump beam from the source to the sample, and then from the sample to the detector. The rail system used to mount the fibre couplers and sample also allowed for robust and repeatable alignment of the probe beam. The images in Figure 3.2 show the actual layout of the setup, corresponding to the simplified diagram in Figure 3.1. Not visible in the photographs, the hexagonally packed end of a round-to-linear fibre bundle was used to collect the probe beam transmission, allowing the linear bundle end to output to the camera and match the geometry of the slits.

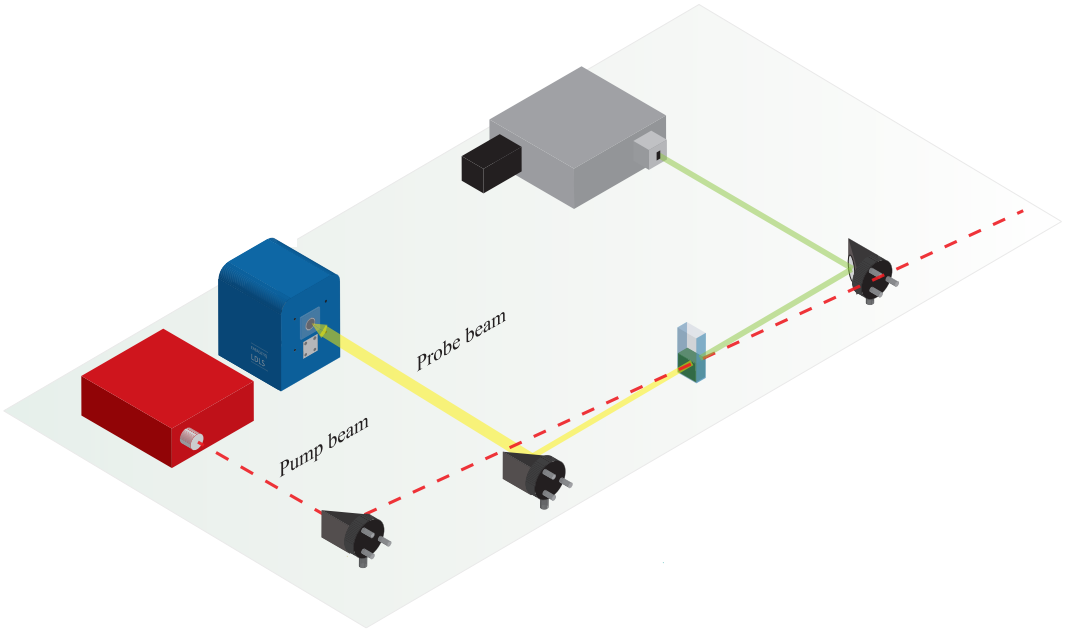

FIGURE 3.1: Simplified experimental setup for transient absorption spectrometer.

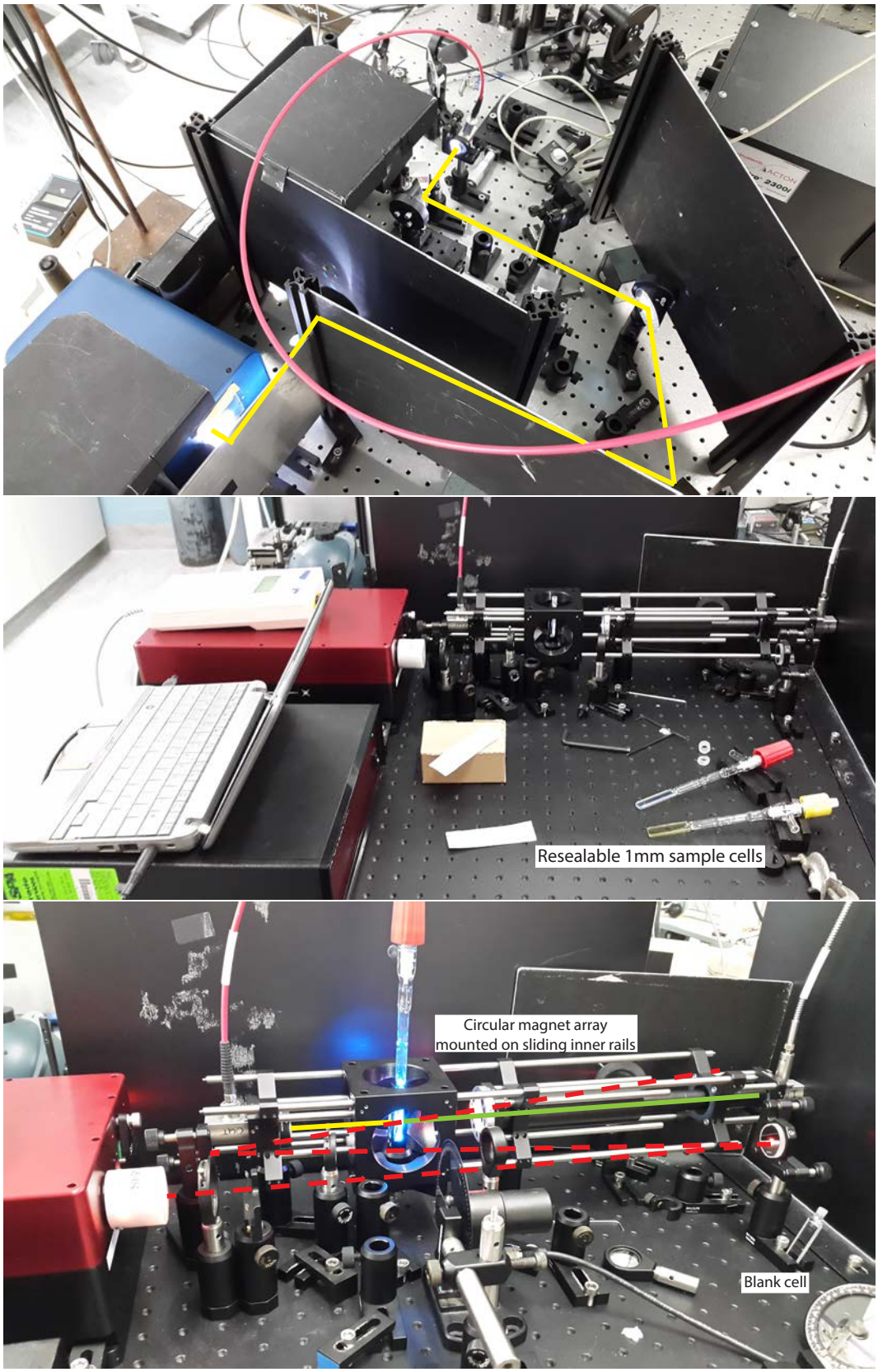

FIGURE 3.2: Photographs of actual transient absorption spectrometer implementation. Top: Coupling of broadband probe beam source (yellow graphic) into optical fibre (red). The coupler displaces the optical splitter corresponding to part (2) in Figure 2.3. Middle: Outcoupling of red probe beam fibre onto trolley mounted OPO table and into rail mounting system for TA alignment and magnetic field control. Bottom: Optical paths of pump and probe beam for probe beam transmission.

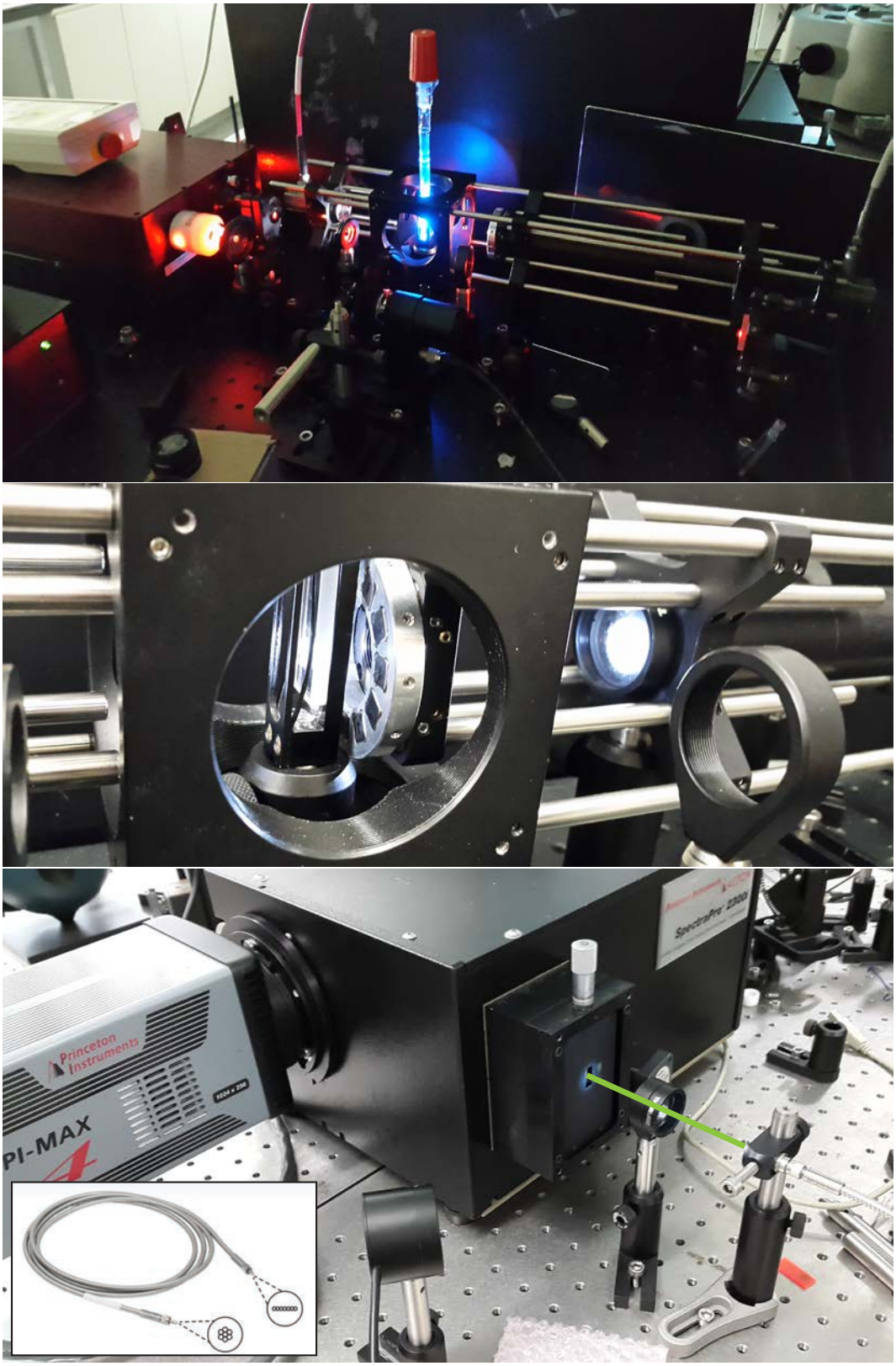

FIGURE 3.2: Photographs of actual transient absorption spectrometer implementation. Top: Actual operation of spectrometer with pump, probe and sample emission visible. Middle: Close up of Halbach array, in position to apply maximum magnetic field. Bottom: Outcoupling of probe beam transmission fibre to spectrograph/CCD, back on the original (immobile) optical table. Inset of Thorlabs round to linear fibre bundle.

3.2.2.1 Applying Magnetic Fields

Magnetic fields have been shown to impact UC fluorescence intensity, most likely either by modulating k_2 or η.[128,228–240] As a method that can determine k_2 more directly than TRPL, TA was identified as a promising technique to further investigate this effect while simultaneously determining the absolute rate constants at zero field. The open design of the TA spectrometer beam paths and sample loading area also allowed straightforward addition of components to apply magnetic fields to the UC sample.

To apply these fields, electromagnets were immediately excluded due to the heat load they generate when energised. This ohmic heating has the potential to increase k_2 by simply lowering the viscosity of the sample solvent at higher temperatures, leading to faster collisions. Instead, a circular Halbach array of permanent magnets (shown in Figures 3.2 and 3.3) was purchased and fixed with adhesive to a rail mountable lens holder. When assembled correctly, the magnetic fields of the individual magnets in the array add and cancel to generate a uniform field in the plane of the ring, which falls with axial distance.[241] The pump and probe beams passed unimpeded through the centre of the ring, and the magnetic field applied to the UC sample was varied by moving the entire array closer or further along its mounting rails.

To characterise the field strength of the magnet at different distances, it was first mounted on a two dimensional translation stage and moved around a Hall effect gaussmeter. Measurements were made in 1 mm increments to map out the magnetic field strength in the plane of the ring, and repeated at several axial distances. Figure 3.3 shows the field line patterns of this array, and its symmetry was exploited to build slices of a three dimensional field strength map from a small set of individual measurements.

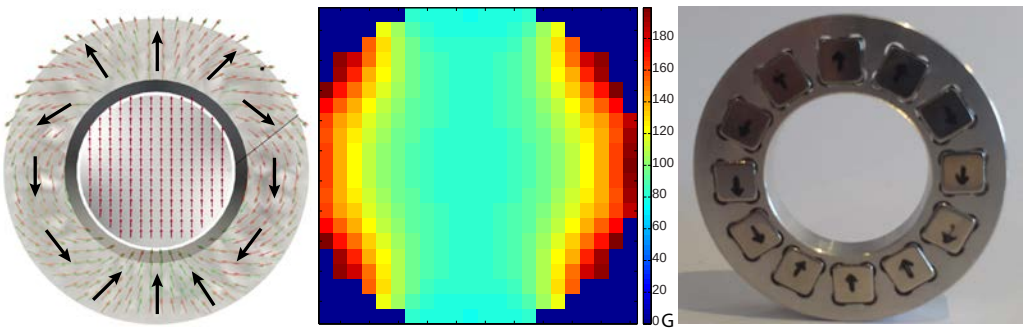

FIGURE 3.3: Magnetic field in the plane of a circular Halbach array.
Left: Magnetic field vectors, uniform at centre, adapted from Bruckner *et al.*[242]
Middle: Strengths of vertical magnetic field component (in Gauss, 1 T= 10^4G) in the plane of the actual array (inside the hole). Actual measurements were taken in the lower left quadrant only, with individual pixels correspond to the 1×1 mm grid of measurement points. Blue/black pixels correspond to points where the metal frame of the array restricted further motion of the gaussmeter probe.
Right: The actual array, with inner and outer diameters of 2.5 and 4.6 cm.

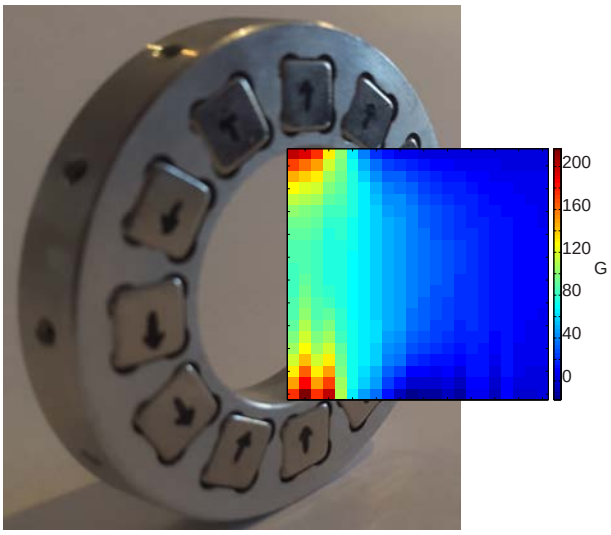

FIGURE 3.4: Magnetic field along the axis of a circular Halbach array. Many pixel values (462 total) were interpolated by symmetry from a smaller set of measurements (278) on a 1×1 mm grid. The image and inset are displayed to the same scale.

Only a slight tilting of the gaussmeter probe away from the array axis maximised the measured magnetic field, confirming that the field direction was almost entirely vertical at each point. Nonetheless, as the measured values strictly sampled the vertical field component, these values are all conservative underestimates. Figure 3.4 shows that these fields were roughly uniform (moving vertically) near the centres of planes perpendicular to the array axis, and decreased in strength with increasing distance. Axial distances of 10, 12, 15, 20, and >200 mm between the magnet and the TA sample were chosen to apply magnetic fields of 40, 30, 20, 10, and 0 mT respectively, and reliably set using mounting rails purchased with etched on distance markers for this purpose.

3.2.2.2 Data Collection

For each sample (UC or otherwise), spectra were collected in the following manner. Firstly, an unsealed 1 mm pathlength absorption cell filled with toluene only was set in the sample holder. With the laser flashlamps firing as a triggering source (but Q-switch disabled), the electronic gating of the CCD was set to collect 1001 single shot frames with constant 100 ns gate width and 100 ns pump-probe delay increment between shots. This meant that the measurements uniformly covered a total temporal range of 100 μs, in 0.1 μs increments. The spectrograph slits were then narrowed so that the CCD signal generated by the probe beam only was just below saturation level, and a set of "blank" time-resolved spectra recorded. These spectra corresponded to the probe beam filtered by the transparent toluene and glass that physically supported later UC samples, and were taken to represent I_0. With a laser pulse repetition rate of 20 Hz, each set of spectra collected this way took approximately one minute of real time to acquire.

Next, the blank cell was replaced with a sample of interest, the laser Q-switch enabled, and the lamp blocked. For the different sensitisers studied, the laser was always set to excite at the absorption maximum of the sensitiser's longer wavelength Q band feature. The initial delay setting between the Q-switch and the CCD acquisition was adjusted in the camera software so that the laser pulse arrived on roughly the thirtieth frame, and was not changed again for the remainder of an experiment. With otherwise identical camera settings as before, a set of spectra was then collected of the sample emission induced by the pump beam. Although the length of the probe collection arm was chosen to prevent most of this from reaching the detector, acquiring these "laser induced fluorescence" (LIF) spectra allowed this signal to be formally subtracted in later analysis. For sensitiser only samples this LIF is more accurately described as laser induced phosphorescence, but the same label will be used here for all kinds of samples.

Without changing the laser or camera settings, the lamp was then unblocked and another set of spectra collected. This set of spectra corresponded to the transmission of the sample, with changes in the transmission due to excitation by the pump beam.

This entire process was then repeated at up to four grating positions, corresponding to wavelength ranges of 260–540 nm, 420–700 nm, 620–850 nm, and 710–980 nm. In the following discussion and figures these ranges will be referred to as UV, VIS, NIR1, and NIR2 in order of ascending wavelengths, each containing 1024 pixels. The specific wavelengths of these ranges were chosen with some overlap between the intensified CCD sections of adjacent ranges, so that absorbance values determined from different spectra could be compared for uniformity. Unfortunately the intensifier of the available camera was significantly smaller than its CCD pixel array, and so large segments at the edges of all spectra contained pixels with no appreciable blank or transmission signal, leading to wild variations in calculated absorbance.

At this stage all of the intensity spectra required to generate TA spectra had already been collected, but for completeness two additional TRPL spectra were also taken. The spectrograph slits were opened fully, CCD intensifier gain set to maximum, lamp output blocked, and sets of spectra collected to capture phosphorescence from S^* and UC from E^*. These spectra are in fact qualitatively the same as the LIF spectra, but taken with maximum detection sensitivity. Emission from the different sensitisers and emitters was usually observed in the NIR1 and VIS ranges respectively.

For each sample this entire process was then repeated at four additional magnetic fields by moving the magnet to different predetermined positions along its mounting rail.

3.2.2.3 Data Processing

For ease of processing, spectra from the different wavelengths regions were first concatenated to give single spectra for the blank, LIF, and transmission measurements. The large non-intensified regions at the edges of the component spectra resulted in these composite spectra having large "canyons" in them, which clearly mark out the different wavelength regions. Due to the overlap between different wavelength regions, a unique mapping of pixel number (1024 pixels per wavelength range) to wavelength could not be determined without deletion of some data. For this reason, the data was processed and analysed using pixel number, and approximate wavelength axes were added to the following figures as a final step. The wavelengths in these figures therefore have discontinuities wherever wavelength regions have been concatenated.

Although it is standard practice to combine spectral regions onto a single wavelength axis (with overlapping regions used to scale intensities), for most TA data figures in this document this additional processing has been deliberately forgone. It would later be found that significant data troubleshooting and a fundamental change of approach were required to overcome some of the hardware limitations of the TA spectrometer. As this chapter has as a primary concern the commissioning and validity checking of the ns-TA implementation, presenting data in this closer-to-raw form is important to avoid misrepresenting the true outputs of the instrument — conflating the data itself with the processing that was later applied to it. This presentation also highlights irregularities in the raw data, the nature of which informed the troubleshooting process and identification of hardware issues. While it would be appropriate to process data figures further for a publication of the photophysical results (including removal of overlapping regions and baseline correction), as this document is also intended to serve as a technical guide for those performing similar experiments in the future this extra technical detail has been left in.

It should be noted that the camera slit widths (and therefore signal scaling factors) were not the same for different wavelength regions of a single figure, but were the same for the same wavelength regions in different spectra. The upper spectrum in Figure 3.5 shows a typical set of these unprocessed time-resolved spectra for the probe beam intensities. The lower spectrum shows what the probe beam spectrum looks like with a uniform intensity scale and single wavelength axis, determined by scaling the data to the same height in regions of overlap (and then truncating the overlap from one set).

To calculate absorbance, I and I_0 from Equation 3.5 were first generated by correcting the transmission and blank spectra for LIF and camera background signal. For I_0, the blank spectra were averaged at each wavelength across the different acquisition frames,

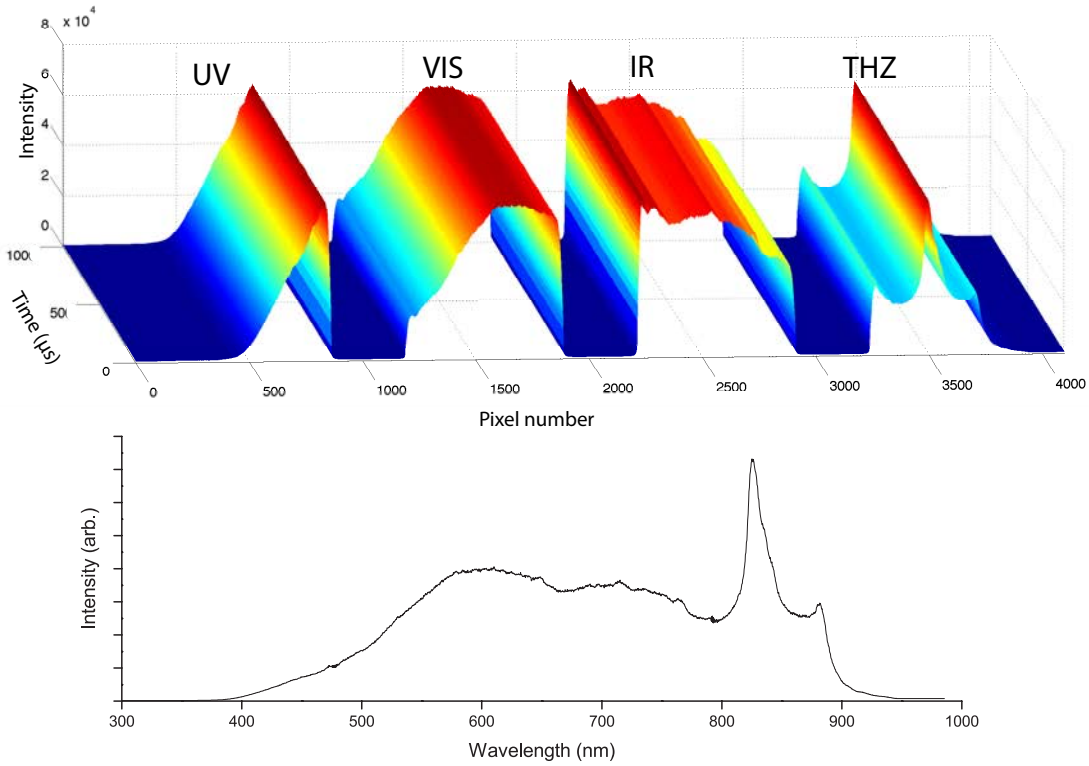

FIGURE 3.5: Concatenated blank spectra, showing (top) probe beam intensity in the different wavelength regions remaining roughly constant for 1001 frames acquired in 100 ns delay inincrements. Pixels outside of the CCD intensifier lead to the canyons between the wavelength ranges, despite some intensified overlap between their edges. To generate the probe beam spectrum (bottom), a time slice of the upper spectrum has been replotted on uniform intensity and wavelength axes.

and the camera background subtracted at each wavelength using the average of the LIF spectra from frames taken before the laser pulse arrived. For I, both LIF and camera background were corrected for simultaneously in the transmission spectra by subtracting the LIF spectra element by element. The absorbance was then calculated for each frame using Equation 3.5 and the corrected values of I and I_0.

To assist in identifying new absorbance features induced by the pump beam, absorbance difference spectra (ΔA) were also generated by subtracting the initial absorbance spectrum of the sample, averaged from frames before the pump beam arrived (A_0) :

$$\Delta A(\lambda, t) = A(\lambda, t) - A_0(\lambda) = \sum \epsilon(\lambda) \Delta c(t) l \tag{3.6}$$

where the sum is over all absorbing species in the solution, including E, E^*, S, and S^*.

To generate kinetics traces for fitting, features in the A or ΔA spectra were first selected corresponding to concentrations or changes in concentrations of absorbing species. These features were then integrated across an appropriate wavelength range to improve signal

to noise. Traces generated from the integrated absorbance spectra were then converted back into absolute absorbance units (1 OD = 10 % transmission) by scaling such that the value of the trace before the pump beam arrived was equal to the peak value of A_0 for the feature of interest. Although absolute unit restoration was not possible for traces generated from the ΔA spectra (which had a uniform value of zero before the pump beam arrived), these traces could still be used to determine decay rate constants.

For the TRPL spectra corresponding to S^* phosphorescence or UC fluorescence, the spectra were integrated across the wavelengths of the entire emission feature. Camera background was estimated using the average value of the traces before the pump pulse arrival, and for UC measurements a square root function was applied to give a trace proportional to $[E^*]$.

This entire process was then repeated to generate kinetic traces for the selected absorptions, sensitiser phosphorescence, and UC fluorescence of each sensitiser and UC solution. Each of these could then be fit with equations appropriate to the specific sample and type of measurement.

3.3 Results and Discussion

3.3.1 Sensitisers

In order to be able to identify and distinguish absorption features of the emitters in UC systems, the sensitisers were first investigated so that their absorption features could later be safely ignored. By fitting the kinetics of the sensitisers alone, their values of k_s could also be determined for use in later analysis of UC systems. In addition, as this experimental setup was constructed for this work (and therefore completely untested), measurement and literature comparison of simpler single component systems was desirable to assess the validity and accuracy of results generated by these means. Before this assessment could be made, all results from this setup were initially viewed with a healthy skepticism.

3.3.1.1 TPTBPt

The CW absorption spectrum and A_0 spectrum of TPTBPt are shown in Figure 3.6. Aside from discontinuities in the composite TA spectrum, the matching shapes of these spectra was a pleasing initial indication that the TA experiment was working as intended. The values of the absorbance and the known value of ϵ at 615 nm for this compound were used to calculate the concentration of the sample, which turned out to be 3.35 μM. This

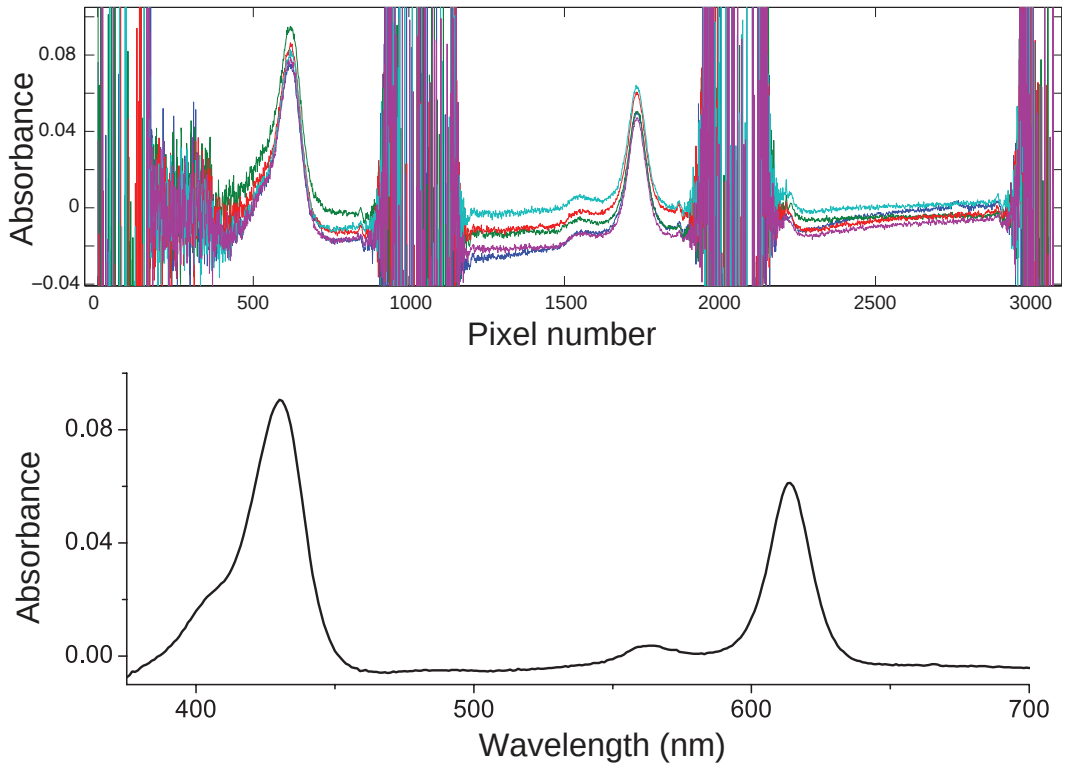

FIGURE 3.6: Absorption spectra of TPTBPt using TA (top) and CW (bottom) instruments. The multiple top traces are from scans at different magnetic fields.

was in good agreement with the expected concentration of 3.45 μM based on gravimetric preparation and volumetric dilution of the stock solution.

The full TA spectrum of TPTBPt is shown in Figure 3.7, and a slight dip can be seen at its strongest UV and VIS absorption bands (430 and 615 nm) just after the arrival of the pump beam. Due to the large size of these absorption features dominating the colour scale, not much else can be easily discerned. Turning to the absorption difference spectrum reveals additional information by subtracting A_0, and is shown in Figure 3.8. The bleaches of the ground state absorption wavelengths can be clearly seen, as well as a new broad absorption not belonging to S. This new absorption feature is attributed to S^*, and its shape matches previously reported studies of TPTBPt excited state absorption.[168] In addition to absorption spectra, the phosphorescence of TPTBPt was observed in the expected wavelength range (peak emission at 770 nm, partially truncated by the intensifier edge), and is shown in Figure 3.9.

Close inspection of the different frames of Figure 3.7 and 3.8 revealed that the TPTBPt spectrum did not change shape over time. For TPTBPt only, an additional set of measurements were taken using Soret band (430 nm) excitation. These measurements resulted in identically shaped absorption and phosphorescence spectra, with similar exponential decay kinetics. These results lend significant support to the assertion that

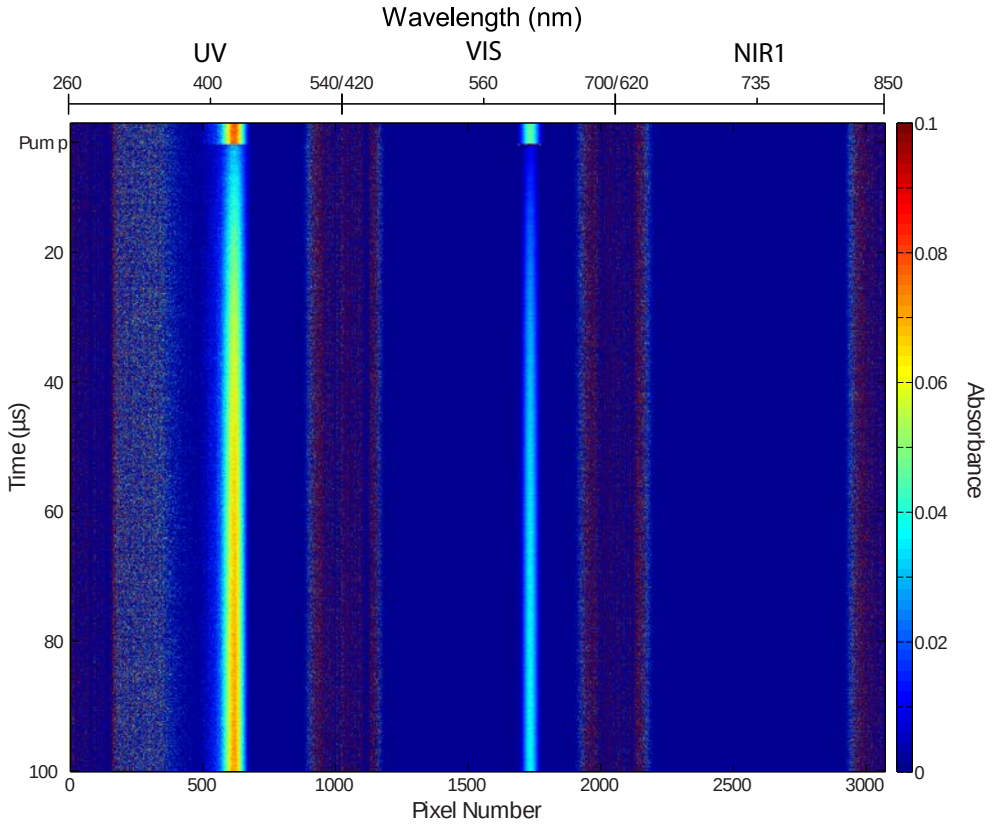

FIGURE 3.7: Transient absorption spectrum of TPTBPT.

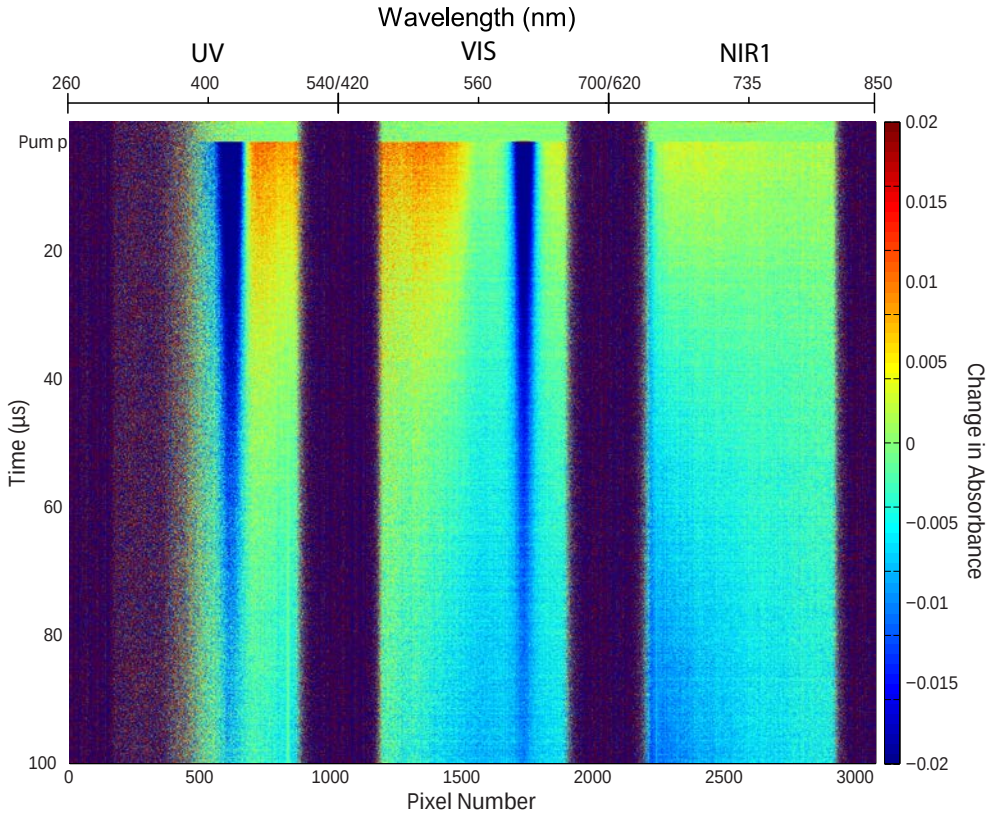

FIGURE 3.8: Transient absorption difference spectrum of TPTBPt.

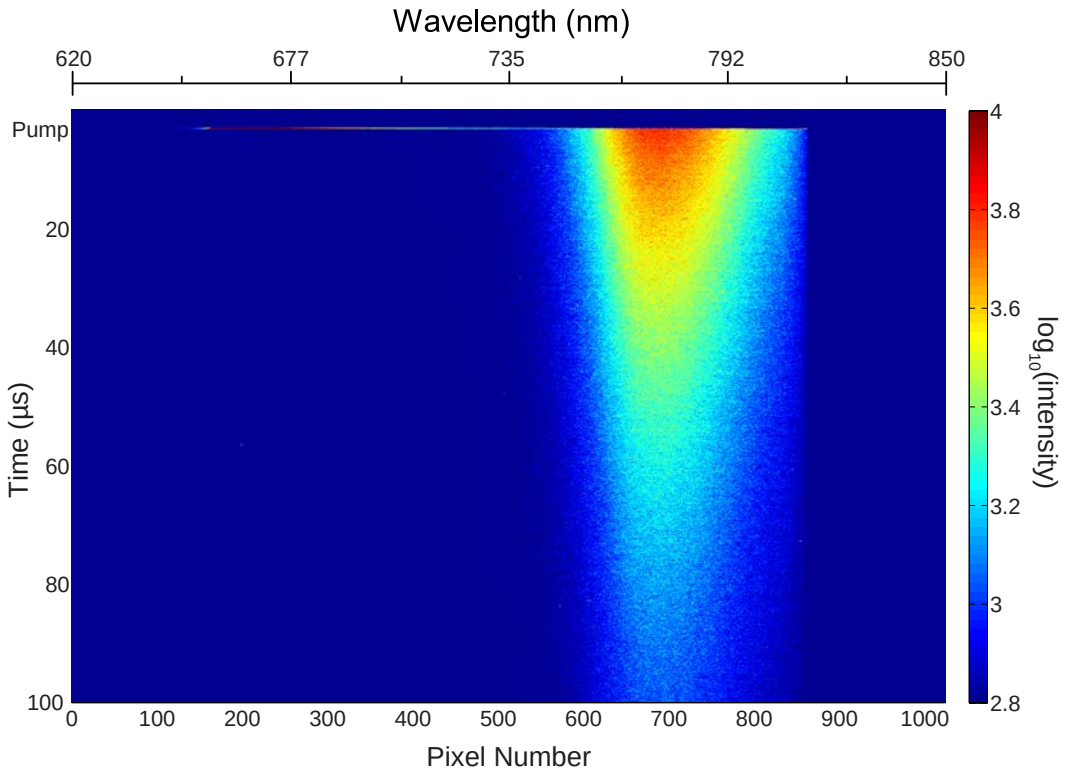

FIGURE 3.9: TRPL spectrum of of TPTBPt phosphorescence.

sensitiser ISC happens rapidly from S^* (even if S^* itself forms from internal conversion from higher excited states), as otherwise an additional rapidly decaying fluorescence component would be expected with a different initial spectral shape. The microsecond timescale TA kinetics of the sensitiser were therefore taken to represent only the triplet excited state.

Kinetics traces were then generated by integrating wavelength bands corresponding to the phosphorescence, absorption bleaches, and transient (induced) absorptions. These traces were generally found to be well fit by single exponential functions, although additional terms were sometimes required to achieve good fitting in later frames. For most traces the necessary extra term was a linear contribution to the time evolution of A or ΔA, which was interpreted as arising from slow drift in the probe beam power. A limitation of the data collection method previously described was that the blank spectra were often collected several minutes before the transmission spectra that they corresponded to, giving time for lamp power drift to occur. Supporting this hypothesis, the value of the linear constant was itself found to vary roughly linearly with the number of pixels in the range of wavelength integration. Examples of both unremarkable and pathological traces with fits are shown in Figure 3.10.

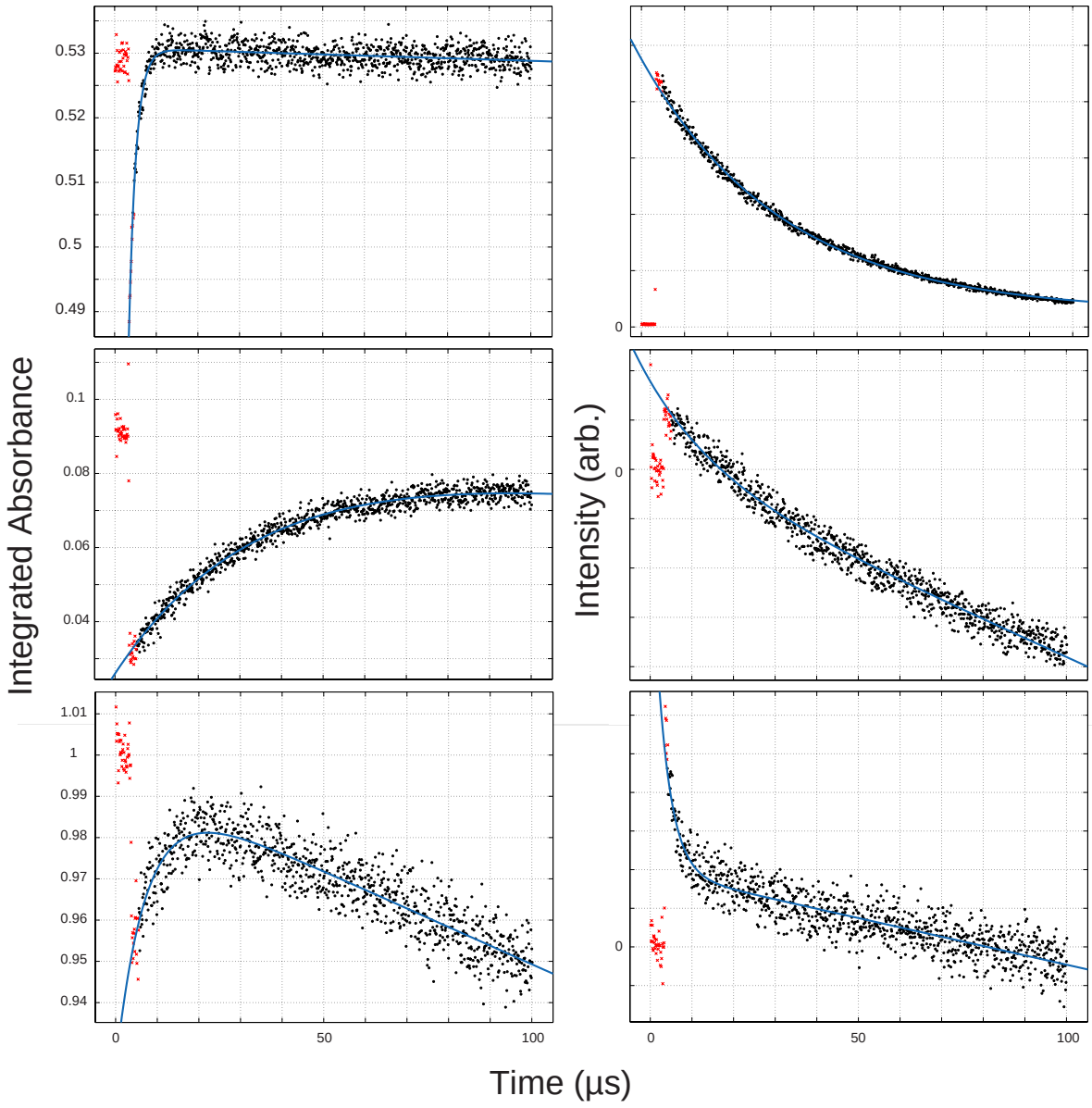

FIGURE 3.10: Examples of traces and achievable fits from TA data. Red points were excluded from the blue fit curves. Without correction, all traces should have ideally returned to the average value of these red points after long times.
Top row: Good fits without correction were found for some bleaches (left) and most phosphorescence traces (right). The rapid decay of the left absorption trace indicates a shorter delay increment may have been more appropriate for that specific scan.
Middle row: Some bleach traces (left) required a constant correction terms, and many induced absorption traces (middle) required linear correction terms.
Bottom row: Some bleach (left) and induced absorption traces (right) required both significant linear and constant corrections.

For some absorption traces an additional constant term was require for fitting, although these were generally small compared to the initial value (A_0 in spectra of A) or exponential amplitude (in spectra of ΔA). These adjustments effectively changed the model value of A_0 from its measured value, and were interpreted as a shift in the absorption baseline before and after the pump pulse. A possible explanation for this behaviour is lingering saturation effects in the CCD or its internal phosphor when exposed to scatter from the pump laser. The P43 phosphor of the camera (of no relation to perylene UC samples in Chapter 2) had an intrinsic decay time of either 1.5 or 3.2 ms (for 100 % to either 10 or 1 %), while the laser pulse repetition time was 50 ms.[243] Although the instrument response of the camera should have therefore been fully cleared from one pump laser shot to the next, this figure is presumably reported by the manufacturer in the absence of additional background illumination. In this experiment the phosphor was relaxing to a much higher (almost saturated) background level due to the constant probe beam exposure, which may have caused relaxation with a slower time constant. The resulting "leakage" of signal from the pump beam exposure into subsequent absorption frames may have been what necessitated the extra constant term. As the LIF scans were taken with the probe beam blocked (and the P43 phosphor decaying back to 0 %), its subtraction would not account for the proposed saturation effects.

The general form of the fitting function used for bleaches of absorption bands is then given in Equation 3.7:

$$A(t) = (A_0 + a) - be^{-k_s t} + ct \tag{3.7}$$

where a is the constant correction term from lingering phosphor excitation, b is the bleach amplitude (equal to $\epsilon l[S^*]_0$), and c is the linear correction term from probe beam drift. For transient absorptions found in the absorption difference spectra, Equation 3.8 was used:

$$\Delta A(t) \propto a + be^{-k_s t} + ct \tag{3.8}$$

where A_0 is shifted into ΔA, and the lack of a reference point for scaling means that the absolute values of ΔA and b were no longer meaningful. Finally for phosphorescence Equation 3.9 was used:

$$I(t) = a + I_0 e^{-k_s t} \tag{3.9}$$

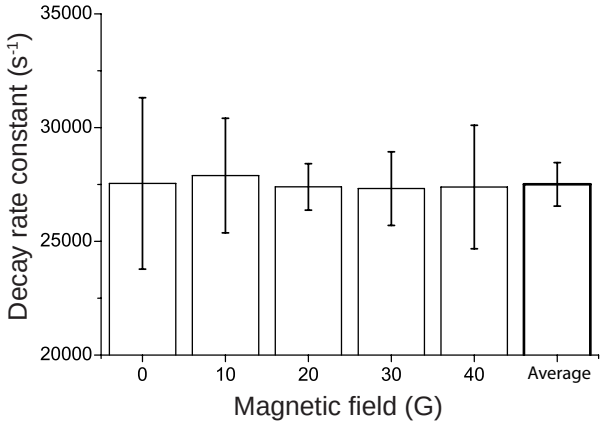

FIGURE 3.11: Variation in decay rates of TPTBPt with magnetic field. The single values for each magnetic field are averages across absorption and emission features, with error bars representing 95 % confidence intervals. Magnetic invariance of kinetics is claimed from these kinds of comparisons for all sensitiser and UC systems studied.

where a is another constant correction term, this time representing the camera background signal. In all cases the fitted value of a for phosphorescence traces matched well with the average values of the traces before the laser pulse arrival.

The values of k_s, a, b, and c with 95 % confidence intervals were determined for each trace using the MATLAB curve fitting tool. The value of k_s was found to not change significantly with magnetic field for all absorption and emission features studied, and so was averaged across repetitions (with outlier traces removed) to give single values for each selected absorption feature. The magnetic field variance of k_s for values averaged across the different TPTBPt absorption and emission features is shown in Figure 3.11. Of the averaged values of k_s, the one generated from the phosphorescence kinetics was treated as the most trustworthy (for identifying outliers), as this method has no intrinsic background signal. The value of $[S^*]_0$ (derived from b, and important for later UC systems) taken from the Q band bleach measurements was identified as most likely to represent the true value, as this was the absorption feature targeted by the pump beam.

To generate final values of k_s for comparison and use in later analysis, outlier measurement sets (corresponding to individual spectral features across all magnetic fields) were first excluded and the remaining values from different absorption and emission features at different magnetic fields re-averaged as a single pool of values. The excluded outlier sets most commonly included the induced absorptions, although the values from these sets were often still within ∼30 % of the others. New confidence intervals were calculated for the final values, using the same formula as in section 2.3.3.

From this process, the final value of k_s for TPTBPt was found to be $(2.750 \pm 0.095) \times 10^4$ s^{-1} — a relative uncertainty of 3.5 %. This value was generated using 15 separate values of k_s from the restore of the Soret and Q band bleaches (in the UV and VIS

wavelength ranges), as well as the phosphorescence decay. This compares favorably with published triplet lifetimes of TPTBPt, corresponding to k_1 values of $2.6\times10^4\,s^{-1}$.[168] This close agreement was taken as confirmation that the above approach, though somewhat convoluted and requiring several correction terms, was indeed still valid. For ease of comparison between S and UC systems, sample concentrations and rate constants from this and all other systems investigated are presented together in Table 3.1.

3.3.1.2 OEPPd

Having established an analysis routine for TPTBPt, OEPPd was quickly found to yield to the same method. Happily, the absence of absorption features in the NIR meant that spectra for this sample only needed to be taken in the UV and VIS regions. The CW absorption, absorption difference, and phosphorescence spectra of OEPPd are shown in Figures 3.12, 3.13, and 3.14. The absorption difference spectra were found to broadly match the shape of a similar study on a UC system of OEPPd with anthracene.[131]

Using the phosphorescence decay, Soret band bleach restore, and short wavelength induced absorption kinetics (14 total traces), the final value of k_s was found to be $(1.18\pm0.07)\times10^5\,s^{-1}$ ($\pm6.3\,\%$). This is roughly thirty times faster than a published value of $\sim4\times10^3\,s^{-1}$, which may be a result of oxygen ingress contributing to k_s through triplet quenching, or possibly an effect of the neglected second order decays (such as TTA) between excited sensitiser molecules.[131] Luckily, the samples of OEPPd and its UC system with DPA were prepared on the same day using identical procedures. Therefore even if oxygen was contributing to give a higher k_s, its uniform effects in the sensitiser and UC samples would not directly invalidate later analysis of the UC results for the emitter. An active sensitiser TTA channel cannot be dismissed in the same way, as its contribution

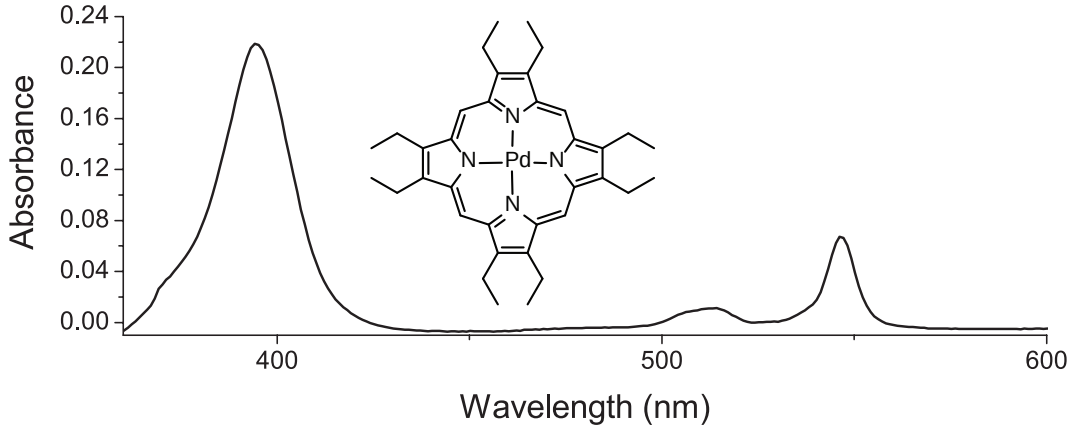

FIGURE 3.12: Absorption spectrum and structure of OEPPd.

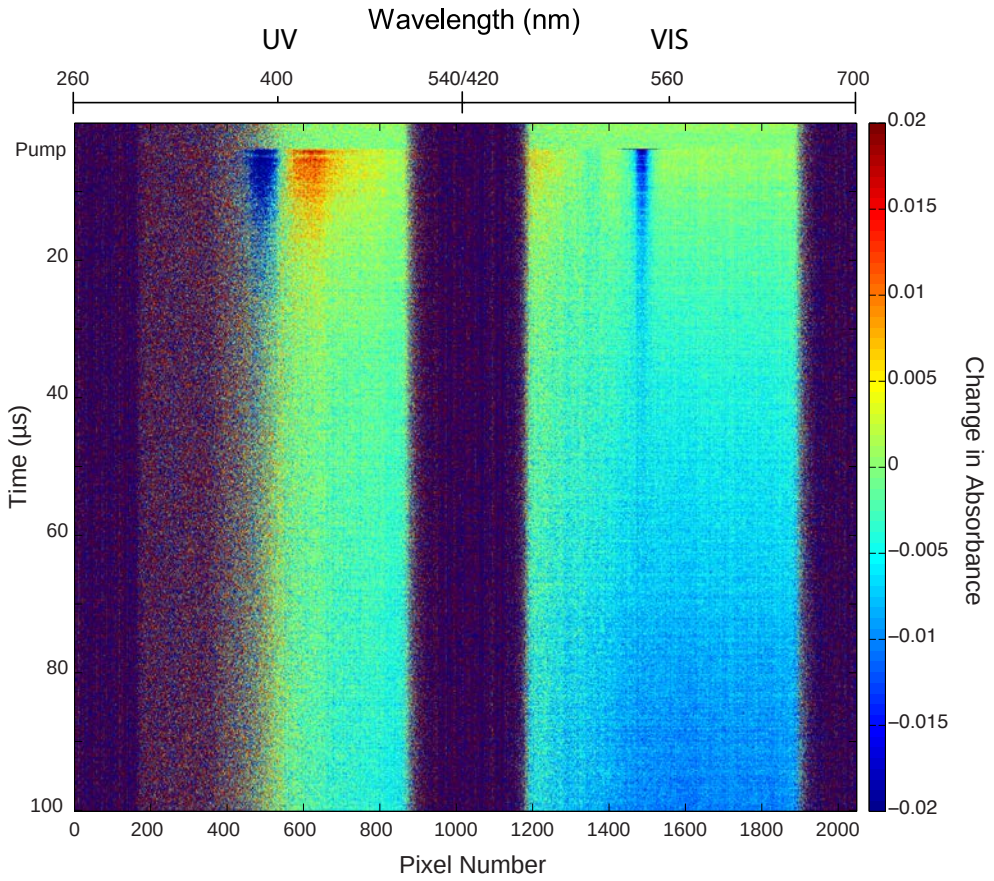

FIGURE 3.13: Transient absorption difference spectrum of OEPPd.

would not change linearly with $[E]$. In this regard the good fitting of single exponential functions (especially for the phosphorescence) was taken as evidence that the TTA channel was not significantly active over the long timescales of the experiment.

3.3.1.3 PQ_4Pd

For the third and final sensitiser, spectra of the absorptions and emission of PQ_4Pd were collected in all four wavelength regions. The CW absorption, absorption difference, and phosphorescence spectra are shown in Figures 3.15, 3.16, and 3.17.

The value of k_s was calculated from 25 traces across the phosphorescence, two Soret band bleaches in the UV, a duplicate of the the longer wavelength Soret bleach in the VIS (overlapping with UV), and the Q band bleach in NIR1. The final value of k_s was $(2.34\pm0.06)\times10^4\,s^{-1}$ ($\pm2.6\,\%$). As for OEPPd, this is significantly faster than the previously reported value of $7\times10^3\,s^{-1}$, although it does match the "saturated" triplet decay rates obtained at the highest laser powers in the same study.[170] The use of two rate constants in the published study meant that it was unclear what this difference meant in terms of the reliability of the TA method, although the broad agreement (within

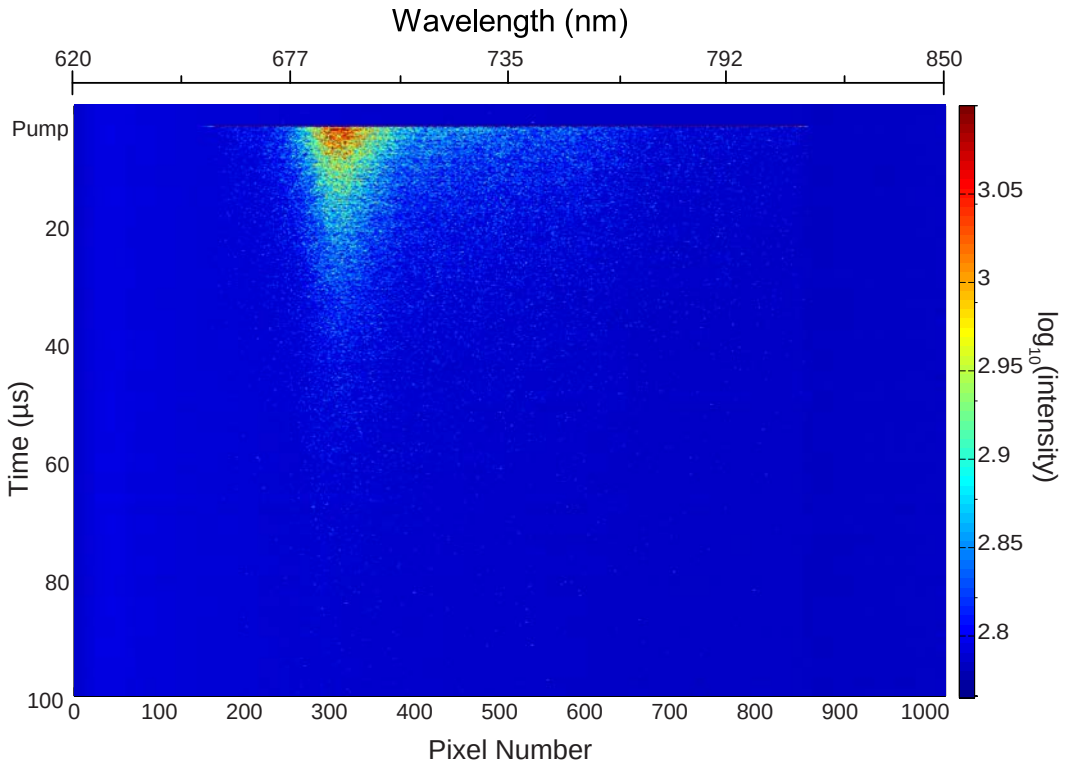

FIGURE 3.14: TRPL spectrum of of OEPPd phosphorescence.

an order of magnitude) was at least somewhat encouraging. Paradoxically, the larger reported value of k_s was interpreted in that study as evidence of an active TTA channel, while in this study the good fitting of single exponential decays to the phosphorescence trace indicated that it was not significantly active. This paradox was not investigated further, and instead the following analysis of emitter properties in UC systems (which uses this value) was performed taking the k_s determined above at face value.

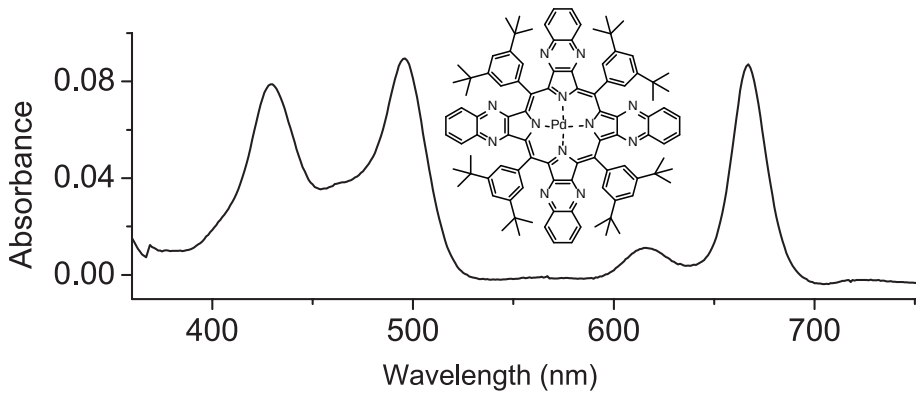

FIGURE 3.15: Absorption spectrum and structure of PQ_4Pd.

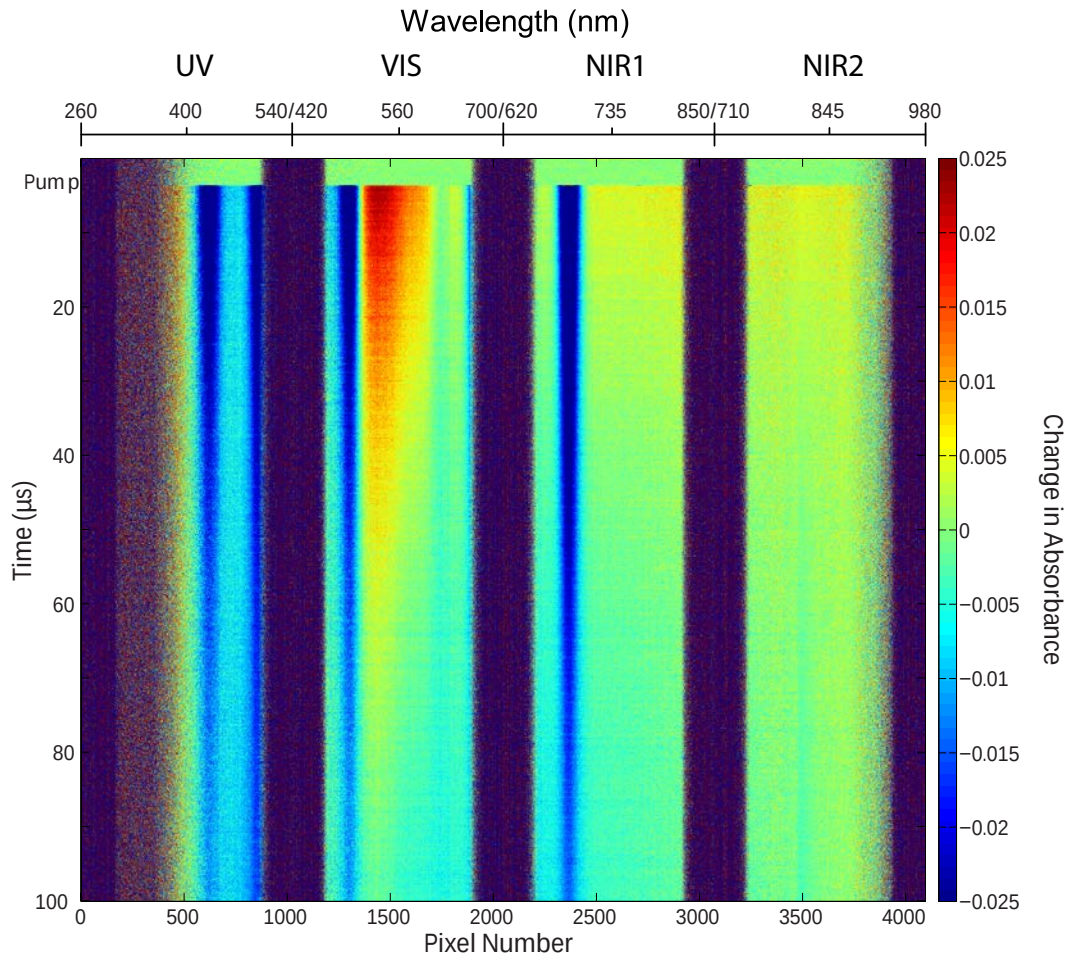

FIGURE 3.16: Transient absorption difference spectrum of PQ_4Pd.

3.3.2 UC systems

Absorption and absorption difference spectra were collected and processed in the same way for a range of UC systems, in addition to their sensitiser phosphorescence and UC fluorescence kinetics. In their analysis, having previously determined the shape of the absorption difference spectra for the sensitisers alone, the spectra of the UC systems were examined for any new features due to the emitter. Both bleaches in the emitter A_0 features and new absorptions corresponding to E^* were expected. These new features would then be converted into traces for fitting to extract the emitter k_1 and k_2.

To the author's great displeasure, no such features could be found. Figure 3.18 shows the absorption difference spectrum of a TPTBPt and perylene UC system, and aside from a slight asymmetry in the TPTBPt Soret band bleach feature, it is identical in spectral shape to the spectrum in Figure 3.8. An attempt was made to isolate this asymmetry contribution by subtracting from Figure 3.18 an array constructed with the same decay rate and initial amplitude as it, but with the spectral shape of Figure 3.8. Unfortunately this only resulted in a single small, broad component near the TPTBPt Soret band that

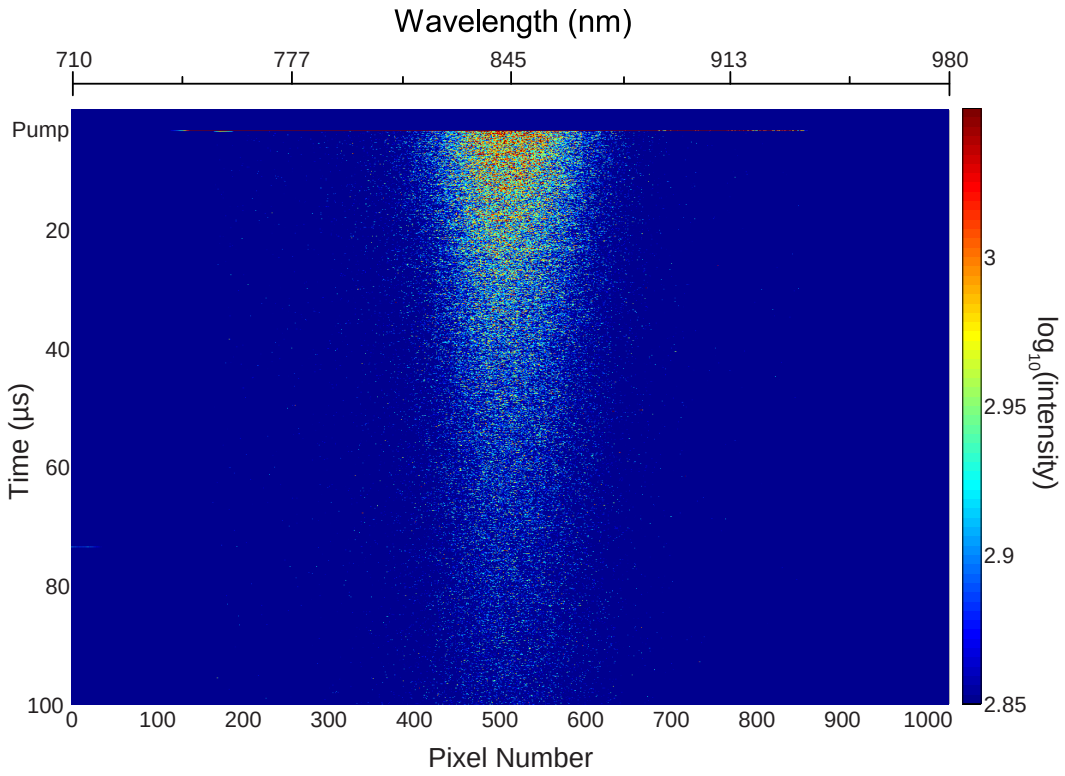

FIGURE 3.17: TRPL spectrum of of PQ_4Pd phosphorescence.

did not at all resemble the perylene CW absorption spectrum. This feature was not investigated further, and was perhaps merely an artefact due to the different decay kinetics in the sensitiser and UC systems. All other UC absorption difference spectra were found to be spectrally the same as those of their sensitisers, and the features of these spectra were therefore taken to represent properties of the sensitiser only.

It would later be determined that the choice of low concentration UC solutions had led to maximum achievable values of $[E^*]$ and $\Delta[E]$ (determined primarily by the amount of S available to absorb the pump beam) that were below the sensitivity limit of the TA spectrometer. This sensitivity was about 5 mOD using single exposures at each time point, or worse in regions of the spectrum where the probe beam was weaker. Ultrafast TA experiments can often be sensitive to changes in absorption in the range of 0.1 mOD or smaller, and may have been able to resolve absorptions and bleaches of E^* and E.[132,226,244] These instruments present a clear opportunity to improve and expand on this study in the future, although were not available for use at the time (ultrafast TA would also have been limited to investigating only the earliest parts of the kinetics). Commercial ns-TA instruments (such as the Edinburgh Instruments LP980 and Ultrafast Systems EOS) were later found to have single shot sensitivities in the same order of magnitude as the implementation used here — itself approximately one order of magnitude away from that required to observe emitter triplet signal.

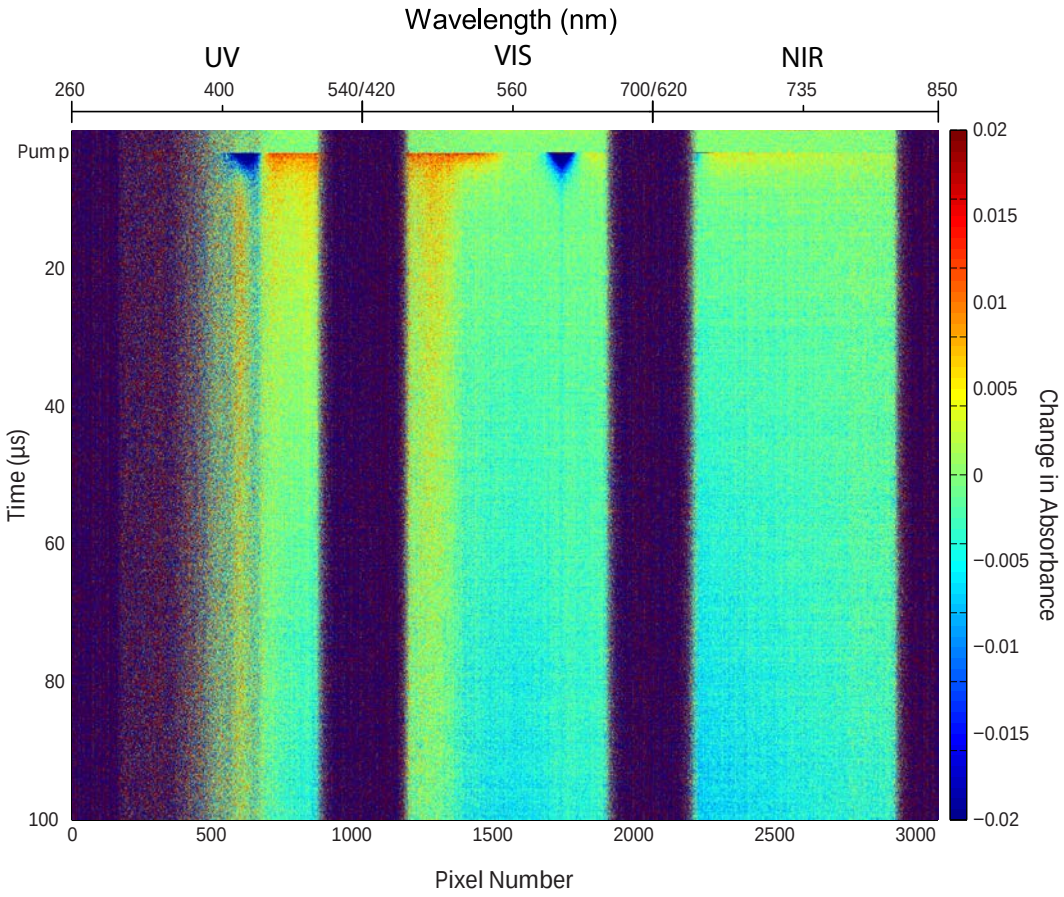

FIGURE 3.18: Transient absorption difference spectrum of TPTBPt with perylene.

Further frustrating detection of E^*, partially overlapping ground state absorption bands of S and E meant that any emitter bleaches were hidden amongst the sensitiser bleaches, which were much larger due to the higher extinction coefficients of the sensitisers. Similarly, the broad induced absorptions of the sensitiser in the NIR1 and NIR2 ranges masked any potential long wavelength induced absorptions of the emitter.

Despite deficiencies in the data, a method was still devised to determine kinetic properties of E^* from these measurements by utilising previous TRPL measurements (collected concurrently "just in case"). Crucially, the UC emission spectra of the different samples had shapes that matched the expected UC fluorescence of the emitter, and were taken to be proportional to $[E^*]^2$ (as in Equation 3.4). Due to the low concentrations and resulting low collision rates for TET and TTA, these TRPL spectra had very slow kinetics and could not be fit with the mixed kinetics model. The solution given by Equation 2.15 only applies for impulsive initial transfer of excitation from S^* to E, but Equation 3.3 can still be applied using numerical techniques even when an analytic solution is not known. Unlike normal TRPL studies, for these spectra $[S^*]_0$ could be determined quantitatively from the amplitude of sensitiser bleaches, and k_{TET} was assumed to be

entirely responsible for the larger k_s observed for S^* in the presence of E. The concentrations of S and E were already known from the sample preparation, but were also confirmed from the CW absorption spectra. While direct measurement of the emitter bleach or triplet absorptions would have been strongly preferred, the above framework was found to be sufficient to extract absolute values of k_1, k_2, and k_{TET} for the different UC samples.

3.3.2.1 Perylene and TPTBPt

The CW absorption spectrum of the TPTBPt and perylene system is shown in Figure 3.19, while the absorption difference spectrum was already used as an example in Figure 3.18. The phosphorescence of the sensitiser is shown in Figure 3.20, and matches the shape of the pure sensitiser phosphorescence in Figure 3.9 (plotted with the same intensity scale for ease of comparison) but with a more rapid decay. A trace generated from the phosphorescence is shown in Figure 3.21, and its fit to a single exponential is expected from Equation 3.2 by approximating TET as a quasi-first order process (with $[E]$ large and approximately constant).

The value of the new sensitiser decay constant was averaged from the different magnetic field measurements of absorbance bleach and phosphorescence features, and found to be $(5.7\pm0.1)\times10^5\,\mathrm{s}^{-1}$ ($\pm2.3\,\%$). This value was set equal to $(k_{TET}[E] + k_s)$, which along with the previously established value of k_s for the sensitiser in isolation, allowed k_{TET} to be determined as $4.52\times10^9\,\mathrm{M}^{-1}\mathrm{s}^{-1}$. This analysis is mathematically equivalent to the Stern–Volmer emitter concentration series commonly used to determine k_{TET} for E quenching of S^*, but with only two data points for $[E]$ (with the analysis in the previous section corresponding to $[E] = 0$).[70] The fact that only the *difference* in the S^* decay rate was considered means that only the effect of the emitter contributed to the calculation of k_{TET}, with systematic inaccuracies in k_s that were independent of

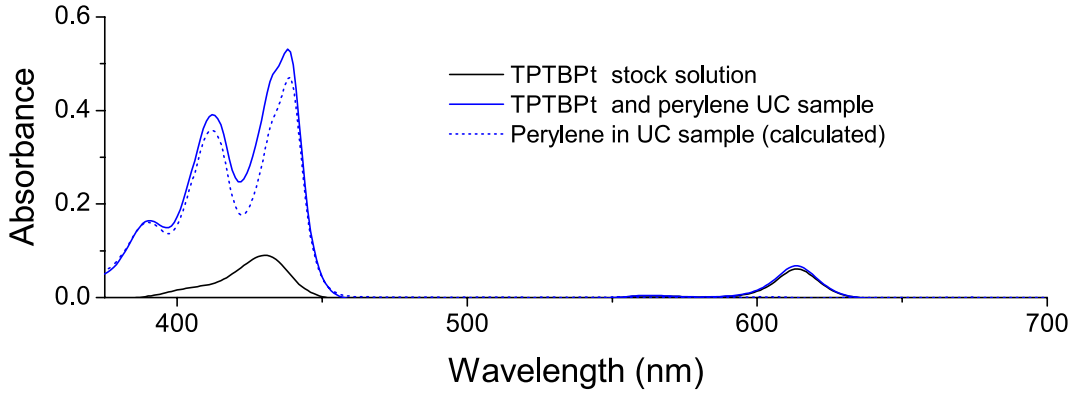

FIGURE 3.19: Absorption spectra of TPTBPt and perylene in a UC sample.

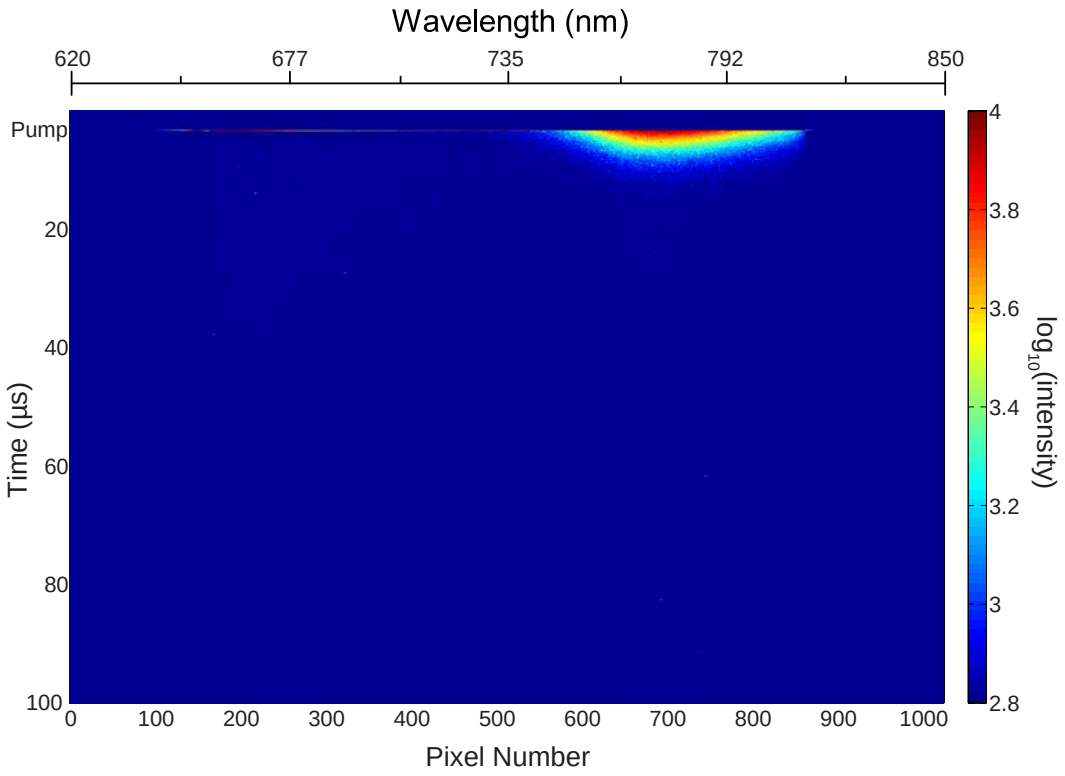

FIGURE 3.20: TRPL spectrum of TPTBPt phosphorescence in a perylene UC system. The intensity scale is chosen for ease of comparison with Figure 3.9.

$[E]$ excluded. This includes quenching by oxygen, as well as leading order contributions from S^* TTA — assuming these were unchanged in the two samples. The resulting value compares well with a published value of k_{TET} for TPTBPt and perylene in benzene of $4.08\times10^9\,\mathrm{M^{-1}s^{-1}}$, further dispelling the author's initial skepticism and indicating that this method indeed produced somewhat believable data.[163] Unfortunately that same

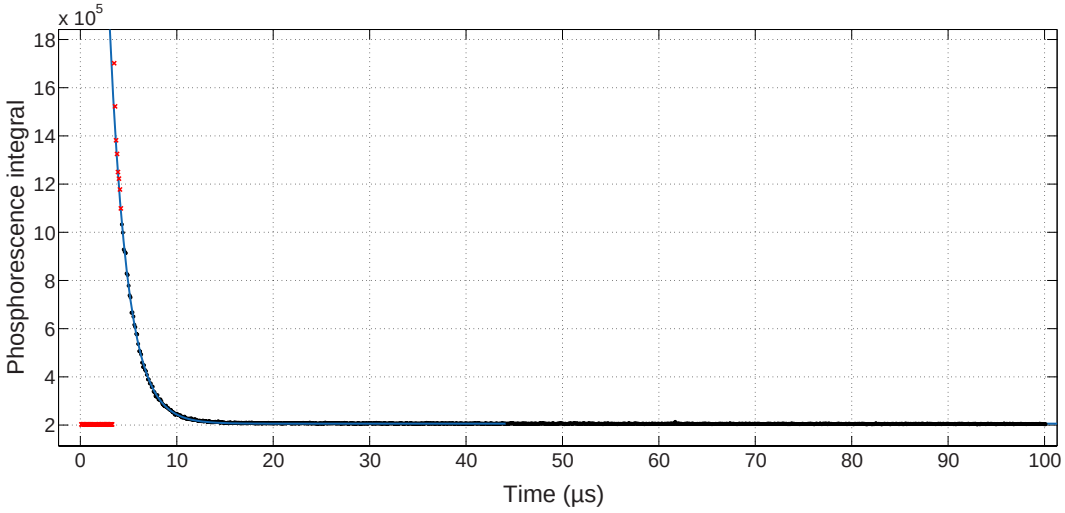

FIGURE 3.21: Exponential fitting of TPTBPt phosphorescence in a perylene UC system. Red points were excluded from the fitting of data to generate the blue curve.

study did not go so far as to also determine comparison values for k_1 and k_2, exemplifying the gaps in knowledge that this work was intended to address.

From the amplitude of the sensitiser absorbance bleach, $[S^*]_0$ was estimated individually for each of the magnetic field measurements to be in the range of $\sim$3 μM. This value indicates that almost all of the available sensitiser molecules (3.7 μM) were initially excited by the pump. These values were not averaged across magnetic fields because the different camera slit widths and slight variations in laser pulse energies for each scan meant that these values, unlike the rate constants, were not intrinsic to the UC system.

The UC fluorescence is then shown in Figure 3.22, and broadly matches the emission spectrum of perylene from Figures 2.5 and 2.9. The slow and delayed onset of the emission is understood to be a result of infrequent collisions associated with the low sample concentrations (3.7 and 120 μM in S and E). This led to slow absolute rates of TET to populate the emitter triplets, and slow TTA to depopulate it through emission. For fitting and determination of the emitter k_1 and k_2, the UC emission band was integrated across wavelength in each frame to give a single signal value (M), and background subtracted before a square root was applied ($y = \sqrt{(M-a)} = \sqrt{\Lambda[E^*]^2}$). By combining Equations 3.3 and 3.4 a differential equation for the transformed "observable" y could then be constructed, with the initial value of y set as zero:

$$\begin{aligned}\frac{dy}{dt} &= \sqrt{\Lambda}\frac{d[E^*]}{dt} \\ &= k_{TET}[E][S^*]_0 e^{-(k_{TET}[E]+k_s)t} - k_1 y - \frac{k_2}{\sqrt{\Lambda}}y^2\end{aligned} \tag{3.10}$$

where the only unknown constants in Equation 3.10 are k_1, k_2, and Λ. Like $[S^*]_0$, Λ was not assumed to be constant for the different magnetic fields, as the position of the magnet array could have altered the amount of UC emission reaching the detector.

The MATLAB ODE45 function was used to generate numerical solutions of Equation 3.10 for specific parameter values, and the Fminsearch function was used to find values of k_1, k_2, and Λ that minimised the sum of squared residuals between a test solution and the experimental data at different magnetic fields. An example of the traces and fits for y is shown in Figure 3.23. This was done separately for the different magnetic field measurements (with slightly different $[S^*]_0$ and Λ), with the resulting set of k_1 and k_2 values averaged and confidence intervals calculated once outliers were removed. As with k_s, no significant difference was observed for the magnetic field strengths used.

For perylene this process yielded a final value of k_1 equal to $(4.5\pm0.5)\times10^2\,\mathrm{s}^{-1}$ ($\pm$11%). For k_2 a value of $(6.92\pm0.47)\times10^9\,\mathrm{M}^{-1}\mathrm{s}^{-1}$ ($\pm$6.7 %) was obtained. This value of k_1 is

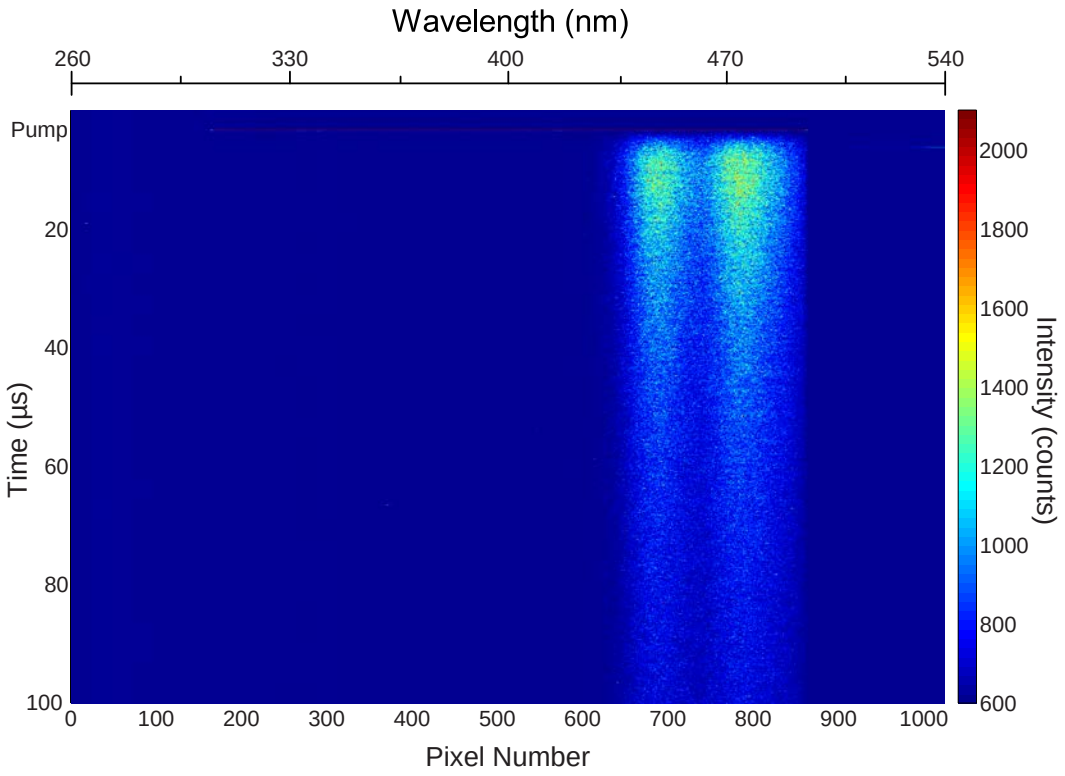

FIGURE 3.22: TRPL spectrum of UC emission from TPTBPt and perylene.

much lower than the one reported in Chapter 2, but compares favorably to a reported value in crystal studies of $200\,s^{-1}$.[194] Potential reasons for this difference were discussed in the previous chapter. In contrast, a reported value of perylene k_2 in UC systems could not be found, which was foreshadowed in the early sections of Chapter 2 as part of the motivation for this work. The value here nonetheless compares well with the diffusion limit of bimolecular collisions in toluene, $1.1\times10^{10}\,M^{-1}s^{-1}$.[171]

The entire procedure was also performed for a UC sample that instead contained d-perylene. This emitter came from the same source as the P98 emitter investigated in

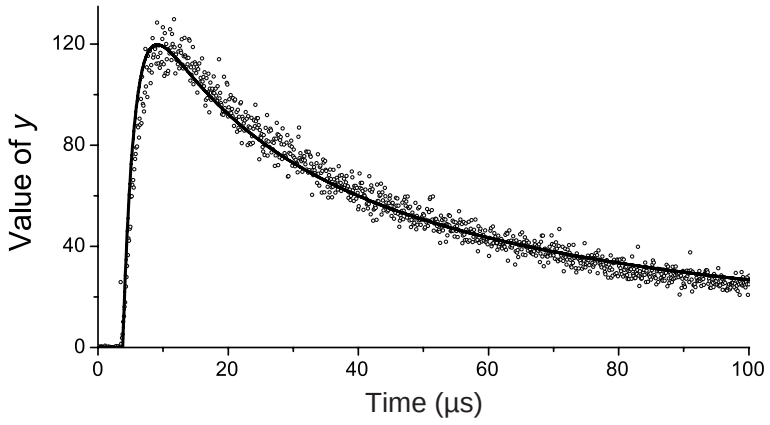

FIGURE 3.23: Typical achievable fitting of perylene UC TRPL using Equation 3.10.

Chapter 2, and UC component concentrations were within 5 % of the previous sample. For this system k_{TET} was found to be $4.61\times10^{9}\,\mathrm{M^{-1}s^{-1}}$; as expected, very similar to that of h-perylene. Similarly, k_1 was found to be $(4.9\pm0.2)\times10^{2}\,\mathrm{s^{-1}}$ ($\pm4.6\,\%$), while k_2 was $(2.16\pm0.07)\times10^{10}\,\mathrm{M^{-1}s^{-1}}$ ($\pm3.4\,\%$).

The difference in k_1 for the different perylene UC systems was too small to defensibly claim the same reduction discussed in Chapter 2. Despite opposite ordering, the results presented here are not necessarily inconsistent with a decrease in perylene k_1 upon deuteration, thanks to the large relative uncertainty for the hydrogen isotopologue. Ultimately this larger uncertainty arose because TRPL measurements in the previous chapter used 1000 shots per frame, while this study used just one. The smaller k_1 values for both perylenes are also consistent with the previously discussed hypothesis that oxygen had contributed to k_1 in both for the samples in Chapter 2, and diminished the calculated relative deuteration enhancement.

For k_2 the fourfold difference was not expected, and may be an indication of the inherent variability of this method. It could alternatively correspond to a real deuteration effect on k_2 (discounted previously), consistent with the edges of the confidence intervals presented for Bk_2 in the previous chapter. A later measurement of h-perylene in a UC system with PQ_4Pd yielded a value of k_2 right in between the values above, and so the specific values here should be treated with an appropriate level of skepticism.

As previously mentioned, the low values of $[S^*]_0$ calculated for this and other UC samples explains why bleaches in the absorption of E were not observed. Assuming full and instant transfer of the maximum observed $[S^*]_0$ ($\sim3\,\mu$M) to bleach the same quantity of E, the moderate value of ϵ of the perylene peak absorption ($38989\,\mathrm{M^{-1}cm^{-1}}$) across the 1 mm sample cell would result in a detectable absorbance difference signal of 11 mOD.[245] Instead, excitation transfer occurred over an extended duration due to the low concentration and collision rate, as evidenced by the slow build of signal in Figure 3.22. Once fitted to determine Λ, traces like that shown in Figure 3.23 could be transformed into traces of $[E^*]$ $\left(=\frac{y}{\sqrt{\Lambda}}\right)$ to determine the actual maximum value of $[E^*]$ during each measurement. Taking into account S^* first order decay and sinks on $[E^*]$ from both first order decay and TTA, it makes sense that this maximum value would be smaller than the theoretically maximum attainable 3 μM. For perylene it was found to be instead closer to 2 μM, a level of excitation corresponding to a maximum perylene ground state bleach of $\sim$8 mOD — similar to the lowest levels detectable by this instrument. Assuming similar values of ϵ for E and E^*, this also explains why no additional induced absorptions were identified either. Compared to $[S^*]_0$, this value did indicate relatively efficient transfer of excitation to perylene though.

In addition to rationalising the disappointing results in this section (that is, absence of emitter bleach or induced absorptions), the technique of generating traces of $[E^*]$ from y and Λ would later prove invaluable in analysis of a dual emitter UC system.

3.3.2.2 DPA and OEPPd

Having established an analysis routine for TPTBPt with perylene, OEPPd with DPA was quickly found to also behave qualitatively in the same way. The CW absorption spectrum of the UC sample is shown in Figure 3.24, while the phosphorescence and UC emission are shown in Figures 3.25 and 3.26. The TA and absorption difference spectra were identical in shape to those of plain OEPPd, and kinetics of the the phosphorescence and sensitiser bleaches (14 traces) were used to determine the average k_{TET} across the different magnetic field strengths. The values of $[S^*]_0$ were calculated for each scan from the amplitude of the Q band bleach only.

For this sample and using the previously determined value of k_s, k_{TET} was found to be $1.43\times10^9\,\mathrm{M^{-1}s^{-1}}$, which matches exactly another report of the same system that had stopped short of also determining k_1 and k_2.[129] For DPA, fitting the UC fluorescence to Equation 3.10 yielded a final value of k_1 equal to $(7.6\pm0.1)\times10^3\,\mathrm{s^{-1}}$ ($\pm1.9\,\%$), with k_2 of $(1.8\pm0.4)\times10^9\,\mathrm{M^{-1}s^{-1}}$ ($\pm26\,\%$).

The entire procedure was also performed for a deuterated DPA UC sample. For this system k_{TET} was found to be $1.54\times10^9\,\mathrm{M^{-1}s^{-1}}$, almost identical to that of the normal DPA. Similarly, k_1 was found to be $(1.9\pm0.4)\times10^3\,\mathrm{s^{-1}}$ ($\pm21\,\%$), while k_2 was $(4.8\pm0.7)\times10^9\,\mathrm{M^{-1}s^{-1}}$ ($\pm15\,\%$).

These values of k_1 and k_2 for DPA are broadly similar to reported values for an otherwise identical anthracene UC system ($7\times10^3\,\mathrm{s^{-1}}$ and $5\times10^9\,\mathrm{M^{-1}s^{-1}}$), and to another study of DPA with OEPPt in dichloromethane ($2\times10^4\,\mathrm{s^{-1}}$ and $1\times10^{10}\,\mathrm{M^{-1}s^{-1}}$).[131,246] In another

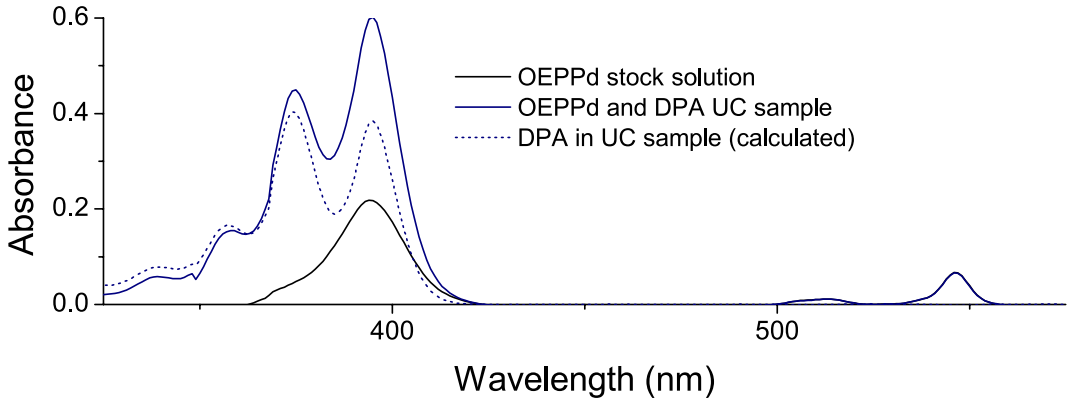

FIGURE 3.24: Absorption spectra of OEPPd and DPA in a UC sample.

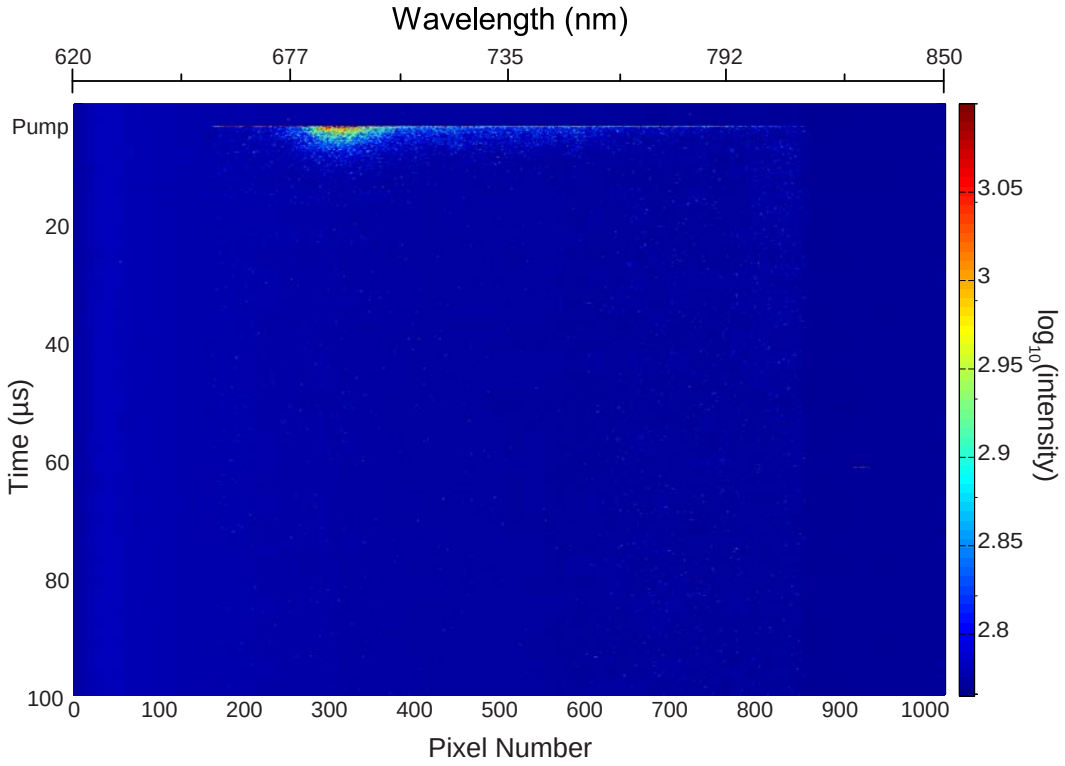

FIGURE 3.25: TRPL spectrum of of OEPPd phosphorescence in a DPA UC system. The intensity scale is chosen for ease of comparison with Figure 3.14.

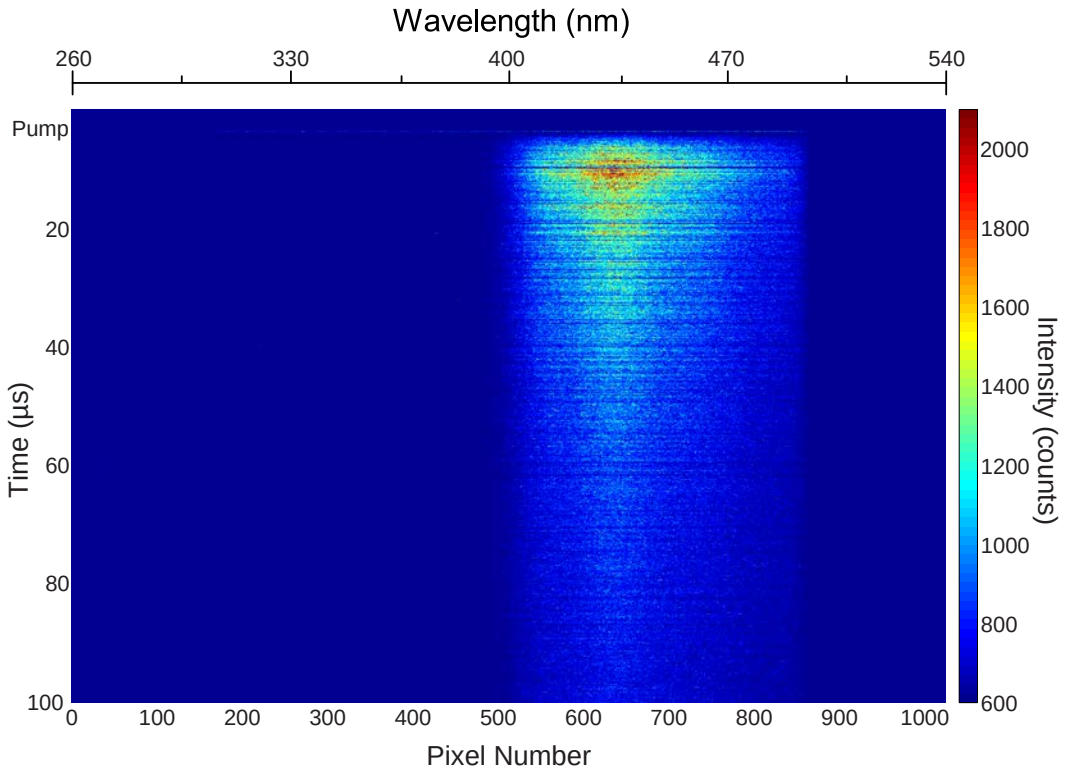

FIGURE 3.26: TRPL spectrum of UC emission from OEPPd and DPA. The intensity scale is chosen for ease of comparison with Figure 3.22.

study of DPA with OEPPt in toluene, a much lower value of k_1 was found ($1\times10^2\,s^{-1}$), although the value of k_2 matched well ($2.5\times10^9\,M^{-1}s^{-1}$).[165] The large value of DPA k_1 may have been due to oxygen in the sample (as suggested for the large OEPPd k_s). As with perylene though, no reported k_1 and k_2 values in a truly identical UC system could be found, and so some uncertainty remains regarding the true values for DPA.

While the large observed decrease in k_1 for deuterated DPA (75 % lower) was initially exciting, the similar increase in k_2 raised some suspicion about these results as a whole. As explained in Chapter 2, k_2 was not expected to change under deuteration for the same reasons used to explain the observed invariance in k_{TET}. Deuterated DPA may well be significantly better in UC systems than its normal isotopologue (especially if k_2 can be altered through the presence of some non-resonant triplet channel), but additional replication studies would be necessary to dispel remaining doubts about some of values generated in this study.

3.3.2.3 Rubrene and PQ_4Pd

The CW absorption spectrum of a PQ_4Pd and rubrene system is shown in Figure 3.27, while the phosphorescence and UC emission are shown in Figures 3.28 and 3.29. The TA and absorption difference spectra were identical in shape to those of plain PQ_4Pd, and kinetics of the the phosphorescence and sensitiser bleaches (22 traces) were used to determine the average k_{TET} across the different magnetic field strengths. The values of $[S^*]_0$ were calculated for each scan from the amplitude of the Q band bleach in the NIR1 range only.

For this sample and using the previously determined value of k_s, k_{TET} was found to be $2.71\times10^8\,M^{-1}s^{-1}$, which matches well with another report of the same system ($3.1\times10^8\,M^{-1}s^{-1}$) that went the extra mile in also determining k_1 and k_2.[151] Fitting

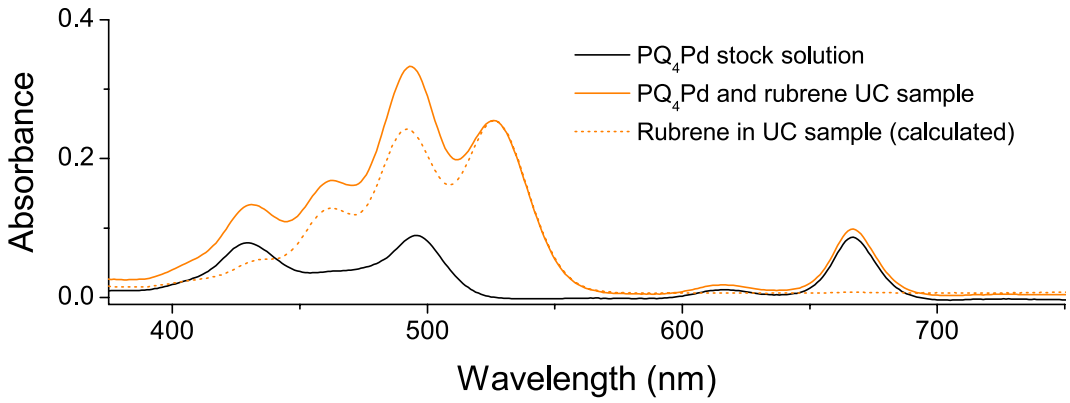

FIGURE 3.27: Absorption spectra of PQ_4Pd and rubrene in a UC sample.

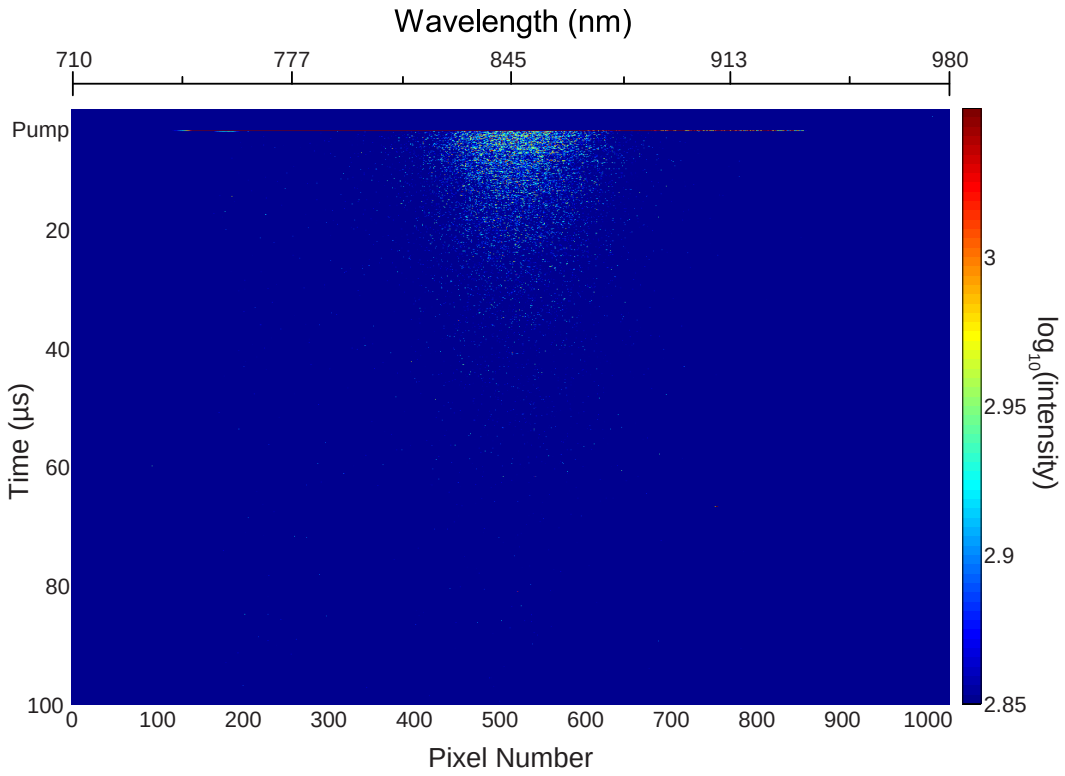

FIGURE 3.28: TRPL spectrum of of PQ_4Pd phosphorescence in a rubrene UC system. The intensity scale is chosen for ease of comparison with Figure 3.17.

of the rubrene emission kinetics yielded a final k_1 value of $(8.9\pm0.4)\times10^3\,s^{-1}$ ($\pm4.4\,\%$), with k_2 of $(2.0\pm0.1)\times10^8\,M^{-1}s^{-1}$ ($\pm4.8\,\%$).

The entire procedure was also performed for a deuterated UC sample. For this system k_{TET} was found to be $2.47\times10^8\,M^{-1}s^{-1}$, almost identical to that of the normal rubrene. Similarly, k_1 was found to be $(7.7\pm0.4)\times10^3\,s^{-1}$ ($\pm6.0\,\%$), while k_2 was $(1.97\pm0.22)\times10^8\,M^{-1}s^{-1}$ ($\pm11\,\%$).

This rubrene UC system was the only one for which a kinetics study could be found that had also reported k_1 and k_2 for rubrene using the same sensitiser in the same solvent. This reference TRPL study was in fact performed in the same research group some years earlier by Dr Dennis Cheng, using the same equipment as the TRPL in Chapter 2.[247] The values reported in that study compared well to those generated by the TA method, for all of k_{TET} (above), k_1 ($8\times10^3\,s^{-1}$) and k_2 ($1\times10^8\,M^{-1}s^{-1}$). This close agreement was taken as further evidence that the modified TA+TRPL analysis — developed here to compensate for the absence of direct emitter TA signal — was truly working as intended. Indeed, as mentioned earlier, this analysis is analogous to using TRPL methods like Equation 2.15 on the emitter TTA, along with a directly measured value of $[S^*]_0$ (from the sensitiser TA data) in order to successfully use Equation 2.17.

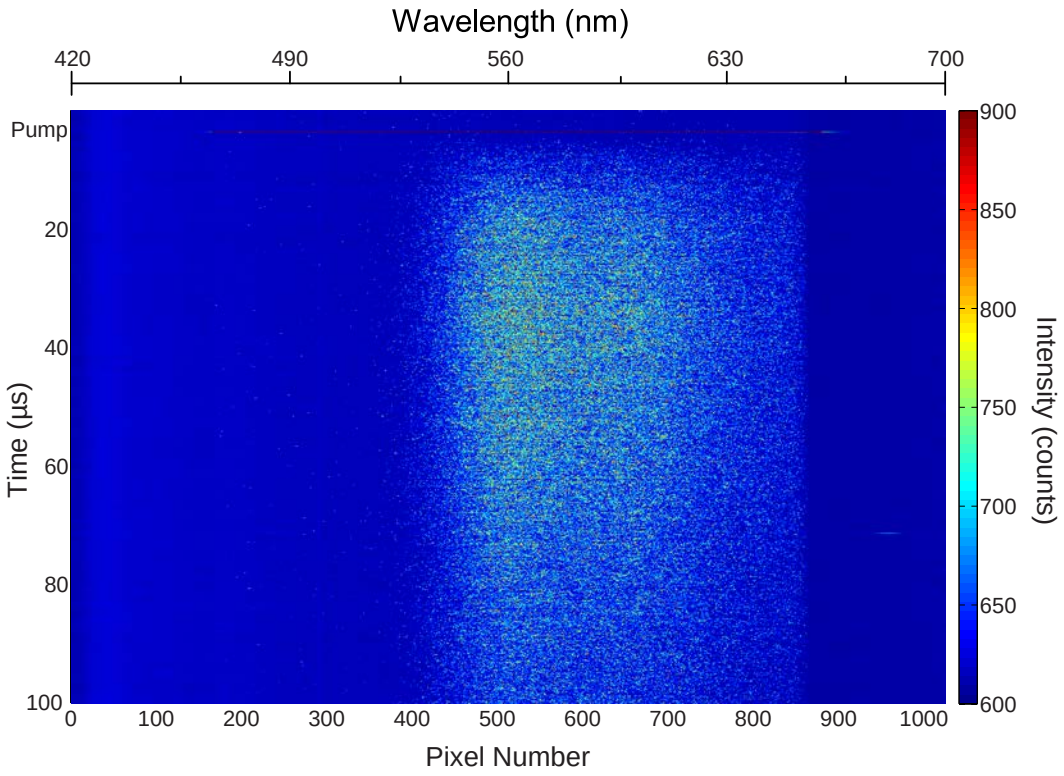

FIGURE 3.29: TRPL spectrum of UC emission from PQ_4Pd and rubrene. Note the greatly reduced range of the colour scale for intensity (with same minimum) compared to UC systems with perylene and DPA (different wavelength ranges).

Rubrene was also found to have similar k_1 and k_2 in a UC system with TPTBPt, discussed in the following sections. Additionally, an earlier measurement run on a contaminated rubrene and PQ_4Pd UC sample also yielded the similar k_1 and k_2 values ($7.4\times10^3\,s^{-1}$ and $1.7\times10^8\,M^{-1}s^{-1}$), but a much larger k_{TET} ($5.5\times10^8\,M^{-1}s^{-1}$). The larger TET rate was thought to arise from S^* quenching by the contaminant, which was itself thought to be some non-emissive form of photo-oxidised or photo-fragmented rubrene. A discussion of the photostability of UC systems, including lessons learned from this contaminated sample, is presented in the following sections. Nonetheless, the uniformity of the rubrene kinetic rate constants in these different experiments was taken as further support for the validity of the TA+TRPL method.

Concerning the actual values of these constants, rubrene proved to be somewhat distinct from the other UC emitters investigated in this study. Its low values of both k_{TET} and k_2 are potentially explained by the steric bulk of its four substituent paddles, which frustrate close collisions between S^* and E, as well as E^* and E^*. Despite this, rubrene can form high efficiency UC systems, which has been interpreted as evidence of a particularly large and compensatory intrinsic value of η.[47] The role of its substituent bulk in frustrating and directing the orientations of molecular collisions is investigated further in the next chapter.

On deuteration, the k_1 of rubrene decreased by a statistically significant 12±9 %, while k_2 was left relatively unchanged. This result is reminiscent of that found for d-perylene, and perhaps of even wider scientific interest due to the widespread use of rubrene in OLEDs.[228] It is the author's intent to prepare this result along with the NDF synthesis method for future publication.

3.3.2.4 BPEA and PQ_4Pd

The CW absorption spectra of a PQ_4Pd and BPEA UC system is shown in Figure 3.30, while the BPEA emission is shown in Figure 3.31. The transient absorption and phosphorescence again had the same shape as plain PQ_4Pd, but with faster decay kinetics attributed to quenching by BPEA. Kinetics of the phosphorescence and sensitiser bleaches (23 traces) were used to determine k_{TET}, while the bleach amplitudes were used to determine $[S^*]_0$.

For this sample, k_{TET} was found to be $6.75\times10^8\,M^{-1}s^{-1}$. This value is smaller than that found for most of the other UC systems, but is still about three times faster than for PQ_4Pd quenching by rubrene. Together these comparisons indicate that the steric bulk of both rubrene and PQ_4Pd were likely contributing factors to the particular low value of k_{TET} in their combined UC system. For BPEA, k_1 and k_2 were found to take values of $(1.2\pm0.3)\times10^4\,s^{-1}$ (±25 %) and $(6.5\pm2.5)\times10^9\,M^{-1}s^{-1}$ (±33 %). These values are in reasonable agreement with the k_2 used to model results in another study of BPEA with TPTBPt in tetrahydrofuran ($4.2\times10^9\,M^{-1}s^{-1}$, converted from cm^3s^{-1} in the original publication), although is quite different in the value of k_1 ($370\,s^{-1}$, reported in Hz in the original publication).[248]

For deuterated BPEA, k_1 and k_2 were $(1.0\pm0.3)\times10^4\,s^{-1}$ (±31 %) and $(1.0\pm0.1)\times10^{10}\,M^{-1}s^{-1}$ (±13 %). From these values it appears that deuteration may decrease k_1 for BPEA as well, although the effect sizes observed for both constants in this study were not large

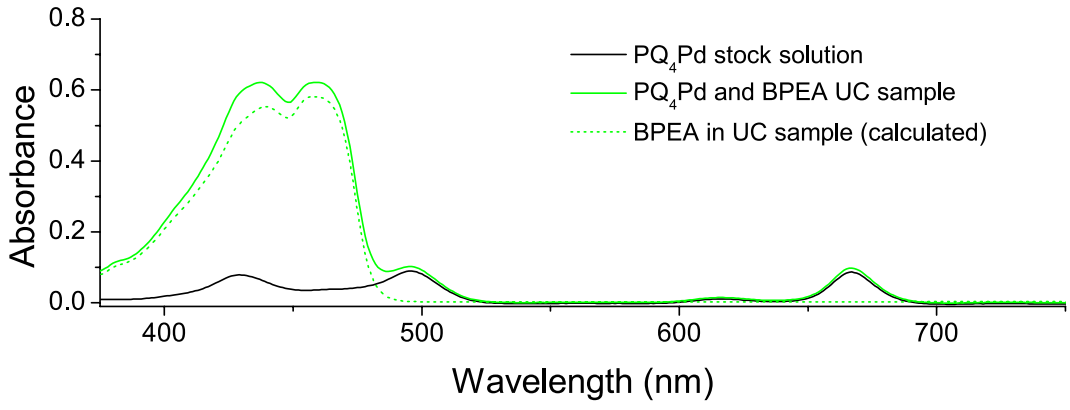

FIGURE 3.30: Absorption spectra of PQ_4Pd and BPEA in a UC sample.

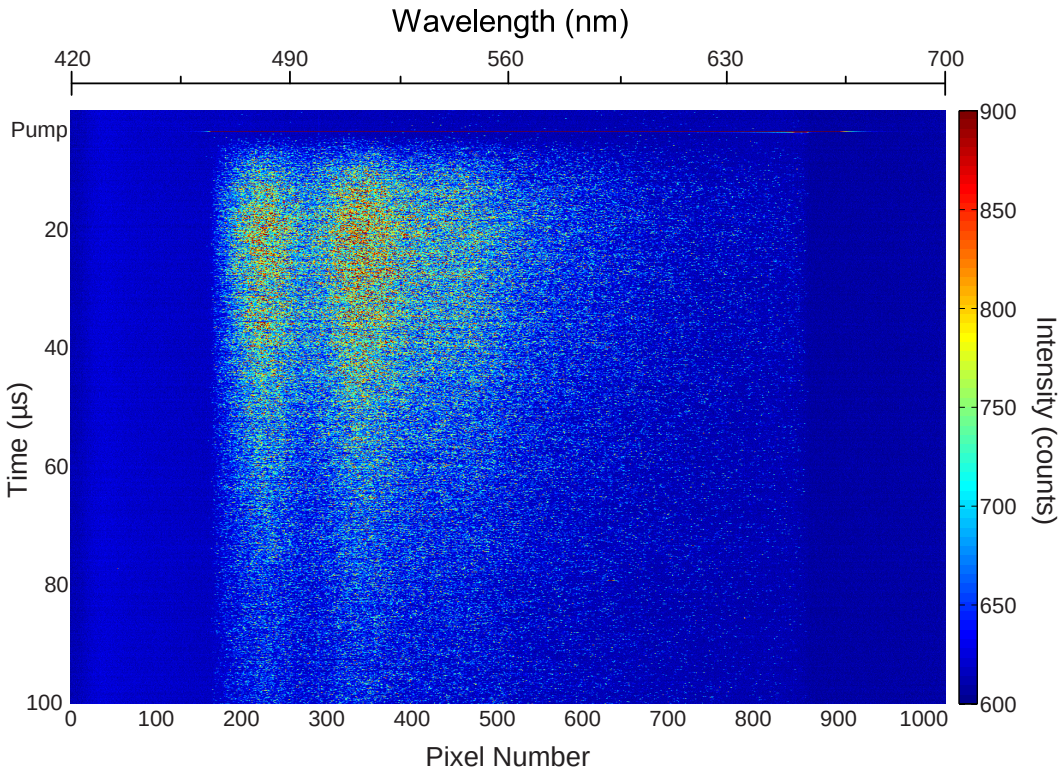

FIGURE 3.31: TRPL spectrum of UC emission from PQ_4Pd and BPEA. The intensity scale is chosen for ease of comparison with Figure 3.29.

enough to claim statistical significance. Once again, the unexpected difference in k_2 is a cause for concern regarding the data generated by this method, but in this case the edges of the confidence intervals also (just) overlap.

3.3.2.5 Perylene and PQ_4Pd

In this system, also previously studied by Dr Cheng, the energies of S^* and E^* are deliberately mismatched so that TET is considerably endothermic.[170] In that previous study the entropic driving of TET was examined, but here the system was used to check for variations in perylene's own rate constants — which ideally should be independent of the sensitiser (that is, constant).[170] The CW absorption spectra and UC emission are shown in Figures 3.32 and 3.33, and k_{TET} was calculated from the sensitiser phosphorescence and bleaches (22 traces).

In this system the value of k_{TET} was found to be $1.6\times10^8\,M^{-1}s^{-1}$, calculated in the same way as in previous sections. This compares poorly to the value in the previous report ($2\times10^7\,M^{-1}s^{-1}$), although in that study careful effort was spent to separate this from the rate of back–TET by only considering the initial S^* decay rate (when $[E^*]$ was close

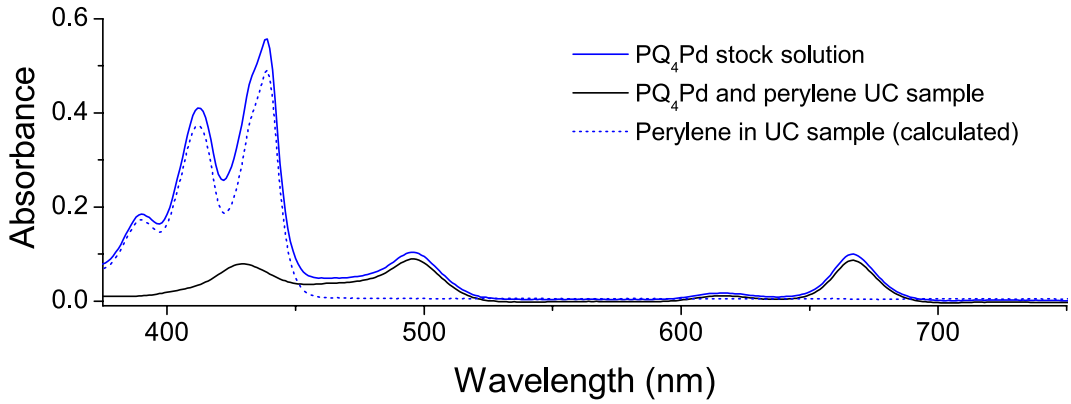

FIGURE 3.32: Absorption spectra of PQ_4Pd and perylene in a UC sample.

to zero). Nonetheless, the thirtyfold decrease in quenching compared to perylene with TPTBPt was expected from its endothermicity. Furthermore, the quenching of PQ_4Pd by perylene was comparable to that of rubrene (exothermic with collisions sterically hindered), but slower than that of BPEA (exothermic and less hindered). This slower excitation transfer to E^* helps to explain the much slower and weaker build up of perylene UC emission in this sample compared to when paired with TPTBPt.

In this system the values of k_1 and k_2 for the perylene were found to be $(5\pm1)\times10^2\,\mathrm{s}^{-1}$ ($\pm19\,\%$) and $(1.2\pm0.1)\times10^{10}\,\mathrm{M}^{-1}\mathrm{s}^{-1}$ ($\pm10\,\%$). These values compare well with those

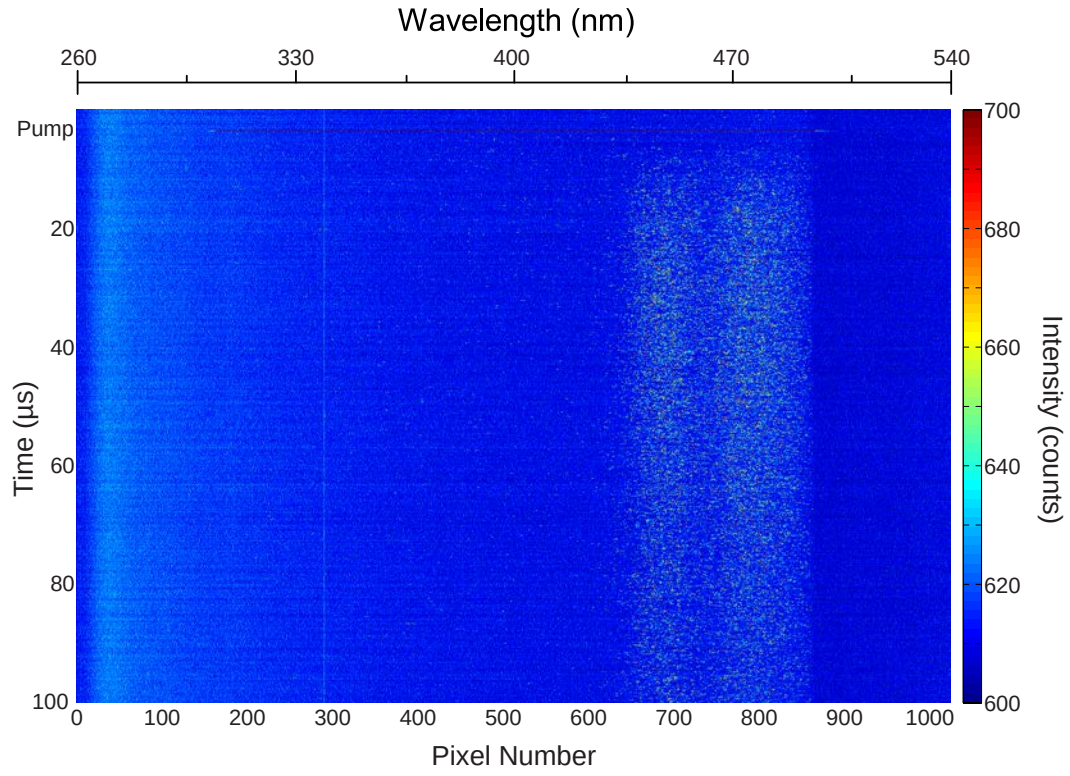

FIGURE 3.33: TRPL spectrum of UC emission from PQ_4Pd and perylene. Note the use of a greatly reduced colour scale for intensity compared to perylene with TPTBPt.

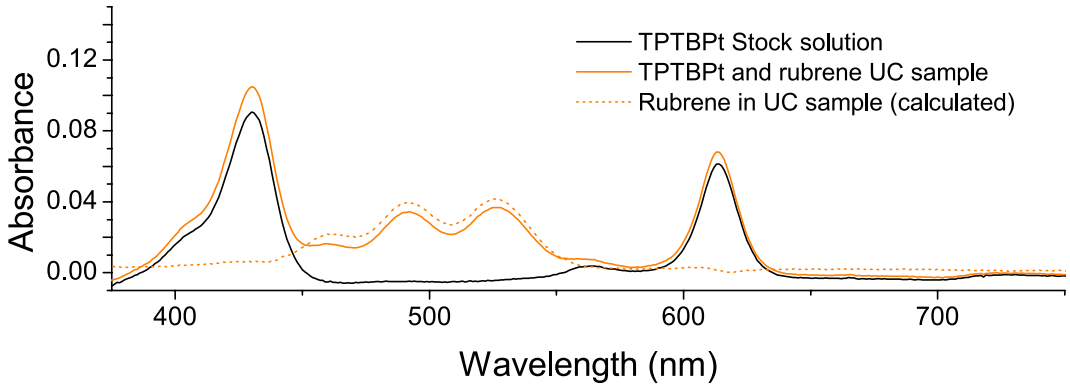

FIGURE 3.34: Absorption spectra of TPTBPt and rubrene in a UC sample. The calculated rubrene amount here is a slight overestimate (dotted orange line above solid).

found for the h-perylene and TPTBPt system, but reveal significant variability in the measured values of k_2, which were expected to be the same for all systems.

3.3.2.6 Rubrene and TPTBPt

In this system, rubrene and TPTBPt were deliberately chosen to investigate the effect of sensitiser reabsorption of UC emission. Figure 3.34 shows the CW absorption of the sample, with non–trivial S absorption across the 550–600 nm emission band of rubrene. Figure 3.35 shows the UC emission kinetics from the pump beam alone.

For this system, the reduced bulk of TPTBPt and increased exothermicity of TET led to a much higher k_{TET} than with PQ_4Pd; $1.2\times10^9\,M^{-1}s^{-1}$ compared to $2.7\times10^8\,M^{-1}s^{-1}$. This was still slower than that for perylene with TPTBPt though ($4.2\times10^9\,M^{-1}s^{-1}$), once again indicating that intrinsic properties of rubrene are partly responsible for its slow kinetics — most likely its bulk and associated slower diffusion. This larger k_{TET} is likely responsible for the similar UC emission intensity observed with PQ_4Pd, despite the use of much lower rubrene concentrations in the TPTBPt sample.

As for perylene with PQ_4Pd, the values of k_1 and k_2 for rubrene with a different sensitiser were not found to be vastly different. The actual values were $(9.00\pm0.06)\times10^3\,s^{-1}$ ($\pm0.72\,\%$) and $(2.1\pm0.3)\times10^8\,M^{-1}s^{-1}$ ($\pm13\,\%$). The effect of UC emission being reabsorbed were not considered further in this study, supported by this result as well as the generally low sample thickness and concentrations. In contrast, in UC systems designed for PV applications the outward propagation of emission through a dense absorbing medium is a key engineering concern.[249]

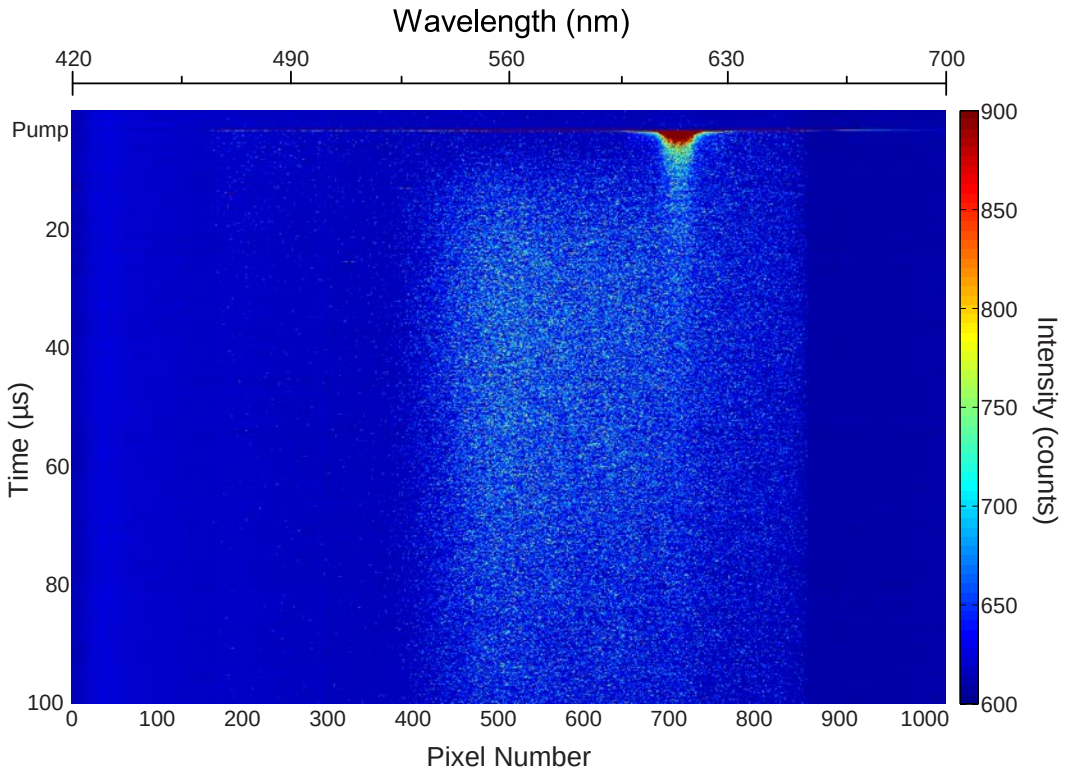

FIGURE 3.35: TRPL spectrum of UC emission from TPTBPt and rubrene. The feature through 615 nm corresponded to reflections of the pump beam entering the camera, and was not included in traces for fitting. The intensity scale is the same as in Figure 3.29.

3.3.3 A Hybrid Emitter UC system

In addition to the previous two component UC systems, a single three component system comprised of PQ_4Pd with both rubrene and BPEA was also investigated. The same UC system had previously been shown to perform better than a linear combination of its components would predict in direct CW augmentation of a dye sensitised solar cell.[47] Although unconfirmed, two potential mechanisms were proposed by the authors of that study: either BPEA was acting as a fast moving exciton shuttle to more rapidly populate rubrene triplets, or highly efficient heterogeneous TTA reactions were occurring between BPEA and rubrene triplets. Both mechanisms were consistent with the previously determined values of k_2 and reported or assumed values of η for the different emitters, implying fast diffusion but low efficiency collisions for BPEA and slow diffusion but efficient collisions for rubrene.[67,151] The possibility of both mechanisms operating simultaneously was also considered for this study.

A UC sample was prepared from these three components using 7.9 μM of PQ_4Pd, 130 μM of BPEA, and 77 μM of rubrene. A 3:1 ratio of $[B]$:$[R]$ was targeted to match the best performing UC solution in the original publication, in which any hybrid effects would be maximised. The same measurement and analysis of the S phosphorescence and bleaches

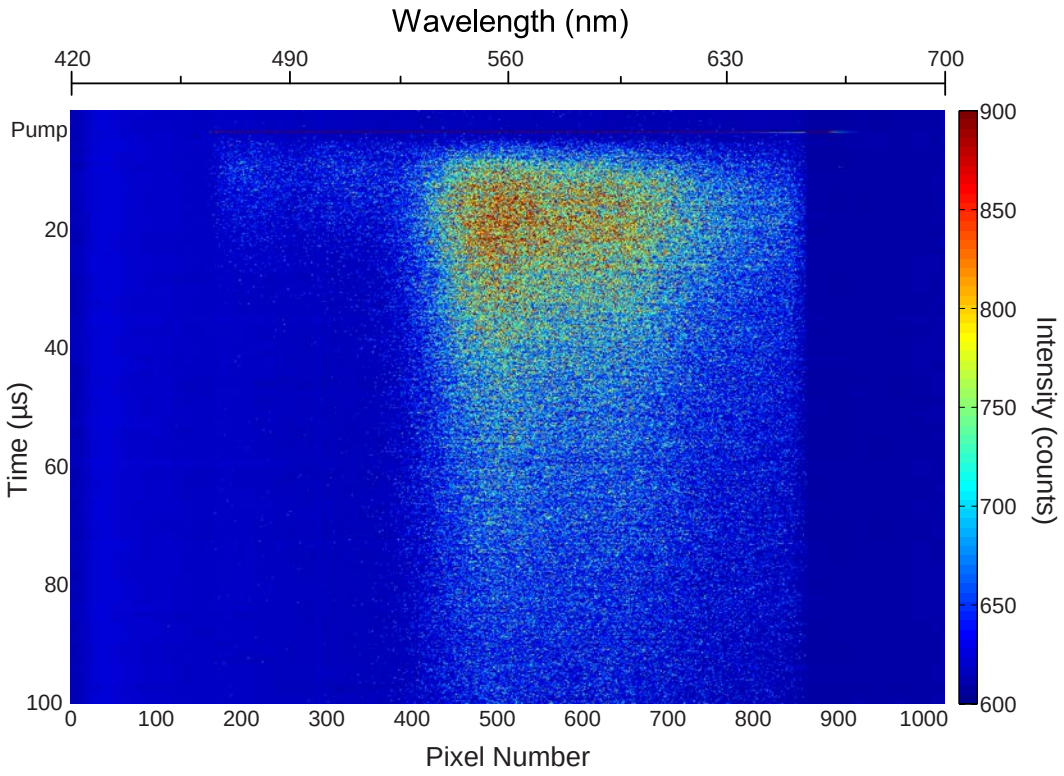

FIGURE 3.36: TRPL spectrum of UC emission from PQ_4Pd with BPEA and rubrene.

was performed to determine the total rate of TET, as well as the values of $[S^*]_0$ at each magnetic field.

The UC emission was also measured, with two distinct bands matching those of pure rubrene and BPEA observed in the VIS region. The UC emission from the hybrid system is shown in Figure 3.36, and its shape appears to be a combination of that seen in Figures 3.29 and 3.31. The same procedure was also repeated for another sample containing deuterated BPEA and deuterated rubrene, but not for mixed h/d emitters.

The accelerated decay of $[S^*]$ was again used to determine the total rate of TET, and this was divided by the total emitter concentration ($[E] = [B] + [R]$) to yield a combined k_{TET} of $5.52 \times 10^8\,\mathrm{M^{-1}s^{-1}}$. In comparison, the mole ratio weighted average of k_{TET} for BPEA and rubrene individually quenching PQ_4Pd was calculated from values in previous sections to be $5.2 \times 10^8\,\mathrm{M^{-1}s^{-1}}$. This close agreement indicated that these two mechanisms of quenching were occurring simultaneously as independent processes.

Inspecting the UC emission in Figure 3.36 shows that the BPEA feature is much smaller and shorter lived when in the presence of rubrene, while the rubrene emission is much larger and faster than it was without BPEA (despite the lower rubrene concentration, $[R]$, used here). In the heterogeneous collisions hypothesis, emission is assumed to come from the lower energy rubrene singlet that forms during TTA (used earlier to explain the

green emission of perylene OLEDs). As a result, emission from heterogeneous BPEA and rubrene collisions is not directly separable from homogeneous rubrene TTA emission. In contrast, BPEA emission is taken to represent only homogeneous BPEA collisions. Put into equations, the underlying assumption of the following analysis can then be expressed as modified versions of Equation 3.4:

$$\begin{aligned} M_B &= \Lambda_B[B^*]^2 \\ M_R &= \Lambda_R[R^*]^2 + \Gamma[B^*][R^*] \end{aligned} \tag{3.11}$$

where M_R and M_B are the signal from the rubrene and BPEA emission regions (pixel numbers 450–800 and 200–400 respectively), Λ_R and Λ_B are the molecular and hardware scaling factors for rubrene and BPEA homogeneous TTA, and Γ is the scaling factor for heterogeneous TTA. Importantly, since emission corresponding to Λ_R and Γ was measured simultaneously at the same wavelength, they are assumed to differ only due to the molecular parameters associated with the heterogeneous and rubrene homogeneous TTA processes. In contrast, Λ_B was measured at a different wavelength and could not be compared to Λ_R or Γ in a similar way.

As a result, the kinetics of $[B^*]$ were first investigated by generating traces from only the BPEA emission region. This was because the "y method" of Equation 3.10 could still be applied with only slight modification. An example of the BPEA emission y traces is included in Figure 3.37.

Due to the small amplitude and rapid decay of the BPEA emission, the signal to noise ratio in the raw data corresponding to Figure 3.37 was higher than in previous measurements, even after wavelength integration. Due to this noise, background subtraction of M_B resulted in some negative data points, most notably before the pump pulse and at long times ($t > 50\,\mu$s). Since a square root was required to convert M_B into y, these negative values were addressed by using only the real part of the complex square root function — which returns zero for negative real input and the same as the standard square root function for non-negative reals. Although this was satisfactory from an analytic point of view, it resulted in the data having the appearance of a poor background subtraction when plotted. In Figure 3.37 some of the data points mapped to zero by the square root can be seen on the time axis, but these did not significantly alter the fitting in the region of interest ($5 < t < 30\,\mu$s, where the B^* emission was above the noise baseline).

Although the BPEA emission decays much faster than in the absence of rubrene, its emission spectrum and decay kinetics were still of a comparable shape to the simpler

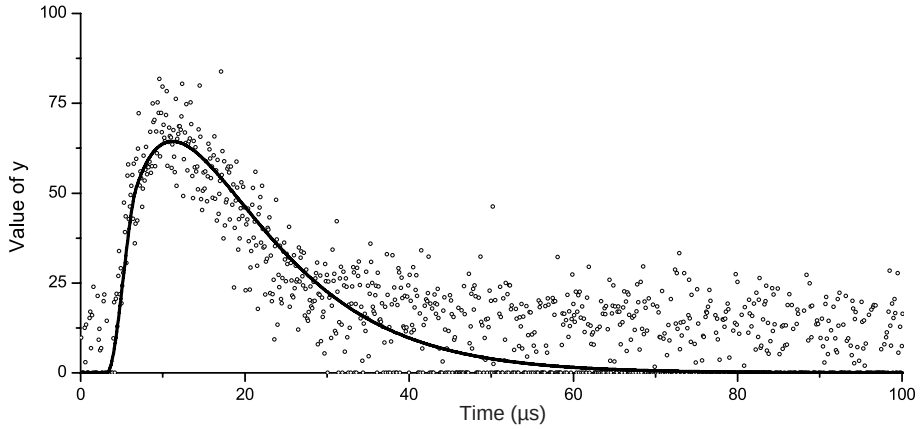

FIGURE 3.37: Typical achievable fitting of BPEA emission TRPL using Equation 3.12. Data points with values made negative by the initial baseline subtraction were set to zero by using the real part of the complex square root function, resulting in the appearance of poor background subtraction. Curves such as this were approximated with analytical forms to give $[B^*](t)$ for use in Equation 3.13.

two component UC system. In the exciton shuttle hypothesis, this increased decay rate is attributed to quenching of B^* by R, which like the quenching of S^* by B can be treated as quasi-first order. Adding B^* to R quenching to Equation 3.3 resulted in a good fit to the experimental data for B^* emission, with the modified equation given by:

$$\frac{d[B^*]}{dt} = k_{TET}^{B}[B][S^*]_0 e^{-(k_{TET}[E]+k_s)t} - (k_1 + k_q[R])[B^*] - k_2[B^*]^2 \tag{3.12}$$

where k_{TET}^{B} is the rate constant for TET in the two component BPEA system measured previously, and k_q is the rate constant for B^* quenching by R. In this fitting k_2 was set to its previously determined value for BPEA and not allowed to vary, resulting in only $(k_1 + k_q[R])$ and Λ_B as fitting parameters when using a slightly modified version of Equation 3.10.

Equation 3.12 includes a significant simplifying approximation that deserves explicit mention. The lack of a term in $[B^*][R^*]$ means that heterogeneous TTA is not specifically addressed. This was necessary to construct a tractable ODE for $[B^*]$, as $[R^*]$ (which varies with time) could not be immediately extracted from M_R, which itself had an unknown and varying component of heterogeneous TTA. As a result, this equation represents an exclusive adoption of the exciton transporter model, while in reality exciton transport and heterogeneous TTA are not mutually exclusive. Nonetheless, the large value of $[R]$ and small values of $[R^*]$ (calculated later) make this assumption (that rubrene quenching vastly outcompetes heterogeneous TTA in the kinetics of B^*) perhaps not so bad for this data set. Addition supporting evidence for this claim is the good fits generated by solutions to Equation 3.12, and the fact that M_B emission had significantly decayed before M_R had reached its peak in Figure 3.36.

Despite this simplification k_q was still calculated, with a value of $1.6\times10^9\,\mathrm{M^{-1}s^{-1}}$. This value is large for rubrene compared to rate constants of other things it can quench, indicating that the smaller size and high mobility of the BPEA was indeed allowing it to act as a rapid exciton transporter. This would then be consistent with the faster and larger buildup observed for M_R, despite a small value of $[R]$ in this system. From the fit values of Λ_B traces of $[B^*](t)$ were also calculated. Intended for use in a subsequent ODE for $[R^*]$, these numerical $[B^*]$ traces were then approximated by analytic functions of the form $Ae^{(a-bt)} - Be^{(c-dt)}$, or in later cases by a fifth order Fourier expansion (because there is no kill like overkill). The approximated analytic $[B^*]$ traces were checked for consistency by comparing their values of $\Lambda_B[B^*]^2$ to M_B, and found to be good replacements in all cases.

With $[B^*](t)$ now known and available for use, a similar approach was then taken to analyse M_R. By once again assuming that exciton transport was the dominant interaction between BPEA and rubrene, another ODE was constructed for $[R^*]$:

$$\frac{d[R^*]}{dt} = k^R_{TET}[R][S^*]_0 e^{-(k_{TET}[E]+k_s)t} - k_1[R^*] + k_q[B^*][R] - k_2[R^*]^2 \tag{3.13}$$

where k^R_{TET} is the rate constant for TET in the two component rubrene/PQ_4Pd system measured previously. The appearance of $[B^*](t)$ in Equation 3.13 reveals why the effort to generating function approximating it was so important.

As with Equation 3.12, Equation 3.13 also fails to account for decay due to heterogeneous TTA. To address this, solutions to 3.13 were fit to traces of M_R, *but only using the later frames of* M_R *where* M_B *had already decayed well below detection* ($\sim$70 μs onwards). Similarly to BPEA, most constants in Equation 3.13 were at this point already known, with Λ_R the only fitting parameter needed. As a result, this fitting procedure essentially back–extrapolated a deliberate underestimate of $[R^*]$ using an ODE that was missing a variable but uniformly negative term (Equation 3.13, missing a term in $[R^*][B^*]$). This underestimate instead represented the required values of $[R^*]$ to explain the UC emission at long times purely through homogeneous TTA, using $M_R = \Lambda_R[R^*]^2$. The emission at these times was attributed with confidence to homogeneous TTA, as there was no M_B signal at these times and so vanishingly small $[B^*]$. Later comparison of calculated $[B^*]$ and $[R^*]$ values in this period indicated that R^* outnumbered B^* by at least 30:1, confirming that heterogeneous TTA was probably a negligible process in that timeframe.

With all of $M_R, [B^*], [R^*]$ and Λ_R now known, Equation 3.11 could then be used to find Γ. Figure 3.38 shows an example of how the experimental M_R was matched to homogeneous and heterogeneous components. Practically this meant that the difference between the observed emission and the back–extrapolated homogeneous R^* emission

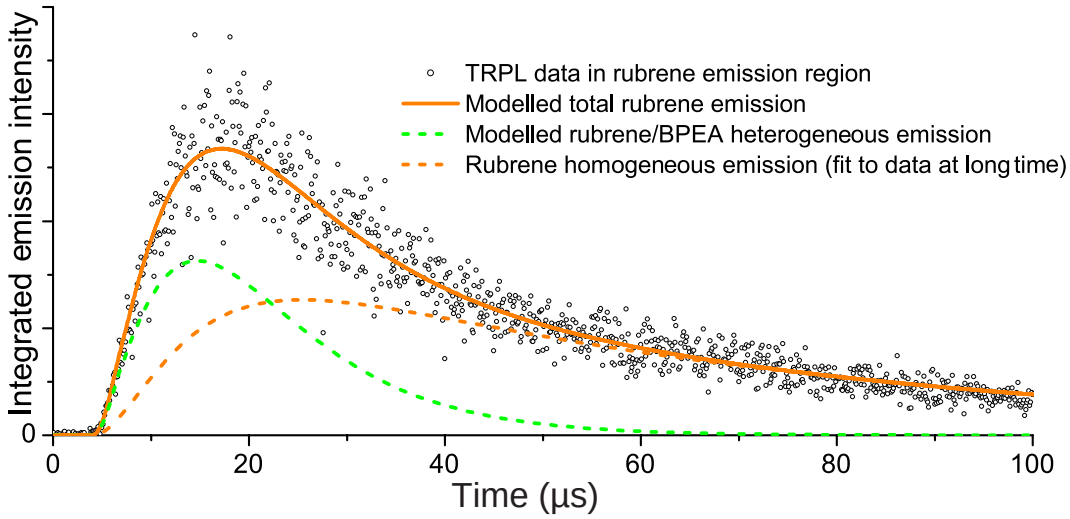

FIGURE 3.38: Typical achievable fitting of rubrene emission TRPL using Equation 3.11. Rubrene emission from homogeneous TTA was first fit to the data at long times (when heterogeneous TTA must be negligable due to low $[B^*]$) using the values of $[R^*](t)$ generated from Equation 3.13, and then varying the parameter Λ_R. The parameter Γ could then be determined by matching the sum of contributions from the homogeneous and heterogeneous TTA processes to the total emission.

was attributed to heterogeneous TTA. Since values of $[R^*]$ and therefore also $\Lambda_R[R^*]^2$ were identified as underestimates, this meant that the necessary values of Γ needed to make up the difference in M_R are conservative overestimates. That is, heterogeneous TTA is likely less active than the values from this analysis would otherwise indicate.

From this entire process, the values of Λ_R and Γ were found to vary significantly in different traces. This was as expected, as they depend on hardware settings that changed in different scans. Instead, by identifying that these hardware settings and rubrene emission Φ were identical for both mechanisms in the same scan (since both result in fluorescence from rubrene molecules), the ratio of these fitting constants could be used to compare properties of the homogeneous and heterogeneous TTA channels. Indeed, the molecular parameters included in Λ_R and Γ are given by combining Equations 3.11 and 2.4, which allows their ratio to be expressed as:

$$\frac{\Gamma}{\Lambda_R} = \frac{(k_2\eta)_{RB}}{(k_2\eta)_{RR}} \tag{3.14}$$

where the components of the product $k_2\eta$ are as previously defined, but with different values for homogeneous (RR) and heterogeneous (RB) TTA. This ratio worked out to be the same for scans at different magnetic fields, with an average value of 0.61 ± 0.04 ($\pm7.6\,\%$), and 0.50 ± 0.07 ($\pm14\,\%$) for the deuterated hybrid system.

Although not measured in this study, the value of η for rubrene has been reported as $\sim$0.6 in the same solvent and with the same sensitiser.[151] This study also reported the value of k_2 that was used for comparison earlier. These values allowed the absolute value of $(k_2\eta)_{RB}$ to be determined as $7.35\times10^7\,\mathrm{M^{-1}s^{-1}}$, with a similar $6.0\times10^7\,\mathrm{M^{-1}s^{-1}}$ for the deuterated system (using $(k_2\eta)_{RR} = (2\times10^8)\times0.6$ for both).

Following the arguments of Schmidt and Schulze,[173] chemical intuition can also be used to estimate the heterogeneous k_2. The authors of that study claimed that the heterogenous k_2 should be similar to either k_q or half of the k_2 of BPEA (here taking the role of sensitiser), as both TET and TTA come about through bimolecular collisions of B^* and R or B^* and R^*.[166,173] Indeed it was found that k_q ($1.2\times10^9\,\mathrm{M^{-1}s^{-1}}$) was similar to half the k_2 of BPEA alone ($(6.5\pm2.5)\times10^9\,\mathrm{M^{-1}s^{-1}}$), presumably as a result of the faster collisions of two highly mobile emitters in k_2, compared to one mobile and one immobile species in k_q. This approximation of heterogeneous k_2 also compares well to the averaged k_2 of separate homogeneous BPEA and rubrene UC systems.

Using the approximate heterogeneous k_2 along with $(k_2\eta)_{RB}$ from the Γ/Λ_R ratio resulted in a value of heterogeneous η of just 0.06, corresponding to highly inefficient collisions compared to homogeneous rubrene. No published value of η for BPEA in solution could be found for comparison to the alternative homogeneous TTA process. An alternate approach to separating $(k_2\eta)_{RB}$ was to keep η roughly the same for heterogeneous and homogeneous rubrene emission, although this generated values of heterogeneous k_2 slightly lower than that of homogeneous rubrene — which does not seem consistent with the faster diffusion of BPEA. In either case, it seems that shuttle accelerated TTA of highly efficient homogeneous rubrene TTA is a better use of excitons than either inefficient (low η) or slow (low k_2) heterogeneous TTA.

Restating the above conclusion: although the individual values of k_2 and η for heterogeneous TTA could not be rigorously separated, the low value of the product (even for this stated overestimate of heterogeneous TTA) means that this process must be "bad" in some way. It also means that the majority of the previously observed hybrid enhancement effect should be attributed to the simpler exciton shuttle mechanism, justifying (though with somewhat circular logic) the use of Equations 3.12 and 3.13. This was a surprising result, although it is in retrospect entirely consistent with traces like those shown in Figure 3.38. If heterogeneous TTA was "good", significantly greater heterogeneous emission would be expected in the time region where [R*] and [B^*] are both large ($\sim$15 μs in Figure 3.38), but instead the contributions from the different mechanisms are (only) about equal.[166]

Apart from fundamental interest, this result also has significant implications for future designs of advanced UC materials, and in particular those without solvents to mediate

exciton transport through simple diffusion. It is the author's intent to prepare this result for future publication.

3.3.4 Photostability of UC Systems

During all TA experiments the CW absorption spectra of the samples were periodically retaken to check for sample degradation. This was done in direct response to the particularly large pump and probe powers used (across all wavelengths at once), although no changes in the CW absorption were observed over the several hours that each sample was measured. The long term photostability of the UC system components was not only important for the validity of these experiments, but is also a key factor in the longevity and economic feasibility of UC applications. In PV devices the UC components must survive extended solar exposure at elevated outdoor temperatures, while TTA may be a mechanism of device degradation in some blue emitting OLEDs. Observations regarding the photostability of the UC systems (mostly qualitative) are collected in this section — from the work in this chapter as well as elsewhere.

In contrast to the discussed TA samples, a stock solution of rubrene left in the sample preparation glovebox was found to significantly decay over the several days between preparation and use. At this time the glovebox had been newly installed and suffered several early overnight faults, and so the presence of trace oxygen could not be excluded. Critically, its internal lighting was also left on, illuminating the rubrene stock solution. Permanent bleaching of the other emitter stock solutions was not observed once the glovebox oxygen level stabilised, and also because aluminium foil was subsequently used to shield the stock vials from illumination. Stock solutions exposed to atmosphere but stored in the dark have been used routinely in preparing functional UC solutions, which confirms that the observed singlet bleaching of rubrene is somehow photoactivated.

When a UC sample was made using this rubrene stock with PQ_4Pd, the first clue that something had gone wrong was that the rubrene peak absorption was about one tenth of the expected value based on the stock solution preparation. When the spectra from this sample were analysed, the UC emission was very small and slow, while the value of k_{TET} was very large compared to the other rubrene samples at $5.5\times10^8\,\mathrm{M^{-1}s^{-1}}$. It is possible that the rubrene had oxidised to form some new powerful quenching species that was not accounted for in determining k_{TET}.[250,251] By monopolising supply of excitons from S^*, this quenching species would also explain the poor UC performance of the sample, even if oxygen had later been purged from the glovebox. A similar explanation was given for the strange kinetics of partially deuterated perylene UC systems in the previous chapter. Similarly, complete cessation of UC was repeatedly observed in CBPEA UC

samples (prepared for magnetic field studies in the next chapter) when the rubber sealing O–rings eventually failed due to swelling on exposure to toluene vapours.

While the effects above can be explained by reactivity of singlet excited rubrene with oxygen, other researchers in the group had also reported anecdotes of rubrene emission photobleaching, even for the glass sealed samples prepared in Chapter 4. While some oxygen may have been present at the time of sealing, this was expected to be quickly consumed through reactions with R^*. These reports strongly suggested some form of anoxic photobleaching, and the effect was most pronounced for the high pump powers of the action spectrum instrument and in samples with immersed silver beads as a back reflector to the UC system (providing interstitial regions of concentrated optical excitation).[249] Bleaching of rubrene emission from both direct (singlet) excitation and indirect (triplet) sensitisation was observed. No such effects were observed for the perylene UC systems in Chapter 2, adding to perylene's reputation as a particularly durable dye.

BPEA in particular was found to be extremely susceptible to these photobleaching effects, possibly due to its reactive triple bonds (unique to this emitter) or tendency of its anthacene core to dimerise. In a magnetic field experiment on a PQ_4PD and BPEA system under strong S excitation (∼300 mW of CW 670 nm), UC emission signal could be seen to drop steadily over a number of minutes, eventually ceasing completely (see Figure 4.9). This was assumed to be due to poor degassing, but was investigated further by transferring the entire sample back into the inert glovebox before opening. Upon adding a small amount of a rubrene stock solution to the dead UC system, rubrene UC was found to immediately commence — indicating that oxygen had not been present as the BPEA UC solution had bleached. This demonstrates that an oxygen–free photobleaching mechanism exists at least for B^* triplets, as in this experiment the BPEA was excited indirectly with a triplet sensitiser. UC systems based on rubrene and perylene also exhibited signal decay in this magnetic field experiment, although over much larger timescales consistent with O–ring failure.

Once TA spectra had been collected, further investigations were performed on the degassed rubrene and BPEA UC systems. Like BPEA, rubrene in a UC system with PQ_4Pd was also found to photobleach under the strong S excitation in an oxygen–free sample, indicating some fragility of the rubrene triplet state. The previous observation of rubrene photobleaching on direct excitation in the sealed action spectrum samples indicated that its singlet excited state was also fragile.

On the basis of the above observations, additional tests were performed to try to understand the mechanism of photobleaching in BPEA and rubrene UC systems. Fragility of the BPEA singlet excited state was confirmed by exposing a degassed portion of the BPEA stock solution (with no sensitiser) to the full power of the TA spectrometer

probe beam, as well as the maximum output of the pump beam OPO. This pump beam wavelength (450 nm) fortunately happened to coincide with absorption features of both BPEA and rubrene. Over about two hours the absorbance of the BPEA sample dropped to about half of its original value, with an exponential looking decay shape. At this point it could be claimed that both BPEA and rubrene are destroyed by sustained excitation to their singlet or triplet excited states.

As the solutions were prepared and the equipment already booked, the next obvious step was to see what happened in the hybrid system. As rubrene is lower in energy in both its singlet and triplet levels, it was expected that it would quench and protect the directly excited BPEA singlets (and sensitised triplets) and therefore be destroyed more rapidly. To investigate singlet bleaching an unsensitised 1:1 BPEA and rubrene solution was prepared and subject to maximum pump and probe illumination for several hours. CW absorbance spectra were taken at half hour intervals to track the concentrations of the components. During this time the CW sample fluorescence could be seen to match the colour of rubrene, although a small amount of BPEA emission (with the same spectrum as the TRPL in Figure 3.36) was also detected with a fibre spectrometer.

Figure 3.39 shows the time evolution of the absorption in this sample, and the surprising result that the rubrene remained completely intact while the BPEA was significantly bleached. Although the BPEA was more strongly absorbing at the pump wavelength, its own emission overlapped strongly with the absorption of rubrene (allowing for sequential emission and reabsorption), and the CW fluorescence indicated that most of the escaping emission did in fact come from rubrene. It was also expected that singlet excitation could transfer from BPEA to rubrene through Forster resonance, or collisional quenching as for TET in the hybrid UC system. Therefore, while the eventual decay of the BPEA was unsurprising, the anomalous durability of the rubrene (while also shouldering the excitation from BPEA) could not be explained. This result is therefore truly perplexing, and a coherent explanation has yet to be developed.

Even more baffling, when the TA hybrid UC samples were exposed to the same extreme S excitation at 670 nm, their absorption features evolved with time as shown in Figure 3.40. Here, the rubrene triplet excited state was once again protected by BPEA by some unknown mechanism, while a small new absorbance feature steadily grew in at around 500 nm. When examined in isolation this new absorbance feature was found to be a single asymmetric blob, and not similar to the spectra of either BPEA or rubrene. It remains unknown what this feature corresponds to, or how it arises.

In all of the experiments above, the sensitiser was always left completely intact as the emitters bleached. This was contrary to a previous study by a Dr Tim Schulze, where both components of a perylene and palladium meso-tetrakis(3,5-di-tert-butylphenyl)

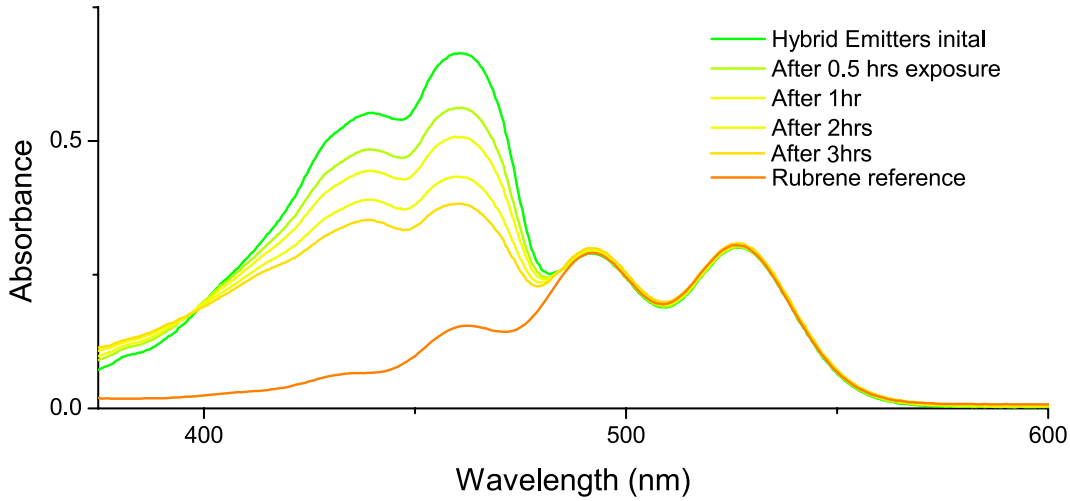

FIGURE 3.39: Absorption spectra of an unsensitised 1:1 BPEA/rubrene solution after exposure to maximum excitation power from the pump (450 nm) and probe beams.

porphyrin system were found to decay in tandem under sustained excitation.[173] This study was performed in a silicone oil solvent under constant vacuum pumping to definitively remove oxygen, but was monitored through decay of the UC emission intensity rather than the absorption of the components. However, this study made extensive use of the low efficiency regime assumption (Equation 2.7) in calculating changes in $[S]$ and $[E^*]$ from I. This assumption may have invalidated its key finding — that the component decay occurred in tandem and was bimolecular — considering the high excitation powers used and the rapid rollover to high efficiency observed for perylene in the previous chapter. Any unimolecular sensitiser decay in that study was also probably assisted by slow quenching by the dilute emitter, as that study used $[E]$ to $[S]$ ratios no

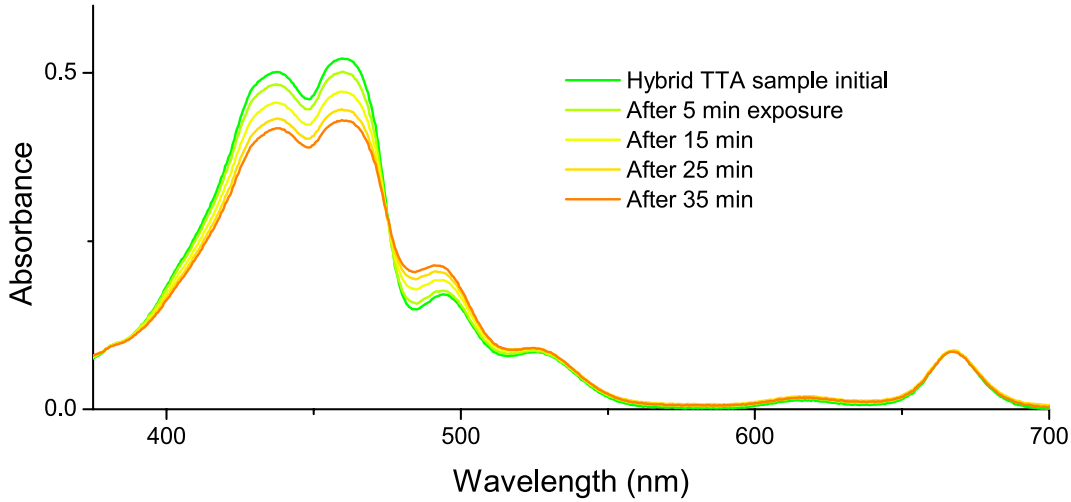

FIGURE 3.40: Absorption spectra of hybrid UC system after exposure to ~300 mW 670 nm fibre laser. Note that the absorptions from rubrene (525 nm) and PQ_4Pd Q band (670nm) do not decay, but an isosbestic point is visible at 475 nm, implying the growth of a new absorption in that region.

greater than 1:5 (compared to 1:10 or greater in this work). It is even more confusing then why the same argument (that a large concentration of quencher should protect a compound from photodamage) does not successfully predict the behaviour of the BPEA and rubrene hybrid system.

3.4 Outlook and Further Work

3.4.1 General Comments

Despite the challenges encountered in data processing and analysis, the TA+TRPL method was deemed a success in measuring the properties of a range of common UC emitters. The key values extracted from the preceding sections are summarised in Table 3.1, with indicative average values reported for $[S^*]_0$ and maximum $[E^*]$ for each system. Although they are discussed at relevant points in the preceding sections, reference values have not been included in Table 3.1. This is because in most cases the best reference values that could be found were of similar but not identical systems, such that out of context comparison be avoided.

Comparing the values of k_1 and k_2 for the different emitters, there are no particularly strong performers, although rubrene is identified as having a particularly low k_{TET} and k_2. The low values of k_1 here for perylene are also somewhat tempered by the much higher values in the previous chapter and elsewhere. Otherwise, this uniformity of rate constants means that the common uncomplicated approach to selecting UC systems, based simply on matching the spectral properties of S and E, will usually result in decent overall efficiencies. It is the author's intent to prepare these results for future publication.

TABLE 3.1: Constants and Fitting Parameters for UC Systems

Method	CW Absorption		TA and Phosphorescence			TRPL and ODE Fitting		
Result	$[S]$ (μM)	$[E]$ (μM)	$[S^*]_0$ (μM)	$(k_s + [E]k_{TET})$ ($\times 10^4\,\mathrm{s}^{-1}$)	k_{TET} ($\times 10^9\,\mathrm{M}^{-1}\mathrm{s}^{-1}$)	$[E^*]_{max}$ (μM)	k_1 ($\times 10^2\,\mathrm{s}^{-1}$)	k_2 ($\times 10^8\,\mathrm{M}^{-1}\mathrm{s}^{-1}$)
TPTBPt	3.4		2.8	2.7±0.1(= k_s)				
OEPPd	11		5.5	11.8±0.7				
PQ_4Pd	8.4		7.9	2.34±0.06				
TPTBPt & h-perylene	3.7	120	3.1	57±1	4.2	2	4.5±0.5	69±5
TPTBPt & d-perylene	3.7	115	1	56±1	4.6	0.7	4.9±0.2	216±7
PQ_4Pd & perylene	9.1	124	5.6	4.3±0.3	0.16	1.4	5±1	123±12
OEPPd & h-DPA	11	340	5.5	54±2	1.4	3.5	76±1	18±4
OEPPd & d-DPA	11	340	6.4	55±5	1.5	3.5	19±4	48±7
PQ_4Pd & h-rubrene	8.7	234	2.5	8.7±0.4	0.27	1.2	89±4	2.0±0.1
PQ_4Pd & d-rubrene	8.6	150	2.3	6.0±0.4	0.25	1.0	77±5	1.9±0.2
TPTBPt & rubrene	3.7	36	3.2	7.3±0.2	1.27	1.3	90.0±0.7	2.1±0.3
PQ_4Pd & h-BPEA	9.1	164	2.0	13±1	0.68	1.1	123±31	65±24
PQ_4Pd & d-BPEA	8.3	176	1.4	14±1	0.65	0.75	103±33	104±14
Hybrid systems		$[B]$ and $[R]$			for total $[E]$	$[B^*]$ and $[R^*]$	$k_q(\times 10^9\,\mathrm{M}^{-1}\mathrm{s}^{-1})$	$(k_2\eta)_{RB}$
PQ_4Pd & h-hybrid	7.9	129 & 77	2.6	13.7±0.7	0.55	0.7 & 0.3	1.2	0.7
PQ_4Pd & d-hybrid	8.6	118 & 48	2.6	12.7±0.7	0.62	0.6 & 0.2	1.64	0.6

To engineer better UC emitters, some lessons can still be drawn from the comparison of rubrene to the other emitters. As previously discussed, the low values of k_2 and k_{TET} of rubrene are attributed to its steric bulk, making it slow moving and unable to closely approach other molecules. This may in part be a blessing though, as a recent study has suggested that the slow rotational diffusion of rubrene is responsible for its large value of η, while unpublished molecular dynamics simulations indicate that the mechanism for this may be the substituent paddles guiding rubrene collisions into favorable orientations for TTA.[166,246]

On the other hand, quenching and TTA with smaller emitters like perylene and DPA was much faster, although their values of η are not widely reported (for perylene a single report places this close to 1).[187] The challenge with using these smaller PAHs is that their smaller aromatic systems result in higher energy absorption and emission features, which may be unsuitable for specific applications such as enhancing low bandgap PV devices. In perylene this can be addressed by adding imide groups to extend the chromophore and redshift its spectra, but necessarily adds to the steric bulk.[252] A promising recent trend in this regard is the use of controlled size semiconductor crystal "quantum dots" as sensitisers, an approach which may in future be extended to provide customisable yet compact (and fast diffusing) alternatives to PAH emitters.[253–257]

Restricting focus to the PAHs though, it seems that η is the final remaining emitter parameter where headroom may exist to design or discover significantly improved UC systems. Significant attention is given to η in the next chapter. Although this parameter was not measured in this study, to do so would be a natural extension of this work. With the TA method able to determine $[S^*]_0$ here, and even $[E^*]$ in future iterations, this approach would likely provide a more straightforward method to determine η than the published methods used for rubrene and perylene.[162,187]

Extending the work on d-perylene from the previous chapter, this work also shows that deuterated rubrene is also enhanced by a lower k_1. Although inconclusive, the results also suggest that BPEA might also benefit in the same way. For DPA, the large change in k_2 throws doubt on the observed change in k_1. It is the author's intent to reconfirm these results with smaller confidence intervals, and prepare them for future publication

3.4.2 Improvements to the Spectrometer

While the inability to resolve $[E^*]$ directly using the TA spectrometer was disappointing, several modifications are presented here that could significantly boost its measurement sensitivity and reliability for future studies that use similar methods. Achieving this confident and direct measure of $[E^*]$ would obviate several of the approximations and

significant effort needed to model the TRPL emission — for example, all instances of Λ as a fitting parameter would become unnecessary. This improved future measurement capability would be particularly valuable in monitoring the decay of $[R^*]$ and $[B^*]$ in the hybrid system.

The first and simplest of these improvements would be to use additional shots acquired on the CCD, as well as software averaging for each time point of each spectrum. In contrast single shots were used throughout this pilot study, although this may have been a blessing in light of the suspected camera phosphor saturation. Additional shots or averages on the CCD may have exacerbated this problem. Nonetheless, the high repetition rate of the pump laser should in future allow signal to noise ratios to grow rapidly at a low additional time cost.

In determining k_{TET} for each system, only two measurement values were used. In contrast, typical Stern–Volmer quenching studies often use four or more concentration points (really, as many as is practical) to determine the quenching rate constant from their slope.[70] This was not performed here, but doing so would lend significant additional statistical weight to the reported quenching rate constants.

No magnetic field effects were detected in the experiment, although this had the silver lining of ultimately allowing the different measurement sets to be averaged and uncertainty determined. In future attempts, much stronger magnetic fields could be applied to determine its effects on k_1, k_2, and η. The time-resolved nature of this experiment would also allow investigation of these effects right after the pump pulse, while any spin polarisation generated upon S excitation undergoes decoherence.[258–260] Direct attempts to build platforms capable of this kind of measurement are presented in the next chapter.

All spectra in this study used exactly the same timebase for the frame interval and total time window examined. For some systems this happened to be an appropriate choice, but for rapidly decaying systems this made fitting of exponential decay rates and amplitudes difficult — as the signal had decayed below detection after only a few tens of frames. This effect likely contributed to the large uncertainties for the BPEA system. For slowly decaying systems, reliably fitting of k_1 usually requires very long scans so that the signal baseline level can be appropriately fit. In this study, the measurement of signal levels before the pump pulse avoided this problem, but scans that extend out to complete signal decay would have lent further credibility to the fitted rate constants. Additionally, using very long times in the UC emission scans may allow the use of the much simpler mixed kinetics model in their fitting. Instead of (or in addition to) changing the camera settings, larger $[E]$ could also be used to accelerate the TET kinetics of these systems, although fine tuning would be necessary to find the optimum balance for each setting.

Due to the shape of the probe lamp spectrum (shown in Figure 3.5), some areas of the resulting TA spectra had much higher or lower sensitivities. Using a lamp with a flatter output profile would improve the average sensitivity of the instrument and avoid "blind spots',' such as that found below ∼400 nm (visible in Figure 3.6). Although the manufacturer specification of the probe lamp used in this study (Energetiq LDLS) was exceptionally flat, the transmission and reflectivity cutoffs of the reflective couplers and fibres used to direct the probe beam likely contributed to the low probe intensities below 400 nm. Using a single optical table and freespace propagation would have avoided this problem, but in this case fibres were necessary to move the beam on and off the pump laser trolley. The fibres and couplers used in this study had originally been purchased for a different purpose, which is why their low transmission at short wavelengths had not been considered before measurements commenced.

In additional to generally greater probe beam intensities the probe beam could also be filtered to generate TA scans of individual wavelengths; increasing sensitivity, but at the cost of greatly increasing the amount of time required to build a landscape of the TA features. Rapid throughput was identified as one of the key advantages of the broadband TA method used here, in complement and contrasting to to high sensitivity single wavelength measurements available through other methods.

While the drift of the probe beam power was addressed in the fitting procedure, it may be possible in future to redesign the spectrum acquisition procedure so that it can be addressed in hardware. A chopper wheel synchronised to the pump beam repetition rate and set to block every second pulse would achieve this by interleaving the probe-only and probe-with-pump transmission spectra. With the spectra for calculating absorbance collected in pairs rather than in sequential large blocks, this would eliminate the effects of probe power drift in the experiment. Although these pairs of spectra would only be able to generate ΔA (from the change in transmission), this could easily be added to an independently collected CW absorbance spectrum (A_0) to generate the full TA spectra.

As mentioned previously, the concentrations of TA samples must be optimised for successful detection of transmission as well as reasonable UC operation. While the balance was struck about right in this study, the use of thinner sample cells will always improve the final outcome. The 1 mm cell was the thinnest available for use with air sensitive solutions, although yet thinner cells would allow the use of more highly concentrated and still weakly absorbing samples. This would hasten the rates of TET and TTA, while still maintaining an approximately uniform excitation density across the sample.

Although TRPL was measured using this setup, it was not designed with this in mind. The long distance between the sample and the collection fibre was instead chosen so that isotropic emission from the sample *would not* reach the detector easily. Instead,

only the collimated transmitted probe beam would be able to travel this distance and be effectively collected for detection. This explains why the signal level in the TRPL scans was so low, despite maximum camera sensitivity settings being used. If used to collect TRPL spectra in future, removing the collection fibre from its coupler and instead mounting it directly against the thin edge of the sample cuvette would allow it to collect an enormous amount of the UC emission just by virtue of its larger subtended solid angle, without the camera or spectra becoming saturated by the (perpendicularly propagating) pump and probe beams.

Although not attempted here, the presence of oxygen in these samples could potentially be monitored by its long wavelength phosphorescence.[261] Being able to quantitatively check the oxygen concentration of different samples would allow the variability in perylene k_1 (for example) to be attributed to either variability in sample preparation or instead as inherent the measurement instrument and procedure.

Finally, although the porphyrins used here are advantageous in applied UC studies and devices, more appropriate sensitisers may exist for this kind of fundamental study. In particular, the long wavelength induced absorptions of the sensitisers here were able to mask any absorptions from $[E^*]$, while the ground state bleaches for S also overlapped with those expected for E. Sensitisers that absorb far in the UV could be used, and although this would result in TTA downconversion, the values found for k_1, k_2, and η would hopefully be the same. Such short wavelength absorbers would also hopefully have their own induced absorptions also at short wavelengths, giving a clear window for detecting E^* absorbance features. Customisable semiconductor quantum dots once again present an opportunity to develop such ideal sensitiser for fundamental studies.

3.4.3 Determining the Hybrid Mechanism

The work performed on the hybrid UC system would have been significantly more persuasive and easier to analyse if both $[B^*]$ and $[R^*]$ had been directly measurable from TA spectra. Unlike the approach required here, this would have immediately allowed the contribution to M_R from homogeneous and heterogeneous TTA to be separated by again fitting Λ_R and Γ. It may have also made the approximations in Equations 3.12 and 3.13 unnecessary, and allowed for formal inclusion of a term in $[R^*][B^*]$ and fitting to determine the heterogeneous k_2 directly. This would then also lead to a single reportable value for η_{RB}. Nonetheless, the work here still presents a compelling case for the exciton shuttle mechanism being responsible for UC enhancement in this hybrid system. Heterogeneous TTA occurs simultaneously, but with a surprisingly low efficiency or rate constant, and should be avoided — at least for the solvated BPEA and rubrene pair.

To further investigate the hybrid effect, another hypothetical UC system is proposed for study, although its components are not identified. By deliberately mismatching the energy levels of S and one of the two emitters, it may be possible to significantly diminish TET from S to the lower energy emitter. As a result, the lower energy emitter (corresponding to rubrene in this study) would only be populated by quenching the higher energy emitter (here BPEA). The resulting delayed emission from the lower energy emitter would be dominated by heterogeneous TTA at early times, allowing for more isolated study of this process. This may be achieved for a system such as OEPPd with perylene and rubrene, although TET between OEPPd and rubrene is unstudied as those two components together would at best produce TTA downconversion. Additionally, systems in which the lower energy emitters are separated and immobilised (such as in a dye-pendant polymer) would deactivate homogeneous TTA and allow for a more targeted study of the activity of emitter exciton shuttling and heterogeneous TTA.

Finally, spin resonance techniques explored in the next chapter may someday be able to directly detect B^*, R^*, or even the encounter complex formed by collisions of the two. The kinetics of the homogeneous and heterogeneous encounter complexes would present an even more direct window onto the balance between these processes. Similar work has already been demonstrated for the triplet pairs generated in singlet fission systems, although these systems benefit from being able to generate a much higher concentration of triplet pairs (1 per photon that stimulates fission, compared to 1 per pair for TTA).[144]

3.4.4 Photostability of UC Systems

While the photobleaching of UC emitters observed in this and other projects is concerning for future UC applications, the fact that the sensitisers were uniformly left intact is relieving — as these are usually the most expensive components. Nonetheless, the different behaviour of the rubrene, BPEA, hybrid, and perylene UC systems seems to indicate that a range of photobleaching mechanisms may exist in different UC systems. As a result, each combination may have its own unique longevity based on its components, concentrations, and specific excitation strength. For highly fluorescent emitters like perylene this is predicted to be less of an issue, as the near unity quantum yield for fluorescence means that there are not many other active processes that can occur from the singlet excited state. This does not take into account decay from the triplet state though, which has been observed for both BPEA and rubrene. Oxygen will also always be an issue for UC systems, and so significant research effort is currently being expended to identify ways to easily exclude it in semisolid materials.[70–77]

For UC applications this may not be as damning a conclusion as it initially appears. A real PV enhancing module will typically be placed behind the cell, such that the cell itself acts as a filter for high energy photons. This is in contrast to parts of this study and the one by Schulze, where 450 and 532 nm photons may have had sufficient energy for emitter bond destabilisation to occur, indirectly leading to cleavage. The excitation density in real solar applications will also be significantly lower than in either study, unless considerable optical concentration is used. [262] These factors indicate that real UC devices may still be adequately robust, as long as oxygen is rigorously excluded.

To conclusively demonstrate their feasibility, an experimental study on the real ageing of PV shielded, perfectly degassed and permanently sealed UC samples under direct or simulated sunlight is necessary. Some planning towards this experiment was undertaken as part of this project, and the use of CW absorption spectra for monitoring along with remote datalogging of actual sunlight dosage (using the current from a PV cell) appears to be a viable and low effort way to carry this experiment out over timescales spanning several months to a year. The original concept of the action spectrum technique, once troubleshot for different UC systems, would also be a rapid way to periodically check the Φ_{TTA} of these systems after specific amounts of solar exposure.

The decay of the rubrene BPEA hybrid system also gives one last clue on its mechanism. The rapid decay of the BPEA and simultaneous protection of the rubrene may be a result of heterogeneous TTA providing energies to the BPEA sufficient to break it up, with a rate that competes with rubrene singlet emission and other outcomes of TTA. This cleavage might occur through destabilisation the BPEA triple bonds, potentially even while the excited emitter pairs are still part of a TTA encounter complex. This hypothesis does not explain the singlet excited state fragility of R and B, nor the protection effects enjoyed by rubrene in the mixed systems. It is nonetheless consistent with the evidence that the heterogeneous collisions probably have low η, and that when sensitised together BPEA is bleached while rubrene is not.

In the case where heterogeneous TTA might have a large rate constant but a low probability of emission, the energy accessed from TTA has to go somewhere. A triplet pair state for TTA has been suggested to explain this missing energy in the past, but emitter destruction and UC aging may be a competing outcome. Similar mechanisms are proposed for the emissivity decay in some OLEDs, where TTA may again provide sufficient energy to activate chemical reactions in the device. [87,111–113] If destructive TTA is indeed the root cause of device and UC ageing, then the tabulation of η for different UC emitters and studies to understand the molecular properties that determine it (already good ideas in their own right) should become urgent priorities amongst the UC research community — and are already being addressed by leaders in the field for OLEDs. [228]

Chapter 4

Towards Magnetic Resonance

"Because great acts are all made up of small deeds, the wise man attempts nothing very big."

—Narrator, *Saiyūki (Monkey)*, NTV 1978–1980

In this chapter, magnetic fields are revisited as a way to influence and investigate the annihilation process that underpins upconversion. Static magnetic fields are shown to affect upconversion fluorescence intensity, modulating the efficiency of the annihilation step. Resonant fields were anticipated to be able to alter the population distribution of the three triplet exciton spin states, thus revealing the relative importance of each in the annihilation event.

Several attempts are detailed towards building spectrometer platforms capable of measuring magnetic field effects on fluorescence intensity, as well as magnetic resonance *via* optical, electrical, or microwave detection. Specific design choices are justified, and promising early data presented. Despite (and sometimes because of) failure to observe resonance, these experiments provide valuable direction for future experimental efforts, as well as some clues regarding the nature of the triplet exciton spin.

Finally, a less ambitious set of experiments was performed and static field effects once again shown to impact steady-state upconversion fluorescence. Resonant signal remained elusive in this attempt as well, but a discussion of simulation and modelling of earlier results provides some valuable insight on the role of spin states and emitter pair orientation in the triplet-triplet annihilation process.

4.1 Annihilation Efficiency and Spin

While the preceding chapters have explored the importance of emitter k_1 and k_2 to upconversion efficiency, observant readers will note that spin — the title topic of this document — has not been required to explain the role or size of either. Instead, the main conclusions drawn were that k_1 can be controlled by tuning vibronic coupling between the triplet and singlet states, and that k_2 seems to be largely determined by the size and mobility of emitter molecules in solution.

Along with k_1 and k_2, the third key emitter parameter that determines the efficiency of UC systems is η; the probability for second order decay events to populate an emissive E^* singlet state. Since this is the best possible outcome of TTA, η can also be thought of as the efficiency of the TTA step, embedded as a factor in the overall UC efficiency. In the limit where all triplet excitons decay in second order processes this would also make η the limiting efficiency of the overall UC process, although this interpretation is complicated by the possibility for excitons to survive non–emissive TTA and undergo emissive TTA in subsequent collisions. Under any definition, η is the parameter for which spin is understood to be a critical factor, but is also the least well understood and least directly studied of the three.

Part of the challenge of optimising η is that, like k_1 and k_2, it is difficult to measure and not commonly reported. As a result there is no clear direction on what kinds of molecular properties may contribute to high or low values, and there remains a pressing need for systematic tabulation of all three parameters for common and novel UC emitters. Separate but complementary to this top down approach, a major aim of this research project was to investigate the fundamental principles and molecular structural properties that determine η. This bottom-up understanding would allow for identification of means by which η may be rationally optimised, either by modifying the emitter molecules themselves or their environment.

4.1.1 Outcomes of Triplet Interactions

In order to visualise the TTA process, an "encounter complex" theory of triplet interactions is commonly employed for solution based UC.[122,162] Similar to the transition state in reaction dynamics, the encounter complex forms reversibly from collisions between pairs of E^* and represents an intermediate stage in the energy transfer from one to the other. As TTA is a spin allowed process, the spin of the encounter complex depends on the spin states of the participating triplets, and this in turn determines whether the desired formation of an emissive singlet can proceed.

As described in section 1.3.1, the spin states of triplet excitons can be constructed from individual electron spins, and expressed in terms of the emitter molecular axes (giving the "Cartesian" basis set $|x\rangle, |y\rangle$, and $|z\rangle$), or relative to an external magnetic field (giving the "high field" basis set $|1\ \pm 1\rangle$, and $|1\ 0\rangle$). Nine pair states corresponding to variants of the encounter complex can then be constructed by concatenating pairs of elements from within the same basis set. Alternatively, as it arises from the angular momentum coupling of a pair of spin one particles, a third basis set for representing the encounter complex in terms of its total spin can be constructed using the Clebsh-Gordon coefficients — as given by Equation 1.4. This "total spin" basis set also has nine elements, of which only the $|0\,0\rangle$ has a singlet multiplicity and can directly give rise to delayed fluorescence. The overlap between this emissive pair state and any other (prepared in an arbitrary basis set of individual excitons) can be determined using the projection operator. Applying this operator yields the singlet character of the arbitrary pair state, the square of which is taken to be proportional to its probability to undergo emissive TTA.[97,122,123]

Assuming that each of the three specific types of triplet excitons are populated with equal probability, it seems reasonable to conclude that η should be equal to 11% — representing the chance of the $|0\,0\rangle$ pair state randomly forming from the 9 possible collision outcomes. Other collisions would lead to a triplet or quintet pair state formation, which cannot emit without some kind of ISC or other (most likely slow) spin conversion process. While seemingly reasonable, the outcome of this analysis has been shown to be flawed by kinetic experiments that demonstrated a value of $\sim$0.6 for the η of rubrene, as well as CW experiments that show η approaching one for perylene.[162,187,228,263] A deeper consideration of the encounter complex states is required in this context, and in particular the ultimate fate of triplet and quintet pair states.

The implicit assumption used to generate the 11 % limiting efficiency for TTA is that exciton pairs are immediately destroyed upon accessing anything other than the emissive pair state. Like the formation of triplet excitons in LEDs though, "incorrect" pair state multiplicity need not be a loss mechanism in its own right. Conversely, it should not be assumed that TTA from the singlet pair state leads exclusively to emission. If the ageing of BPEA in sensitised hybrid UC samples in the previous chapter does in fact come about through TTA activated bond breaking, it is yet unknown which of the pair state surfaces this reaction occurs on — perhaps even all of them. Nonetheless, dissociation of non–emissive pair states followed by reformation in an emissive configuration (with the same pair partner or another) cannot be ruled out for the mobile UC emitters in solution, and is likely a contributor to the "limit breaking" efficiencies observed for some TTA and UC systems.[67]

In the case of tetracene triplets populated by singlet fission, beats in the delayed emission from subsequent TTA demonstrates that the pair state multiplicity is not even a fixed quantity for particular pairs of emitter excitons. The pair states generated by concatenation of single excitons are themselves not eigenstates of the Hamiltonian in most circumstances, which in this study led to the singlet character of the pairs (and thus the fluorescence intensity) dephasing and rephasing due to the different energies (and thus frequencies) of the components of the prepared states.[264] This result further demonstrates the deficiencies in treating TTA to the emissive singlet as an "all or nothing" event.

Even for exciton pairs that do undergo TTA from non–emissive pair states, there is strong evidence that this is not the end of their role in UC systems. Although they were not observed in the TA experiments of Chapter 3, reported absorptions of emitter triplet excited states show that allowed optical transitions can exist between their lowest triplet excited state (T_1) and higher energy triplet excited states (T_2,T_3, *etc.*).[132,265] For emitters where the energy of the T_2 state does not significantly exceed twice that of the T_1, TTA from triplet multiplicity pair states may proceed to disproportionate energy into one ground state emitter, and one in the T_2 state. As with normal TTA, in which the singlet pair state gives rise to a ground and singlet excited emitter, this is still a spin conserving process for the exciton pair. The existence of optical excitations between T_1 and T_2 then means that reverse processes — decay from T_2 to T_1, radiatively or otherwise — is probably also allowed. This mechanism would allow TTA from triplet pair states to consume two triplet excitons as expected, but also return one back to the population of triplet excitons. This is not a strictly desirable outcome, but it makes the triplet channel for TTA half as lossy as previously assumed. This recycling of excitons was used in part to explain the large reported η of rubrene.[162]

Formation of quintet excited emitters from TTA of quintet pair states, although still spin conserving, is usually discounted on the basis of the large energies needed to access even the Q_1 state.[162,266] Quintet pair states have been recently observed in materials capable of singlet fission, although in this case the energy provided to excite the singlet state is greater than the energies of the individual triplets formed.[144] If they do form from TTA, it is possible that resulting Q_1 emitters could undergo ISC into the excited singlet or triplet states, or undergo non–radiative decay directly back to the ground state. From the density of destination states for the different outcomes of ISC from Q_1, the return of a triplet exciton (as in the formation of T_2) seems the more likely possibility. These potential outcomes of TTA for quintet pair states would make them indistinguishable from either fully lossy (the original hypothesis), half lossy (recycling one exciton), or emissive TTA (singlet excited state) based on the UC fluorescence kinetics alone.

As was performed for the singlet fission system, emitter Q_1 or quintet pair states would give rise to multiple spin sublevel transitions, allowing them to be identified directly in ESR measurements. One of the aims of this work was to therefore develop spin resonance techniques for UC systems; to determine whether Q_1 emitters or quintet emitter pairs do in fact form, and how they then contribute or detract from the overall efficiency of UC systems. Similar studies were also envisioned to determine the presence and role of triplet multiplicity pair states, which were hoped to exhibit different linewidths and couplings compared to the signal from the individual emitter triplet excitons.

If both the triplet and quintet pair states are inactive in UC systems, then the overall efficiency of UC is not limited by the formation of other multiplicity states. This may or may not be the case for the current generation of PAH based UC emitters, but could potentially be engineered in future emitters by tuning both the Q_1 and T_2 states to be energetically inaccessible through TTA.

4.1.2 Measuring and Defining Annihilation Efficiency

4.1.2.1 Measuring TTA Efficiency

Rubrene is one of the few UC emitters for which η has been reported, with a value of 0.6 when used in the same PQ_4Pd UC system studied in the previous chapter.[151,162] In order for the authors to arrive at this value, the overall UC efficiency of a sample (Φ_{UC}) was first determined by comparing the intensity of fluorescence generated by exciting the sensitiser, and by exciting the emitter directly. Standardising the signal from each by the number of photons in the different wavelength excitation pulses and using the known value of Φ_F for the emitter then allowed the ratio of photons in and out to be calculated for UC emission. This was then doubled to give the overall quantum yield of TTA (Φ_{TTA}), equivalent to the ratio of emissive TTA events to pairs of input photons. This value was found to increase with excitation pulse power, with an eventual plateau as the UC system was driven further and further into the high efficiency regime ($k_1[E^*] \ll k_2[E^*]^2$).

Armed with the quantum yields of emissive TTA, the value of η was then determined as a conditional probability. It is the ratio of emissive TTA arising only from emitter triplets that are given to have decayed through second order processes. Excitons that decayed through first order processes would diminish Φ_{TTA}, but were not of interest for this study and had to be excluded. From fitting kinetic traces and using Equation 2.16, the fraction of emitter triplets that decayed only through second order processes (f_2) could be determined for each measurement. While Φ_{TTA} is the ratio of TTA events per

pair of absorbed photons, f_2 is then the ratio of second order decays per pair of emitter triplets. To link these two quantities together, Φ_{TET}, the ratio of absorbed photons to emitter triplets, was assumed to take a value of 100 % and amalgamated into Φ_{TTA}. This makes the combined expression a conservative underestimate of the ratio of TTA events per pair of emitter triplets, as not all of the excitation photons would give rise to emitter triplets in the real system. Finally, Φ_{TTA}/f_2 then gave the ratio of emissive TTA events to second order decays, which was taken to represent η.

Despite differences in Φ_{TTA} for the different scans, η was found to be roughly the same in all cases, indicating that some fundamental property of the system had been derived. The size of this purely experimental value immediately contradicted the notion that spin statistics significantly capped the attainable efficiencies of UC systems. Two possible mechanisms for this limit breaking efficiency were proposed in that report; that both the quintet and triplet pair states were either inactive, or less lossy through recycling.

The revised efficiency limits for TTA in these different cases were then calculated by imagining a set of 18 emitter excitons and tracking their outcomes in 9 TTA pairs. It was first considered that one of these would immediately form the singlet pair state and emit, while the other 5 quintet pairs and 3 triplet pairs would quench both, one, or neither of their participants. In the case where both the quintet and triplet pairs were recycling, this led to an average of 10 excitons (5 pairs) being consumed to produce one emissive pair, and a limiting TTA efficiency of 20 %. The limit from this case was immediately discarded based on the experimental result, as too was the one derived from disabled quintet and recycling triplet pairs (40 %). These results then seemed to imply that the final possibility — that both quintet and triplet pair state formation were disabled, and there was no fundamental limit on η — was the case for rubrene. This conclusion was further justified on the basis of the rubrene T_1 and T_2 energy levels.[162,267]

4.1.2.2 Redefining TTA Efficiency

At this point a subtle but important aspect of the definition for η must be addressed. The use of η in Equation 2.4 implies that it is the average probability of emissive TTA arising from second order decays over the entire timescale of an experiment. Similarly, the values of f_2 from data fitting represent the total fraction of second order decays across the experiment, and therefore so must the η calculated from them. The values of Φ_{TTA} used are also for the average quantum yield of this process over the entire direct and delayed fluorescence events used to calculate it. The upper bounds for TTA efficiency derived from the accounting of excitons above correspond to this average too, but at their core still rely on the assumption that the different emitter pair states form with

the probabilities expected from spin mixing of random triplet excitons. That is, there is still an intrinsic 11 % efficiency limit imposed for individual TTA events, although the average figure is revised upwards when the other outcomes are assumed to be inactive or less lossy. Whether the use of this intrinsic limit is indeed justified is another aspect of TTA for which the role of spin remains poorly understood. This also raises the concern that if the triplet and quintet channels are disabled, it is unclear what other processes compete with emission to actually make η less than 1 for the TTA events. The emitter bleaching discussed in the previous chapter may be one of these processes, but it is not known which surface these bleaching reactions may occur on.

This focus on the average TTA efficiency is understandable, as it is the most readily accessible version of η from experiments. In contrast, emitter pairs where the encounter complex simply dissociates (or never "truly" forms) cannot be easily detected by standard spectroscopic techniques since they result in no change in the final state of the sample (nor emission). Nonetheless it is this "intrinsic" efficiency of emissive TTA, measured relative to individual emitter collisions rather than the average across second order decays, in which the greatest insight for optimising emitter structures may lie. Analogous in form to Equation 2.4, Equation 4.1 defines this alternate η more precisely:

$$I = \Phi \frac{\eta}{2} k_c [E^*]^2 \tag{4.1}$$

where the absolute rate of E^* collisions is given by $k_c[E^*]^2$, and η now represents the probability of success for these collisions rather than for second order decay events.

An illustrative example of why this "per collision" efficiency is more valuable than the "per second order decay" or time average efficiency is a hypothetical emitter for which *every* second order decay results in TTA emission, but most collisions lead to encounter complexes that simply dissociate. Such an emitter would have 100 % experimental efficiency measured relative to second order decays, while the emission efficiencies for specific collisions would be very low. This low intrinsic efficiency would instead manifest in a low value of k_2 in TRPL experiments, as collisions leading to second order decays would be rare. The low k_2 and high η for rubrene may arise from just this kind of scenario — with most collisions simply dissociating, while those that do undergo TTA giving emission with high probabilities.

Comparing k_2 to k_c to determine this alternate η is challenging, as emitter collisions are indistinguishable from normal solute diffusion to standard spectroscopic methods. At present many experimental studies are instead limited to comparing k_2 to the diffusion limit of the solvent (a proxy for k_c), but this does not distinguish between emitters that have low k_2 due to slow diffusion and infrequent collisions, or instead due to a prevalence

of dissociative collisions.[166,268] The formation of the encounter complex itself may be possible to quantify though their ESR or TA transitions, but is also challenging to detect due to its very low concentrations at any specific instant in a UC system.

In contrasting these two versions of η, the question naturally arises: if the average TTA efficiency for a system is high, then why bother pursuing the intrinsic efficiency? The answer to this question goes all the way back to the analysis of overall UC efficiencies in section 2.1.3. While a large average η guarantees that excitons which decay through second order processes will lead to emissive TTA, the low k_2 associated with a low intrinsic efficiency means that emitters will have plenty of time to decay through k_1 processes as well. This means that a significantly higher excitation rate would be needed to access the high efficiency regime for the overall UC process. Conversely, it is difficult to imagine a scenario where a large intrinsic η could give rise to a low average efficiency of TTA, while it would also result in a value k_2 approaching its upper limit of k_c. As such, in the pursuit of large UC system efficiencies, a large average η is a necessary condition, while a large intrinsic η is a sufficient condition.

Having defined and discussed the differences between these two versions of TTA efficiency, the symbol η will be used in this chapter to refer to the intrinsic version, except where explicitly stated otherwise.

4.1.3 Magnetic Field Effects and Spin Pair Eigenstates

Recent and not-so-recent reports have shown that UC fluorescence intensity is sensitive to magnetic fields, along with TET and similar recombination processes for radicals pairs.[128,228–240,269–273] This is not surprising given the magnetically active spin states of the individual triplet excitons and the encounter complex, but importantly provides a new tool for investigating UC systems — and in particular η. Rather than tabulating absolute values of average η for different emitters to look for top down trends (although this should still be done!), the approach taken in this study was to first look for changes in the intrinsic η at different magnetic fields, and build models to explain these relative changes from basic principles. Achieving this outcome would then provide a framework for predicting η in different systems, allowing it to be systematically and rationally optimised for future UC emitters.

Due to the challenge in determining the absolute value of the intrinsic η only relative changes were sought, making comparison of CW fluorescence intensities an appropriate general method of investigation. In the expression for UC fluorescence intensity given in Equation 4.1 it also seemed unlikely that magnetic fields would impact the collision rate or properties of singlet fluorescence, making any observed change attributable exclusively

to η. This cannot be claimed for the alternate version Equation 2.4 presents, as magnetic field effects on the intrinsic η would result in changes in both the average η and k_2.

Similar studies of CW magnetic field effects on UC have been performed by others, both for molecular solids, films, and solutions.[230,231,274,275] In most, an initial increase in emission is observed for small magnetic fields, followed by a decrease at larger fields. Models that adapt the original work by Merrifield on delayed fluorescence in crystals are often employed to explain this behaviour, by attempting to construct the probability of UC emission from the singlet character of the triplet pair states formed.[130,276,277] In these models, the wavefunction for an arbitrary triplet pair is first considered in the basis set of total spin pair states:

$$|\Psi\rangle = \sum_{i=1}^{5} Q_i \,|2\,i\rangle + \sum_{i=1}^{3} T_i \,|1\,i\rangle + S\,|0\,0\rangle \tag{4.2}$$

where the normalised constants Q_i, T_i and S are determined by projection of the appropriate total spin wavefunction with $|\Psi\rangle$. These constants express the quintet, triplet, or singlet character of the particular emitter pair. By including an additional term for triplet pair dissociation these projections can be used to build an expression for η, for a specific pair:

$$\eta(|\Psi\rangle) = \frac{|S|^2}{|S|^2 + |\Sigma T_i|^2 + |\Sigma Q_i|^2 + P_{dis}} \tag{4.3}$$

where P_{dis} is the probability of an encounter complex dissociating before any kind of TTA process can occur.

The next step is to average this η across the distribution of collision types (and therefore types of $|\Psi\rangle$) expected in solution, allowing prediction of how the resulting emission from this distribution will vary in magnetic field experiments. The exact method of doing this is not made explicit in Merrifield's original publications (presumably done by hand), and it is this step where modern attempts frequently introduce misconceptions.[122,123,130] The key realisation must be made that, while every $|\Psi\rangle$ will have specific values of S, T_i, and Q_i, only the set of stationary $|\Psi\rangle$ which are Hamiltonian eigenfunctions will have projections that are constant in time. These eigenstates are the natural set of $|\Psi\rangle$ for which η should be calculated, and can then be averaged across their occupancy at different magnetic fields. This distribution is itself uniform if thermal energies are sufficiently large compared to the energy differences between the eigenfunctions.

To apply this model to later experiments in this chapter, three kinds of spin interactions were identified in order to construct a Hamiltonian for emitter pairs — so that it could be

diagonalised to reveal its eigenstates. These interactions are those within the individual triplets, those between the triplet partners, and between the triplets and an external magnetic field.[278]

By themselves, the emitter triplets states have a small energy level splitting due to the dipole interactions of the two spin $\frac{1}{2}$ particles that couple to make the triplet state in the first place. The spin Hamiltonian for this interaction is given by:

$$\mathcal{H}_0 = \begin{pmatrix} \frac{1}{3}D - E & 0 & 0 \\ 0 & \frac{1}{3}D + E & 0 \\ 0 & 0 & -\frac{2}{3}D \end{pmatrix} \tag{4.4}$$

where D and E are the zero field splitting parameters for the molecule of interest. This Hamiltonian is expressed in the Cartesian basis set, and the fact that this choice makes $\mathcal{H}_0$ diagonal means that the spin wavefunctions $|x\rangle$, $|y\rangle$, and $|z\rangle$ are indeed eigenfunctions in the absence of external magnetic fields. The resulting uniform population of these states is not surprising, as the values of D and E are typically on the order of of hundredths of cm^{-1} compared to several hundreds available at room temperature.[98,279,280] This means that the different triplet states can be validly treated as degenerate in most standard spectroscopic techniques that do not include the use of magnetic fields to separate these states.

In the presence of a strong magnetic field, the energies of the different triplet states become dominated by Zeeman splitting. The relevant spin Hamiltonian instead becomes:

$$\mathcal{H}_B = \begin{pmatrix} +g\mu_B B & 0 & 0 \\ 0 & -g\mu_B B & 0 \\ 0 & 0 & 0 \end{pmatrix} \tag{4.5}$$

where g is the g factor for the exciton (assumed to be isotropic), μ_B is the Bohr magneton, and the basis set has been changed to the eigenstates for high fields, $|1\ \pm 1\rangle$, and $|1\,0\rangle$ — aligned to the direction of the external magnetic field ($\mathbf{B} = B\hat{\mathbf{B}}$). As this Hamiltonian is diagonal, the energy differences between the eigenstates can be seen to depend on the magnetic field strength. As a result these states may not be evenly distributed in situations where the thermal energy becomes small compared to $g\mu_B B$. Nonetheless, as $g\mu_B$ is on the order of $10^{-23}\,\mathrm{JT}^{-1}$, large spin polarisations are not anticipated at room temperature since the accessible thermal energies are over one hundred times larger than the Zeeman splitting for fields as large as 1 T. Indeed, cryogenic temperatures and large magnetic fields are often required to generate and preserve this polarisation, and are routinely used to increase the sensitivity of ESR measurements.[281–283]

The Zeeman contribution can alternatively be expressed in the Cartesian basis set, and is then given by:

$$\mathcal{H}_B = \begin{pmatrix} 0 & -ig\mu_B B_z & ig\mu_B B_y \\ ig\mu_B B_z & 0 & -ig\mu_B B_x \\ -ig\mu_B B_y & -ig\mu_B B_x & 0 \end{pmatrix} \tag{4.6}$$

where the magnetic field is now expressed in components relative to the frame of the molecular axes ($\mathbf{B} = B_x\hat{\mathbf{x}} + B_y\hat{\mathbf{y}} + B_z\hat{\mathbf{z}}$).

To construct a 9×9 Hamiltonian for triplet pairs, these contributions from zero field and Zeeman splitting are combined with a small symmetry breaking contribution ($\mathcal{H}_X = \epsilon$ or zero) that applies for otherwise degenerate pairs such as $|x\rangle|y\rangle$ and $|y\rangle|x\rangle$. To finally put together $\mathcal{H}_0, \mathcal{H}_B$, and $\mathcal{H}_X$, a critical realisation is that while $\mathcal{H}_B$ can be expressed in the exciton molecular frame, these frames will not in general be the same for the two members of the triplet pair.[122,123] Instead, if the magnetic field is expressed relative to the axes of the first emitter, $\mathcal{H}_0$ for the second emitter must be rotated by the same orientation factor between the triplets themselves. Alternatively the same magnetic field must be reexpressed in the frame of the second molecule. If this is neglected, then the pair states formed from the concatenation of triplet wavefunctions will correspond to entities like $|x\rangle|y'\rangle$, where the prime indicates a $|y\rangle$ state in the second molecule's frame rather than the first. This mixed frame state is distinct from the $|x\rangle|y\rangle$ state unless the two emitters are perfectly aligned, and is therefore vanishingly likely to map onto the quintet, triplet, and singlet pair state wavefunctions in the same way as defined by Equations 1.3 and 1.4.

The elements of this total spin Hamiltonian can then be determined by evaluating the following expression for all pairs of the pair state basis vectors $|i\rangle$ and $|j\rangle$:

$$\begin{aligned} (\mathcal{H}_{9\times9})_{ij} &= \langle i|\mathcal{H}_{9\times9}|j\rangle \\ &= \langle 1_a|\langle 2_b|\left(\mathcal{H}_0^1 + \mathcal{H}_B^1 + R^T\mathcal{H}_0^2 R + \mathcal{H}_B^2 + \mathcal{H}_X\right)|1_c\rangle|2_d\rangle \end{aligned} \tag{4.7}$$

where R (transpose R^T) is the rotation matrix that relates the physical orientations of the two excitons (labelled 1 and 2), which are themselves in individual Cartesian states $|a\rangle, |b\rangle, |c\rangle$ or $|d\rangle$ chosen from $|x\rangle, |y\rangle$, or $|z\rangle$. Computing these elements is made significantly easier by having expressed all of the component terms of $\mathcal{H}_{9\times9}$ in the same Cartesian basis set (with orthogonal elements), and by the fact that these Hamiltonian components only act upon their own exciton. For example, $\mathcal{H}_0^1|1_a\rangle|2_b\rangle = (\mathcal{H}_0^1|1_a\rangle)\times|2_b\rangle$.

In terms of the actual matrix generated, this operation corresponds to some strange combination of a tensor product between $(\mathcal{H}_0^1 + \mathcal{H}_B^1)$ and $(R^T\mathcal{H}_0^2R + \mathcal{H}_B^2)$, but with elements given instead by the direct sum, and $\mathcal{H}_X$ (which is already 9×9) added afterwards.

It is unlikely that analytical expressions for the eigenstates of $\mathcal{H}_{9\times9}$ exists, but they can still be approximated numerically for specific magnetic field values. [284] These eigenstates can then be projected with $|0\,0\rangle$ and other total spin pair states, and combined with an estimate or parameter P_{dis} to determine η for each. These values of η can then be averaged across the different eigenstates to generate a number that corresponds to the experimental UC fluorescence, and varies in magnetic fields.

The observed decrease in UC fluorescence under large magnetic field can then be explained in term of the partitioning of singlet character amongst the different eigenstates. At zero field, exactly three triplet pairs have non–zero singlet character: $|x\rangle\,|x\rangle$, $|y\rangle\,|y\rangle$, and $|z\rangle\,|z\rangle$. At high fields, three pairs formed from the high field exciton eigenstates are also expected to have non–zero singlet character, namely $|1\,0\rangle\,|1\,0\rangle$, $|1\,1\rangle\,|1\,-1\rangle$, and $|1\,-1\rangle\,|1\,1\rangle$. This at first appears to imply no change in η at high fields, but just as the degenerate pair of single electron wavefunctions giving rise to singlet and triplet excitons, here as well symmetric and antisymmetric combinations of the degenerate pairs $|1\,1\rangle\,|1\,-1\rangle$ and $|1\,-1\rangle\,|1\,1\rangle$ emerge as the actual eigenstates. These combinations are purely singlet or triplet in character, and so at high field only two of the spin pair eigenstates have singlet character, leading to a lower average η for collisions. At intermediate fields the singlet character can be more evenly distributed, leading to an increase in the number of pair states that can access the emissive singlet pair state and an increase in UC fluorescence. Depending on the orientation of the emitters this increase can be depressed though, and for some specific orientations it can even vanish.

It should be noted that the total amount of singlet character to be shared amongst the nine eigenstates does not change. Along with the total triplet or quintet character, these remain normalised across the eigenstates. The fact that this model is able to predict the magnetic behaviour of UC systems just by comparing the number of pair eigenstates with *any* non–zero amount of singlet character (rather than weighting by the probability of singlet formation) means that the TTA from triplet and quintet pair states must be inactive. Otherwise, these processes would become more active for some pairs with low but still non–zero singlet character. The original works by Merrifield explicitly state this assumption, and considers the only outcomes of encounter complex formation to be emission or dissociation. [130,269,270,277] In the case where the other outcomes of TTA are neglected, careful attention should be paid to the normalisation of the denominator in Equation 4.3, although in more recently published reports this rarely occurs. The

exclusion of triplet and quintet TTA once again makes experimental η values that are large but less than 1 difficult to explain, as the singlet emission from second order decays is now defined to be operating in the absence of competing processes that would detract from it.

Since this model was originally developed for crystals, it understandably treats the molecular orientations as fixed — both relative to the magnetic field and to each other. Impressively, this orientation factor was later exploited to model spatial anisotropy in the magnetic field effects on delayed fluorescence as the crystal was rotated relative the the field.[277] This is unlikely to also be the case for liquids though, where tumbling in solution can cause R and potentially even the spin pair eigenstate occupancy to vary over the lifetime of the encounter complex. Nonetheless, this model has been applied with varying degrees of success to solutions and thin films.[122,123,246,275] This orientation dependance may explain why the magnetic field effects observed in solids and films (where orientation is fixed) are generally larger than those for solutions (where any effect is averaged across all orientations). It may also explain some of the temperature effects on UC systems, as at lower temperatures the emitters pairs are expected to more rapidly relax into a restricted set of low energy orientations as well as dissociate less rapidly. These orientations may then be beneficial or detrimental to the average singlet character of collisions, depending on the specific shape of the emitter molecule..

Separate to this approach, the use of Redfield density matrices by Atkins and Evans has the ability to take into account time evolution of the individual triplet spin states comprising the pair.[285] This can also be used to approximate changes in the pair state due to molecular tumbling, but it does not seem possible to separate these two sources of spin evolution. While the Merrifield approach is limited by essentially freezing both the emitter orientations and spin states as soon as they form the encounter complex, it is still favored by chemists for its more intuitive picture of spin mixing. The Redfield approach finds preferential use amongst physicists for its ability to predict a range of spin level transitions in the emitters and the encounter complex.[286,287]

4.1.4 Spin Polarisation and Resonance Effects

Extending beyond static magnetic fields, the ability to generate a polarisation of emitter spin states would have profound effects on the observed UC emission, and represents a new frontier in fundamental studies of UC. As mentioned, under normal circumstances thermal energies are sufficient to rapidly scramble spin polarisation even with moderate magnetic fields applied. This means that the properties of the triplet excitons are almost always measured as an average of the three degenerate states. Time-resolved ESR studies

have shown that spin polarisation generated in exciting the sensitiser can be transferred by TET though, and the possibility exists that properties like k_1, k_2, and η may be different for the different individual triplet spin states. [258,288]

A degree of spin polarisation is also required to detect the absorptions and emissions arising from transitions between spin sublevels of the triplet excitons and encounter complexes in ESR. Consider that if all spin levels are equally populated, the exposure to resonant electromagnetic radiation is just as likely to cause additional absorption as it is to stimulate emission — with no detectable net effect in the applied field. Despite this challenge, application of resonance techniques to UC systems still holds promise as a way to directly detect and identify the emitter excitons and pair states. [289–292]

Controlling exciton populations using saturated resonant transitions between the triplet states may then allow the distribution of emitter collisions to be biased towards or away from those likely to undergo emissive TTA. For example, biasing towards an excess of $|1\,0\rangle$ high field triplets would make the high singlet character pair states formed by pairs from this spin sublevel more prevalent, increasing the emission intensity. Alternatively, collisions between $|1\,1\rangle$ triplets have low singlet character, and so pumping transitions that generate these could cause a diminishment of UC emission. Using optical detection for magnetic resonance experiments (ODMR) can greatly improve the sensitivity, which assists in circumstances where the spin polarisation (and therefore maximum ability to bias triplet populations) is low. [293–295]

4.2 Early Attempts

The original aim of this entire project was to develop an experimental platform capable of measuring the CW changes in UC emission with magnetic fields. This would then be used to reproduce existing reports of the magnetoluminescence (ML) effect, and later expanded to perform ODMR experiments. Since the UC emission was known to change with the same magnetic fields required to achieve resonance, the ML measurements would also serve as a background, with additional effects on UC emission expected when resonant fields were also applied to bias the population of triplets. Standard microwave detection ESR techniques were also planned in parallel to this approach.

The first iteration of ML spectrometer was therefore extremely basic. As illustrated in Figure 4.1, a commercial Bruker EMX CW ESR spectrometer (a shared instrument at the University of Sydney School of Chemistry) was interfaced with a DAQ card and laptop using LabView, which allowed the laptop to trigger programmable magnetic field sweeps. A UC sample was placed in the EMX resonator, and its microwave bridge set

to maximum attenuation to observe just the static magnetic field effects. The sample itself was degassed in a custom sealable ESR tube, which allowed for the attachment of a vacuum feedthough for optical fibres. A single optical fibre hanging immersed in the UC solution allowed simultaneous optical excitation and UC emission detection. A fibre coupled laser was run into this sample though a fibre splitter, with the return arm passing to a fibre spectrometer (OceanOptics HR4000) through a short pass excitation filter. The fibre spectrometer itself was interfaced with the same laptop used to control the EMX, so that spectra could be collected at the different magnetic field strengths in the sweep. The elegance of this platform was that it would immediately allow for the collection of standard ESR and ODMR spectra once the ML effect was characterised at the magnetic fields of interest.

Sadly this was not to be. The EMX microwave bridge broke about three months into the project, just as the necessary optical parts were being assembled and tested. Although this should not have affected the use of the spectrometer as a dumb magnet, its proprietary software would not allow any kind of use in the absence of a handshake with the microwave bridge. As an old and low-use shared faculty instrument, there was no official instrument technician nor a departmental plan in place for maintenance and repair. With no clear plan to restore the EMX to working order, experiments of this kind were put on indefinite hold.

Thankfully, in the following months access to a large standalone electromagnet was secured in a research laboratory in the University of Sydney School of Physics. This meant that the optical parts acquired for the EMX spectrometer could be directly transplanted, and measurements commenced. Although this second setup lacked the resonance transducer coils needed to perform ESR or ODMR, later addition of custom coils driven by an arbitrary waveform generator was planned to enable this afterwards.

A sample of CBPEA (1.5 μM) with linear PQ_2Pd (0.75 μM, analogous to PQ_4Pd but missing two opposite quinoxalino groups) as sensitiser was degassed and prepared for measurement. The choice of sensitiser was to match its absorption to the 632 nm output of the available fibre laser, and the absorption and emission spectra of the UC components are shown in Figure 4.2. The magnetic field and spectrometer were interfaced using MATLAB, with data collection automated using scripts written by Thomas Keevers. The spectral shape of the UC emission was found to remain the same at magnetic fields up to 1 T, and so the UC emission feature in each spectrum was integrated to generate single numbers for comparison. Due to low signal to noise ratios for the spectrometer, data acquisition and averaging were run overnight, although this was limited by the swelling of the sealing KF-16 O–rings and subsequent ingress of oxygen. The entire measurement was also repeated at low temperatures (195 K), achieved by immersing

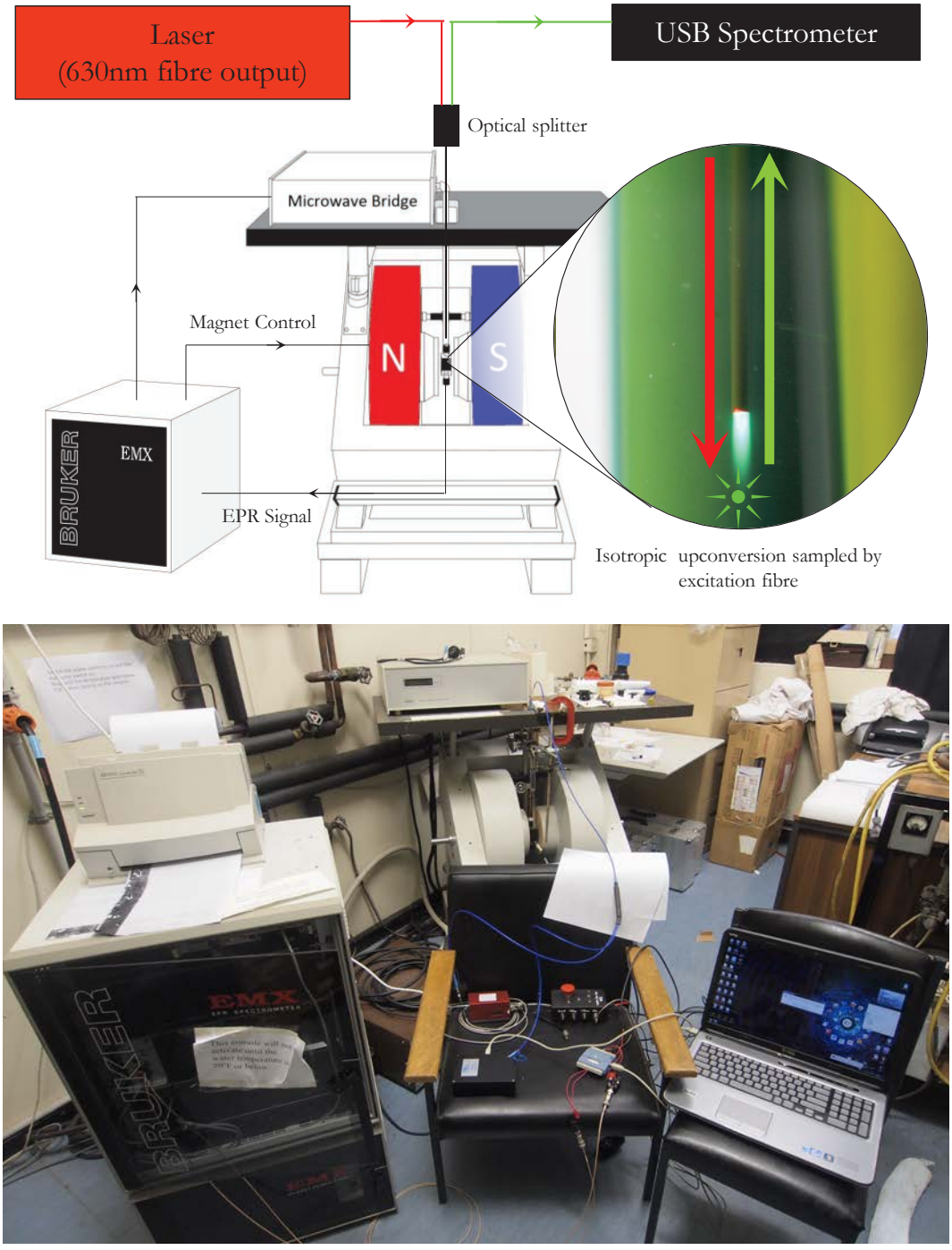

FIGURE 4.1: Diagram and photograph of EMX spectrometer adapted for concurrent optical excitation, magnetic resonance, and emission sampling of UC systems.

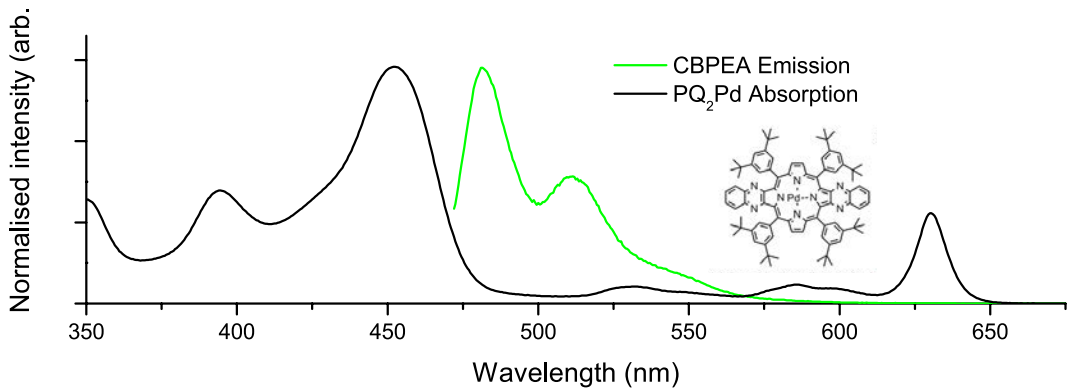

FIGURE 4.2: Absorption and emission spectra of CBPEA and PQ_2Pd.

the sample in a dry ice and ethanol bath, which by happy coincidence was close to but (critically) above the freezing point of the solvent (178 K) — the minimum temperature that UC can be easily studied at for toluene. The changes in emission with magnetic field for both temperatures are shown in Figure 4.3, with the low temperature measurement displaying the expected enhancement at low fields. The UC emission was found to diminish for both temperatures at high fields.

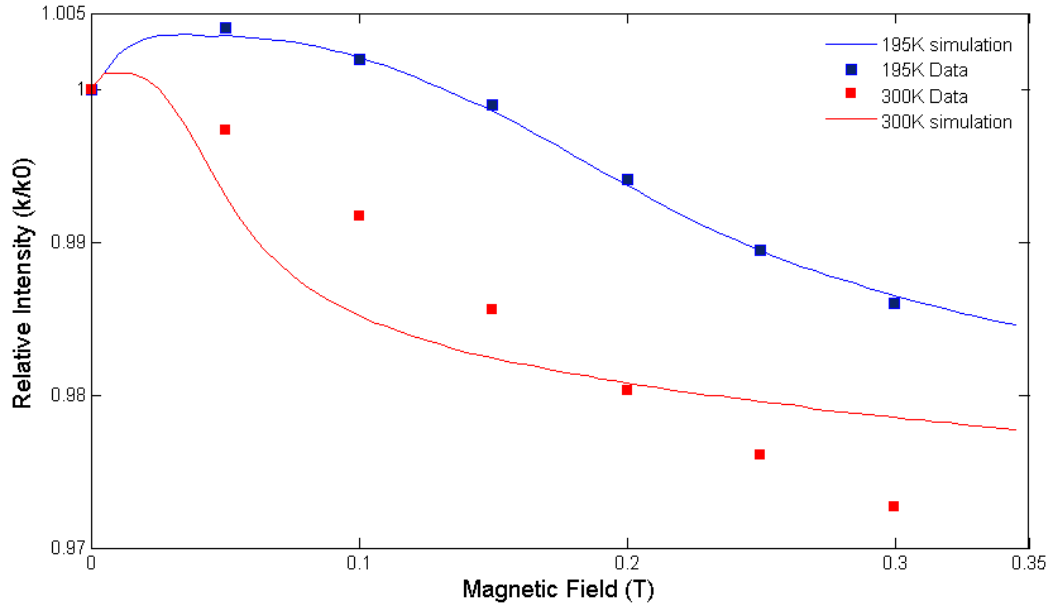

FIGURE 4.3: Changes in the relative integrated CBPEA UC emission intensity at different magnetic fields. Apart from at zero field, the data points in the figure are the averages of two measurements taken in a symmetric magnetic field sweep.

4.2.1 Static Collision Model

To try and better understand the results in Figure 4.3 (and especially the different behaviours at different temperatures) a version of the Merrifield model outlined in the previous section was implemented and coded primarily by Timothy Schmidt.[284] The Hamiltonian defined by Equation 4.7 was diagonalised using numerical techniques, and η calculated for its eigenstates using a modified version of Equation 4.3 that had the triplet and quintet channels disabled. The values of η were then averaged across the different eigenfunctions, with the values of $\mathbf{B}, D, E$, P_{dis} and R entering as parameters. For specific values of B, averaging of η across the different $\hat{\mathbf{B}}$ and R was performed using Monte Carlo methods. To ensure random sampling of $\hat{\mathbf{B}}$ and R for this averaging a random vector in 3D Cartesian space was chosen and normalised to give $\hat{\mathbf{B}}$. Similarly, another random direction and an additional cosine value chosen between zero and some upper limit $X \leq 1$ were used to construct a unit quaternion. This quaternion was then converted into an equivalent rotation matrix R, which avoided the problem of biased sampling that arises from a simpler choice of random Euler angles to construct R.[296]

After averaging and plotting relative values of η at different magnetic fields, this approach reduced the number of free parameters in the model to four. These were the zero field splitting parameters D and E, along with an upper limit for emitter rotation X, and the ratio of singlet pair formation to dissociation W. These parameters were varied to give the best model fit to the data shown in Figure 4.3, and it was anticipated that at least D and E could be measured in later planned ESR experiments. The relative effects of X and W were also explored, with example curves from their parameter space shown in Figure 4.4. These parameter sweeps show that a large rate of dissociation (small W) give rise to both low field enhancements and high field depressions in UC, while a higher degree of orientational alignment (smaller X) uniformly increases the UC emission at all fields. Both X and W were expected to contribute the observed temperature effect through changes in translational and rotational diffusion.

The limitations of the Merrifield model discussed in the previous section meant that the model curves in Figure 4.3 only roughly fit the data at best, despite the many free parameters. This fit was much better at lower temperatures — thought to be due to the slower molecular rotation and more solid-like (static) collisions as thermal energy was reduced. Nonetheless, with data for fitting at only 7 magnetic strengths, and with the model predicting an unobserved UC enhancement in between the first and second experimental magnetic field values at room temperature, the need for additional measurements was obvious at this stage.

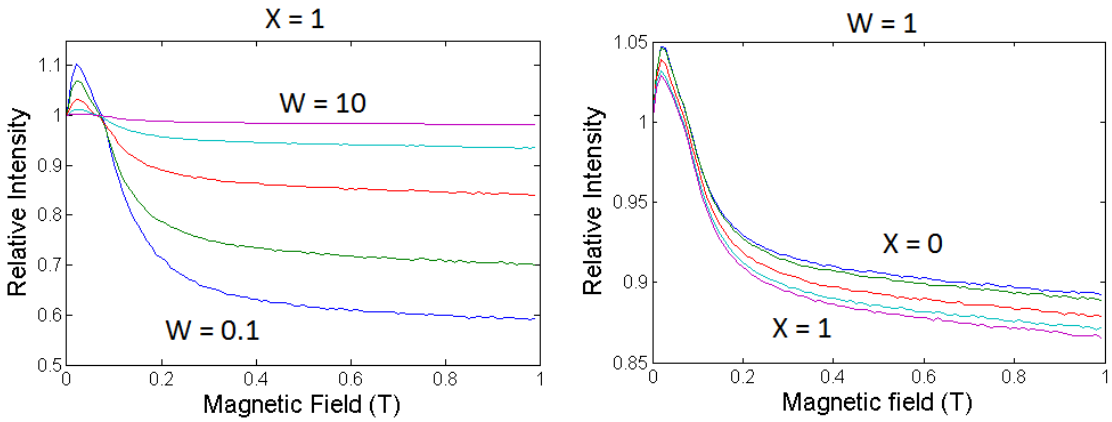

FIGURE 4.4: Effect of model parameters X and W on ensemble averages of η. The step size of the explored parameter was uniform in both cases, with 0.1 added to the final value for W to prevent a trivial simulation with no UC at all fields.

Sadly at around this time the experimental setup itself was banned from the hosting physics laboratory. Nominally this was due to safety concerns regarding the fibre laser and use of dry ice as a cryogen, although these had been previously approved by the appropriate supervisor at the time. In hindsight, this outcome was more likely due to tensions arising from the joint yet inequitable ownership of the electromagnet with the manager of that laboratory.

4.2.2 Molecular Dynamics Modelling

One approach that was identified to improve upon the Merrifield model was to iteratively recalculate the Hamiltonian, its eigenstates, and η across their distribution in regular time intervals over the duration of a molecular collision. In essence this would allow the dynamics of the collision to be accounted for by taking a series of static "snapshots" as the collision event unfolded. To do this would require an existing knowledge of how emitter collisions progress, a problem that is most readily addressed by molecular dynamic simulations. These simulations would also potentially reveal emitter self orientation in collisions, as well as give a reasonable estimate on the collision and encounter complex dissociation rates.[297–302]

As proof of principle for concept, a coarse grained model for perylene in toluene was developed with Dr David Huang, and simulations performed using the LAMMPS package. This allowed for low cost simulation of solution molecular dynamics, and successive frames like that shown in Figure 4.5 could be stitched together to make videos of the microscopic emitter collisions. The main limitation of this technique was that, despite simplification of the molecular structures, large volume and lengthy simulations could

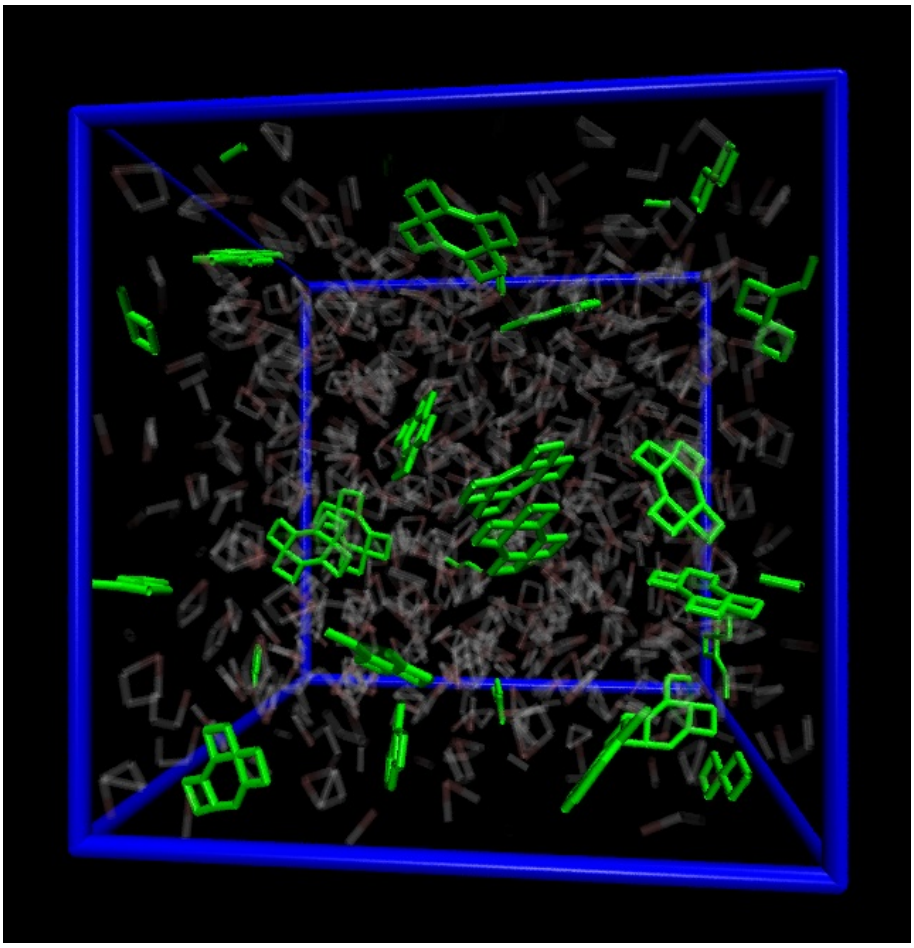

FIGURE 4.5: Rendering of a frame in a simulation of coarse grained perylene (green) in explicitly simulated toluene (transparent). The blue box represents the edge of the 45 nm cube simulation space, with periodic boundary conditions. Pi system stacking can be seen between some pairs of perylene molecules that are undergoing collisions.

not be run with available computing resources. In response to this limitation, unrealistically large emitter concentrations had to be used to give any simulation run a reasonable chance of observing emitter collisions. Nonetheless, the limited simulations performed already indicated π–π stacking of perylene caused its collisions to have a preferential orientation, and that these stacked emitters stayed in close proximity for extended periods.

These simulations were later continued by Simon Blacket and extended by Patrick Tapping under the supervision of David Huang. Moving to an all atomic model for rubrene in toluene, they found that this emitter only rarely forms close collision pairs in orientations where the substituent paddles interleave, but that these emitter pairs then remain in close proximity for a long time. These insights are further support for the proposed explanations of the large average η but low k_2 for rubrene measured in the previous chapter, although these simulations have not yet been published.

This mechanism may also explain the low ηk_2 values for heterogeneous BPEA and rubrene TTA in the previous chapter, as the BPEA molecule are likely the wrong shape to easily fit in the restricted space available for close approach with rubrene. This would lead to a very low experimental k_2, as most collisions would be unable to even form the encounter complex. It raises the possibility that the poor performance of heterogeneous TTA observed earlier may be a property of that specific emitter pair, and that other emitter pairs may be able to take advantage of heterogeneous TTA for significantly enhanced UC.

Later measurements of kinetic rate constants (from the previous chapter) and magnetic field effects (from the following sections) on rubrene and perylene UC systems were sent as simulation targets for combining the emitter molecular dynamics with an iterative Merrifield approach, and work on this continues.[123,303]

4.3 A Compact Platform for Magnetic Resonance

With a specialised team of computational chemists working on UC simulations, efforts were refocussed on collecting experimental results for them to work from. To address the safety concerns raised regarding the previous iteration of ML spectrometer, a new implementation was required. This next generation design would be built hanging from a KF-50 flange cap, and sit directly inside an Oxford Instruments CF935 cryostat which had been found and secured for use near the abandoned EMX spectrometer. This cryostat would provide temperature control as well as complete optical enclosure of the UC samples. The cryostat in turn hung between the poles of the electromagnet, held aloft by brackets in a custom optical table with a central hole. A separate fibre coupled laser with safety interlock features was also purchased, able to excite PQ_4Pd at 670 nm.

The engineering problems to address were then threefold; how to get excitation in, how to get emission out, and how to mount an air sensitive liquid in the confined cryostat sample space. Due to the depth of the cryostat, optical fibres once again seemed a natural choice for the first two concerns. Rather than using a fibre splitter, two separate fibres were used, with an excitation filter between the collection fibre and detector. In contrast, due to their side bulbs necessary for degassing, resealable EPR tubes or cuvettes such as those used previously and in the later work of Chapter 3 would not fit into the cryostat. Instead, miniature and permanently sealed UC samples were produced using glassblowing techniques. Both tube and tile shaped samples were prepared by vacuum degassing of rubrene with PQ_4Pd UC systems, and then permanently sealed using an acetylene torch to melt the glass around this solution. The quality of the sealing is evident from the fact that these samples still display UC emission four years

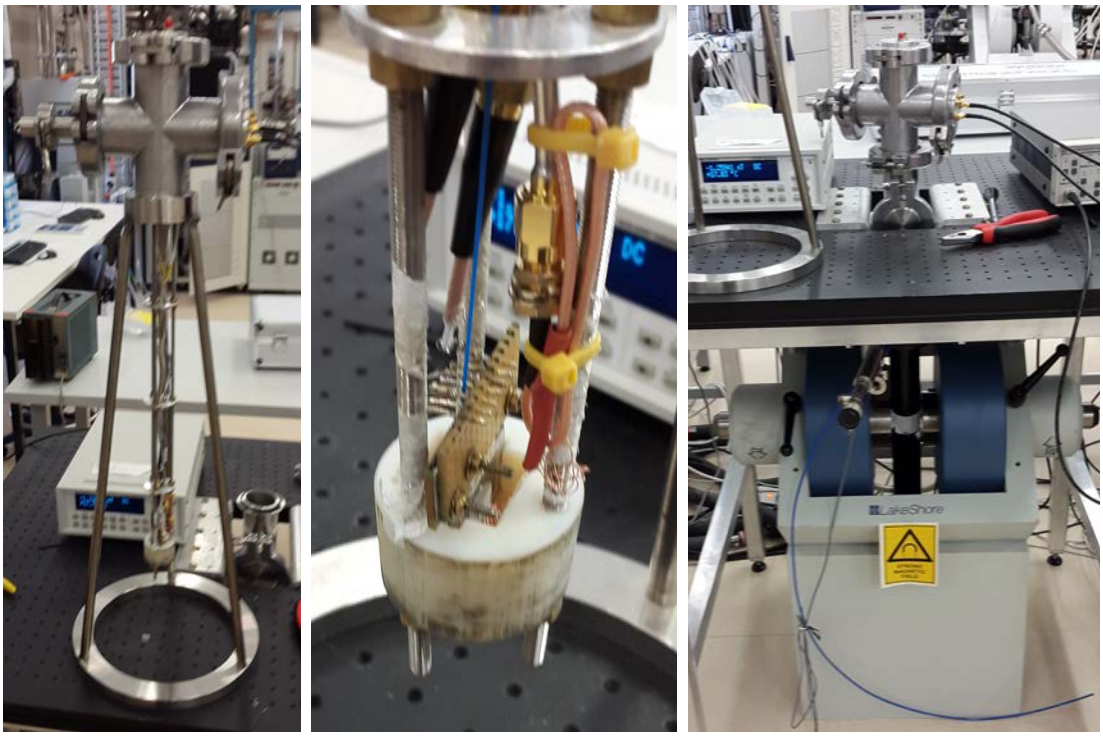

FIGURE 4.6: Photographs of the compact platform sample stage.
Left: Optical ports and vertical structural rails are mounted on the top KF-50 flange cap, as well as thermocouple and electrical interconnects horizontally. All of the caps are held in place by a crosspiece and clamps.
Middle: At the bottom of the rails, 3D printed sample holders swap out for performing experiments on UC systems or LEDs. In this photograph an LED is slotted in place, electrically contacted with a top mounting sandwich bracket made of PBC.
Right: The caps and rails slide into the cryostat, which is held aloft in a custom optical table. The sample holder then sits between the poles of the electromagnet underneath.

after degassing. The convenience of the tile samples was also highly advantageous for the development of the action spectrum instrument, and were used to generate the data for the original publication of that method.[192]

To hold the UC sample in place relative to the excitation and collection fibres, a custom 3D printed sample holder was developed along with Thomas Keevers, and printed by Dr Stephen Beirne at the University of Wollongong. In this design the vertical fibres would address the sample horizontally, using an embedded 3 mm right angled prism for reflection of both excitation and emission. This design also incorporated transducer coils to apply resonant magnetic fields to the sample for more advanced spectroscopic techniques, and could alternatively accommodate LEDs instead of tile or tube UC samples. When measuring LEDs, the excitation and collection fibres could both be used to instead track the effects on the EL with magnetic fields. Images and illustrations of the measurement platform, UC solutions, and sample holder are included in Figures 4.6 and 4.7.

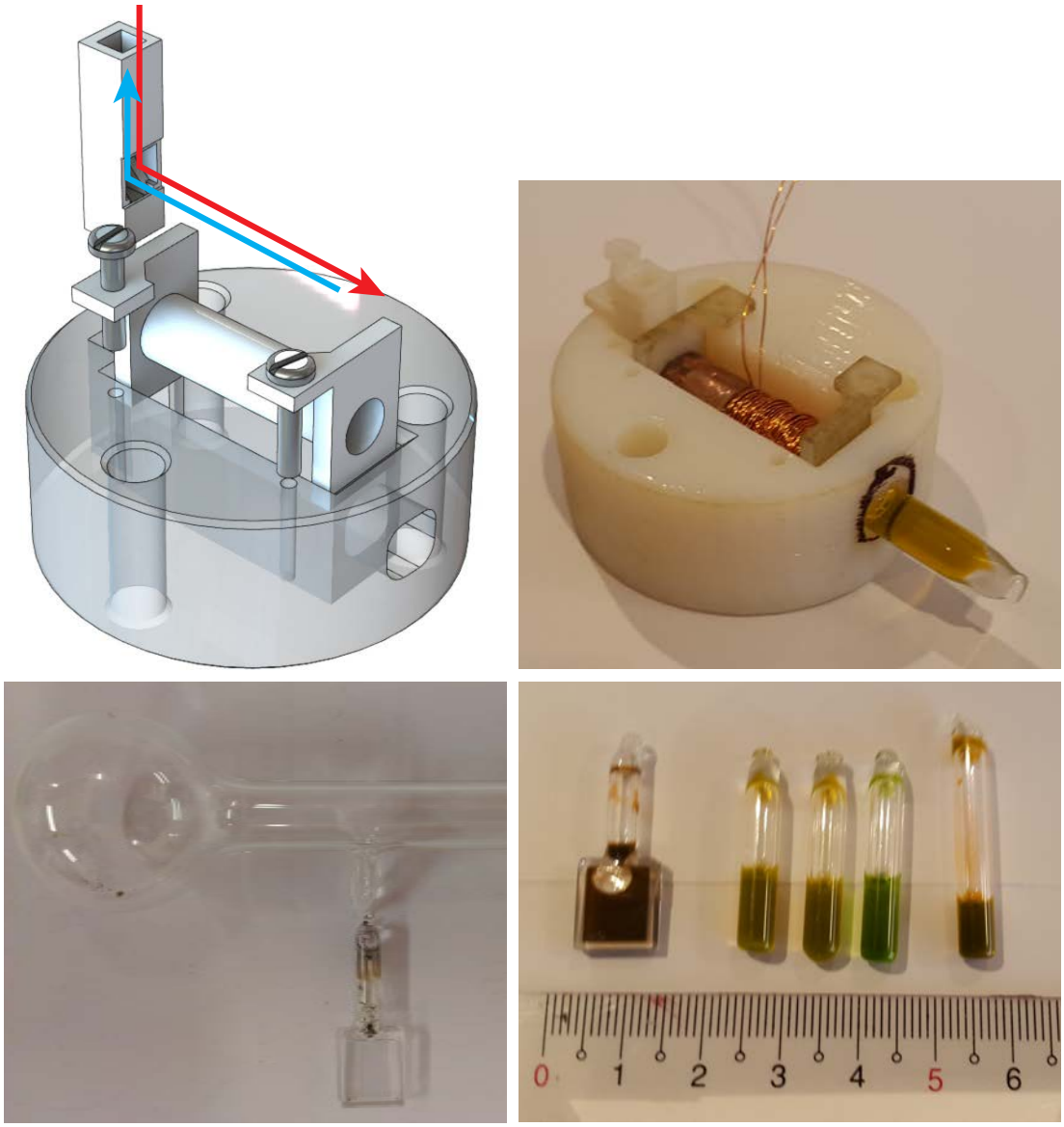

FIGURE 4.7: 3D printed sample holders and permanently sealed UC samples.
Top: Sample holder for tube shaped samples (all 3D renderings produced by Dr Beirne). Excitation and emission (red and blue arrows) are directed with vertical fibres and a prism (not shown) lodged in a cavity in the plastic column. The sample itself lies horizontal, surrounded by a wire coil for applying resonant fields.
Bottom: Production of permanently sealed samples from consumable glassware. The solutions was first degassed in a bulb, then transferred to the sample area for sealing. Tile and tube shaped samples were produced, including tubes with flat and round bottoms. A centimetre ruler is shown for scale.

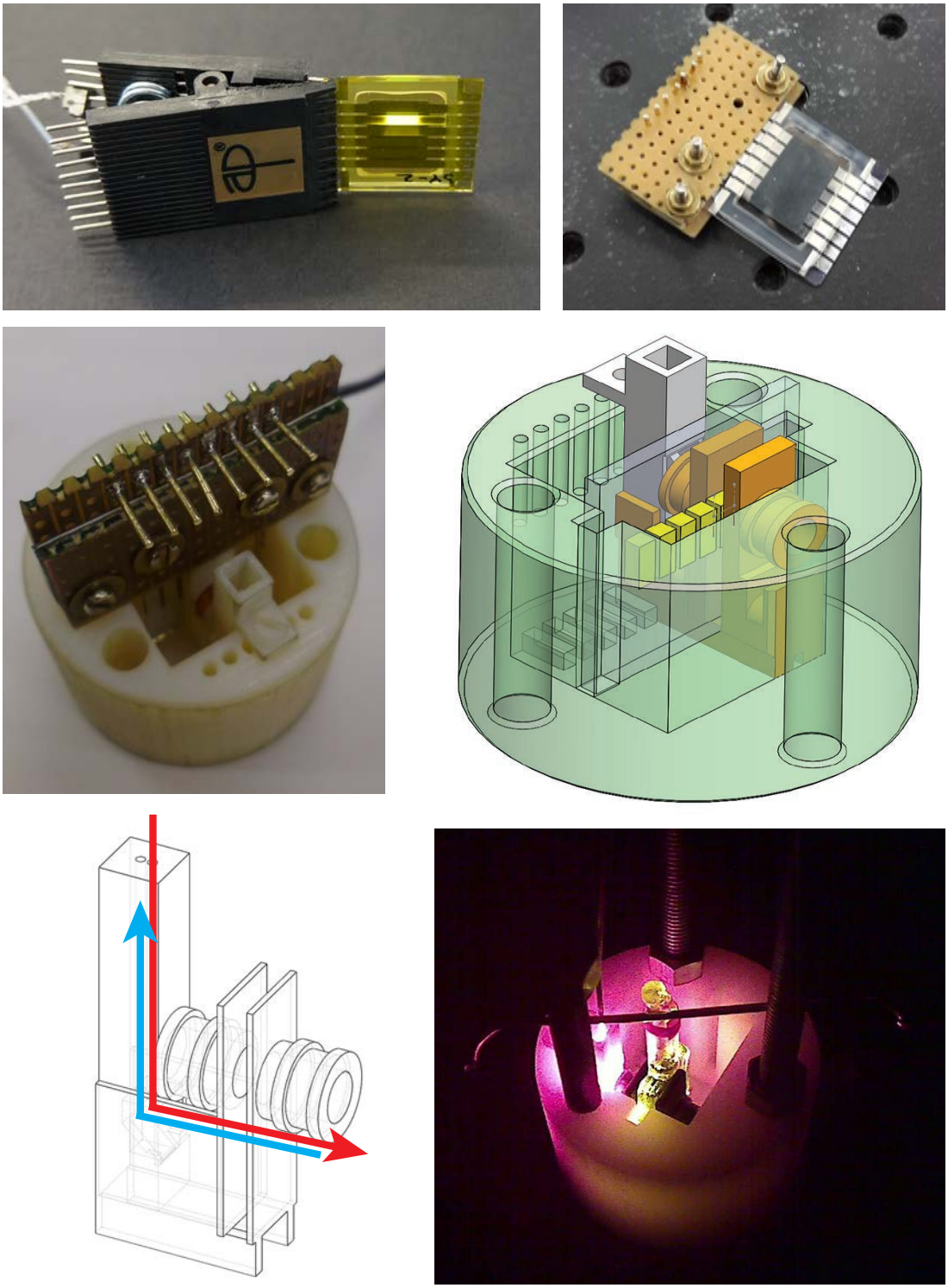

FIGURE 4.7: 3D printed sample holders and permanently sealed UC samples. Top: LEDs had aluminium deposited on the edge of the glass to address individual pixels. These LEDs were contacted using a custom PCB sandwich across one edge. Middle: The contacted LED fit into its sample holder, which allowed emission measurements while sitting between the electromagnet poles and resonant coils. Bottom: Fibres were used for optical excitation and emission sampling of a UC sample. A prism was placed so that the fibres were aligned with the cylindrical plastic tubes upon which the resonant coils were wound, although these are misaligned in the figure.

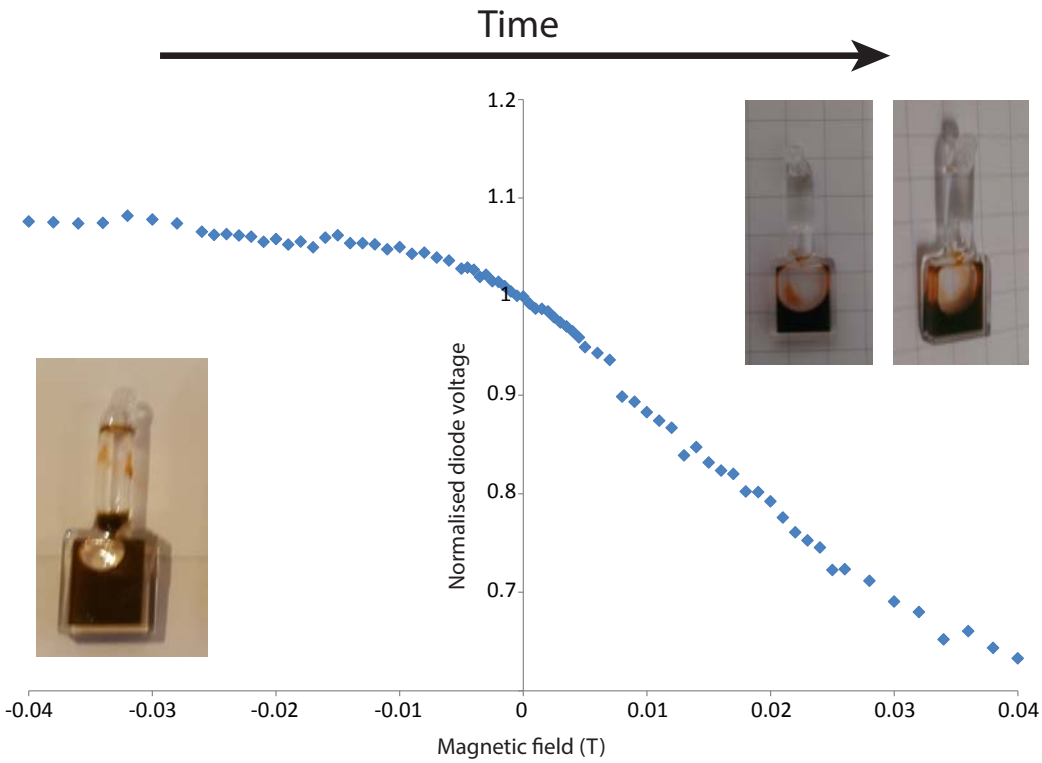

FIGURE 4.8: Magnetic field effects and laser distillation of a tile shaped UC sample. Measurements were taken across a symmetric magnetic field sweep. The very large and asymmetric magnetic field effects were the first clue that something had gone wrong. Laser distillation of the UC sample was observable when the sample was retrieved from the cryostat, with clear toluene accumulating in the neck of the sample and held in place by capillary forces. The sample readily remixed upon shaking, but this could not be done during measurements when it was seated in the sample stage and cryostat.

Unfortunately it was soon discovered that the powerful excitation of the fibre laser was able to evaporate the UC solution, moving the solvent to the cooler far end of the horizontal tube samples, with the UC components drying out to form an opaque layer of solids at the near end. Although these compounds readily redissolved, it meant that long scans at high excitation powers — necessary for the averaging required to reveal the small magnetic field effects — could not be performed. A similar problem was also found for the tile shaped samples, with laser distilled toluene accumulating in the neck of the tile. Experimental results for this measurement run are included in Figure 4.8, with magnetic field effects on UC convolved with decreasing signal over time due to the evaporation (and the resulting decrease of sample volume illuminated by the laser). For the planned LED studies, the limited access to and rapid degradation of test devices (as described in Chapter 2) meant that little could be achieved on this part of the project, which was intended to be the centrepiece of Thomas Keevers' doctoral studies.

An obvious and immediate solution to the laser heating of UC samples was to simply use the cryostat that these samples were housed in for temperature control. Sadly, and much like the EMX spectrometer it was found alongside, this device became inoperable soon

after initial test runs. Documents found with the cryostat indicated that it had initially been purchased in 1993, so permanent failure by 2013 was perhaps understandable. Attempts to address the laser heating of the sample were also attempted by modulating the laser output with a low duty cycle, with measurement points in the magnetic field sweep interspersed by long cool down periods. While this greatly increased the measuring time for the scan, the permanently sealed samples did not have the same upper limit on this in the way that O–ring failure had limited resealable tubes earlier (and later).

Although initially promising, further experiments were interrupted at this point by the movement of research groups from the University of Sydney, and establishment of new work spaces at the University of New South Wales. For the physics laboratory, rolling delays in the installation of a recirculating water chiller (and several incidents requiring repair and maintenance downtime after installation) meant that an identical replacement electromagnet could not be used to continue either the UC or OLED experiments. Despite assurances of imminent equipment access, suggested routes to repair or replacement were not pursued in earnest or with urgency over the two years that followed. In hindsight this outcome was particularly upsetting, considering how close this approach was to producing large amounts of meaningful data.

At that time though, promises that infrastructure for these experiments would soon be secured were taken at face value, and work was commenced on other side projects. All of the work presented in Chapter 2 occurred during this interim period, as well as the majority of planning for the work in Chapter 3. This opportunity to be at the forefront of research in this area has since been seized by other research groups, who have developed the same experimental capabilities envisaged here and applied them to both UC and OLED systems with great success.[228–231,246,304]

4.4 Later Attempts

4.4.1 Adapting a Pulsed Resonator

Several years later, and now established at UNSW, the heavily delayed arrival of a Bruker E580 pulsed ESR spectrometer (along with eventual provisioning of cooling water) provided additional opportunities to pursue ML and ODMR experiments. Although this spectrometer also came equipped with a suitable replacement cryostat for the compact platform in the previous section, it was found to be faulty soon after commissioning. This began a protracted repair process, which meant that it was not practically available for addressing the laser heating problem in the previous section. Suggestions of

negotiating a replacement or loan instrument from the supplier during this time did not find traction in planning meetings.

Some efforts were instead expended to adapt the E580 system itself for UC measurements in its pulsed resonator. Like the original EMX implementation, this was anticipated to then allow rapid advancement to ODMR and ESR studies, as well as pulsed variations of these which could reveal magnetic field effects on UC rate constants and spin coherence lifetimes. As this new resonator presented an even more restricted sample space designed for 1 mm tubes, the only clear solution for optical access was to use a fibre bundle inserted directly into the UC sample. Similar to the fibre splitter used in the earlier iteration, the bundle allowed simultaneous excitation and emission collection — each split out to separate arms.

As this arrangement could not be sealed for degassing, an immiscible layered solvent system was investigated to exclude oxygen from the UC sample. Dubbed "magic water", this system used a UC systems dissolved in chloroform, with a layer of water resting on top. The water had a mixture of sodium sulfite, sodium hydrogenphosphate, sodium bishydrogenphosphate, and cobalt ions dissolved in it which slowly but eventually cleared the organic layer of oxygen.[305–307] This allowed UC emission to be observed in capped vials without direct degassing after only a few hours of dissolved gas exchange. It was soon discovered that the magic water approach was highly inappropriate for the E580. Chloroform was found to completely absorb the microwaves intended to pump ESR transitions, which in hindsight should have been predictable from its high dielectric constant.[308] When attempting to return to toluene as the UC solvent, the (denser) water would eventually sink beneath it (accelerated by the presence of the fibre across the layer interface). A search of common solvents was unable to find a replacement for chloroform that was denser than water, yet with a low microwave absorptivity like toluene.

Several attempts at observing effects on UC or even just sensitiser phosphorescence were nonetheless attempted, using the short time window in which the water was meta-stably balanced on top of the toluene layer. Like chloroform, water would completely attenuate the microwave signal, and so was set afloat on a tall column of toluene to keep it out of the resonant cavity. No magnetic field or resonance effects (CW or pulsed) were found in the emission or spin signal of any of these kinds of samples (S or UC). At first this was thought to be because of broad or small spin signals at room temperature, themselves due to heavy metals like palladium and low spin polarisation. To exclude this possibility replications of published room temperature ESR studies on zinc porphyrins were attempted, although these too were found to generate no optical or microwave signal with static or resonant magnetic fields.[309–311]

Eventually, the recurring, rapid, and permanent bleaching of UC samples in this setup was taken as evidence that oxygen was not being adequately excluded from the open ESR tube despite the use of magic water. This conclusion was further supported by the observation of spin signal in singlet fission systems using the same equipment, which are less sensitive to oxygen and for which only optical excitation was needed. With no fibres needed to collect emission, these samples could be crudely sealed with rubber stopping caps in the same glovebox used for degassing in Chapter 3, which had arrived at about this time (and could not be used for degassing earlier). These experiments demonstrated that the pulsed laser and ESR spectrometer were certainly powerful and sensitive enough to excite and detect modest numbers of spins. The absence of signal in the UC samples meant that emitter triplets probably were not present, and instead rapidly quenched by oxygen.

The pink emission seen from the zinc porphyin samples prepared when replicating earlier ESR studies — previously thought to be the phosphorescence, and taken as a sign that the magic water approach was working — was thus reinterpreted as fluorescence. Fluorescence is not commonly observed in other UC sensitisers due to their heavier metals (which are chosen in order to maximise their rates of ISC), which is why this misidentification had occurred in the first place. This also explained why no changes were observed in the pink emission intensity under static and resonant magnetic fields, now understood to come from magnetically inactive singlet states.

4.4.2 Back to Basics

In one final attempt, the E580 pulsed resonator was later switched out for a CW version, making it almost identical to the original EMX setup. This resonator's larger sample tube diameter and open top allowed the original ESR sample holder and EMX optical equipment to be reused, with the E580 now acting as a dumb magnet. In contrast to the original ML measurements, for these a filtered diode and was used for optical detection, and hardware lock-in amplification of the diode voltage signal was achieved by modulating the "static" applied magnetic field.

Although this filter removed signal from the excitation, a fair amount of sensitiser phosphorescence also made its way to the detector. This was confirmed by first measuring the spectrum of the sample emission using a fibre spectrometer (Thorlabs CSS200), with examples for different systems shown in Figure 4.9. Blocking bands of the dichroic excitation filter can be seen at 670 and 520 nm, with PQ_4Pd phosphorescence at 850 nm and other emitter emission matching spectra seen in the previous chapter. For UC samples this sensitiser phosphorescence feature was confirmed to be small compared to the UC

emission, and did not change significantly for the duration of the experiment. Similarly, the amount of laser excitation passing through the edges of the filter blocking bands was small compared to the UC emission signal, and did not change for the duration of an experiment.

Similar to the sequence of experiments in Chapter 3, ML studies were first performed on the sensitiser alone so that these could be safely excluded in later experiments on UC. Thankfully, this phosphorescence was found to not change with magnetic fields, and as a result would be entirely filtered out by the lock-in amplification achieved by modulating the field. Moving on to the UC systems, magnetic field effects on the emission were once again detected, but this time with a much greater sensitivity and resolution in magnetic field. Although the effect was small, averaging of multiple scans allowed for the derivative traces in Figure 4.10 to be generated for rubrene and perylene UC systems at room temperature.

A BPEA system was also investigated but found to rapidly bleach under sustained excitation. That UC emission was restored when rubrene was added to this sample without further degassing provided clues on the bleaching mechanism, and was discussed in Chapter 3. A DPA UC system was attempted as well, but as shown in Figure 4.9 no UC emission could be detected. This was most likely due to the extreme endothermicity of TET from PQ_4Pd, with the triplet levels of DPA residing even higher than that of perylene based on its shorter wavelength fluorescence. Further evidence for this explanation is provided by the stronger sensitiser phosphorescence in this sample, as there was nothing to effectively quench S^*. No differences were observed in the emission spectra of deuterated emitters, while the signal amplitudes slowly decayed for all samples over time — consistent with a slow leak of oxygen through the sealing O-ring.

The derivative traces in Figure 4.10 were then converted back to relative changes in emission by calibration of the E580's built in lock-in amplifier, using a second amplifier that could output the derivative signal in absolute units (voltages). This was done by first measuring the detection diode voltage levels at zero field with the laser off (background) and laser on (signal). The difference between these values then gave the absolute amplitude of the detector signal, which was taken as proportional to the intensity of UC emission (although this ignored the small contribution from sensitiser phosphorescence). The lock-in signal from the diode was also remeasured at magnetic fields corresponding to the peaks of the E580 derivative trace using the calibrated lock-in amplifier. This allowed the signal obtained from the E580 to be expressed in volts, whereas in normal microwave detection it is left as a relative value without units. The derivative signal could then be integrated to give the absolute signal voltage change at different magnetic fields, using the 20 G magnetic field modulation width as the

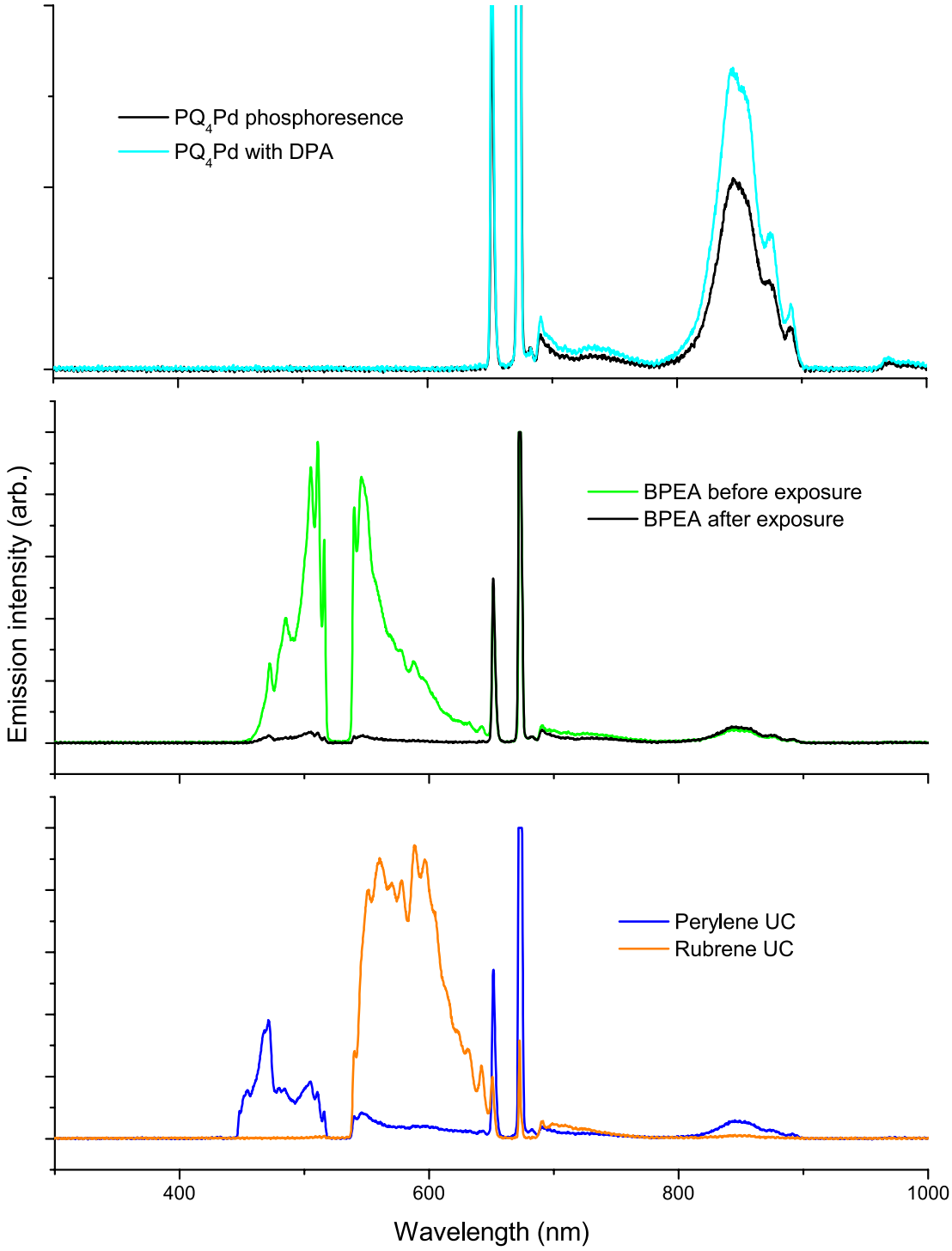

FIGURE 4.9: Fibre coupled and filtered emission spectra of UC solutions. Excitation filter blocking bands can be observed at 670 and 520 nm, with blocking band shapes responsible for the altered shapes of the emitter fluorescence spectra.
Top: Emission from PQ_4Pd, and an inoperant DPA system (different vertical scales).
Middle: Emission of a BPEA UC system before and after ∼5 minutes of laser exposure.
Bottom: Emission spectra from perylene and rubrene UC systems (different scales).
The larger sensitiser phosphorescence in the perylene system (despite a smaller scale) indicate that it is unable to efficiently quench this sensitiser, as perylene's large triplet energy makes this prohibitively endothermic.

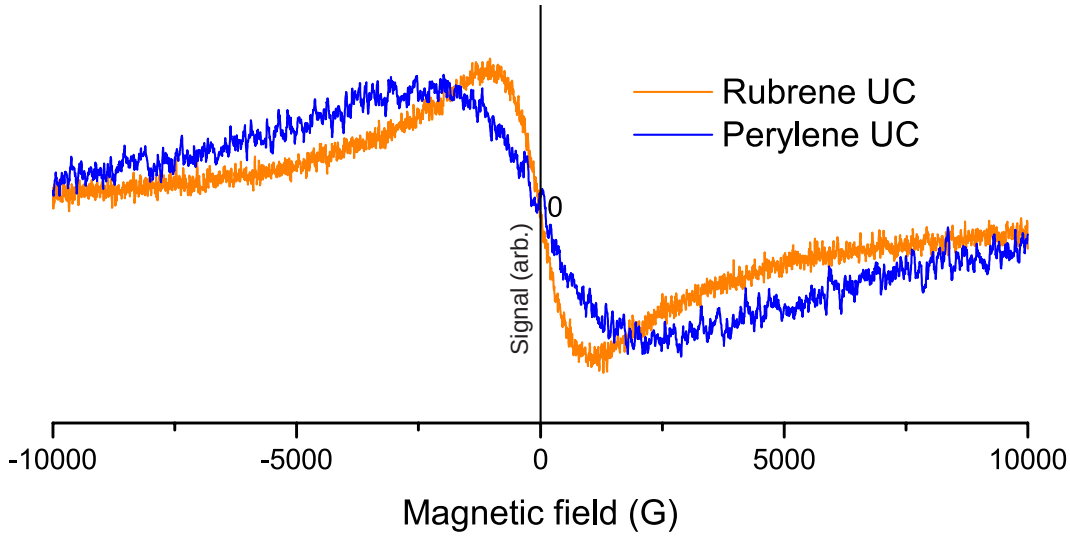

FIGURE 4.10: Lock-in amplified magnetic field effects on UC systems at room temperature. The units of the vertical axis are arbitrary, with the data centred and normalised.

derivative step size. Adding this to the absolute zero field voltage and dividing through by the same value converted these into relative changes in UC, and were sent as modelling targets to collaborators. These curves are shown in Figure 4.11, and are reminiscent of the early data originally obtained room temperature CBPEA.

The small relative changes in Figure 4.11 then explain why no magnetic field effects were observed in Chapter 3, where the magnetic field was only varied over 0—40 G. It was also found that these curves could be fit with a modified Lorentzian function, taken from literature reports of magnetic field effects in OLEDs:[312]

$$\frac{I(B)}{I_0} = 1 - A\frac{B^2}{(B + B_p)^2} \tag{4.8}$$

where A is a scaling factor and B_p is a fitting parameter. The value of A was immediately discarded here due to the slow decay of signal over the duration of these experiments. The remaining fitting parameter B_p was not explained from microscopic properties or processes in these reports, and so not much can be learned from its values. Nonetheless, since the values were different for rubrene and perylene, but the same for their deuterated versions, it is inferred to be somehow linked to emitter shape and geometry. Although tenuous, this dependance on shape and collision orientation is the same conclusion reached from the analysis of TTA and intrinsic η.

Experiments that would reveal the effect of magnetic fields on UC kinetics were also investigated. This was done by replacing the CW diode laser with the trolley mounted OPO used in Chapter 3. Unfortunately it was found that the response time of the detection diode was too slow ($\sim$200 μs) compared to the UC kinetics at the high gain

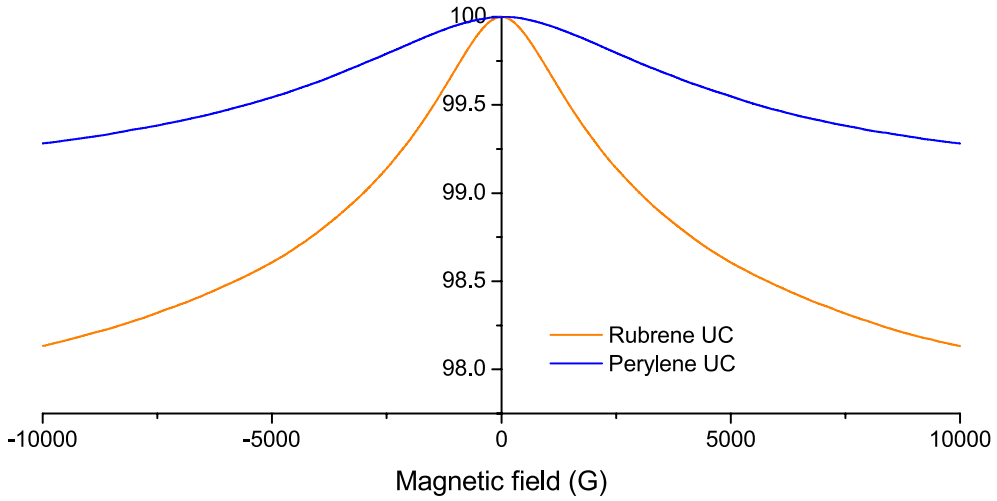

FIGURE 4.11: Relative changes in UC emission at different magnetic fields. The data was processed by integrating the lock-in signal in Figure 4.10 and comparing to the signal generated by a calibrated lock-in amplifier. The data is normalised to the value at zero field, with the units of the vertical axis in percent.

settings needed to observe the weak emission. Manufacturer and distributor quotes for faster and more sensitive diodes were obtained but ultimately never purchased, while the CCD camera used in previous studies was considered too delicate to make the trip from the chemistry to physics laboratories.

Having obtained CWML spectra, scans were then performed to look for differences in this behaviour when also exposed to resonant microwaves. Long scans with significant averaging were set up, both for the entire range of magnetic fields and focussing on fields that were expected to cause resonance at the fixed microwave frequency. No resonant signal was observed though, even for scans running over several days and with maximum microwave powers used. Measurement time was ultimately limited by eventual failure the O–rings that kept the sample sealed. UC emission was clearly visible though, and so triplet excitons and encounter complexes must have been present in the sample. The lack of ESR or ODMR signal from them was attributed to either their degree of spin polarisation being below detection limits, or that the glass ESR tube was absorbing a significant amount of the microwaves.

To address both of these issues at once, a new sealable ESR tube was ordered in quartz, and the E580 CW resonator cyrostat (completely different to the CF935) was installed. Unfortunately, delays in repairing this third cryostat (which had also arrived broken), as well as delays in arranging external glassblowing jobs for the quartz sample holder meant that no time for testing could be set aside. In the final days of work on this project, it was found that the extra depth of the resonator with cryostat installed meant that the quartz ESR tube was now too short to reach the sample position. This last disappointment marked the final exhaustion of time and passion for these experiments.

4.5 Outlook and Further Work

In hindsight a lot of the problems and delays encountered in this project can be attributed to the simultaneous pursuit of ODMR and ESR signal. This ambition only compounded the inherent challenges of studying photoexcited species in air sensitive liquids. Ancient wisdoms prevailed in this regard, with "no man [able to] serve two masters", and "better [being] the enemy of good". Had optical detection been strategically set as a lower priority, only excitation fibres would have been needed for UC samples. These would not have had to sit directly in the sample for emission collection, and would have allowed the use of permanently sealed quartz ESR tubes in the EMX and E580 resonators (both CW and pulsed). Proper sealing in these experiments may have potentially led to successful observation of ESR signal, as was the case for singlet fission. Alternatively had optical detection been made the top priority, prompt repair of the cryostat for the compact platform would have been even more justified, and might have even happened. This more flexible mindset would also have justified ignoring the arrival of the E580 pulsed system, and instead allocating the limited remaining candidature time (after cooling water was established) to the development of the laser duty cycle approach for the compact platform. Indeed, earlier results (Figures 4.3 and 4.8) demonstrated that at least two of the attempted approaches were viable, with magnetic field effects already observed before being abandoned. Identifying failure, planning for setbacks, and enforcing sensible limits to research ambition are perhaps the most valuable lessons taken by the author from postgraduate studies.

In the absence of experiments that observed them, it cannot be said with certainty what the effects of spin polarisation are on UC. The difficulty in observing any ESR signal strongly implies that this polarisation is not a feature of room temperature systems though, and that it is unlikely to be directly relevant in the development of UC applications. Instead, from the ML spectra and modelling performed in this work it seems very likely that molecular orientation in TTA is the critical factor in determining η. By engineering covalently linked emitter pairs with choreographed collisions and controlled orientations this might be exploited in the future, although the performance of such dimers may suffer from the low probability of both parts being simultaneously excited.[313–315]

Alternatively, recent reports of increased UC performance in microencapsulated emitter environments already seems to show that even very basic control of emitter collisions can improve UC systems. The intersection of the UC and molecular self assembly research communities is most likely a "Buddha's western paradise" towards which enterprising researchers should gravitate.[316–320] This insight may also have profound consequences in the field of OLEDs, where device morphology and the orientation of molecules in

the solid layers and films can be controlled using different fabrication methods, and examined using X-ray and neutron scattering techniques.[301,302,321]

For the continuation of fundamental studies, the further work from this project is clear. A working cryostat, an appropriate optical detector, and UC samples sealed in quartz should together be able to perform CW and pulsed ML, ODMR, and ESR — with time resolution in both spin and optical detection. The concurrent use of all three spectroscopic techniques would allow for a much more complete understanding of spin in the the encounter complex and TTA process, and possibly even some degree of control over it.

Finally, molecular dynamics simulations of UC emitter solutions should be pursued by those with an aptitude for computational chemistry. These may present the only way to link together the intrinsic and experimental average versions of η, and to suitably apply the Merrifield model to room temperature solutions. Such simulations may also allow rapid screening of proposed novel emitters to see if their naturally occurring collision orientations will lead to high UC performance, as well as pointing the way towards self-assembled structural targets for macromolecular chemists.

Chapter 5

Conclusion

"The way is never easy. Life hurts. To cure this pain is easy; just wait.
It will go away soon enough.
Yet there are things to be done.
Do them now, or they must be done next time, or the next, or the next."

—Narrator, *Saiyūki (Monkey)*, NTV 1978–1980

In this final chapter the research presented separately in previous chapters is brought together and reviewed. New contributions to knowledge and experimental capabilities from each of these endeavours are restated, as well as advances that have arisen from the interplay of efforts across these areas.

As always, new answers bring with them new questions. Recommendations are made for further work which may solidify or extend the preceding conclusions. Promising new avenues of inquiry for further understanding and optimising UC are also identified, either from the clarity of hindsight or the relentless expansion of scientific literature.

Finally, the question posed by the title of this document is addressed directly: What exactly *is* the role of spin in triplet-triplet annihilation upconversion?

5.1 General Comments

From the main work presented in Chapter 2, the kinetic and steady-state models for UC kinetics seem to work well enough for the specific situation investigated, and allow for k_1 to be determined in a straightforward manner. These kinds of models will continue being the roadmap to progress for UC system efficiencies, with emitter deuteration presenting one path to this through its effect on k_1. The limitations of the action spectrum method nonetheless demonstrate that simplifying assumptions (in this case the low efficiency regime Equation 2.7) should not be uncritically used as the basis of quantitative models.

The additional work in Chapter 2 shows that TTA likely already plays a role in some high efficiency OLEDs, and will almost certainly be consciously exploited for future high performance devices. Doing this kind of work to a high standard will require much closer collaborations between device fabricators and spectroscopists.

From the main work presented in Chapter 3 it was demonstrated that measuring k_2, although challenging, is achievable. Due to the potential ability of TA to directly detect emitter excitons, this kind of method is anticipated to become the standard for future kinetics studies. Of the different emitters investigated, most are similar in k_1 and k_2, with only limited changes upon deuteration. The low k_2 and high η for rubrene is attributed to directed but frustrated collisions, while rubrene UC enhancement in the presence of BPEA is most likely due to more rapid exciton transport. Heterogeneous TTA was found to have surprisingly poor performance, but this may be a property of the specific emitter pair used rather than a general feature of heterogeneous TTA.

The additional work in Chapter 3 shows that UC emitters can be bleached by sustained excitation even in the absence of oxygen, although the precise mechanism remains a mystery. Nonetheless, in real conditions this is unlikely to significantly detract from UC device longevity, as unrealistically high photon energies and fluxes were used in testing.

From the main work in Chapter 4, a pressing need to investigate, formalise, and tabulate η was identified. Magnetic field effects on η were pursued through simulations and experiments, and experimentally found to be small for liquid UC systems. Magnetic resonance techniques may be able to reveal more about the molecular and spin properties that give rise to η, but measuring platforms for these studies are not yet sufficiently developed — although in several attempts this project came tantalisingly close.

The absence of resonant signal in even the final attempt at these measurements implies that there is no significant spin polarisation of emitter triplets at room temperature. In contrast, the cryogenic conditions and spin polarisation needed for ESR present a large departure from the real conditions in which a UC device is likely to operate.

5.2 Future Work

Several improvements to the TA spectrometer were outlined previously, which in future may allow for the detection of emitter bleaches and triplet state absorptions. This is in contrast to the approach that was devised here, which inferred their populations from TRPL. A more sensitive implementation of TA would give rise to greatly simplified analysis procedures, avoiding heavy reliance on kinetic models. Eventually, this high throughput method of determining k_1 and k_2 could serve to enable a range of rigorous parameter studies on UC systems, including the effects of temperature, solvent, and component concentrations. At present the effects of these sorts of secondary system properties are at best assumed from models, but most commonly ignored. [322,323]

Similar to the tabulation of k_{TET}, k_1, and k_2, a tabulation study of η for different emitters is strongly justified at this point. This is despite the differences in definition between the (experimentally accessible) average and (theory based) intrinsic versions of η. Although it has been confirmed that the average efficiency of TTA is not limited by spin statistics, it remains to be seen whether this is the case for individual collisions. In tandem with experimental studies, molecular dynamics may be able to predict these intrinsic values, and how directed or frustrated collisions can add to η and detract from k_2. With this understanding, new emitters may be designed that maximise both properties, leading to a new class of highly efficient, choreographed UC emitters.

A robust implementation of ESR and ODMR would also give significant insight into the TTA process, although this may be some years away from implementation. Nonetheless, the ability to directly detect and manipulate spin species in TTA is an exciting prospect. With sufficient sensitivity, the formation of triplet and quintet pair states may even be directly confirmed or conclusively ruled out. It may in future even be possible to combine this technique with TRPL or TA, in order to observe time-resolved changes in decay rates as magnetic fields are applied and triplet populations biased using resonance.

All of these suggestions apply just as validly for OLEDs, where TTA processes will likely take on different properties due to the fixed orientations of emitters. While UC applications to PV are ultimately an attempt to address civilisation's energy supply, applications of UC to OLEDs can in tandem partially address energy demand.

Finally, a true UC ageing study is also proposed, to see how well these systems cope with sustained excitation under realistic conditions. Such feasibility studies will almost certainly become necessary as the responsibility for development of UC technology passes from fundamental to applied scientists, and then on to engineers and finally businesses.

5.3 Epilogue

Spin is clearly an important feature of triplet states, and its conservation in TTA is a key channel by which emission can be achieved. At room temperature the emitter spin states remain near degenerate though, and there is little evidence of spin polarisation in real UC systems under CW excitation. While an initial spin polarisation of the sensitiser may exist (flowing on to the emitter through spin coherent TET), extended spin polarisation for room temperature solutions seems an unlikely outcome or goal. With the spin states randomised, emitter pairs only need to access the singlet pair state briefly, and the pair state multiplicity will itself continue to evolve as the individual exciton wavefunctions dephase and rephase. For emitters with inaccessible T_2 and Q_1 states, the only clear outcomes competing with emission are dissociation or k_1 decay. Therefore all emitter collisions may potentially be emissive, regardless of individual exciton spin states.

From this analysis it appears that the specific spin state of emitter triplets does not matter that much in practical circumstances. While spin related spectroscopies will undoubtedly be a useful tool for fundamental studies (and especially in detecting and understanding the nature of the encounter complex), direct control of spin is unlikely to be a critical factor in future applications of UC. It is overwhelmingly likely that improved understanding will lead to improved UC performance, although — as with all future research — precisely how this might happen cannot be predicted with certainty.

Favorable collision orientations then emerge as the key determining factor for η, as hinted at by the large magnetic field effects observed for ordered crystals and films. By maximising the singlet character of directed collisions, encounter complexes may form singlet pair state faster than other states and pair dissociation. Rubrene is already thought to take advantage of this, resulting in its large average η but small k_2. This raises the possibility that highly efficient emitters could be engineered *via* covalent or directed intermolecular forces. This insight aligns with current research themes to design scaffolded materials for maximising $[S]$ and $[E]$ in UC systems, which will also require control over orientation and packing to prevent aggregate quenching.

So, what then *is* the role of spin in TTA UC? At present it seems that spin may in fact have no practical role in UC beyond simply being conserved, allowing TTA to occur in the first place. Although a somewhat anticlimactic conclusion, the unparalleled wisdom of *Monkey* once again provides some perspective, and a fitting concluding remark:

> *"A man may waste a lifetime growing rich or chasing power.*
> *What is a life that's not wasted? Perhaps one in which we learn a little."*
>
> —Narrator, *Saiyūki (Monkey)*, NTV 1978–1980

Bibliography

[1] *BP Statistical Review of World Energy*; BP P.L.C., 2016.

[2] DeLong, J. *Estimating World GDP, One Million B.C. - Present*; Department of Economics, U.C. Berkeley, 1988.

[3] *Gross Domestic Product 2015*; The World Bank DataBank, 2015.

[4] *The World at Six Billion*; Population Division, Department of Economic and Social Affairs, United Nations, 1999.

[5] *World Population Prospects: The 2015 Revision*; Population Division, Department of Economic and Social Affairs, United Nations, 2015.

[6] Smil, V. *Energy Transitions: History, Requirements, Prospects*; Praeger, 2010.

[7] Wolczuk, K. *Eurasian Geography and Economics* **2016**, *57*, 113–137.

[8] Jones, T. C. *Journal of American History* **2012**, *99*, 208.

[9] *Nature Clim. Change* **2017**, *7*, 87–87.

[10] Qi, D.; Chen, L.; Chen, B.; Gao, Z.; Zhong, W.; Feely, R. A.; Anderson, L. G.; Sun, H.; Chen, J.; Chen, M.; Zhan, L.; Zhang, Y.; Cai, W.-J. *Nature Clim. Change* **2017**, *7*, 195–199.

[11] Grätzel, M. *Accounts of Chemical Research* **2009**, *42*, 1788–1798, PMID: 19715294.

[12] *International Technology Roadmap for Photovoltaic: Results 2016, Eighth Edition*; International Technology Roadmap for Photovoltaic, 2017.

[13] U.S. Department of Energy, *International Energy Outlook 2015*; Energy Information Administration, 2015.

[14] Hirth, L.; Steckel, J. C. *Environmental Research Letters* **2016**, *11*, 114010.

[15] Obama, B. *Science* **2017**.

[16] Farrell, J.; Grimley, M. *Public Rooftop Revolution*; Institute for Local Self-Reliance, 2015.

[17] Bakulin, A. A.; Rao, A.; Pavelyev, V. G.; van Loosdrecht, P. H. M.; Pshenichnikov, M. S.; Niedzialek, D.; Cornil, J.; Beljonne, D.; Friend, R. H. *Science* **2012**, *335*, 1340–1344.

[18] Green, M. A. *Solar Cells -Operating Principles, Technology and System Application*; Prentice-Hall: Englewood Cliffs, N.J., 1992.

[19] Goetzberger, A.; Knobloch, J.; Voss, B. *Crystalline Silicon Solar Cells*; Wiley, 1998.

[20] Shockley, W.; Queisser, H. J. *J. Appl. Phys.* **1961**, *32*, 510–519.

[21] Bremner, S. P.; Levy, M. Y.; Honsberg, C. B. *Appl. Phys. Lett.* **2008**, *92*, 171110.

[22] Hirst, L. C.; Ekins-Daukes, N. J. *Progress in Photovoltaics: Research and Applications* **2011**, *19*, 286–293.

[23] Tayebjee, M. J. Y.; McCamey, D. R.; Schmidt, T. W. *J. Phys. Chem. Lett.* **2015**, *6*, 2367–2378.

[24] Green, M. A. *Progress in Photovoltaics* **2009**, *17*, 183–189.

[25] Shah, A.; Torres, P.; Tscharner, R.; Wyrsch, N.; Keppner, H. *Science* **1999**, *285*, 692–698.

[26] *Thin-film Silicon Solar Cells*; Shah, A., Ed.; EPFL Press: Lausanne, Switzerland, 2010.

[27] Kayser, D. *Applied Energy* **2016**, *174*, 144–152.

[28] *National Renewable Energy Laboratory: Best Research-Cell Efficiencies*; National Renewable Energy Laboratory, United States Department of Energy, 2017.

[29] Hagfeldt, A.; Boschloo, G.; Sun, L.; Kloo, L.; Pettersson, H. *Chem. Rev.* **2010**, *110*, 6595–6663.

[30] Daeneke, T.; Mozer, A. J.; H., K. T.; Duffy, N. W.; Holmes, A. B.; Bach, U.; Spiccia, L. *Energ. Environ. Sci.* **2012**, *5*, 7090–7099.

[31] O'Regan, B.; Grätzel, M. *Nature* **1991**, *353*, 737–740.

[32] Grätzel, M. *J. Photoch. Photobio. C* **2003**, *4*, 145–153.

[33] Yella, A.; Lee, H.-W.; Tsao, H. N.; Yi, C.; Chandiran, A. K.; Khaja Nazeeruddin, M.; Diau, E. W.-G.; Yeh, C.-Y.; ; Zakeeruddin, S. M.; Graetzel, M. *Science* **2011**, *334*, 629.

[34] Green, M. A.; Emery, K.; Hishikawa, Y.; Warta, W.; Dunlop, E. D. *Prog. Photovolt: Res. Appl.* **2012**, *20*, 606–614.

[35] Green, M. A.; Emery, K.; Hishikawa, Y.; Warta, W.; Dunlop, E. D. *Prog. Photovolt: Res. Appl.* **2014**, *22*, 701–710.

[36] Horiuchi, T.; Miura, H.; Sumioka, K.; Uchida, S. *J. Amer. Chem. Soc.* **2004**, *126*, 12218–12219.

[37] Green, M. A.; Ho-Baillie, A.; Snaith, H. J. *Nat Photon* **2014**, *8*, 506–514.

[38] Green, M. A. *Third generation photovoltaics advanced solar energy conversion*; Springer: Berlin; Heidelberg; New York, 2006.

[39] de Wild, J.; Meijerink, A.; Rath, J. K.; van Sark, W. G. J. H. M.; Schropp, R. E. I. *Solar Energy Materials and Solar Cells* **2010**, *94*, 1919–1922.

[40] Fischer, S.; Goldschmidt, J. C.; Löper, P.; Bauer, G. H.; Brüggemann, R.; Krämer, K.; Biner, D.; Hermle, M.; Glunz, S. W. *J. Appl. Phys.* **2010**, *108*, 044912.

[41] Johnson, C. M.; Conibeer, G. J. *Journal of Applied Physics* **2012**, *112*, 103108.

[42] Kirk, A. P.; Fischetti, M. V. *Phys. Rev. B* **2012**, *86*, 165206.

[43] *Optimal Materials and Deposition Technique Lead to Cost-Effective Solar Cell with Best-Ever Conversion Efficiency (Fact Sheet). NREL (National Renewable Energy Laboratory)*, 2012.

[44] Green, M. A.; Emery, K.; Hishikawa, Y.; Warta, W. *Prog. Photovolt: Res. Appl.* **2011**, *19*, 84–92.

[45] Karam, N. H. et al. *Solar Energy Materials and Solar Cells* **2001**, *66*, 453–466.

[46] Green, M. A.; Keevers, M. J.; Thomas, I.; Lasich, J. B.; Emery, K.; King, R. R. *Progress in Photovoltaics: Research and Applications* **2015**, *23*, 685–691, PIP-14-309.R1.

[47] Cheng, Y. Y.; Nattestad, A.; Schulze, T. F.; MacQueen, R. W.; Fuckel, B.; Lips, K.; Wallace, G. G.; Khoury, T.; Crossley, M. J.; Schmidt, T. W. *Chem. Sci.* **2016**, *7*, 559–568.

[48] Cheng, Y. Y.; Fückel, B.; MacQueen, R. W.; Khoury, T.; Clady, R. G. C. R.; Schulze, T. F.; Ekins-Daukes, N. J.; Crossley, M. J.; Stannowski, B.; Lips, K.; Schmidt, T. W. *Energy Environ. Sci.* **2012**.

[49] Schulze, T. F.; Czolk, J.; Cheng, Y.-Y.; Fückel, B.; MacQueen, R. W.; Khoury, T.; Crossley, M. J.; Stannowski, B.; Lips, K.; Lemmer, U.; Colsmann, A.; Schmidt, T. W. *The Journal of Physical Chemistry C* **2012**, *116*, 22794–22801.

[50] van der Ende, B. M.; Aarts, L.; Meijerink, A. *Phys. Chem. Chem. Phys.* **2009**, *11*, 11081–11095.

[51] Shen, Y. R. *The Principles of Nonlinear Optics*; Wiley-Interscience: New York, 1984.

[52] Boyd, R. *Nonlinear Optics*; Electronics & Electrical; Academic Press, 2003.

[53] Hayat, A.; Nevet, A.; Ginzburg, P.; Orenstein, M. *Semiconductor Science and Technology* **2011**, *26*, 083001.

[54] Baluschev, S.; Yakutkin, V.; Miteva, T.; Wegner, G.; Roberts, T.; Nelles, G.; Yasuda, A.; Chernov, S.; Aleshchenkov, S.; Cheprakov, A. *New J. Phys.* **2008**, *10*, 013007.

[55] Baluschev, S.; Miteva, T. Non-Coherent Up-Conversion in Multi-Component Organic Systems. In *Next Generation of Photovoltaics: New Concepts*; Springer, 2012; pp 157–190.

[56] Atre, A. C.; Dionne, J. A. *J. Appl. Phys.* **2011**, *110*, 034505.

[57] Auckett, J. E.; Cheng, Y.; Khoury, T.; Clady, R. G. C. R.; Ekins-Daukes, N. J.; Crossley, M. J.; Schmidt, T. W. *Journal of Physics: Conference Series* **2009**, *185*, 012002:1–4.

[58] Singh-Rachford, T. N.; Castellano, F. N. *Coord. Chem. Rev.* **2010**, *254*, 2560–2573.

[59] Parker, C. A.; Hatchard, C. G. *Trans. Faraday Soc.* **1961**, *57*, 1894–1904.

[60] Parker, C.; Hatchard, C. *Transactions of the Faraday Society* **1963**, *59*, 284–295.

[61] Lehnhardt, M.; Riedl, T.; Rabe, T.; Kowalsky, W. *Organic Electronics* **2011**, *12*, 486–491.

[62] Dexter, D. L. *J. Chem. Phys.* **1953**, *21*, 836–850.

[63] Adachi, C.; Kwong, R. C.; Djurovich, P.; Adamovich, V.; Baldo, M. A.; Thompson, M. E.; Forrest, S. R. *Applied Physics Letters* **2001**, *79*, 2082–2084.

[64] Islangulov, R. R.; Kozlov, D. V.; Castellano, F. N. *Chem. Commun.* **2005**, 3776–3778.

[65] Parker, C. A. *Proc. Roy. Soc. A* **1963**, *276*, 125–135.

[66] Monguzzi, A.; Tubino, R.; Meinardi, F. *Physical Review B* **2008**, *77*, 155122, PRB.

[67] Gray, V.; Dzebo, D.; Abrahamsson, M.; Albinsson, B.; Moth-Poulsen, K. *Physical Chemistry Chemical Physics* **2014**, *16*, 10345–10352.

[68] Clark, J. L.; Rumbles, G. *Phys. Rev. Lett.* **1996**, *76*, 2037–2040.

[69] Tao, Y.; Yuan, K.; Chen, T.; Xu, P.; Li, H.; Chen, R.; Zheng, C.; Zhang, L.; Huang, W. *Advanced Materials* **2014**, *26*, 7931–7958.

[70] Sripathy, K.; MacQueen, R. W.; Peterson, J. R.; Cheng, Y. Y.; Dvorak, M.; McCamey, D. R.; Treat, N. D.; Stingelin, N.; Schmidt, T. W. *J. Mater. Chem. C* **2015**, *3*, 616–622.

[71] Baluschev, S.; Jacob, J.; Avlasevich, Y. S.; Keivanidis, P. E.; Miteva, T.; Yasuda, A.; Nelles, G.; Grimsdale, A. C.; Müllen, K.; Wegner, G. *ChemPhysChem* **2005**, *6*, 1250–1253.

[72] Keivanidis, P. E.; Baluschev, S.; Lieser, G.; Wegner, G. *ChemPhysChem* **2009**, *10*, 2316–2326.

[73] Duan, P.; Yanai, N.; Kimizuka, N. *J. Am. Chem. Soc.* **2013**, *135*, 19056–19059.

[74] Hofmann, C.; Herter, B.; Gutmann, J.; Löffler, J.; Fischer, S.; Wolf, S.; Piper, R.; Ekins-Daukes, N.; Treat, N.; Goldschmidt, J. C. Proc. SPIE 91400H–91400H–9, 2014.

[75] Islangulov, R. R.; Lott, J.; Weder, C.; Castellano, F. N. *J. Am. Chem. Soc.* **2007**, *129*, 12652–12653.

[76] Kang, J.-H.; Reichmanis, E. *Angew. Chem.* **2012**, *124*, 12011–12014.

[77] Keivanidis, P. E.; Baluschev, S.; Miteva, T.; Nelles, G.; Scherf, U.; Yasuda, A.; Wegner, G. *Adv. Mater.* **2003**, *15*, 2095–2098.

[78] Tayebjee, M. J. Y.; Gray-Weale, A. A.; Schmidt, T. W. *J. Phys. Chem. Lett.* **2012**, *3*, 2749–2754.

[79] Hanna, M. C.; Nozik, A. J. *Journal of Applied Physics* **2006**, *100*, year.

[80] Chan, W.-L.; Ligges, M.; Zhu, X. Y. *Nat Chem* **2012**, *4*, 840–845, 10.1038/nchem.1436.

[81] Smith, M. B.; Michl, J. *Chemical reviews* **2010**, *110*, 6891–6936.

[82] Walker, B. J.; Musser, A. J.; Beljonne, D.; Friend, R. H. *Nat Chem* **2013**, *5*, 1019–1024.

[83] Auzel, F. *Chemical Reviews* **2004**, *104*, 139–173.

[84] Ivaturi, A.; MacDougall, S. K.; Martín-Rodríguez, R.; Quintanilla, M.; Marques-Hueso, J.; Krämer, K. W.; Meijerink, A.; Richards, B. S. *J. Appl. Phys.* **2013**, *114*, 013505.

[85] Fischer, S.; Fröhlich, B.; Steinkemper, H.; Krämer, K.; Goldschmidt, J. *Sol. Energ. Mat. Sol. C.* **2014**, *122*, 197 – 207.

[86] MacDougall, S. K.; Ivaturi, A.; Marques-Hueso, J.; Krämer, K. W.; Richards, B. S. *Sol. Ener. Mat. Solar Cells* **2014**, *128*, 18 – 26.

[87] Kondakov, D. Y. *Philosophical Transactions of the Royal Society of London A: Mathematical, Physical and Engineering Sciences* **2015**, *373*, year.

[88] Yersin, H.; Rausch, A. F.; Czerwieniec, R.; Hofbeck, T.; Fischer, T. *Coordination Chemistry Reviews* **2011**, *255*, 2622–2652.

[89] Adachi, C. *Japanese Journal of Applied Physics* **2014**, *53*, 060101.

[90] Forrest, S. R. *Nature* **2004**, *428*, 911–918.

[91] Kersten, S. P.; Schellekens, A. J.; Koopmans, B.; Bobbert, P. A. *Physical Review Letters* **2011**, *106*, 197402–.

[92] Naber, W. J. M. *Journal of Physics D: Applied Physics* **2007**, *40*, R205–.

[93] Kondakov, D. Y. *Journal of Applied Physics* **2007**, *102*, –.

[94] Ameri, T.; Dennler, G.; Lungenschmied, C.; Brabec, C. J. *Energy Environ. Sci.* **2009**, *2*, 347–363.

[95] Miteva, T.; Yakutkin, V.; Nelles, G.; Baluschev, S. *New J. Phys.* **2008**, *10*, 103002.

[96] Ullah, M.; Yambem, S. D.; Moore, E. G.; Namdas, E. B.; Pandey, A. K. *Advanced Electronic Materials* **2015**, *1*, 1500229–n/a.

[97] Zare, R. N. *Angular momentum : understanding spatial aspects in chemistry and physics*; Wiley: New York, 1987.

[98] Atherton, N. M. *Principles of Electron Paramagnetic Resonance*; Ellis Horwood Limited, Chichester, England, 1993.

[99] Köhler, A.; Bässler, H. *Materials Science and Engineering: R: Reports* **2009**, *66*, 71–109.

[100] Bässler, H.; Köhler, A. Charge transport in organic semiconductors. In *Unimolecular and Supramolecular Electronics I*; Springer, 2012; pp 1–65.

[101] Janssen, P.; Wouters, S. H.; Cox, M.; Koopmans, B. *Organic Electronics* **2014**.

[102] Behrends, J.; Lips, K.; Boehme, C. *Physical Review B* **2009**, *80*, 045207.

[103] Herring, T. W.; Lee, S.-Y.; McCamey, D. R.; Taylor, P. C.; Lips, K.; Hu, J.; Zhu, F.; Madan, A.; Boehme, C. *Physical Review B* **2009**, *79*, 195205–.

[104] Kaplan, D.; Solomon, I.; Mott, N. F. *Journal de Physique Lettres* **1978**, *39*, 51–54.

[105] Pawlik, T. D.; Kondakova, M. E.; Giesen, D. J.; Deaton, J. C.; Kondakov, D. Y. *Journal of the Society for Information Display* **2009**, *17*, 279–286.

[106] Rao, A.; Chow, P. C. Y.; Gelinas, S.; Schlenker, C. W.; Li, C.-Z.; Yip, H.-L.; Jen, A. K.-Y.; Ginger, D. S.; Friend, R. H. *Nature* **2013**, *500*, 435–439.

[107] Baldo, M. A.; Segal, M.; Shinar, J.; Soos, Z. G. *Physical Review B* **2007**, *75*, 246202–.

[108] Jankus, V.; Snedden, E. W.; Bright, D. W.; Whittle, V. L.; Williams, J. A. G.; Monkman, A. *Advanced Functional Materials* **2013**, *23*, 384–393.

[109] Reineke, S.; Walzer, K.; Leo, K. *Physical Review B* **2007**, *75*, 125328.

[110] Sheng, Y.; Nguyen, T. D.; Veeraraghavan, G.; Mermer, ; Wohlgenannt, M. *Physical Review B* **2007**, *75*, 035202–.

[111] Shan, T.; Gao, Z.; Tang, X.; He, X.; Gao, Y.; Li, J.; Sun, X.; Liu, Y.; Liu, H.; Yang, B.; Lu, P.; Ma, Y. *Dyes and Pigments* **2017**, *142*, 189 – 197.

[112] Gardonio, S.; Gregoratti, L.; Melpignano, P.; Aballe, L.; Biondo, V.; Zamboni, R.; Murgia, M.; Caria, S.; Kiskinova, M. *Organic Electronics* **2007**, *8*, 37–43.

[113] Reese, M. O.; Morfa, A. J.; White, M. S.; Kopidakis, N.; Shaheen, S. E.; Rumbles, G.; Ginley, D. S. *Solar Energy Materials and Solar Cells* **2008**, *92*, 746–752.

[114] Aziz, H.; Popovic, Z. D.; Hu, N.-X.; Hor, A.-M.; Xu, G. *Science* **1999**, *283*, 1900–1902.

[115] King, S. M.; Cass, M.; Pintani, M.; Coward, C.; Dias, F. B.; Monkman, A. P.; Roberts, M. *Journal of Applied Physics* **2011**, *109*, year.

[116] Popovic, Z. D.; Aziz, H.; Hu, N.-X.; Ioannidis, A.; dos Anjos, P. N. *Journal of Applied Physics* **2001**, *89*, 4673–4675.

[117] Schmidt, T. D.; Buchschuster, A.; Holm, M.; Nowy, S.; Weber, J. A.; Brütting, W. *Synthetic Metals* **2011**, *161*, 637–641.

[118] Xiang, C.; Peng, C.; Chen, Y.; So, F. *Small* **2015**, *11*, 5439–5443.

[119] Kohler, A.; Bassler, H. *Journal of Materials Chemistry* **2011**, *21*, 4003–4011.

[120] Wilson, J. S.; Dhoot, A. S.; Seeley, A. J. A. B.; Khan, M. S.; Köhler, A.; Friend, R. H. *Nature* **2001**, *413*, 828–831.

[121] *Electron paramagnetic resonance : from fundamental research to pioneering applications Zavoisky Award / [scientific editor, Kev M. Salikhov]*; AXAS Publishing Ltd.: Wellington, New Zealand :, 2009; p 209, (Kev Minullinovich).

[122] Piland, G. B.; Burdett, J. J.; Kurunthu, D.; Bardeen, C. J. *The Journal of Physical Chemistry C* **2013**, *117*, 1224–1236.

[123] Tapping, P. C.; Huang, D. M. *The Journal of Physical Chemistry C* **2016**, *120*, 25151–25157.

[124] Sakurai, J. J.; Tuan, S. F. *Modern quantum mechanics*; Addison-Wesley Reading (Mass.), 1994; Vol. 104.

[125] Johnson, R. C.; Merrifield, R. E. *Physical Review B* **1970**, *1*, 896–.

[126] Benk, H.; Sixl, H. *Molecular Physics* **1981**, *42*, 779–801.

[127] Forrest, S. R. *Philosophical Transactions of the Royal Society of London A: Mathematical, Physical and Engineering Sciences* **2015**, *373*, year.

[128] Atkins, P.; Evans, G. *Molecular Physics* **1975**, *29*, 921–935.

[129] Haefele, A.; Blumhoff, J.; Khnayzer, R. S.; Castellano, F. N. *J. Phys. Chem. Lett.* **2012**, *3*, 299–303.

[130] Johnson, R. C.; Merrifield, R. E. *Physical Review B* **1970**, *1*, 896–902, PRB.

[131] Deng, F.; Blumhoff, J.; Castellano, F. N. *J. Phys. Chem. A* **2013**, *117*, 4412–4419.

[132] Deng, F.; Lazorski, M. S.; Castellano, F. N. *Philosophical Transactions of the Royal Society of London A: Mathematical, Physical and Engineering Sciences* **2015**, *373*, year.

[133] Atherton, N. M. *Principles of electron spin resonance*; Ellis Horwood and PTR Prentice Hall, Physical Chemistry Series, Ellis Horwood, Chichester, 1993.

[134] Behrends, J. Ph.D. thesis, Freie Universität Berlin, Germany, 2010.

[135] Atkins, P. W.; Friedman, R. S. *Molecular quantum mechanics*; Oxford University Press: New York, 1996.

[136] Barrett, S. E.; Tycko, R.; Pfeiffer, L. N.; West, K. W. *Physical Review Letters* **1994**, *72*, 1368.

[137] Boehme, C.; L., K. *Physical Review B* **2003**, *68*, 245105.

[138] Dreher, L.; Hoehne, F.; Morishita, H.; Huebl, H.; Stutzmann, M.; Itoh, K. M.; Brandt, M. S. *Physical Review B* **2015**, *91*, 075314.

[139] Boehme, C.; McCamey, D. R.; van Schooten, K. J.; Baker, W. J.; Lee, S.-Y.; Paik, S.-Y.; Lupton, J. M. *physica Status Solidi (b)* **2009**, *246*, 2750–2755.

[140] Ernst, R. R.; Bodenhausen, G.; Wokaun, A. *Principles of nuclear magnetic resonance in one and two dimensions*; Oxford University Press, 1991.

[141] Hahn, E. L. *Physical Review* **1950**, *80*, 580.

[142] Schweiger, A.; Jeschke, G. *Principles of Pulsed Electron Paramagnetic Resonance*; Oxford University Press, 2001.

[143] Slichter, C. P. *Principles of Magnetic Resonance*, third edition ed.; Springer: New York, 1989.

[144] Tayebjee, M. J. Y.; Sanders, S. N.; Kumarasamy, E.; Campos, L. M.; Sfeir, M. Y.; McCamey, D. R. *Nat Phys* **2017**, *13*, 182–188.

[145] Bain, A. D. *Journal of Magnetic Resonance (1969)* **1984**, *56*, 418–427.

[146] Swanson, L. S.; Shinar, J.; Yoshino, K. *Physical Review Letters* **1990**, *65*, 1140–.

[147] Duan, P.; Yanai, N.; Kimizuka, N. *J. Amer. Chem. Soc.* **2013**, *135*, 19056–19059.

[148] Fückel, B.; Roberts, D. A.; Cheng, Y.; Clady, R. G. C. R.; Piper, R. B.; Ekins-Daukes, N. J.; Crossley, M. J.; Schmidt, T. W. *Journal of Physical Chemistry Letters* **2011**, *2*, 966–971.

[149] Johnson, R. C.; Ern, V.; Wiley, D. W.; Merrifield, R. E. *Chemical Physics Letters* **1971**, *11*, 188–191.

[150] Monguzzi, A.; Mezyk, J.; Scotognella, F.; Tubino, R.; Meinardi, F. *Phys. Rev. B* **2008**, *78*, 195112.

[151] Cheng, Y.; Khoury, T.; Clady, R. G. C. R.; Tayebjee, M. J. Y.; Ekins-Daukes, N. J.; Crossley, M. J.; Schmidt, T. W. *Phys. Chem. Chem. Phys.* **2010**, *12*, 66–71.

[152] Bachilo, S. M.; Weisman, R. B. *J. Phys. Chem. A* **2000**, *104*, 7711–7714.

[153] Cao, X.; Hu, B.; Zhang, P. *J. Phys. Chem. Lett.* **2013**, *4*, 2334–2338.

[154] Zhao, J.; Ji, S.; Guo, H. *RSC Adv.* **2011**, *1*, 937–950.

[155] Auckett, J.; Cheng, Y. Y.; Khoury, T.; Clady, R. G. C. R.; Ekins-Daukes, N. J.; Crossley, M. J.; Schmidt, T. W. *J. Phys.: Conf. Ser.* **2009**, *185*, 012002.

[156] Kim, J.-H.; Deng, F.; Castellano, F. N.; Kim, J.-H. *Chem. Mater.* **2012**, *24*, 2250–2252.

[157] Laquai, F.; Wegner, G.; Im, C.; Büsing, A.; Heun, S. *J. Chem. Phys.* **2005**, *123*, 074902.

[158] Monguzzi, A.; Bianchi, F.; Bianchi, A.; Mauri, M.; Simonutti, R.; Ruffo, R.; Tubino, R.; Meinardi, F. *Adv. Energ. Mater.* **2013**, *3*, 680–686.

[159] Hoseinkhani, S.; Tubino, R.; Meinardi, F.; Monguzzi, A. *Phys. Chem. Chem. Phys.* **2015**, *17*, 4020–4024.

[160] Simon, Y. C.; Weder, C. *J. Mater. Chem.* **2012**, *22*, 20817.

[161] Zhao, J. Z.; Ji, S. M.; Guo, H. M. *Rsc Advances* **2011**, *1*, 937–950.

[162] Cheng, Y.; Fückel, B.; Khoury, T.; Clady, R. G. C. R.; Tayebjee, M. J. Y.; Ekins-Daukes, N. J.; Crossley, M. J.; Schmidt, T. W. *J. Phys. Chem. Lett.* **2010**, *1*, 1795–1799.

[163] Singh-Rachford, T. N.; Castellano, F. N. *J. Phys. Chem. Lett.* **2009**, *1*, 195–200.

[164] Singh-Rachford, T. N.; Castellano, F. N. *J. Phys. Chem. A* **2008**, *112*, 3550–3556.

[165] Gray, V.; Dzebo, D.; Lundin, A.; Alborzpour, J.; Abrahamsson, M.; Albinsson, B.; Moth-Poulsen, K. *J. Mater. Chem. C* **2015**, *3*, 11111–11121.

[166] Schmidt, T. W.; Castellano, F. N. *The Journal of Physical Chemistry Letters* **2014**, *5*, 4062–4072.

[167] Monguzzi, A.; Tubino, R.; Hoseinkhani, S.; Campione, M.; Meinardi, F. *Phys. Chem. Chem. Phys.* **2012**, *14*, 4322–4332.

[168] Singh-Rachford, T. N.; Castellano, F. N. *Inorg. Chem.* **2009**, *48*, 2541–2548.

[169] *9,10-Bis(phenylethynyl)anthracene*, `http://omlc.org/spectra/PhotochemCAD/html/044.html`, Accessed: 2017-03-30.

[170] Cheng, Y. Y.; Fückel, B.; Khoury, T.; Clady, R. G. C. R.; Ekins-Daukes, N. J.; Crossley, M. J.; Schmidt, T. W. *J. Phys. Chem. A* **2011**, *115*, 1047–1053.

[171] Mongin, C.; Golden, J. H.; Castellano, F. N. *ACS Applied Materials & Interfaces* **2016**, *8*, 24038–24048, PMID: 27479333.

[172] Ye, C.; Zhou, L.; Wang, X.; Liang, Z. *Phys. Chem. Chem. Phys.* **2016**, *18*, 10818–10835.

[173] Schulze, T. F.; Schmidt, T. W. *Energy Environ. Sci.* **2015**, *8*, 103–125.

[174] Sugunan, S. K.; Tripathy, U.; Brunet, S. M. K.; Paige, M. F.; Steer, R. P. *J. Phys. Chem. A* **2009**, *113*, 8548–8556.

[175] Baluschev, S.; Yakutkin, V.; Wegner, G.; Miteva, T.; Nelles, G.; Yasuda, A.; Chernov, S.; Aleshchenkov, S.; Cheprakov, A. *Applied Physics Letters* **2007**, *90*, 181103.

[176] Fischer, S.; Ivaturi, A.; Fröhlich, B.; Rudiger, M.; Richter, A.; Kramer, K.; Richards, B.; Goldschmidt, J. *IEEE J. Photovolt.* **2014**, *4*, 183–189.

[177] Goldschmidt, J. C.; Loper, P.; Fischer, S.; Janz, S.; Peters, M.; Glunz, S.; Willeke, G.; Lifshitz, E.; Kramer, K.; Biner, D. Advanced upconverter systems with spectral and geometric concentration for high upconversion efficiencies. *Conference on Optoelectronic and Microelectronic Materials and Devices (COMMAD)*, 2008; pp 307–311.

[178] Shalav, A.; Richards, B. S.; Green, M. A. *Solar Energy Materials and Solar Cells* **2007**, *91*, 829–842.

[179] Yu, Z.-G. *Physical Review Letters* **2011**, *106*, 106602.

[180] Sun, J.; Zhong, F.; Yi, X.; Zhao, J. *Inorg. Chem.* **2013**, *52*, 6299–6310.

[181] Zhao, W.; Castellano, F. N. *J. Phys. Chem. A* **2006**, *110*, 11440–11445.

[182] Yakutkin, V.; Aleshchenkov, S.; Chernov, S.; Miteva, T.; Nelles, G.; Cheprakov, A.; Baluschev, S. *Chem. – Eur. J.* **2008**, *14*, 9846–9850.

[183] Yella, A.; Mai, C.-L.; Zakeeruddin, S. M.; Chang, S.-N.; Hsieh, C.-H.; Yeh, C.-Y.; Grätzel, M. *Angew. Chem.* **2014**, *126*, 3017–3021.

[184] Whited, M. T.; Djurovich, P. I.; Roberts, S. T.; Durrell, A. C.; Schlenker, C. W.; Bradforth, S. E.; Thompson, M. E. *Journal of the American Chemical Society* **2011**, *133*, 88–96, PMID: 21142032.

[185] Peng, J.; Jiang, X.; Guo, X.; Zhao, D.; Ma, Y. *Chem. Commun.* **2014**, *50*, 7828–7830.

[186] Eickelkamp, T.; Roth, S.; Mehring, M. *Molecular Physics* **1998**, *95*, 967–972.

[187] Hoseinkhani, S.; Tubino, R.; Meinardi, F.; Monguzzi, A. *Phys. Chem. Chem. Phys.* **2015**, *17*, 4020–4024.

[188] Singh-Rachford, T. N.; Castellano, F. N. *Coordination Chemistry Reviews* **2010**, *254*, 2560 – 2573, 18th International Symposium on the Photochemistry and Photophysics of Coordination Compounds Sapporo, 2009.

[189] Hutchison, C. A.; Mangum, B. W. *The Journal of Chemical Physics* **1960**, *32*, 1261–1262.

[190] Lin, S. H.; Bersohn, R. *The Journal of Chemical Physics* **1968**, *48*, 2732–2736.

[191] Siebrand, W. *The Journal of Chemical Physics* **1967**, *47*, 2411–2422.

[192] MacQueen, R. W.; Cheng, Y. Y.; Danos, A. N.; Lips, K.; Schmidt, T. W. *RSC Adv.* **2014**, *4*, 52749–52756.

[193] Danos, A.; MacQueen, R. W.; Cheng, Y. Y.; Dvořák, M.; Darwish, T. A.; McCamey, D. R.; Schmidt, T. W. *J. Phys. Chem. Lett.* **2015**, *6*, 3061–3066.

[194] Parker, C. A.; Joyce, T. A. *Chem. Commun. (London)* **1966**, 108b–109.

[195] Siebrand, W. *Chemical Physics Letters* **1970**, *6*, 192 – 194.

[196] Henry, B. R.; Siebrand, W. *The Journal of Chemical Physics* **1971**, *54*, 1072–1085.

[197] Turro, N. J.; Ramamurthy, V.; Scaiano, J. C. *Principles of molecular photochemistry : an introduction*; University Science Books: Sausalito, Calif., 2009.

[198] Burland, D. M.; Robinson, G. W. *The Journal of Chemical Physics* **1969**, *51*, 4548–4559.

[199] van der Est, A.; Asano-Someda, M.; Ragogna, P.; Kaizu, Y. *The Journal of Physical Chemistry A* **2002**, *106*, 8531–8542.

[200] Gray, V.; Börjesson, K.; Dzebo, D.; Abrahamsson, M.; Albinsson, B.; Moth-Poulsen, K. *The Journal of Physical Chemistry C* **2016**, *120*, 19018–19026.

[201] Shen, K.; Fu, Y.; Li, J.-N.; Liu, L.; Guo, Q.-X. *Tetrahedron* **2007**, *63*, 1568 – 1576.

[202] Krause-Heuer, A. M.; Yepuri, N. R.; Darwish, T. A.; Holden, P. J. *Molecules* **2014**, *19*, 18604.

[203] Lee, S.-Y.; Paik, S.-Y.; McCamey, D. R.; Yu, J.; Burn, P. L.; Lupton, J. M.; Boehme, C. *Journal of the American Chemical Society* **2011**, *133*, 2019–2021, PMID: 21275069.

[204] Beeby, A.; Parker, A. W.; Simpson, M. S.; Phillips, D. *Journal of Photochemistry and Photobiology B: Biology* **1993**, *17*, 205 – 207.

[205] Birks, J. *Journal of Research of the National Bureau of Standards Section A: Physics and Chemistry* **1976**, *80A*, 389.

[206] Hamai, S.; Hirayama, F. *The Journal of Physical Chemistry* **1983**, *87*, 83–89.

[207] Levitus, M.; Garcia-Garibay, M. A. *The Journal of Physical Chemistry A* **2000**, *104*, 8632–8637.

[208] Lewitzka, F.; Löhmannsröben, H. G. *Z. Phys. Chem. Neue Folge* **1986**, *150*, 69–86.

[209] Nguyen, T. D.; Hukic-Markosian, G.; Wang, F.; Wojcik, L.; Li, X.-G.; Ehrenfreund, E.; Vardeny, Z. V. *Nature Materials* **2010**, *9*, 345–352.

[210] Tong, C. C.; Hwang, K. C. *The Journal of Physical Chemistry C* **2007**, *111*, 3490–3494.

[211] Tsuji, H.; Mitsui, C.; Nakamura, E. *Chem. Commun.* **2014**, *50*, 14870–14872.

[212] Shao, M.; Keum, J.; Chen, J.; He, Y.; Chen, W.; Browning, J. F.; Jakowski, J.; Sumpter, B. G.; Ivanov, I. N.; Ma, Y.-Z.; Rouleau, C. M.; Smith, S. C.; Geohegan, D. B.; Hong, K.; Xiao, K. *Nature Communications* **2014**, *5*, 3180.

[213] Ng, T.-W.; Lo, M.-F.; Lee, S.-T.; Lee, C.-S. *Organic Electronics* **2012**, *13*, 1641 – 1645.

[214] Wu, C. C.; Lin, Y. T.; Chiang, H. H.; Cho, T. Y.; Chen, C. W.; Wong, K. T.; Liao, Y. L.; Lee, G. H.; Peng, S. M. *Applied Physics Letters* **2002**, *81*, 577–579.

[215] Chiang, C.-J.; Kimyonok, A.; Etherington, M. K.; Griffiths, G. C.; Jankus, V.; Turksoy, F.; Monkman, A. P. *Advanced Functional Materials* **2013**, *23*, 739–746.

[216] Nicolai, H. T.; Kuik, M.; Wetzelaer, G. A. H.; de Boer, B.; Campbell, C.; Risko, C.; Brs, J. L.; Blom, P. W. M. *Nat Mater* **2012**, *11*, 882–887, 10.1038/nmat3384.

[217] Hoehne, F.; Dreher, L.; Suckert, M.; Franke, D. P.; Stutzmann, M.; Brandt, M. S. *Physical Review B* **2013**, *88*, 155301.

[218] Baker, W. J.; McCamey, D. R.; van Schooten, K. J.; Lupton, J. M.; Boehme, C. *Physical Review B* **2011**, *84*, 165205.

[219] Baker, W. J.; Ambal, K.; Waters, D. P.; Baarda, R.; Morishita, H.; van Schooten, K.; McCamey, D. R.; Lupton, J. M.; Boehme, C. *Nature Communications* **2012**, *3*, 898.

[220] Baker, W. J.; Keevers, T. L.; Boehme, C.; McCamey, D. R. *arXiv preprint arXiv:1502.05471* **2015**.

[221] Behrends, J.; Schnegg, A.; Lips, K.; Thomsen, E. A.; Pandey, A. K.; Samuel, I. D. W.; Keeble, D. J. *Physical Review Letters* **2010**, *105*, 176601–.

[222] Devir-Wolfman, A. H.; Khachatryan, B.; Gautam, B. R.; Tzabary, L.; Keren, A.; Tessler, N.; Vardeny, Z. V.; Ehrenfreund, E. *Nature Communications* **2014**, *5*, year.

[223] Hu, B.; Yan, L.; Shao, M. *Advanced Materials* **2009**, *21*, 1500–1516.

[224] Hsu, J. W. P.; Yan, M.; Jedju, T. M.; Rothberg, L. J.; Hsieh, B. R. *Physical Review B* **1994**, *49*, 712.

[225] Virgili, T.; Cerullo, G.; Lüer, L.; Lanzani, G.; Gadermaier, C.; Bradley, D. D. C. *Physical Review Letters* **2003**, *90*, 247402–.

[226] Xu, W.-L.; Zeng, P.; Wu, B.; Zheng, F.; Zhu, F.; Smith, T. A.; Ghiggino, K. P.; Hao, X.-T. *The Journal of Physical Chemistry Letters* **2016**, *7*, 1872–1879, PMID: 27140304.

[227] Tayebjee, M. J. Y.; Clady, R. G. C. R.; Schmidt, T. W. *Phys. Chem. Chem. Phys.* **2013**, *15*, 14797–14805.

[228] Di, D.; Yang, L.; Richter, J. M.; Meraldi, L.; Altamimi, R. M.; Alyamani, A. Y.; Credgington, D.; Musselman, K. P.; MacManus-Driscoll, J. L.; Friend, R. H. *Advanced Materials* **2017**, 1605987–n/a, 1605987.

[229] Thompson, N. J.; Hontz, E.; Chang, W.; Van Voorhis, T.; Baldo, M. *Philosophical transactions. Series A, Mathematical, physical, and engineering sciences* **2015**, *373*, 20140323, 25987573[pmid] rsta20140323[PII] Philos Trans A Math Phys Eng Sci.

[230] Mani, T.; Vinogradov, S. A. *The Journal of Physical Chemistry Letters* **2013**, *4*, 2799–2804, PMID: 24143268.

[231] Mani, T.; Tanabe, M.; Yamauchi, S.; Tkachenko, N. V.; Vinogradov, S. A. *The Journal of Physical Chemistry Letters* **2012**, *3*, 3115–3119, PMID: 26296015.

[232] Steiner, U. E.; Ulrich, T. *Chemical Reviews* **1989**, *89*, 51–147.

[233] Suna, A. *Physical Review B* **1970**, *1*, 1716.

[234] Okazaki, M.; Toriyama, K. *The Journal of Physical Chemistry* **1995**, *99*, 17244–17250.

[235] Groff, R. P.; Suna, A.; Avakian, P.; Merrifield, R. E. *Physical Review B* **1974**, *9*, 2655.

[236] Hiromitsu, I.; Kaimori, Y.; Kitano, M.; Ito, T. *Physical Review B* **1999**, *59*, 2151.

[237] Ern, V.; Merrifield, R. E. *Physical Review Letters* **1968**, *21*, 609–.

[238] Benk, H.; Sixl, H. *Molecular Physics* **1981**, *42*, 779–801.

[239] Gorelik, V. R.; Maeda, K.; Yashiro, H.; Murai, H. *The Journal of Physical Chemistry A* **2001**, *105*, 8011–8017.

[240] Kandrashkin, Y.; van der Est, A. *Chemical Physics Letters* **2003**, *379*, 574–580.

[241] Vogel, M. W.; Giorni, A.; Vegh, V.; Pellicer-Guridi, R.; Reutens, D. C. *PLoS ONE* **2016**, *11*, e0157040, PONE-D-16-02834[PII] 27271886[pmid] PLoS One.

[242] Bruckner, F.; Abert, C.; Wautischer, G.; Huber, C.; Vogler, C.; Hinze, M.; Suess, D. *Scientific Reports* **2017**, *7*, 40816.

[243] *Image Intensifier: Phosphor screen*, `http://stanfordcomputeroptics.com/technology/image-intensifier/phosphor-screen.html`, Accessed: 2016-03-21.

[244] Piper, R. B.; Yoshida, M.; Farrell, D. J.; Khoury, T.; Crossley, M. J.; Schmidt, T. W.; Haque, S. A.; Ekins-Daukes, N. *RSC Adv.* **2014**, *4*, 8059–8063.

[245] *Perylene*, `http://omlc.org/spectra/PhotochemCAD/html/023.html`, Accessed: 2017-03-30.

[246] Yokoyama, K.; Wakikawa, Y.; Miura, T.; Fujimori, J.-i.; Ito, F.; Ikoma, T. *The Journal of Physical Chemistry B* **2015**, *119*, 15901–15908, PMID: 26683847.

[247] Cheng, Y. Y.; Fückel, B.; Khoury, T.; Clady, R. G. C. R.; Tayebjee, M. J. Y.; Ekins-Daukes, N. J.; Crossley, M. J.; Schmidt, T. W. *J. Phys. Chem. Lett.* **2010**, *1*, 1795–1799.

[248] Monguzzi, A.; Meinardi, F. *The Journal of Physical Chemistry A* **2014**, *118*, 1439–1442, PMID: 24494929.

[249] Schulze, T. F.; Cheng, Y. Y.; Fückel, B.; MacQueen, R. W.; Danos, A.; Davis, N. J. L. K.; Tayebjee, M. J. Y.; Khoury, T.; Clady, R. G. C. R.; Ekins-Daukes, N. J.; Crossley, M. J.; Stannowski, B.; Lips, K.; Schmidt, T. W. *Aust. J. Chem.* **2012**, *65*, 480–485.

[250] Murov, S. L.; Carmichael, I.; Hug, G. L. *Handbook of Photochemistry*; Marcel Dekker Inc.: New York, 1993; p 208.

[251] Schmidt, R. *Journal of Photochemistry* **1983**, *23*, 379 – 386.

[252] Davis, N. J. L. K.; MacQueen, R. W.; Roberts, D. A.; Danos, A.; Dehn, S.; Perrier, S.; Schmidt, T. W. *J. Mater. Chem. C* **2016**, *4*, 8270–8275.

[253] Monguzzi, A.; Braga, D.; Gandini, M.; Holmberg, V. C.; Kim, D. K.; Sahu, A.; Norris, D. J.; Meinardi, F. *Nano Letters* DOI: 10.1021/nl503322a.

[254] Fasth, A., C. Fuhrer; Björk, M. T.; Samuelson, L. *Nano Letters* **2005**, *5*, 1487–1490.

[255] Haase, M.; Schäfer, H. *Angew. Chem. Int. Ed.* **2011**, *50*, 5808.

[256] Im, J.-H.; Lee, C.-R.; Lee, J.-W.; Park, S.-W.; Park, N.-G. *Nanoscale* **2011**, *3*, 4088–4093.

[257] Son, H.-J.; Jin, S.; Patwardhan, S.; Wezenberg, S. J.; Jeong, N. C.; So, M.; Wilmer, C. E.; Sarjeant, A. A.; Schatz, G. C.; Snurr, R. Q.; Farha, O. K.; Wiederrecht, G. P.; Hupp, J. T. *Journal of the American Chemical Society* **2013**, *135*, 862–869, PMID: 23249338.

[258] Clarke, R. H. *Chemical Physics Letters* **1970**, *6*, 413–416.

[259] El Sayed, M. A.; Tinti, D. S.; Yee, E. M. *The Journal of Chemical Physics* **1969**, *51*, 5721–5723.

[260] McLauchlan, K. A.; Shkrob, I. A.; Yeung, M. T. *Chemical Physics Letters* **1994**, *217*, 157–162.

[261] Nosaka, Y.; Daimon, T.; Nosaka, A. Y.; Murakami, Y. *Phys. Chem. Chem. Phys.* **2004**, *6*, 2917–2918.

[262] Baluschev, S.; Miteva, T.; Yakutkin, V.; Nelles, G.; Yasuda, A.; Wegner, G. *Phys. Rev. Lett.* **2006**, *97*, 143903.

[263] Kondakov, D. Y.; Pawlik, T. D.; Hatwar, T. K.; Spindler, J. P. *Journal of Applied Physics* **2009**, *106*, year.

[264] Burdett, J. J.; Bardeen, C. J. *Journal of the American Chemical Society* **2012**, *134*, 8597–8607.

[265] Porter, G.; Windsor, M. W. *Discuss. Faraday Soc.* **1954**, *17*, 178–186.

[266] Dick, B.; Nickel, B. *Chem. Phys.* **1983**, *78*, 1–16.

[267] Herkstroeter, W.; Merkel, P. *Journal of Photochemistry* **1981**, *16*, 331–341.

[268] Yoichi, M. *Chemical Physics Letters* **2011**, *516*, 56–61.

[269] Groff, R. P.; Avakian, P.; Merrifield, R. E. *Phys. Rev. B* **1970**, *1*, 815–817.

[270] Merrifield, R. E. *The Journal of Chemical Physics* **1968**, *48*, 4318–4319.

[271] Werner, H. J.; Schulten, Z.; Schulten, K. *Journal of Chemical Physics* **1977**, *67*, 646–663.

[272] Schulten, K.; Epstein, I. R. *Journal of Chemical Physics* **1979**, *71*, 309–316.

[273] Faulkner, L. R.; Bard, A. J. *Journal of the American Chemical Society* **1969**, *91*, 6495–6497.

[274] Ibrayev, N. K.; Afanasyev, D. A. *Chemical Physics Letters* **2012**, *538*, 39–45.

[275] Mezyk, J.; Tubino, R.; Monguzzi, A.; Mech, A.; Meinardi, F. *Physical Review Letters* **2009**, *102*, 087404.

[276] Yago, T.; Ishikawa, K.; Katoh, R.; Wakasa, M. *The Journal of Physical Chemistry C* **2016**, *120*, 27858–27870.

[277] Merrifield, R. E. *Pure Appl. Chem.* **1970**, *27*, 481–498.

[278] Powell, B. J. *arXiv preprint arXiv:0906.1640* **2009**.

[279] Poole, C. P.; Farach, H. A. *The Theory of Magnetic Resonance*; Wiley-Interscience New York, 1972.

[280] Vahtras, O.; Loboda, O.; Minaev, B.; ren, H.; Ruud, K. *Chemical Physics* **2002**, *279*, 133–142.

[281] ichi Fujisawa, J.; Ohba, Y.; Yamauchi, S. *Chemical Physics Letters* **1998**, *282*, 181 – 186.

[282] Zawadzki, W.; Pfeffer, P.; Bratschitsch, R.; Chen, Z.; Cundiff, S. T.; Murdin, B. N.; Pidgeon, C. R. *Physical Review B* **2008**, *78*, 245203–.

[283] Elzerman, J. M.; Hanson, R.; Van Beveren, L. H. W.; Witkamp, B.; Vandersypen, L. M. K.; Kouwenhoven, L. P. *Nature* **2004**, *430*, 431–435.

[284] Press, W. *Numerical recipes in C: the art of scientific computing. Volume 1 of Fortran numerical recipes*; University Press, 1992.

[285] Redfield, A. G. *IBM Journal of Research and Development* **1957**, *1*, 19–31.

[286] Kollmar, C.; Sixl, H. *Molecular Physics* **1982**, *45*, 1199–1208.

[287] Keevers, T. L.; McCamey, D. R. *Physical Review B* **2016**, *93*, 045210.

[288] Asano-Someda, M.; van der Est, A.; Krüger, U.; Stehlik, D.; Kaizu, Y.; Levanon, H. *The Journal of Physical Chemistry A* **1999**, *103*, 6704–6714.

[289] Dediu, V. A.; Hueso, L. E.; Bergenti, I.; Taliani, C. *Nature Materials* **2009**, *8*, 707–716.

[290] Lupton, J. M.; McCamey, D. R.; Boehme, C. *ChemPhysChem* **2010**, *11*, 3040.

[291] Wang, J.; Chepelianskii, A.; Gao, F.; Greenham, N. C. *Nature Communications* **2012**, *3*, 1191.

[292] Hirota, N.; Yamauchi, S. *Journal of Photochemistry and Photobiology C: Photochemistry Reviews* **2003**, *4*, 109 – 124.

[293] Geschwind, S.; Collins, R. J.; Schawlow, A. L. *Physical Review Letters* **1959**, *3*, 545.

[294] Greenham, N. C.; Shinar, J.; Partee, J.; Lane, P. A.; Amir, O.; Lu, F.; Friend, R. H. *Physical Review B* **1996**, *53*, 13528–.

[295] Wrachtrup, J.; Von Borczyskowski, C.; Bernard, J.; Orritt, M.; Brown, R. *Nature* **1993**, *363*, 244–245.

[296] Karney, C. F. *Journal of molecular graphics modelling* **2007**, *25*, 595–604, Research Support, U.S. Gov't, Non-P.H.S.

[297] Allen, M. P.; Tildesley, D. J. *Computer simulation of liquids*; Clarendon Press: Oxford, 1998.

[298] Babadi, M.; Everaers, R.; Ejtehadi, M. R. *The Journal of Chemical Physics* **2006**, *124*, 174708–10.

[299] DeVane, R.; Klein, M. L.; Chiu, C.-c.; Nielsen, S. O.; Shinoda, W.; Moore, P. B. *The Journal of Physical Chemistry B* **2010**, *114*, 6386–6393.

[300] Ellis, C. R.; Rudzinski, J. F.; Noid, W. G. *Macromolecular Theory and Simulations* **2011**, *20*, 478–495.

[301] Frenkel, D.; Smit, B. *Understanding molecular simulation from algorithms to applications*, 2002. `http://www.engineeringvillage.com/controller/servlet/OpenURL?genre=book&isbn=9780122673511`.

[302] Chiu, M.; Kee, T. W.; Huang, D. M. *Australian Journal of Chemistry* **2012**, *65*, 463–471.

[303] Sato, R.; Kitoh-Nishioka, H.; Yanai, T.; Shigeta, Y. *Chemistry Letters* **2017**.

[304] Bai, J. W.; Chen, P.; Lei, Y. L.; Zhang, Y.; Zhang, Q. M.; Xiong, Z. H.; Li, F. *Organic Electronics* **2014**, *15*, 169–174.

[305] Marsico, F.; Turshatov, A.; Peköz, R.; Avlasevich, Y.; Wagner, M.; Weber, K.; Donadio, D.; Landfester, K.; Baluschev, S.; Wurm, F. R. *J. Am. Chem. Soc.* **2014**, just accepted, DOI: 10.1021/ja5049412.

[306] Snavely, E. *J. Pet. Technol.; (United States)* **1971**, *23:SPE-3262*, .

[307] Weeter, R. F. *J. Pet. Technol.; (United States)* **1972**, *23:SPE-3351*, .

[308] Weber, R. T. *Bruker ELEXSYS E580 User's Manual*, 2005.

[309] Fujisawa, J.; Ohba, Y.; Yamauchi, S. *Journal of the American Chemical Society* **1997**, *119*, 8736–8737.

[310] Giri, N. K.; Ponce, C. P.; Steer, R. P.; Paige, M. F. *Chem. Phys. Letters* **2014**, *598*, 17–22.

[311] Kirste, B.; Tian, P.; Kalisch, W.; Kurreck, H. *J. Chem. Soc., Perkin Trans. 2* **1995**, 2147–2152.

[312] Bobbert, P. A.; Nguyen, T. D.; Van Oost, F. W. A.; Koopmans, v. B.; Wohlgenannt, M. *Physical Review Letters* **2007**, *99*, 216801.

[313] Baluschev, S.; Keivanidis, P.; Wegner, G.; Jacob, J.; Grimsdale, A.; Müllen, K.; Miteva, T.; Yasuda, A.; Nelles, G. *Appl. Phys. Lett.* **2005**, *86*, 061904.

[314] Hoeben, F. J. M.; Jonkheijm, P.; Meijer, E. W.; Schenning, A. P. H. J. *Chemical Reviews* **2005**, *105*, 1491–1546.

[315] Boutin, P. C.; Ghiggino, K. P.; Kelly, T. L.; Steer, R. P. *J. Phys. Chem. Lett.* **2013**, *4*, 4113–4118.

[316] Singh-Rachford, T. N.; Nayak, A.; Muro-Small, M. L.; Goeb, S.; Therien, M. J.; Castellano, F. N. *J. Am. Chem. Soc.* **2010**, *132*, 14203–14211.

[317] Tanaka, K.; Inafuku, K.; Chujo, Y. *Chem. Commun.* **2010**, *46*, 4378–4380.

[318] Ye, C.; Wang, J.; Wang, X.; Ding, P.; Liang, Z.; Tao, X. *Phys. Chem. Chem. Phys.* **2016**, *18*, 3430–3437.

[319] Wohnhaas, C.; Turshatov, A.; Mailander, V.; Lorenz, S.; Baluschev, S.; Miteva, T.; Landfester, K. *Macromolecular Bioscience* **2011**, *11*, 772–778.

[320] Zhang, C.; Zheng, J. Y.; Zhao, Y. S.; Yao, J. *Chem. Commun.* **2010**, *46*, 4959–4961.

[321] Gross, M.; Muller, D. C.; Nothofer, H.-G.; Scherf, U.; Neher, D.; Brauchle, C.; Meerholz, K. *Nature* **2000**, *405*, 661–665.

[322] Singh-Rachford, T. N.; Lott, J.; Weder, C.; Castellano, F. N. *J. Am. Chem. Soc.* **2009**, *131*, 12007–12014.

[323] Monguzzi, A.; Bianchi, F.; Bianchi, A.; Mauri, M.; Simonutti, R.; Ruffo, R.; Tubino, R.; Meinardi, F. *Advanced Energy Materials* **2013**, *3*, 680–686.

Appendix A

Publications

Guse, J. A.; Jones, T. W.; Danos, A.; McCamey, D. R. Recombination Dynamics in Thin-Film Photovoltaic Materials via Time-resolved Microwave Conductivity. Journal of Visualised Experiments: JoVE, **2017**, e55232

Davis, N.; MacQueen, R.; Roberts, D.; Danos, A.; Dehn, S.; Perrier, S.; Schmidt, T. Energy Transfer In Pendant Perylene Diimide Copolymers. J. Mater. Chem. C **2016**, 4, 8270-8275.

Danos, A.; MacQueen, R.; Cheng, Y.; Dvořák, M.; Darwish, T.; McCamey, D.; Schmidt, T. Deuteration Of Perylene Enhances Photochemical Upconversion Efficiency. J. Phys. Chem. Lett. **2015**, 6, 3061-3066.

MacQueen, R.; Cheng, Y.; Danos, A.; Lips, K.; Schmidt, T. Action Spectrum Experiment For The Measurement Of Incoherent Photon Upconversion Efficiency Under Sun-Like Excitation. RSC Adv. **2014**, 4, 52749-52756.

Keevers, T.; Danos, A.; Schmidt, T.; McCamey, D. An Agnostic Approach. Nature Nanotechnology, **2013**, 8, 886-887.

Schulze, T.; Cheng, Y.; Fückel, B.; MacQueen, R.; Danos, A.; Davis, N.; Tayebjee, M.; Khoury, T.; Clady, R.; Ekins-Daukes, N. et al. Photochemical Upconversion Enhanced Solar Cells: Effect Of A Back Reflector. Australian Journal of Chemistry, **2012**, 65, 480.